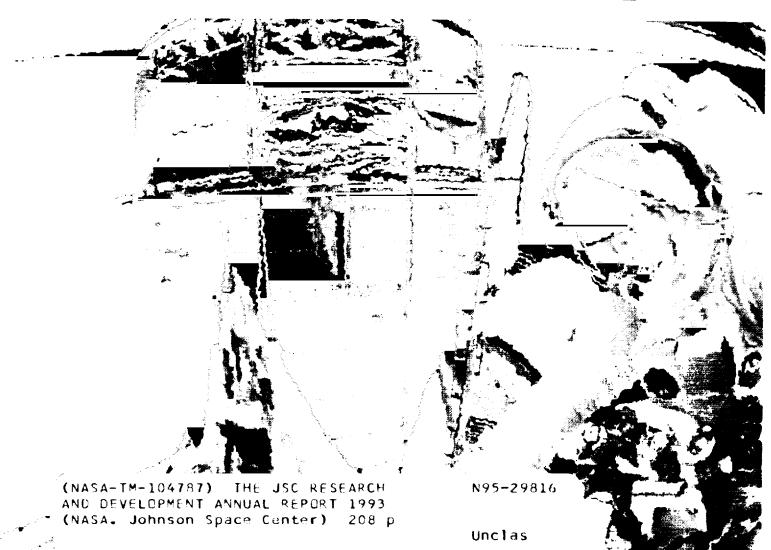
P. 208

Research and Development Annual Report



G3/99 0051491

1994

Research and Development Annual Report 1994

National Aeronautics and Space Administration Lyndon B. Johnson Space Center Houston, Texas

August 1994



Foreword

This is the second year for publication of the Johnson Space Center (JSC) Research and Development Annual Report (RADAR), which serves as a complement to the Research and Technology Annual Report (RTAR). The encouraging comments we received on the first report affirmed the need for this document as an effective mechanism for communicating JSC's accomplishments in the areas of research and technology development.

In the past year, the Agency has developed a new strategic plan. NASA's plan implements our mission and continues to satisfy our customers through five strategic enterprises: Mission to Planet Earth, Aeronautics, Human Exploration and Development of Space, Scientific Research, and Space Technology. One key feature of these enterprises is the contribution to the quality of life on Earth made by knowledge acquired and technology developed as a result of the exploration of space and study of the evolution of life.

Through advanced research and technology efforts, each of NASA's strategic enterprises contributes significantly to our international competitiveness. In turn, these contributions stimulate the economy by developing advanced products and processes for the market place. NASA has developed initiatives that focus on working with the private sector to jointly develop and commercialize new technologies. NASA Administrator Dan Goldin has stated that "Technology transfer is a fundamental mission—it is as important as any other mission—and it must be pursued."

NASA is reassessing, reasserting, and redefining how it works with industry to accelerate the commercialization of its technology. Specifically at JSC, the Center Director, Dr. Carolyn Huntoon, has stated that "you will see us initiating and participating in dual-development consortia, industrial partnerships, regional alliances, small business development, commercial technology acquisition, and fast track mechanisms."

One of JSC's continuing strategic goals is to strengthen the Center as a recognized world-class technical and scientific organization in the conduct of space research and exploration. A key to our success in this, in terms of both excellence in research and technology development and the transfer of that data and technology to the private sector, is enhancing our communication with academia and industry. Because of this, we are committed to publishing the results of our work. Your comments and suggestions are an integral part of that process. Please forward them to me via fax at (713) 244-8452 or by phone at (713) 483-0695.

Kumar Krishen, Ph.D. Chief Technologist

Contents

Foreword	ii
Acronym List	
Computer Hardware and Software	
Applications of Advanced Pattern Classification Methods to Control Center Automation	1-3
C Language Integrated Production System (CLIPS)	1-5
CONFIG—Integrated Engineering of Systems and Operations	1-7
Costmodeler 1.0 An Automated Software Development Cost Estimation Tool	
An Electronic Document Viewing System	
Failure Environment Analysis Tool Applications	
Mission Evaluation Room Intelligent Diagnostic and Analysis System (MIDAS)	
A Prototype Supervised Intelligent Robot for Helping Astronauts	
A Reactive Navigational Controller for Autonomous Mobile Robots	
Reengineering Legacy Software to Object-Oriented Systems	
Virtual Reality in Medical Education and Assessment	
Virtual Reality Library (VRL)	1-48
Medical, Life, and Space Sciences	
The Effect of Gravitational Acceleration on Ventricular Filling:	
Diastolic Ventricular Function in Weightlessness and One-g—Preliminary Results	
Alternative Methods for Measuring Calcium Absorption and Kinetics in Humans Exposed to Microgravity	
Characterization of Spacecraft Humidity Condensate	
Decompression Gas Phase Formation In Simulated Physiological Null Gravity	
Longitudinal Study of Astronaut Health Mortality in the Years 1959-91	
Microgravity Encapsulation of Drugs	
Radiation Damage to Internal Organs from Low Energy Galactic Cosmic Ray Particles	
Radiation Studies on Chromosomal Aberrations in Human Lymphocytes	
Spacecraft Applications of Thermoelectric Refrigeration	
Continuous Blood Pressure Monitor	
Production of Reference Force on the Column of Blood	2-40
Design Considerations in the Development of the Life Sciences Spacelab Refrigerator/Freezer or Why Spaceflight Refrigerators Are Different From Your Domestic Refrigerator	2.49
Gas Analyzer Systems To Support Life Sciences Experiments	
A Passive and Rapid Intravenous Infusion for Use in Spaceflight Experiments	
Refrigerator/Freezer Based on Stirling Cycle Cooler	
Standard Interface Rack (SIR)	
Thermoelectric Freezer	
Mir Interface to Payload Systems (MIPS)	
Estimate of Cancer Risks From Low Earth Orbit Flights	
Stability of White Blood Cells in Whole Blood Stored at Room Temperature	
Discrimination of Ocean Conditions Using Space Shuttle Polarization Photography	
In Situ Resource Utilization — Making Oxygen and Ceramics on the Moon	
Space Systems *	
An Analysis of the Modes and States for Generic Avionics	
Arc-Jet Testing of Damaged RCC-3 Repaired Using Preceramic Polymers	
EMU Electronic Cuff Checklist Development	
Development of Digital Technology for a Reprogrammable Receiver	
Application of Dexterous Space Robotics Technology to Myoelectric Prostheses	
Electromagnetic Probe Technique for Fluid Flow Measurements	
Hybrid Regenerative Water Recovery System	3-28

Hybrid Vision Eye Tracking	3-32
The Materials Chemistry of Atomic Oxygen: Low Earth Orbit (LEO) and the Laboratory	
A Mobile Communications Space Link Between the Space Shuttle Orbiter and	
the Advanced Communications Tracking Satellite	3-48
Orbital Debris Radar Design Study	
Rendezvous and Prox Ops Program New Capability Development	
Standards-Based Autocode Generation for Flight Computers	

Acronym List

A		DPC	distributed pore chemistry
A&RD	Automation and Robotics Division	DPSK	differential phase shift keying
A/D	analog-to-digital	DTO	development test objective
ACD	acid citrate dextrose	DIO	development test objective
ACTS	advanced communications technology	${f E}$	
ACIS	satellite	EM	electromagnetic
ADC	analog-to-digital channels	EMG	electromyographic
ADC	analog-to-digital converter	EMI EMI	electromagnetic interference
AI	artificial intelligence	EMU	extravehicular mobility unit
API	application programming interface	EOIM-III	_
ARC	Ames Research Center	EOIM-III	Evaluation of Oxygen Interactions with Materials-III
		EDE	
ARMSEF	Atmospheric Reentry Materials	ERF	extended real-time FEAT
ACIC	Structures Facility	ESA	European Space Agency
ASIC	application-specific integrated circuit	EVA	extravehicular activity
ATCS	active thermal control system	EVAHR	extravehicular activity helper/retriever
В		F	
BDS	block diagram specification	FDDI	fiber distributed data interface
BFO	blood-forming organs	FDIR	fault detection, isolation, and recovery
BPSK	biphase shift keying	FEAT	failure environment analysis tool
		FES	flash evaporator system
\mathbf{C}		FFT	fast Fourier transform
CAF	computerized anatomical female	FISH	fluorescent in situ hybridization
CAM	computerized anatomical man	FMEA	failure mode effects analysis
CCTV	closed-circuit television	FOV	field of view
CFC	chlorofluorocarbon	FPMM	flow-path management module
CLIM	Common LISP Interface Manager	FRZ	freezer
CLOS	Common LISP Object System	FSSR	Flight Software System Requirements
CPD	crew passive dosimeter	FT/RM	fault tolerance analysis and redundancy
CPU	central processing unit		management
CSDL	Charles Stark Draper Labs		-
CT	computerized axial tomography	\mathbf{G}	
CTSD	Crew and Thermal Systems Division	GAMS	Gas Analyzer Mass Spectrometer
CV/CP	cardiovascular/cardiopulmonary	GASMAP	Gas Analyzer System for Metabolic
CVD	chemical vapor deposition		Physiology
		GCR	galactic cosmic radiation (rays)
D		GI	gastrointestinal
DAC	digital-to-analog channels	GISD	Galveston Independent School District
DAP	digital autopilot	GMT	Greenwich Mean Time
dBi	decibels indirect	GPC	general purpose computer
dBWi	decibels referred to 1 W indirect	GPIB	general purpose interface bus
DC	direct current		
DCS	decompression sickness	H	
DDS	Digraph Data System	HDTV	high definition television
DDT	direct drive test	HL	handheld laser
DGA	digraph analyzer	HMD	head-mounted display
DHM	dexterous hand master	HRM	high rate multiplexer
DIO	digital input/output	HRWRS	hybrid regenerative water recovery
DOE	Department of Energy		system
DOF	degree(s) of freedom	HVAB	high-velocity neutral-atom beam
	-		•

I		MOD	Mission Operations Directorate
I/O	input/output	MRI	magnetic resonance imaging
ICA	infusion cuff assembly	MSL	Model Support Library
ICD	International Classification of Diseases	MTF	modulation transfer function
IEEE	International Electrical, Electronic, and		modulation transfer function
ICCC	Electromechanical	N	
IFTAS	Integrated Fault Tolerant Avionics	NAS	National Academy of Sciences
	System	NCCLS	National Committee for Clinical
IGOAL	Integrated Graphics, Operations, and		Laboratory Standards
	Analysis Laboratory	NCRP	National Council on Radiation
IML	International Microgravity Laboratory		Protection and Measurements
IMU	inertial measurement unit		
IPO	iodinated poppyseed oil	\mathbf{O}	
IRIG-B	interrange instrumentation group B	OAFE	Orbiter/ACTS flight experiment
ISAC	Intelsat solar array coupon	OOM	object orientation manipulator
ISI	Integrated Systems, Inc.	OR/F	Orbiter refrigerator/freezer
IV	intravenous	ORU	orbital replacement unit
т		D	
J		P	
JH	Jameson hand	PC	personal computer
JPL	Jet Propulsion Laboratory	PC-AT	personal computer-advanced
JTC	joint transform correlation	DOM 10 41 1	technology
K cell	killer cell	PCMMU	pulse code master memory unit
KASTA	Ku-Band Automated Self-Test Analyst	PGSC	payload and general support computer
L		PLBAY	payload bay (software)
	To add a company and a	POL	procedure-oriented language
LAN	local area network	PRSD	power reactant storage and distribution
LANL	Los Alamos National Laboratory	PSF PSPA	point spread function
LCD	liquid crystal display	PVC	phase shift/power amplifier module
LDEF	Long-Duration Exposure Facility low Earth orbit	PWM	polyvinylchloride pulse width modulation
LEO LESC	Lockheed Engineering and Sciences	PWW	pulse width modulation
LESC	Company	R	
LET	linear energy transfer	R.O.	reverse osmosis
LSAH	longitudinal study on astronaut health	RAP	reactive action packages
LSF	line spread function	RC	rack controller
LSPD	Life Sciences Project Division	RCS	reaction control system
LV	left ventricle	REF	refrigerator
LVLH	local vertical local horizontal	RFP	request for proposals
BVBII	ioda vortom ioda iodas	RM	redundancy management
M		RMS	remote manipulator system
mAb	monoclonal antibodies	RPOP	Rendezvous and Prox Ops Program
MAN	manual		The state of the s
MDA	materials dispersion apparatus	S	
	McDonnell Douglas Aerospace	SBC	single based computer
MER	Mission Evaluation Room	SCSI	small computer system interface
MET	mission elapsed time	SIR	standard interface rack
MICOM	(Army) Missile Command	SIRA	Shuttle Integrated Risk Assessment
MIDAS	MER Intelligent Diagnostic and	SL-J	Japanese Spacelab [mission]
	Analysis System	SLS	Spacelab life sciences [missions]
MIPS	Mir interface to payload systems	SMR	standardized mortality ratio
mips	million instructions per second	SMU	single motor unit
MIT	Massachusetts Institute of Technology	SOR/F	Stirling Orbiter refrigerator/freezer
MMIC	monolithic microwave integrated circuit	SPAS	Space Pallet Satellite
	č		-

SSEIC Space Station engineering integration

contractor

SSF Space Station Freedom

SSFP Space Station Freedom Program

SSM Solid Surface Modeler

STS Space Transportation System SwRI Southwest Research Institute

T

TCS trajectory control sensor TDS total dissolved solids TEF thermoelectric freezer

TERF thermoelectric refrigerator freezer
TIMS thermal ionization mass spectrometer

TLD thermoluminescent dosimeter TLH translational hand controller

TMIS Technical Management Information

System

TOC total organic carbon TOF time of flight

TTL transistor-transistor logic

U

UCB user code block UCS user clock signal

UMDH Utah/MIT dexterous hand

UMKC University of Missouri/Kansas City
UTMB University of Texas Medical Branch at

Galveston

UV ultraviolet

V

VCXO voltage controlled crystal oscillator
VDAS Video Digital Analysis System
VIVED Virtual Visual Environment Display

VME Versa-Module Eurocard VRL Virtual Reality Library

VR virtual reality VUV vacuum ultraviolet

W

WBC white blood cell
WSF Wake Shield Facility

WWCTS waste water collection and transport

system

 \mathbf{X}

XPS X-ray photoelectron spectroscopy

Computer Hardware and Software

Applications of Advanced Pattern Classification Methods to Control Center Automation

Robert O. Shelton Johnson Space Center/PT

Introduction

Over the past several years, the Software Technology branch (STB) has maintained a state-of-the-art program of research and development in the general area of Advanced Software Architectures (ASAs), a broad area including neural networks, fuzzy logic, signal and image processing, and genetic algorithms. This research has led to a number of papers and patents as well as popular software products such as NETS and Splicer. The subject of this report is an application that has rapidly moved these methods from the laboratory into the Mission Control Center (MCC) as tools for flight controllers.

Problem Statement/Description

In the MCC, controllers visually monitor critical systems on the Space Shuttle Orbiter by means of paper strip chart displays. In some cases, such as that of the Electrical Generation and Integrated Loading (EGIL) system (fig. 1), the controllers must recognize signatures of various events by inspection of the strip chart in order to track the state of the system, i.e., which loads are present at any given time.

With the introduction of the Real-Time Data System (RTDS) which makes over 7500 shuttle telemetry channels available on conventional workstations at JSC as well as other NASA centers, it is now possible for researchers to tap into real-time data in order to develop advanced automation techniques with real, live data. To facilitate the application of advanced software technology to issues of control center automation, it was decided that a tool kit for pattern recognition would be assembled. This set of tools would include software for data acquisition, management of training/test databases, pattern recognition, event detection, signal processing, and application configuration. The applications spawned from the basic tool box would be tailored to specific flight control disciplines, would run on RTDS workstations (including those in the control center), and identify signatures in real time.

Approach

As a first test of the concepts, the EGIL flight control discipline was selected as the target domain for an initial prototype application. The EGIL signatures provide an ideal situation in which advanced pattern recognition methods could be tested and, if successful, contribute significantly to improved efficiency and safety in an

operations environment. To this end, a team was assembled in late 1992 to build the prototype EGIL application. The initial prototype would subsequently be generalized to form the nucleus of the tool kit. In particular, the EGIL application, which accesses electrical power utilization information using RTDS services, includes a screening algorithm that captures events and several pattern recognition algorithms that process these events. The algorithms tested to date include cross correlation, a Bayesian classifier, a back-propagation neural network classifier, a "binary" neural network, and a basis function classifier. This application has run in the MCC as well as on distributed RTDS workstations during six shuttle flights. The classification methods are evaluated post-flight by comparison with controller logs and consultation with EGIL controllers. During the course of the development of the EGIL application three techniques (the Bayesian classifier, the neural network, and the basis function classifier) emerged as viable candidates for on-line processing of EGIL signatures achieving percent correct scores that improved from the low 70's to the current mark, which is in the mid 90's.

Consistent with the original thrust of the project, the initial architecture has been generalized to provide the capability of generating discipline-specific applications. The basic form of the tool kit is the "plug-in module" architecture which allows application developers to write or select existing software modules and generate the desired application by specifying a data flow graph. The plug-in architecture has been used to construct the latest version of the EGIL application and a new application to do spectral analysis of accelerometer output from inertial platforms.

The tool kit is not a showcase for any particular technology, but is sufficiently generic to provide a framework for multiple signal identification methods to be applied to any set of channels supplied by RTDS. To this end, the techniques listed above have been tried and evaluated, with the results documented in post-flight reports. The methods that have been implemented range from the classical cross-correlation algorithm which essentially matches the incoming signal against stored templates to a Bayesian classifier using hand-coded feature extraction, to several purely data-driven methods—the neural network approaches. All of these methods have characteristics which make them desirable in some ways and undesirable in others, and it is clear now that the method used for a final MCC application would include components from neural networks, statistical classifiers (the Bayesian approach) and some sort of nearest

neighbor scheme such as cross correlation. By providing for the construction of hybrid techniques the strengths of each method can be exploited to yield the best possible end application.

The core application was built by David Hammen (The MITRE Corporation) and Dr. Robert Shelton (STB). Important contributions were provided by Dr. Philip Laird (ARC), Ron Saul (Recom Technologies, Mountain View CA.), Dr. Travis Moebes (SAIC Houston), and two STB co-op students, Robert Jones and Robin Benedetti. The team reported directly to Chris Culbert (STB) and Linda Perrine (MOD) in weekly meetings.

Because the project was built from multiple software modules from various sources, an informal but strict system of configuration management was adopted. Early on, the outlines of the final tool kit and the interfaces between components were established. Since the project involved researchers from two centers in geographically separate locations, electronic mail, teleconferences, fax and internet remote login capabilities were used extensively.

Results

Given the success of the prototype EGIL application, this project will extend in two directions during the next year. Along one path, the EGIL application will be improved to include more signatures, and increase the accuracy of identification to a target percentage in the high 90's. The second path will involve the application of the basic tool kit to other MCC disciplines. Work has already begun on the latter path, where an application is being developed to help the Guidance, Navigation, and Control flight controllers analyze inertial measurement unit behavior.

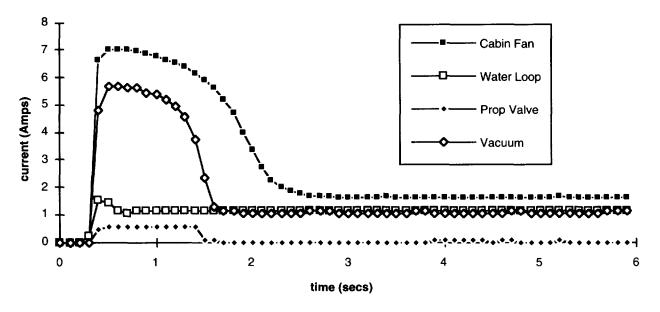


Figure 1. Sample electrical equipment activation signatures.

C Language Integrated Production System (CLIPS)

Gary Riley and Brian Donnell Johnson Space Center/PT

Conventional programming languages, such as FOR-TRAN and C, are designed and optimized for the procedural manipulation of data (such as numbers and arrays). Humans, however, often solve complex problems using very abstract, symbolic approaches which are not well suited for implementation in conventional languages. Although abstract information can be modeled in these languages, considerable programming effort is required to transform the information to a format usable with procedural programming paradigms.

One of the results of research in the area of artificial intelligence has been the development of techniques which allow the modeling of information at higher levels of abstraction. These techniques are embodied in languages or tools which allow programs to be built that closely resemble human logic in their implementation and are therefore easier to develop and maintain. These programs, which emulate human expertise in well defined problem domains, are called expert systems. The potential payoff from expert systems is high: valuable expertise can be captured and preserved, repetitive and/or mundane tasks requiring human expertise can be automated, and uniformity can be applied in decision-making processes. The availability of expert system tools has greatly reduced the effort and cost involved in developing an expert system and an entire industry has grown to support the development of these types of specialized tools.

Despite the wide variety of expert system tools available, expert systems had generally failed to make a major impact in application environments by the mid 1980s. In part, this failure was caused by a lack of options for deploying expert system applications within conventional computing environments. To solve this problem, the Software Technology Branch at JSC developed the initial version of the C Language Integrated Production System (CLIPS) in 1985. CLIPS was designed to address several issues key to NASA. Among these were the ability to run on a wide variety of conventional hardware platforms, the ability to be integrated with and embedded within conventional software systems, and the ability to provide low cost options for the development and delivery of expert systems. At the time of its development, CLIPS was one of the few tools that was written in C and capable of

running on a wide variety of conventional platforms. CLIPS is a continually evolving product with new features and capabilities added on a regular basis. The latest version of CLIPS, version 6.0, was released in May of 1993. Machine specific interfaces have been developed for Apple Macintosh, Microsoft Windows, and X Window environments. Figure 1 shows the CLIPS interface for the Macintosh computer. A version of CLIPS written completely in Ada, CLIPS/Ada, has also been developed.

Although originally developed to aid in the construction of aerospace-related expert systems, CLIPS has become a shining example of NASA's technology transfer program with over 5,000 users worldwide. In addition to its widespread use throughout NASA, the military, and numerous Federal bureaus and agencies, CLIPS is also widely used throughout industry and academia. CLIPS has been made available to the general public for a nominal fee through the Computer Software Management and Information Center, the distribution point for NASA software. At Cornell University, CLIPS was used to develop decision support systems to help in the management of dairy herds. At California Polytechnic State University, CLIPS was used to develop software which automates the complicated and costly process of consultation and revision among architects, structural engineers, and other specialists involved in home or office building design. At Cray Research, Inc., CLIPS was used to develop an expert system for the diagnosis and repair of the Cray-3 supercomputer. At Clarity Software, Inc., CLIPS was used to develop a "smart" mail program to help users manage their electronic mail. At the law firm of Brooke & Brooke, CLIPS is used to decide which facts from a casefile are most pertinent and should be included in a legal pleading for the court. Because the CLIPS source code is readily available, numerous groups have saved years of development time by using CLIPS as the basis for their own expert system tools. To date, three commercially available tools have been derived from CLIPS. In general, the development of CLIPS has helped to improve the ability to deliver expert system technology throughout the public and private sectors for a wide range of applications and diverse computing environments.

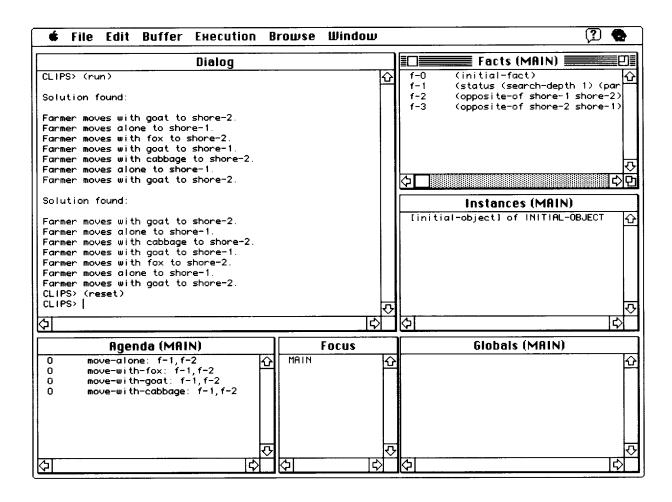


Figure 1. CLIPS Macintosh interface.

CONFIG—Integrated Engineering of Systems and Operations

Jane T. Malin Johnson Space Center/ER

Abstract

CONFIG 3 is a prototype software tool that supports integrated conceptual design evaluation early in the product life cycle. It supports isolated or integrated modeling, simulation, and analysis of the function, structure, behavior, failures, and operation of system designs. Integration and reuse of models is supported in an object-oriented environment providing capabilities for graph analysis and discrete event simulation. Integration is supported among diverse modeling approaches (component view, configuration or flow path view, and procedure view) and diverse simulation and analysis approaches. Diverse design domains, including mechanical and electro-mechanical systems, distributed computer systems, and chemical processing systems, are provided for integrated engineering support.

Introduction

The core of engineering design and evaluation is analysis of physical design. Thus, today's computer-aided engineering software packages often do not provide for conceptual design evaluation early in the life cycle or for engineering for operation, fault management, or supportability (reliability and maintainability). Benefits of engineering for operations and supportability include more robust systems that meet customer needs better and that are easier to operate, maintain and repair. Benefits of concurrent engineering include reduced costs and shortened time for system development. Integrated modeling and analysis of system function, structure, behavior, failures, and operation is needed early in the life cycle.

Problem

Conventional system modeling approaches are not well suited for evaluating conceptual designs early in the system life cycle because they require more knowledge of geometric or performance parameters than is usually available early in design. More abstract models can support early conceptual design definition and evaluation, and also remain useful for some later analyses. Component-connection models provide one such useful abstraction, and discrete events another. Discrete event simulation technology combines both abstractions, for evaluation of conceptual designs of equipment configurations in operations research.³ CONFIG uses these abstractions, with some enhancements, to define and evaluate conceptual designs for several types of systems.

The initial CONFIG project goal was to support simulation studies for design of automated diagnostic

software for new life-support systems⁹. The problem was to design an "expert system" on-line troubleshooter before there was an expert. The design engineer could use a model of the system to support what-if analyses of failure propagation, interaction, observability, and testability. This activity is similar to failure modes and effects analysis⁵, but uses comparative simulations of failure effects to develop diagnostic software. Conventional simulation software was not up to this challenge, but discrete event simulation software has been. CONFIG supports the use of qualitative models for applying discrete event simulation to continuous systems.

CONFIG Goals

A major design goal for CONFIG is to support conceptual design for operations and safety engineering. Major tasks in conceptual design are design definition, evaluation (by simulation and analysis), and documentation. Operations engineering focuses on the design of systems and procedures for operating, controlling, and managing the system in normal or faulty conditions. Safety engineering focuses on prevention of hazardous effects and conditions in the physical system or its operation. In these types of engineering, complex interactions and interfaces among system components and operations must be emphasized.

Another design goal of CONFIG is to bridge the gaps between physical design engineering and other types of engineering. Component-connection representations are well suited for modeling and defining physical system designs (as structures of interacting components) and operations designs (as structures of interacting actions), as well as interactions between system components and operational actions. Discrete event models have been used for this type of modeling for queueing and scheduling problems, but can be extended to support conceptual modeling in operations and safety engineering. This type of modeling is also compatible with systems engineering function diagrams.

Approach

The CONFIG 3 project approach has been to incrementally integrate advanced modeling and analysis technology with more conventional technology. The prototype integrates qualitative modeling, discrete event simulation, and directed graph analysis technologies for use in analyzing normal and faulty behaviors of dynamic systems and their operations. The prototype has been designed for modularity, portability and extensibility. A generic directed graph element design has been used to

standardize model element designs and to promote extensibility. This directed graph framework supports integration of levels of modeling abstraction and integration of alternative types of model elements.

Enhanced Discrete Event Simulation Capabilities

In traditional discrete event modeling and simulation, state changes in a system's entities, called events, occur discretely rather than continuously, at nonuniform intervals of time. Throughout simulation, new events are added to an event list that contains records of events and the times they are scheduled to occur. Simulation processing jumps from one event to the next, rather than occurring at a regular time interval. Computation that results in creation of new events is localized in components, which are connected in a network. Any simulation run produces a particular history of the states of the system. Statistical simulation experiments, using random variables in repeated simulation runs, are used to compare design alternatives.

To enhance this discrete event simulation approach to accommodate continuous systems, a number of new concepts and methods were developed. These include component models with operating modes, types of links connecting components ("relations" and "variable clusters"), state transition structures ("processes"), methods for representing qualitative and quantitative functions ("process language"), and a new simulation control approach.

Digraph Analysis Capabilities

The CONFIG Digraph Analyzer (DGA) makes graph analysis techniques available for evaluating conceptual designs of systems and their operations. The DGA is based on reachability search, and is implemented generically for application to the many types of graph data structures in CONFIG. DGA can support analyses of completeness, consistency, and modularity. Analysis of failure sources and impacts can be done by tracing the paths from a given failure.

System Modeling

Devices are the basic components of a CONFIG system model, connected together in topological model structures with relations. Device behavior is defined in operating and failure modes, which contain mode dependent and mode transition processes. Modes are connected in a mode transition digraph which delineates the transition dependencies among the individual modes.

Device processes define change events in device variables, and are conditionally invoked and executed with appropriate delays during a simulation. Processes define time-related behavioral effects of changes to device input variables, both direction of change and the new discrete

value that will be reached, possibly after a delay. Faults and failures can be modeled in two distinctly different ways. Failure modes can be used to model device faults. Mode-transition processes can be used to model latent device failures that cause unintended mode changes. Relations connect devices via their variables, so that state changes can propagate along these relations during simulations. Related variables are organized into variable clusters, to separate types of relations by domain (e.g., electrical vs. fluid connections). Relations can also connect devices with device-controlling activities in operations models.

Flow Path Modeling

Flow is a property of many systems, whether the substance flowing is a liquid or information. There are two difficulties in modeling flows with local device processes. First, flow is a global property of the topology of the modeled system and the substances flowing within it. Second, while dynamic changes in system structure and flow can occur during operations, process descriptions involving flow must often rely on assumptions of static system topology. These factors would limit the reusability of device descriptions to a limited set of system structures.

A flow-path management module (FPMM) has been implemented to address these problems. The FPMM is separate from the module implementing local device behavior, but the two modules are interfaced via flow-related state variables in the devices. When FPMM is notified during simulation of a local change in device state, it recomputes the global effects on flows produced by the local state change. The FPMM then updates the state of flow in all affected devices. This design permits the user to write reusable local device process descriptions that do not depend on any assumptions concerning the system topology.

FPMM uses a simplified representation of the system, as a collection of aggregate objects, or "circuits." Further abstraction is achieved by identifying serial and parallel clusters in the circuit. In many cases, configuration determination alone is sufficient to verify flow/effort path designs, to establish flow paths for a continuous simulation, for reconfiguration planning, and for troubleshooting analysis (see Ref. 2 on cluster-based design of procedures for diagnosis, test, repair, and workaround in a system).

Operations Modeling

Activities are the basic components of a CONFIG operations model, and are connected together in action structures with relations. They represent procedures or protocols that interact with the system to control and use it to achieve goals or functions. Each activity model can include specifications for what it is intended to achieve or

maintain. Activity behavior is controlled in a sequence of phases, ending in an evaluation of results. Activity behavior is defined by processes that model direct effects of actions, or that control device operation and mode transitions to achieve activity goals. Relations define sequencing and control between activities and connect devices with device-controlling activities.

Operations models are designed to support operation analysis with procedure models. These models are designed to support analysis of plans and procedures for nominal or off-nominal operation. The procedure modeling elements are designed for reuse by intelligent replanning software, and for compatibility with functional modeling in systems engineering.

Model Development & Integration Capabilities and Approach

CONFIG provides intelligent automation to support nonprogrammer and nonspecialist use and understanding. CONFIG embeds object-oriented model libraries in an easy-to-use tool kit with interactive graphics and automatic programming.

CONFIG provides extensive support for three separable yet tightly integrated phases of user operation during a modeling session: Library Design, Model Building, and Simulation and Analysis. This includes a graphical user interface for automated support of modeling during each of the phases including the development of object-oriented library element classes or templates, the construction of models from these library items, model inspection and verification, and running simulations and analyses.

The integration of the phases enables an incremental approach to the modeling process. Lessons learned from analyses can be repeatedly and rapidly incorporated by the user into an initially simple model. Support for these phases as separate user activities fosters the achievement of concurrent engineering goals. Different users can define library elements, build models, and analyze models at different times depending on area of expertise and availability of resources. Support for the model building phases spans all types of modeling that can be performed in CONFIG, including component structure, behavior and flow, and activity goals and structure.

Hosting

CONFIG is implemented in software that is portable to most Unix workstations. The Common LISP Object System (CLOS) is a highly standardized language, with compilers for most of the commonly available workstations. The user interface was implemented using the Common LISP Interface Manager (CLIM), another standardized tool built on CLOS.

Conclusions

CONFIG is designed to model many types of systems in which discrete and continuous processes occur. The CONFIG 2 prototype was used to model and analyze (1) a simple two-phase thermal control system based on a Space Station prototype thermal bus, (2) a reconfigurable computer network with alternate communications protocols, and (3) Space Shuttle remote manipulator system latching and deployment subsystems.⁷ The core ideas of CONFIG have been patented.⁸ CONFIG 3 has added capabilities for graph analysis and for modeling operations and procedures.

The CONFIG prototype demonstrates advanced integrated modeling, simulation, and analysis to support integrated and coordinated engineering. CONFIG supports qualitative and symbolic modeling, for early conceptual design. System models are component structure models with operating modes, with embedded time-related behavior models. CONFIG supports failure modeling and modeling of state or configuration changes that result in dynamic changes in dependencies among components. Operations and procedure models are activity structure models that interact with system models. The models support simulation and analysis both of monitoring and diagnosis systems and of operation itself. CONFIG is designed to support evaluation of system operability, diagnosability, and fault tolerance. It also provides analysis of the development of system effects of problems over time, including faults, failures, and procedural or environmental difficulties.

Acknowledgments

The authors wish to thank Bryan Basham, Leslie Ambrose, Ralph Krog, Debra Schreckenghost, Brian Cox, Daniel Leifker and Sherry Land for their contributions to CONFIG design and implementation.

References

- ¹Alford, M., "Strengthening the System Engineering Process," *Engineering Management Journal*, Vol. 4, No. 1, March, 1992, pp 7-14.
- ²Farley, A. M., "Cluster-based Representation of Hydraulic Systems," *Proc. 4th Conference on AI Applications*, March 1988, pp. 358-364.
- ³Fishman, G. S., *Principles of Discrete Event Simulation*. Wiley, New York, 1978.
- ⁴Forbus, K., "Qualitative Physics: Past, Present, and Future," *Exploring Artificial Intelligence*, edited by H. Shrobe and AAAI, Morgan Kaufmann, San Mateo, CA, 1988.
- ⁵Fullwood, R. R., and Hall, R. E., *Probabilistic Risk Assessment in the Nuclear Power Industry:*

- Fundamentals and Applications. Pergamon Press, 1988
- ⁶Liu, Z., and Farley, A. M., "Structural Aggregation in Common-Sense Reasoning," *Proc. 9th National Conference on Artificial Intelligence (AAAI-91)*, 1991, pp. 868-873.
- Malin, J. T., Basham, B. D., and Harris, R. A., "Use of Qualitative Models in Discrete Event Simulation for Analysis of Malfunctions in Continuous Processing Systems," *Artificial Intelligence in Process* Engineering, edited by M. Mavrovouniotis, Academic Press, 1990, pp. 37-79.
- Malin, J. T., et al., "Discrete Event Simulation Tool for Analysis of Qualitative Models of Continuous Processing Systems," U. S. Patent 4,965,743, October 1990.
- Malin, J. T., and Lance, N., "Processes in Construction of Failure Management Expert Systems from Device Design Information," *IEEE Trans. on Systems, Man, and Cybernetics*, 1987, SMC-17, 956-967.
- Malin, J. T., and Leifker, D. B., "Functional Modeling with Goal-Oriented Activities for Analysis of Effects of Failures on Functions and Operations," *Informatics and Telematics*, 1991, 8(4), pp 353-364.

Costmodeler 1.0 An Automated Software Development Cost Estimation Tool

G. Bernie Roush and Robert G. Phillips*

Johnson Space Center/PT

*MITRE

Introduction

The cost of developing computer software continues to consume an increasing portion of many organizations' total budgets, both in the public and private sector. The capability to produce reliable estimates of the effort and schedule required to develop a candidate software product becomes more important as this trend develops. The program called COSTMODELER (CM) was developed to provide an in-house capability to perform development cost estimates for NASA software projects. CM is an automated software development cost estimation tool which incorporates a generalized cost model template based upon five accepted cost estimation algorithms, including the latest models for Ada development and incrementally developed projects. The principal characteristic that sets CM apart from the other software cost estimation programs is that it uses a model template that supports multiple user-configurable models rather than a single model definition. New models can be designed within the template, and all of the models can be recali-brated and redesigned to better reflect an organization's known productivity data and development environment. Careful use of the capabilities in CM can significantly reduce the risk of cost overruns and failed projects.

Problem Statement/Description

Several commercial software cost estimation tools are presently available. However, their cost makes them most appropriate for use in central cost analysis offices as opposed to being distributed to a fairly large number of middle managers. NASA management therefore decided to initiate the development of an in-house tool that would contain multiple estimating models, could be freely distributed within the agency, and could be completely customized to adapt to the changing NASA software development environment. This tool would also be sufficiently user friendly that it would be useful to people who were not professional cost analysts without requiring formal user training.

The original program, called COSTMODL, was developed in 1986. It provided several distinct models for performing software development cost analysis. This program has enjoyed broad acceptance within the software cost estimation community. It is currently being used at more than 400 installations throughout the aerospace community, government agencies, DOD, and academia. It is a principal estimating tool in use at NATO headquarters in Brussels. It is also being used as a

teaching tool at several universities, and was recently selected as the best overall implementation of the Constructive Cost Model (COCOMO) in a competitive evaluation conducted by MIT's Sloan School of Management. COCOMO is a set of several widely used software costing models originally developed by Dr. Barry Boehm in 1981. COSTMODL is also being distributed to the students and staff at the Defense Systems Management College. This distribution channel results in COSTMODL being introduced to approximately 300 organizations per year throughout DOD.

Program Description

While the individual models in COSTMODL could be calibrated in a limited fashion, they could not be significantly modified. Also, the code had become obsolete in terms of data manipulation and storage, user interface, and maintainability. There were a number of changes needed in COSTMODL that were determined over the course of five years of user support for the old tool. Most importantly, better support for using the estimate throughout the actual development life cycle to monitor progress was desired. This capability would provide incentive for project managers to collect actual development cost data that could be used to better calibrate existing models and develop new models if needed.

To incorporate these needed changes and to better provide for future enhancements, it was decided to completely re-engineer the old tool. Since the new tool was to be a complete replacement, rather than simply an upgrade, the name was changed to CM.

Results

During the 1993 fiscal year, the new program was completely designed, implemented, and tested. Distribution began in October, 1993. The final products were the CM program itself, a users manual, and a technical manual. CM was written in object-oriented Pascal and runs on IBM PCs and compatibles. This platform was chosen because this class of computers is most widely used by managers and project leaders throughout NASA. CM contains many significant features and capabilities, which are discussed following.

CM uses model templates to define the estimation models. Each model consists of five parts: the basic effort and schedule equations, the cost driver definitions, the life cycle definition, the function point sizing definitions, and the language definitions. These various parts can be recombined to form new models, and new parts can be created as desired. CM is shipped with several standard models, including the four most commonly used COCOMO models, a model developed at JSC called KISS, and a COCOMO variant developed by the Air Force called REVIC.

Each estimate can be decomposed into a hierarchy of subcomponents to any desired level of detail. The user can navigate the potentially complex project structure using a graphic structure browser. Extensive use of default values at all levels ensures data consistency and minimizes user inputs.

An incremental development model gives a flexible mechanism for producing estimates for projects that consist of a series of sub-projects, each with its own deliverable.

The subcomponent sizes and cost driver values for each subcomponent can each be defined using a normal, beta, or uniform distribution. These ranges of uncertainty can be used in a Monte Carlo simulation to determine the total uncertainty in project size, effort, and schedule.

Actual project data can be imported and automatically compared with the estimated values to determine where the actual and estimated values have deviated. The estimate can then be revised to better fit the actual, and reasons for the discrepancy can be investigated.

Extensive annotation capabilities can be used to describe all model parts and all components in an estimate. This can be used to document all decisions, sources of information, etc., used to produce the estimates.

A complete data management and protection system provides support for multiple users and password protection. Multiple versions of an estimate can be

created and managed to provide estimates using different scenarios or a time sequence of estimates.

A sophisticated graphical user interface provided many tools for greater productivity, such as context-sensitive hypertext help, on-screen graphs, and reports. Complete reporting capabilities provide access to all data in the system.

Future Plans

CM has already received very favorable reviews from the user community. Future work will emphasize training and user support to maximize the possible benefits. Future plans for CM include developing training material and providing support for cost estimation at JSC. In particular, there are plans to support the software metrics work in other NASA organizations by providing an interface mechanism between other metrics tools and CM. There are several enhancements to CM being considered, including automated model calibration, enhanced printing capabilities, and enhanced import/export capabilities. If there is a need within NASA, the work may also include porting the tool to UNIX, Windows, and/or Macintosh platforms.

References

- A. J. Albrecht, "Measuring Application Development Productivity," SHARE-GUIDE, 1979, pp. 83-92.
- B. W. Boehm, "Software Engineering Economics," 1981.
- B. W. Boehm, "Ada COCOMO: TRW IOC Version," Third Annual COCOMO Users' Group Meeting, November 1987.

An Electronic Document Viewing System

Lui Wang, Bebe Ly, Albert Leigh*, Stan Smith*, Zack Crues*, and Wes White**

Johnson Space Center

*LinCom

**I-Net

NASA's space program, like many other technical programs of its magnitude, is supported by a large volume of technical documents. These documents are diverse as well as abundant. Management, maintenance, and retrieval of these documents is a challenging problem by itself, but relating and cross-referencing this wealth of information when it is all on a medium of paper is an even greater challenge.

HyperMan (Hypertext-Manual) is a software tool which enables the users of technical documentation, such as flight controllers, to have rapid on-line access to information with a full range of hypermedia capabilities. The system supports exact page representation of paper-based documents with hypertext features. The features support functions such as full-text search, key word search, data retrieval, and traversal between nodes of information as

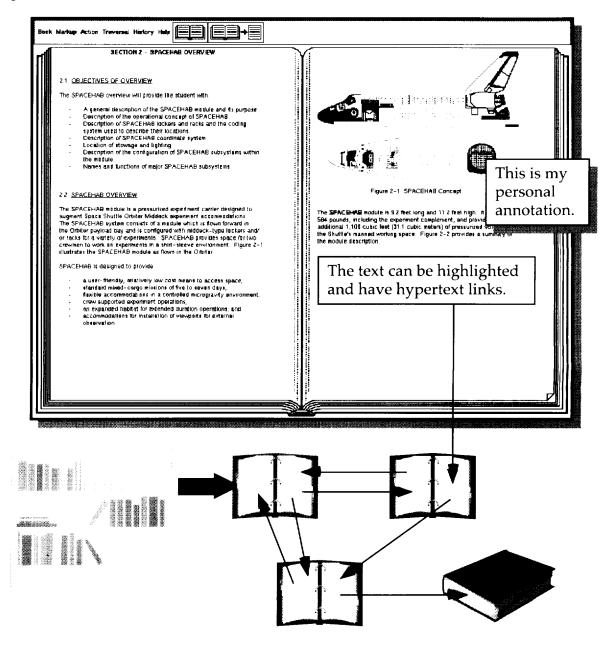


Figure 1. The HyperMan System.

well as speeding up the data access rate. They enable pertinent documents to have relationships and allow the user to explore information naturally through non-linear links. In addition, HyperMan is designed for ease of use and minimum training requirement. It provides hypermedia capabilities for the user without imposing hypermedia theory and skill requirements. HyperMan supports many of the traditional pencil and paper tools for annotation, such as electronic notepads, highlight markers and bookmarks. These capabilities are essential for the flight controllers to perform their normal duties. Figure 1 depicts some basic functions of HyperMan viewer. HyperMan can currently import ProWrite and Microsoft Word documents. HyperMan automatically creates the table of contents and navigational links for direct access

to sections, figures and keywords. Presently, HyperMan is being used as the on-line training manual for the SpaceHab Intelligent Familiarization Trainer (SHIFT).

The original intent of this project is to support the use of electronic document viewing for rapid access of information in the Mission Control Center environment. The HyperMan system is being extended to be used in the office environment, to support heterogeneous platforms, to be able to import various document formats, and to eventually support wide area networking capability. New features such as shared and persistent annotations across different versions of a document are being added. Based on the object modeling technique (OMT) and object-oriented design, the system can further be extended to provide multimedia capabilities.

Failure Environment Analysis Tool Applications

Ginger L. Pack and David B. Wadsworth*

Johnson Space Center

*Lockheed

Abstract

Understanding risks and avoiding failure are daily concerns for the women and men of NASA. Although NASA's mission propels us to push the limits of technology, and though the risks are considerable, the NASA community has instilled within it the determination to preserve the integrity of the systems upon which our mission and our employees' lives and well-being depend. One of the ways this is being done is by expanding and improving the tools used to perform risk assessment. The failure environment analysis tool (FEAT) was developed to help engineers and analysts more thoroughly and reliably conduct risk assessment and failure analysis. FEAT accomplishes this by providing answers to questions regarding what might have caused a particular failure; or, conversely, what effect the occurrence of a failure might have on an entire system. Additionally, FEAT can determine what common causes could have resulted in other combinations of failures. FEAT will even help determine the vulnerability of a system to failures, in light of reduced capability. FEAT also is useful in training personnel who must develop an understanding of particular systems. FEAT facilitates training on system behavior by providing an automated environment in which to conduct "whatif" evaluation. These types of analyses make FEAT a valuable tool for engineers and operations personnel in the design, analysis, and operation of NASA space systems.

Introduction

FEAT was developed as part of an effort to find ways to better identify and understand potential failures that threaten the integrity of NASA systems. Past and current methods of failure assessment consist of developing often enormous amounts of documentation in the form of failure mode effect analysis (FMEA) worksheets. Engineers create these worksheets by attempting to exhaustively enumerate potential system failures and consequences. Hazards analysis is performed in a similar manner; experts are gathered together and are asked to brainstorm about the hazardous manifestations of various failures. System knowledge and experience are necessary for ensuring the comprehensiveness of this approach. However, there are troubling drawbacks to this technique. First, it is difficult to anticipate every scenario. Analysis is also inherently constrained by the limits of actual experience. Further, such methods lack consistency and do not enforce a standard level of coverage. Although there is certainly much to be credited to knowledge

acquired through experience, it is not sufficient to avoid unanticipated interactions which may lead unexpectedly to undesirable consequences. As many industries have learned, experience sometimes comes at too high a cost. NASA has been looking for better ways to anticipate failure and for tools to assist in "designing out" potential problems. FEAT was developed to address this problem.

Technical Approach

FEAT is a software application that uses directed graphs (digraphs) to analyze failure paths and failure event propagation. The behavior of the systems to be analyzed is represented as a digraph. Then, the digraph model of the system is used by FEAT to answer questions concerning the cause and effects of events which are captured in the model. Therefore, the first step in using FEAT is to create the digraph model of the system in which one is interested. Once FEAT has analyzed the digraph, it has the information it needs to perform cause and effect analysis.

What Are Digraphs?

Directed graphs are graphs that consist of a set of vertices and a set of edges, where there is an edge from one vertex a to another vertex b. The vertices are drawn as circles and the edges are drawn as arrows. The direction of the arrows indicates a causal relationship between the vertices (fig. 1). The vertex from which the edge begins is called its source, and the vertex at which the edge terminates is called its target. Direct graph theory is an accepted and established area of mathematical study. Therefore we will only introduce it in this paper to the extent necessary for an understanding of how it is used in FEAT. The interested reader may find further information by consulting the literature.



Figure 1. Direction of arrows indicates causal relationship between vertices.

The structure of the digraph can be represented by a matrix, and consequently can be easily implemented in a computer. The conversion from digraph to matrix is straightforward and is illustrated below in figure 2. This matrix is called the *adjacency* matrix¹, and is the basis from which other information about the graph can be derived. The matrix of the graph is obtained by entering

either zero or one, depending on whether or not an edge connects two vertices. The presence of an edge from a to b in figure 1 indicates an entry of one (1) into the corresponding matrix entry. However, since there is no edge from a to c, a zero (0) would be entered in the corresponding matrix entry.

a b c a 0 1 0 b 0 0 1 c 0 0 0

Figure 2. Conversion from digraph to matrix.

Additional information can be added to the digraph by applying logical operators to express conditional statements. FEAT uses AND and OR operators to accomplish its analysis. The AND operator is represented on the graph as a vertical bar with a horizontally placed arrow at its center. An OR operator is simply two or more edges whose target is the same vertex. Theses operators (fig. 3), and their use in FEAT (figs. 4 & 5), are described below.

The "AND" gate is shown in figure 5. The AND gate is used when both event A and event B must occur in order for event C to occur. Conversely, if only event A occurs or if only event B occurs, then event C does not occur.

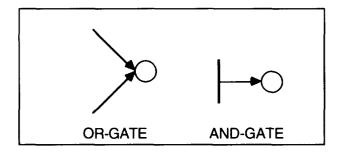


Figure 3. FEAT theses operators.

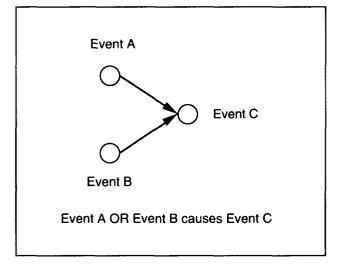


Figure 4. FEAT OR operator.

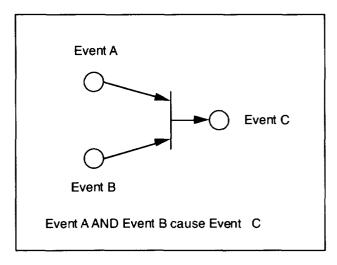


Figure 5. FEAT AND operator.

Analytical Capabilities

The reachability of an event refers to whether there is a path by which other events in the digraph can be reached. A given event is said to reach another, if the first event can cause the second through some path of the graph. Using the adjacency information derived from the digraph, reachability can be computed for every event and pair of events in the digraph. Analysis can be conducted upstream or downstream from an event node. (References 2, 3, and 4 provide a much more detailed discussion of digraphs and reachability.)

Reachability information allows FEAT to answer the following questions about a modeled system:

- What happens to the system if "event A (and event B and event C and ...)" occurs?
- What are the possible causes of "event A"?
- What common cause could account for the simultaneous indication of numerous events?
- What is the susceptibility of the system to new events given that one or more events has already occurred, or the system has been reconfigured due, for example, to maintenance?

Digraph Example

The following example demonstrates how a digraph might be implemented for a light and switch. The digraph provides a methodical way in which to express the topology and behavior of a system. It is worth noting that the digraph itself may have various constructions for the same information contained in it, depending on who created it. Different modelers may lay out the digraph differently. However, for a properly constructed digraph, the same information will be captured. In the following example (figs. 6 & 7), power source A provides current to switch A which connects to the bulb. Similarly, power source B can energize the bulb.

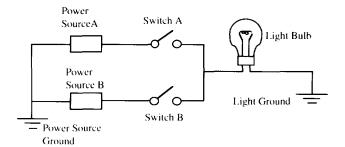


Figure 6. Digraph model 1.

- If "Power Source A Fails" or "Switch A Fails Open" then "Switch A Output Fails." This is an example of **OR** logic and is shown in the digraph by the arrows leading into "Switch A Output Fails."
- If output from both switches A <u>and</u> B fail, then they will cause the "Power at Light Fails." This logic appears as an **AND** gate on the digraph (the vertical line). In this case, the **AND** gate reflects redundancy designed into a system.

Why Digraphs?

Directed graphs are useful because they visually depict the logical topology and dependency relationships of physical and conceptual systems and processes. Because they capture causal effects between events, they can be used to describe system behavior. Directed graphs are also easily converted into a matrix and, because of this, can be readily analyzed in a computer. Creating and laying out the digraph of a system also formalizes the method of evaluation during the analytical process, and provides a standard representation convention. Finally, digraph analysis is mathematically sound, since methods for determining connectivity paths of the digraph vertices can be mathematically proved.

Directed Graphs and FEAT

Digraph construction is facilitated by use of an editor specifically designed for the task. Such an editor is included in the FEAT package which consists of two programs: Digraph Editor and FEAT.

<u>Digraph Editor</u> The Digraph Editor facilitates construction of the digraph model by allowing the user to create event nodes, edges, and the logic operators, and to connect and arrange them into a digraph. Event nodes and edges are laid out and connected using the logic operators. The pieces that make up a digraph are supplied in a digraph toolbox from which items may be selected. These items are placed on the screen and arranged to produce the system digraph.

Other information is needed to complete the digraph and to make it usable by FEAT. Event nodes have an associated text block, which includes information that will identify the event node to FEAT, describe the event for the user, and relate the event to a drawing which contains the component to which the event pertains. This information is extracted from tables that the user creates. Digraph Editor uses the tables to automatically generate a mnemonic reference that FEAT will use to identify the event.

Digraph Editor also provides a number of tools for validating and verifying the model as it is being developed. Digraph Editor will check tables for duplicate entries, check nodes for incorrect form, and determine whether a selected node has a duplicate in the digraph. Digraph Editor also contains an algorithm that allows the user to analyze small or incomplete digraphs while still in the editor. Once the digraph is completed and the paths in it are analyzed, FEAT can return answers to questions regarding the behavior of the modeled system.

Currently, digraph models are created manually by selecting and arranging digraph components; the modeler must interpret drawings and other sources of information

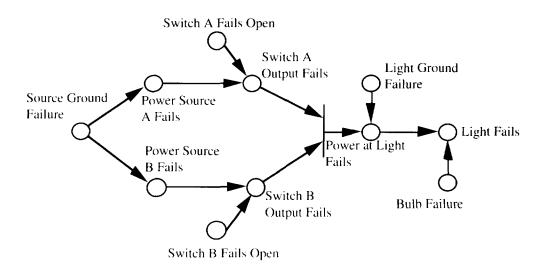


Figure 7. Digraph model 2.

to generate the digraphs. This is a laborious task. Consequently, efforts are under way to develop methods to automatically translate schematics and drawings into corresponding digraph models.

Digraph Editor is currently only available for the Macintosh II class of computer.

FEAT

FEAT is the portion of the package that analyzes single or multiple digraphs, and graphically displays causes and effects of events. Propagation results are shown both on the digraphs and on another associated graphical representation, such as a schematic or block diagram. FEAT uses a multi-step algorithm, described in reference 2, to compute reachability for each event and pair of events in the digraphs. Events are identified to FEAT through the mnemonic that is generated by Digraph Editor. Queries about the behavior of the system are made by selecting events and telling FEAT to return all of the causes of that event (targeting), or by telling FEAT to return all of the effects of that event (sourcing). FEAT displays all of the single events, and all pairs of events that may cause a selected event. Multiple events may also be selected and analyzed. FEAT allows some events to be temporarily removed from the analysis so that answers can be obtained about a reconfigured system.

FEAT also contains a feature which allows users to attach to a schematic, formatted database information and graphics. In this way, component descriptions, parts lists, drawings, etc. may be displayed in conjunction with a schematic.

One of the major advantages of FEAT, as discussed in reference 2, is that it allows the analysis of very large systems. Large systems can be digraphed by creating and connecting a series of smaller digraphs. FEAT understands when propagation occurs across the digraphs.

Planned enhancements to FEAT include the following: increasing the speed with which reachability is computed by improving FEAT's computational algorithm; provision of a method for computing and displaying probabilities of events occurring; and computation and display of the time it takes for an event to propagate through the graph.

FEAT is currently available for the Macintosh II class of computer and for UNIX/X-Windows/OSF-Motif systems. No programming skill is required to use FEAT, but a course in digraph modeling is quite helpful in learning how to construct system models.

Digraphs at NASA

Why NASA Chose Digraphs

NASA's interest in digraphs began as part of the Shuttle Integrated Risk Assessment (SIRA) Project. SIRA was initiated in the wake of the Challenger acci-

dent, in an effort to find better ways of assessing risk and preventing failure. Digraphs support such analysis by providing end-to-end cause and effect analysis of modeled systems. Digraphs also provide a standard and methodical approach for conducting safety analysis and risk assessment. Digraphs capture information in an easily retrievable format, and facilitate the transfer of design information. FEAT takes advantage of these characteristics in a way that aids engineers and analysts with design, assists safety engineers with risk assessment, and promotes understanding of system behavior, thereby making FEAT a good tool for training inexperienced persons.

What Has Been Done at NASA?

The first system to which digraph analysis was applied was the Space Shuttle Main Engine System (SSME). Since then, acceptance of digraphs and the use of FEAT has extended in several directions. Most recently, FEAT has been formally released to the Space Station program Technical Management Information System (TMIS), as Digraph Data System (DDS) Release 1.0. DDS will, through TMIS, be available to Space Station Engineering and Integration, Space Station Combined Control Center, and the various work packages and their contractors. A Macintosh Powerbook version of FEAT will be deployed as a development test objective (DTO) on the STS-52 flight scheduled for October 1992. Reliability and Maintainability personnel at NASA/JSC are using FEAT to construct a model of the Simplified Aid for Extravehicular Activity Rescue. FEAT is also being used to model the redesigned Servo Power Amplifier for the Remote Manipulator System.

Proponents have used FEAT for a variety of analytical tasks, such as fault tolerance analysis and redundancy management (FT/RM); fault detection, isolation, and recovery (FDIR); and "what-if" analysis. Within the Space Station program, FEAT is being used in the performance of integrated risk assessment for the station, which includes FMEA, hazards analysis, and FT/RM. FEAT has also been established as a baselined tool in the Mission Operations Combined Control Center, where flight controllers will use FEAT models to assist with real-time monitoring tasks. FEAT's role is expanding in both Space Station and in Space Shuttle.

Space Station

The Space Station engineering integration contractor (SSEIC) is using FEAT to perform integrated risk assessment. This tasks consists of performing the analysis to ensure the Station design is safe, reliable, and has an acceptable level of risk⁵. The Space Station design consists of modules designed and built by the United States, and of modules which will be designed and built by NASA's international partners. The work to be performed by NASA is divided into four work packages

distributed among different centers. Additionally, a variety of contractors are working in support of the work packages. Consequently, system integration is a paramount concern of the program. SSEIC is tasked with ensuring the integration of these various factions and is using digraph-based FEAT to work the integration problem. Specifically, FEAT supports the following areas of the integrated risk assessment process:

- •. reliability analysis
- · safety analysis
- integrated risk analysis
- · integrated risk assessment

The models being developed for the station integrated risk assessment will eventually be provided to Mission Operations personnel for use in FDIR of the on-orbit Station.

Space Shuttle

FEAT is scheduled to fly on STS-52 as a DTO. A FEAT model of the S-band Communication System has been installed on an AppleTM PowerbookTM, which will be flown aboard the shuttle. Astronauts will use the model to perform on-board fault isolation for the S-band Communication System. They will be able to configure the model to match the actual S-band system configuration, and then will use FEAT to identify possible causes of failures of the S-band system.

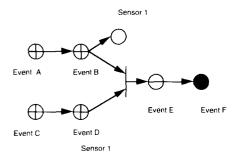
Future Applications of Digraphs

Digraphs are gaining acceptance within the NASA community as a viable method for conducting many kinds of analysis. The Space Station program and Operations have mandated the use of digraph analysis for the Space Station Level II Integration effort, and many others are beginning to take up the banner. Some of the potential areas of application include the following:

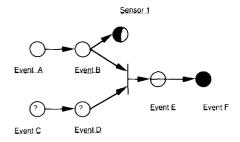
Fault Isolation/Testability

FEAT's ability to model and analyze system failures make it a natural candidate for fault isolation efforts. If a failure event occurs, FEAT can display all of the possible single and paired causes for that event. However, in a large system, potential causes can be enormous in number. A method of pruning the list of possible causes is then necessary. Sensor information associated with the system can be used to remove candidate causes which occur downstream of a known nominal condition. Incorporation of sensor data into the analysis can help to reduce the number of candidate failures to a manageable sum. Then, using traditional techniques, further isolation can be accomplished. Figure 8 shows an example of such a case.

Sensor data may also be combined with FEAT to identify the potential for cascading alarms. For instance, if a fault occurs downstream from a sensor, the sensors



Event F may be caused be Events E or F directly or by Events A or B paired with Events C or D through the AND gate. Sensor 1's state is unknown.



If Sensor 1 reports nominal conditions, this implies that neither Event A or Event B occurred. Since neither Event A or B occurred, then the AND gate condition cannot be met, and the only way Event F can occur is if Events E or F occur. The number of events necessary to be checked to evaluate the cause of Event F has been reduced from 6 to 2.

Figure 8. FEAT's analysis of a failure.

upstream will eventually alarm as a result of the fault. FEAT can show the effects of a fault on the downstream sensors.

This solution is being implemented by NASA in an extension of FEAT called extended real-time FEAT (ERF). ERF automatically prunes the list of possible faults according to sensor information. ERF is being developed as a part of the FDIR system for the On-orbit Control Center Complex. Mission Controllers will use ERF to resolve off-nominal system behavior by reducing the potential number of failure causes.

FEAT developers are pursuing the possibility of incorporating, or interfacing with, a testability analysis tool which will help to evaluate sensor coverage in systems, and make recommendations regarding appropriate sensor locations. ERF is dependent upon adequate sensor information and proper placement of the sensors. Properly placed sensors provide information to quickly and accurately locate faults. The combination of FEAT, ERF, and testability tools will make a very powerful fault isolation system.

Temporal Analysis

Not every event immediately affects the next downstream event. There may be appreciable delays within an event and between events. For example, an inappropriately shut valve may not, for some time, cause the pressure in the system to rise to an unacceptable level.

1-19

In such a situation, time delay is an important aspect of calculating the potential failure space.

This issue will be addressed in FEAT when a modification is made to Digraph Editor to allow modelers to include time delays within events, and delays between events. FEAT will then compute the maximum and minimum time delay between selected events. This capability will be supplied in a future version of FEAT.

Software Modeling

Physical systems are not the only candidates for digraph analysis. Software functions and data flow can be modeled as well. Particularly, the flow and effect of invalid/improper data can be modeled. This can provide insight to the designer in determining mission critical software functions. Additionally, the effect of invalid data on other system functions (both software and hardware) may be shown. For instance, a software functional component that generates invalid data as an event may then provide that data to other software and hardware as an invalid data input event. FEAT can be used to model these behaviors too.

Design Evaluation and Redundancy Management

Digraph models can be used to determine whether or not a system design provides sufficient redundancy. Maintenance and configuration effects on the system can be evaluated by selectively removing (setting) components from the system. The reconfigured system can then be evaluated for induced single and paired events. This can be particularly useful in determining new vulnerabilities after a system has encountered failures and/or has portions of the system secured for maintenance.

FEAT contributes to design evaluation by rapidly displaying all single events caused by the event of interest, and all pairs of events that will result in that event. Unexpected single point common cause events are also quickly identified. As the design is modified to provide additional redundancy, the digraph model can be updated to reflect the changes, and the new set of single events and pairs of events can be evaluated.

Logistics Analysis

Logistics analysis addresses corrective and preventive maintenance tasks, and determines the kinds and numbers of repair parts needed for a system. This type of analysis is associated with the reliability and availability (reference 6) of systems. Reliability is defined as the measure of the mean time between failure and concerns the probability that a system will operate over a specified period of time. No provision is made for repair when calculating reliability. Availability varies from reliability in that it is a measure of the mean time to repair, or the probability that the system will operate over a period of time considering that something can be done to restore

functionality lost as a result of a failure. How system repairs can be supported, or supportability, is important to determining availability. If repairs can be made instantaneously, availability is increased. However, long delays between failure and repairs make the system proportionally less available.

FEAT models can help to identify critical components and the effect of their failure upon the system. Digraph models of the system can, along with specific part reliability, help determine priorities for inventory stocks and schedules for maintenance. Spare parts inventories are a major factor in determining supportability. For example, spares for parts that cause single point common cause events should have higher priority for stocking than parts that contribute to pairs of events.

Maintainability concerns the time it takes to remove and replace a component. Digraph models can identify components prone to low reliability and single common cause failure. Designers can then either improve the reliability of the component or ensure that such items are accessible and easily replaced.

Summary

As NASA continues to search for better and innovative approaches to new and old problems, digraph analysis has emerged as a viable addition to the methods applied to risk assessment. Digraphs are a well established area of mathematical study and analysis, and provide an easily comprehendible visual representation of cause and effect relationships. Conversion of the digraph to an equivalent matrix is straightforward, and allows analysis of digraphs to be mathematically calculated and verified. The nature of matrices also makes them ideally suited for computerized calculations, which in turn provides a vehicle for automating the task of risk assessment and failure analysis.

FEAT uses digraph theory to provide engineers and analysts with a powerful and flexible automated analytic helper. FEAT can provide end-to-end analysis of cause and effect events. Very large systems can be modeled in modules, then connected to form the entire system. This feature also allows digraphs to be arranged in mix and match fashion. FEAT can detect and return information about single point failure vulnerability, failure event pairs, common cause events, and reduced capability analysis. FEAT shows the results of event propagation on system schematics and on the associated digraph. Digraph Editor provides a helpful way for the analyst to create digraphs.

The FEAT Project is funded by the NASA Space Station Advanced Programs Development Office (Code MT) and the Space Station Program Office (Code MS).

References

¹L. Levy. *Discrete Structures of Computer Science*. John Wiley & Sons, 1980.

- ²R. Stevenson, J. Miller and M. Austin. "Failure Environment Analysis Tool (FEAT) Development Status." AIAA Computing in Aerospace VIII, AIAA-91-3803. October 1991.
- ³I. Sacks. "Digraph Matrix Analysis." *IEEE Transactions on Reliability, Vol. R-34, No. 5.* December 1985.
- ⁴I. Sacks, G. Keller, and R. Rauch. "Application of Digraph Matrix Analysis to the Space Station." *RDA*, *Logicon*, *R & D Associates*, *RDS-TR-148400-001*. September 1987.
- ⁵J. Schier. Integrated Risk Assessment (IRA): Defining the Level II Safety & Reliability Job and Implementation Plan using Digraphs. *Unpublished Grumman presentation*. September, 1992.

⁶B. Blanchard. *Logistics Engineering and Management*. 4th Edition. Prentice-Hall, Inc. Englewood Cliff, NJ. 1992.

Bibliography

- D. Haasl, N. Roberts, W. Vesely, F. Goldberg. *Fault Tree Handbook*. GPO Sales Program, U.S. Nuclear Regulatory Commission, Washington, DC. 1981.
- J. Pearl. *Probabilistic Reasoning in Intelligent Systems*. Morgan and Kauffman, 1988.

Mission Evaluation Room Intelligent Diagnostic and Analysis System (MIDAS)

Ginger L. Pack, Jane Falgout*, Joseph Barcio*, Steve Shnurer*, David Wadsworth*, and Louis Flores*

Johnson Space Center

*Lockheed

Abstract

The role of Mission Evaluation Room (MER) engineers is to provide engineering support during Space Shuttle missions for Space Shuttle systems. These engineers are concerned with ensuring that the systems for which they are responsible function reliably, and as intended. The MER is a central facility from which engineers may work in fulfilling this obligation. Engineers participate in real-time monitoring of shuttle telemetry data and provide a variety of analyses associated with the operation of the Shuttle.

JSC's Automation and Robotics Division is working to transfer advances in intelligent systems technology to NASA's operational environment. Specifically, the MER Intelligent Diagnostic and Analysis System (MIDAS) project provides MER engineers with software to assist them with monitoring, filtering, and analyzing Shuttle telemetry data, during and after Shuttle missions. MIDAS off-loads to computers and software the tasks of data gathering, filtering, and analysis, and provides the engineers with information which is in a more concise and usable form needed to support decision making and engineering evaluation. Engineers are then able to concentrate on more difficult problems as they arise.

This paper describes some, but not all, of the applications that have been developed for MER engineers under the MIDAS project. The sampling described herewith was selected to show the range of tasks that engineers must perform for mission support, and to show the various levels of automation that have been applied to assist their efforts.

Introduction

The purpose of the MIDAS project is to provide MER engineers with real-time intelligent software to assist them with monitoring, filtering, and analyzing Shuttle telemetry data, during and after Shuttle missions, and to capture the expertise held by highly experienced engineers. This is accomplished by applying advanced automation and intelligent systems to the tasks required to perform engineering evaluation.

The MER engineers perform a variety of tasks in support of Shuttle missions. They continuously monitor and evaluate the performance and health of their systems, provide engineering analysis support to Mission Operations personnel, and are responsible for certifying the integrity of orbiter systems for subsequent flights. Historically, engineers have had to rely upon several screens full of telemetry data, displayed as ASCII text and

numerical values, to understand the state and operating condition of their system. Information in this form is crammed onto displays that engineers must monitor and interpret (fig. 1). Several of these displays exist for each subsystem. Engineers visually monitor these displays during missions to obtain an understanding of the behavior of their systems. Only one display at a time may be shown. This arrangement precludes the engineer from noticing changes in information that are not contained on the display being viewed. The selection of screens available for viewing is controlled by Mission Operations personnel. Consequently, during missions, engineers must often "chase around" the displays which contain the information they need. This further complicates the duties that engineers must perform, in maintaining the health of the systems for which they are responsible. Additionally, engineers use manual methods to perform analysis. Events are logged by hand, and associated analysis is performed using pencil and paper. This mode of operation can be tedious, time consuming, and vulnerable to the errors that result from distraction and boredom.

Technical Approach

The first task needed to automate the MER was to analyze the current methods of operating, and identify problems and deficiencies. We developed a questionnaire to learn where engineers were spending their time, which tasks were labor intensive, boring, repetitive, and just hard to do within current processes and methods. Discussion of these issues involved knowledge engineering to capture system expertise, and to determine the kinds of analysis with which engineers needed help. We learned that engineers wanted assistance in recognizing trends that were reflected in the data, and evaluating the potential impact on hardware. They also needed to capture the data and perform identification and diagnosis of problems before a critical state is reached. Additionally, engineers wanted help in capturing and analyzing in-flight data to check out and verify the health of the systems for future flights. Finally, they needed relief from the task of visually monitoring and manually gathering the data needed to perform various analyses. Computers and software could provide for these needs, and enable the engineers to focus their efforts on problems as they arise versus investing so much effort gathering and sifting through large amounts of data to evaluate system health and performance. Using the questionnaire as a guide, developers worked with engineers to identify troublesome areas and to reach agreement on which tasks are to be built into software.

F/V 49/105 OGMT 136:02:42:04 OMET 7:03 RGMT 136:02:42:04 U/O RATE 1	RMS STATUS	161 GN 22	RR3582M sh 26	CH029 BF 13
RMS PMR PRI ENTER 8 RMS SEL PORT MCIU I/O ON ORB UNL 8 8 BYPASS 8 SINGLE 8 9	POR -844 POR RT 9.00 HC CNT 9 OCAS -1171	Y Z -0 -414 6.00 0.00 0 -1 0 -544	P Y 359.5 0.1 -0.01 0.01 0.01	R 8.8 9.80 9 NUL 9
SOFT STP ENA ORB LO SEL IND AUTO BRK ENA PL 8 8 ENCOR CK ENA PL 8 8 AUTO 1 8 8 AUTO 2 9 9	ANG ACT -36.8	82.1 -148.0 - 9	MP МУ 99.4 15.2 0 0 -1.7 -1.1 -0.1 -0.1	MR RNG 4 58.6 9 9 CT -9.3 -0.1
PL ID	MADC MCPC ICF ABE/MCIU	EE MODE: CAP RIG GERIG REL	CUR ATTN: SH RIGID CLOS GRY GRY DERIG OPEN BP BP	GRY
IN PROG 0 STOP 0 BRAKES 0 0 SYM STOP 0 START PT 1 SAFING 0 0 RATE VERN IND	EE DERIGIO RELEASE	SY ABE TACH SPA +28V SPA COMMUT MDA	SP EP MP	NY NR
## AUTO VERN ALT JET OP ATT DB 3.899 ALT MAX JE RT LIM 9.289 DLY TIME DSC RT 9.29 ON TIME	EE CMDS EEEU BITE MCIU HC T 3 EXT FS Z TEST BRK 1.90 C/M	JPC CRT POS(ENC) CNT ERR TACH ENVEL STALLED SLUGGISH	1	1
JET OPT P NOM (TAIL) TRANS P LOM-Z 9 Y NOM (TAIL) ROT P ATTITUDE IN RANGE CURR ERR TOT R OR 31.03 19.75 8 RNGE RTE P 158.27 -3.92 -8	Y Z LOSS FS FS FS FS TI ME 230 3 S96 PDRS RC 093 4 S96 PDRS RC 095 FS	TÖNE H EP H SP	4 135:2 12 4 135:2 4 135:2 4 135:2	1:58:01 0:57:55 0:36:23 0:36:23

Figure 1. Information displayed as ASCII numerical values.

Automation requirements are developed through close interaction with Shuttle subsystem engineers. User feedback is solicited and incorporated at every phase of product definition and development. Developers work closely with users while developing the architectural design and implementing the design. Frequent product reviews are also conducted with the user to ensure appropriateness and accuracy of results. User involvement in all phases of development results in products that are familiar to users and fit well to the user's needs. It also ensures user "buy in" to the technology, since they help to define the implementation of the technological solution.

Accomplishments

Discrete Log

The Discrete Monitor and Logging program (fig. 2), was created to relieve engineers of the continuous eyes-on monitoring of system data. Previously, this task was done by having a person watch a screen full of data (fig. 1), noting the occurrence of certain events, and writing them down on a sheet of paper. The Discrete Monitor and Logging program reads the shuttle telemetry stream and automatically detects changes in the state of discrete parameters. The changes are logged and written to the screen, and to a file that may be translated to ASCII format for further manipulation by the user. The entries consist of a description of the changed event, the Green-

wich Mean Time (GMT) and Mission Elapsed Time (MET) of the change, the previous state, the current state, and a comment field. The event descriptor and state changes are entered in English. Comments may be entered from a template or edited by the user. The log entries are painted yellow when data has changed during a period of signal loss. The first version of the log logged each change without regard to how long or how often the parameter had changed or was changing. Consequently, parameters that "fluttered" on and off quickly filled up the log. This was taken care of by adding a module that would wait for the data to stabilize before reporting that the data had changed.

Analog Plot

A companion application to the Discrete Monitor and Logging program is the Analog Plot program (fig. 3). The Analog Plot program graphically depicts system behavior that is described by analog values. The plots appear as real-time strip charts but are defined by conditional logic among the analog values. Thirty minutes of data are shown. The plots are scrolled every ten minutes. Plots are organized in "families" that are made up of pages. These pages can be combined in mix and match fashion to facilitate visual comparison of data. A "snap shot" of interesting data can also be saved and reloaded for comparison against other data.

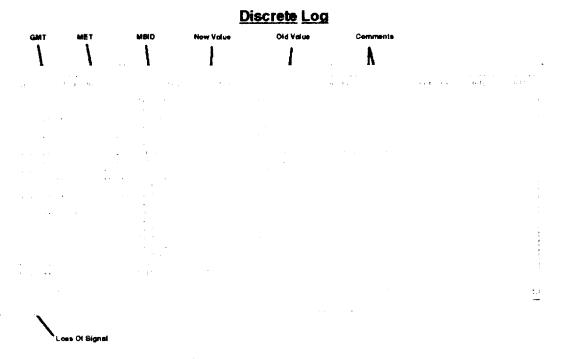


Figure 2. Discrete monitor and logging program.

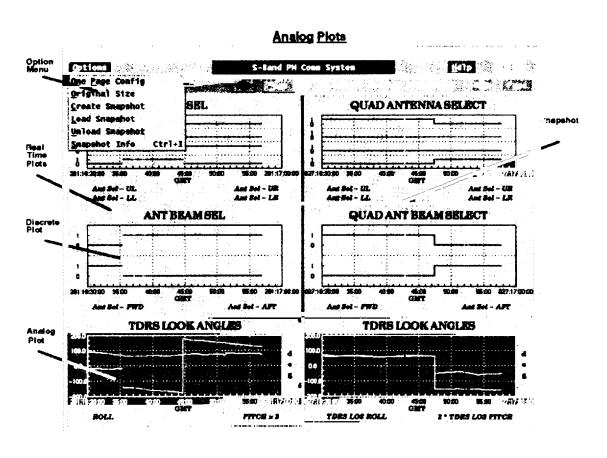


Figure 3. Analog plot program.

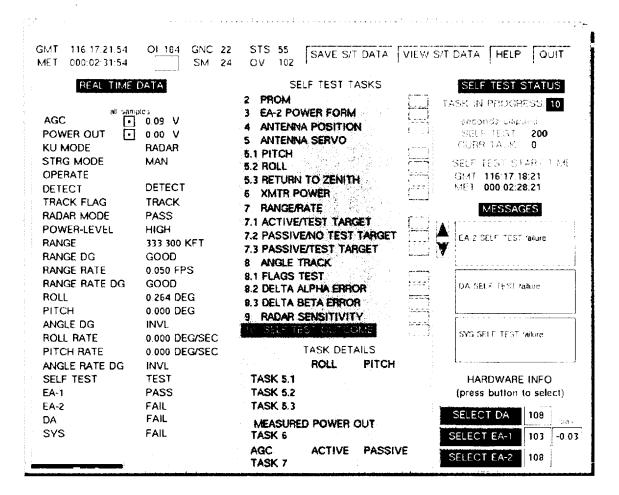


Figure 4. KASTA display.

Ku-Band Automated Self-Test Analyst (KASTA)

The KASTA is an expert system that detects the start of the Ku-Band self-test, and interprets the test results. The self test is done prior to deployment of the shuttle's Ku-band antenna. The purpose of the self-test is to ensure that the Ku-band antenna is healthy and will operate correctly when used. The self-test consists of several subtests whose outcome depends on the success or failure of previous tests. The pass/fail condition of different combinations determines the success or failure of the entire Ku-band self-test, and consequently whether the antenna is fit for use. The expertise for analyzing this test was held by the Ku-band subsystem manager, requiring her to be available for every Ku-band self-test. KASTA allows non-expert personnel to evaluate the self-test.

KASTA evaluates the tests that determine the ability of the Ku-band antenna to achieve proper position within allowed time, verifies the ability of the antenna to track properly, accounts for and manages exceptions to self-test procedure, and recognizes insignificant "failures." KASTA uses telemetry to identify initiation of the self-test, and begins to monitor each test according to pass/fail criteria contained in the knowledge base. Telemetry values are evaluated against rules that determine whether the conditions of the tasks are met, and explanation is provided to support conclusions made by KASTA.

Considerable thought was given to how this information should be conveyed to the user. The application interface provides feedback to the user regarding which task or subtask is in progress, and where in the self-test procedure the task falls. Other types of information also had to be communicated through the user interface. The status of each task, task outcome, and the data associated with each task, such as task duration and parameters checked, had to be presented to the user. Additionally, details concerning the failure of any task to complete had to be communicated. Finally, explanation and supporting data for KASTA's decisions had to be made available.

The objectives of the display were to strive for easily comprehensible presentation of the various kinds of information, and to provide a highly intuitive display in terms of comprehension of data and in terms of human-computer interaction. These goals were met by grouping like information, arranging information in table format, and using color only to convey specific information. Also, groups of information were placed into windows and labeled using names that clearly described the content of the window. The result was a well-organized and highly intuitive display that users could understand and interact with, while having little or no formal instruction (fig. 4).

The most important information was placed in the most prominent position of the display area, the center.

Supporting data was arranged around the center. The center of the display contains the self-test tasks and detailed information pertaining to the tasks. The SELF TEST TASKS window lists each of the tasks that coprise the Ku-band self-test. The task currently being executed is highlighted in this window. A red or green box indicates whether the task passed (green) or failed (red).

The REAL TIME DATA window is located to the left of the display center, and lists the telemetry and corresponding values that are associated with the self-test. Telemetry corresponding to a task that is in progress is highlighted while the task proceeds. To the right of the center the SELF TEST STATUS window contains information concerning which task is in progress, time elapsed for the task, start time for the task, and mission time given as GMT and MET. Below this window is a MESSAGES window that allows KASTA to inform the user which tasks have failed.

Users may also review all of the data that KASTA used to determine the outcome of any task. After the self test procedure has completed, the data that was used to determine the outcome of any task is accessible in two ways: the user may review only the data important to a particular task, or review all of the data important to the entire self-test procedure.

KASTA performs its analysis by cycling through five distinct phases for every second of telemetry data. The first two phases check the incoming data to prevent KASTA from making decisions using unreliable data. An important benefit of this approach is that KASTA's knowledge base always operates on a time-homogeneous set of data. No analysis rules are allowed to fire until the phase in which data acquisition takes place is finished. This promotes consistency for KASTA's analysis. The five analysis phases are data acquisition, post-data acquisition, self-test progress update, task progress update, and task outcome analysis.

KASTA's data acquisition strategy first checks the quality of the data before passing the data on. An overall quality indicator determines how well the frame count transmission was received, and is associated with each second's worth of data. If the quality indicator is not 100%, that second of data will not be used. An individual quality status indicator is associated with each telemetry value.

During the post-data-acquisition phase, the telemetry is submitted to more rigorous quality checks. Conditions checked include recency of data, degraded data quality, and bad status associated with the quality indicator or the timestamps, or questionable timestamps associated with the data. If any of these conditions are met for the frame of data (one second of data), none of the remaining phases will be executed. Conversely, if the data passes screening, the next phase of KASTA's analysis is entered. This phase is referred to as the "self-test progress phase," and contains the rules that determine when the self-test starts and completes. Also included are the rules that determine at any time how far into the self-test procedure the current

analysis is. The third phase of analysis determines how a specific task being executed is progressing. This is the "self-test progress update." This phase contains the rules that determine the identity of the current task, and how far into that task the analysis is, at a given time. The outcomes of the tasks are determined during the "task outcome analysis phase." This set of rules specifies the pass/fail criteria for the self test, and summarizes the results of all the self-test tasks and sub-tasks. KASTA cycles through these phases as long as the self-test is in progress. When the self-test has completed, the data acquisition and post-data acquisition phases will continue to be executed to provide updates to the REAL TIME DATA window.

KASTA is written in Gensysms G2 expert system shell. The logic used to analyze the self-test in real-time is implemented using a combination of rules, objects, and G2 functions. KASTA is used by MER engineers and the Integrated Communications Officers, who are responsible for Shuttle mission support.

RMS Monitor

Since April 1992, the Remote Manipulator System (RMS) Direct Drive Test (DDT) Monitor has supported missions whenever a flight includes use of the Shuttle robotic arm. The DDT Monitor (fig. 5), was constructed to monitor the direct drive test of the RMS joint motors. The six joints of the Shuttle robotic arm are moved by six motors that are individually tested before the arm is deployed. The motors are tested by driving each of them in the forward (positive) and reverse (negative) position. The DDT Monitor automatically detects the initiation of the direct drive test, and plots the results on a screen, as the test occurs. The plot is a visual image of the motor tachometer output, and should produce an expected profile when the motor is operating properly. A warning is issued if the motors are driven beyond 20 seconds—a time limit that, if exceeded, invalidates the test. However, the application continues to plot the profile. The profile can be saved to a historical file, then retrieved and overlaid against current or other historical data for comparison of current behavior to past behavior. If more than one test is done for a joint motor, the application identifies the subsequent tests and assigns an appropriate number. The plotted image of the test is color coded to correspond with the appropriate number test.

Automated In-Flight Checkout

The purpose of the in-flight checkout is to gather and analyze data needed to verify the health and performance of shuttle systems for subsequent shuttle flights.

Performing checkout during flights helps to eliminate the amount of ground testing that must be done between Shuttle flights. Existing methods of performing in-flight checkout required engineers to manually gather data throughout the mission, and to pore over large amounts of historical data in search of the information needed to

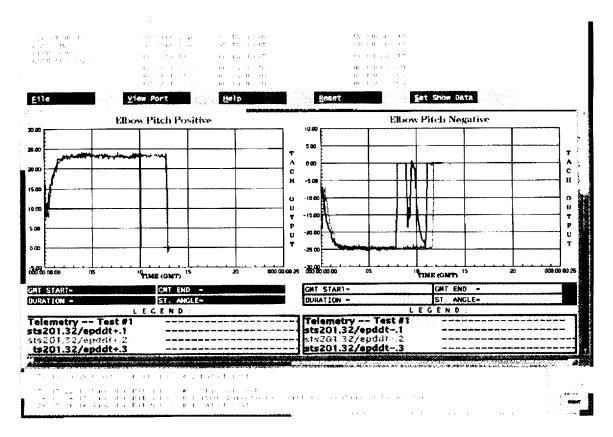


Figure 5. DDT monitor

assess and evaluate the in-flight checkout requirements. The Automated In-Flight Checkout application automatically gathers the data that is used to conduct in-flight tests, evaluates the data against requirement pass/fail criteria, summarizes the results of the tests, and produces the In-Flight Checkout Report. Additionally, when an in-flight checkout requirement is not met, the user is alerted of the discrepancy, and given an opportunity to acknowledge the event and classify it, or to acknowledge it without assigning any classification. The classifications are "failed" for failed requirements that cannot be explained, and "nonproblem failure," for failures that can be explained, and require no action. Each reported requirement is associated with a window that, when opened, explains what conditions and data caused the test to fail (fig. 6).

Power Reactant Storage & Distribution (PRSD) **Trend Analysis**

The PRSD Tank Quantity application assists subsystem personnel in detecting leaks in the Shuttle oxygen and hydrogen fuel tanks, a problem that has proved to be quite challenging. The application calculates and reports the total accumulated average kilowatt and amperage for the last 24 hours of the mission and for the accumulated mission time. The H, and O, tank quantity differences between known consumption demands and measured depletion is calculated and reported over the most recent 24 hours and for the accumulated mission time. A prediction of time remaining at the current usage rate, and at the

average amperage used over the accumulated mission time, is calculated and reported. A two-day reserve is included in the prediction, and reserve quantities for the H, and O, tanks are also reported.

Theoretically, it should be possible to detect leaks by comparing the measurements provided by tank sensors to a calculated consumption that can be obtained from the demands of known system loads. However, the sensor readings are affected by several other factors. Side effects from thruster burns, on/off cycling of mixer heaters, and tank content stratification and destratification render the sensor readings unreliable for positively determining quantities. Consequently, before any progress could be made to detect leaks, the first task was to attempt to accurately determine the amount of fuel in the tanks.

The tank quantity measurements consists of 1) the raw measured total tank quantity of O, and H, throughout the flight, and 2) the calculated consumption of O, and H, based on the power provided by the fuel cells. If the measured tank quantity starts dropping faster than the calculated consumption there may be reason to suspect a leak in one of the tanks. Compensation for the variability in the measured sensor values is obtained by applying an exponential smoothing algorithm to the sensor readings. The smoothed values are plotted against the calculated consumption. A confidence interval is calculated to provide an indication of how well the calculated value tracks the adjusted measured value. A significant diver-gence between the two measurements provides some indication of a possible leak that should be investigated further.

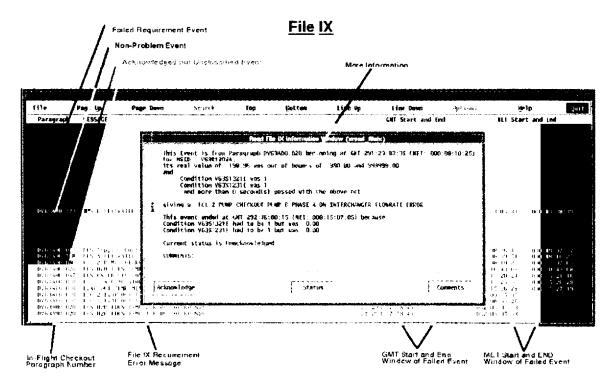


Figure 6. In-flight checkout report display.

The measured tank quantity data contains variability introduced at the sensor. One of these is caused by the heater cycle turning on and off to maintain the tank's pressure at a level such that it will become the active tank. These variations have an oscillation-like characteristic with a period of roughly one to two hours. In order to facilitate the comparison of measured quantity to calculated quantity, an exponential smoothing technique was selected to compensate for these variations. The effect of the exponential smoothing technique is similar to that of a moving average in which the data is weighed heavier toward the leading edge and becomes insignificant in the distant past. Furthermore, since real-time telemetry data contains small gaps, a technique which can handle irregularly spaced data and which was published by D.J. Wright was selected. This technique is an extension of a double exponential smoothing adapted to data occurring at irregular time intervals.

Since the reactant tank quantity data has a trend component (the quantity is decreasing), a double exponential smoothing technique is required. Double exponential smoothing separately smooths both the quantity estimate and the trend value. The smoothed quantity estimate is obtained by using the following equation:

 $O(\mu,SUP3(^{\circ}))SDO3(n + 1) = O(\mu,SUP3(^{\circ}))SDO3(n) + (tSDO3(n + 1) - tsDO3(n))O(\beta,SUP3(^{\circ}))SDO3(n)$

where

The smoothed telemetry quantity measurements may be compared to the quantity estimated based on a separate mathematical model of oxygen and hydrogen consumption. This model uses the voltage and current telemetry data to compute estimated reactant consumption based on the chemical reaction equations for the fuel cell. This consumption estimate contains noise as well and is exponentially smoothed using the same technique used to smooth the telemetry quantity data.

As an aid for the comparison of the two measurements, a confidence level calculation testing that the two slopes are statistically equal is computed. The trend estimates from the mathematical model and the telemetry quantity data are used as input parameters to calculate a t-statistic which represents the probability that the two slopes are equal. This gives a number between 0% and 100% which reflects the degree of certainty that the two slopes are the same. This number is used to alert controllers of anomalous conditions in the fuel cell subsystem.

The next phase of this effort consists of investigating the use of learning algorithms and pattern recognition techniques to identify and classify trends that are reflected in the data.

FY94 Plans

PRSD Trend Analysis

Work in FY94 will continue the trend analysis of the PRSD data. Pattern recognition, neural networks, and learning systems will be investigated and applied to this domain. These technologies are being applied to four tasks that have been identified for this area: recognition and prediction of destratification in the oxygen tanks, prediction of stratification in the oxygen tanks and recognition of the stratification signature, oxygen/manifold leak detection and trend analysis, and hydrogen tank/manifold leak detection and trend analysis.

The resulting drastic pressure drop that occurs when oxygen tank contents are destratified (the remixing of a fluid that is non-uniformly dense [stratified], can be confused with large leaks that would also be indicated by a sharp decline in tank pressure. The ability to determine when and how much of the tank contents become stratified is an important aspect of PRSD failure analysis. It is also important to know when remixing of the contents has occurred. The extent of existing tank content stratification, and the type of thruster burn that is to occur can be used to predict the probability of destratification, and assess its severity. The signature for an impending destrati-fication is identified by a drop in pressure of as much as 300 psi within 15 minutes, caused by the cooling induced by mixing cool, high-density liquid near the tank walls with the hot, low-density liquid near the tank heater. This may occur during a maneuver after a long period of no acceleration of the vehicle. The severity of the destratification is affected by the distance of the tank from the center of gravity and the type and direction of the thruster burn. Over 30 recorded instances of destratifica-tion will be used to train a system to identify the signature of destratification, anticipate the probability of an impending destratification, and assess the severity of tank destratification.

A slow, gradual decrease in measured tank quantity that would indicate a small leak can also be the result of content stratification. Another aspect of PRSD trend analysis is to recognize the signature of stratification, and assess to what degree the contents have become stratified. Stratification affects the reliability of the sensor reading, an effect that will also have to be quantified. Numerable data points on stratification are available and will be used to train the system to recognize the stratification signature.

Active Thermal Control System (ATCS) Diagnostic System

The ATCS consists of several subsystems that together provide cooling for the Shuttle. The ATCS Diagnostic System is to be comprised of diagnosis modules for the flash evaporator, ammonia boiler, radiator, freon coolant loops.

The first diagnostic system to be developed is that of the Shuttle's Flash Evaporator System (FES). The FES provides heat rejection of Shuttle thermal loads. Poor instrumenta-tion and too frequent failures have made this a prime area of investigation for automated diagnosis. The concept for this application was completed in FY93, and develop-ment is proceeding with knowledge capture of system expertise, and development of detailed requirements. The FES Diagnostic System will detect, identify, and diagnose failures that could cause the FES to stop working, a condition known as "FES shutdown." Seven categories of failures have been identified that would lead to FES shutdown: 1) restricted Freon flow to the FES, 2) Freon leakage, 3) water spray valve module failure, 4) steam duct failure, 5) accumulator failure, 6) controller failure, and 7) FES supply water heater failure. The FES diagnostic system will address each class of failures.

Summary

MIDAS applications have provided engineers and flight controllers at JSC with software tools that reduce the amount of work involved in supporting missions, and that capture vanishing system expertise. Midas applications off-load to computers and software the tasks of data gathering, filtering, and analysis, perform automated diagnosis of system problems, and allow engineers to quickly and accurately identify and resolve problems. MIDAS applications have positively affected MER mission support by allowing subsystem managers to reduce MER mission support staffing, and by allowing subsystem personnel to share diminishing corporate knowledge and responsibility for their systems. Additionally, MIDAS applications have eliminated tasks previously required of humans, supplied previously unavailable data and analysis, and eliminated the need for some post-mission analysis. Some applications, such as the Discrete Monitor and Log, Analog Plots, and File IX applications, are reusable and have been cloned to quickly distribute these capabilities to other systems, thereby increasing the cost effectiveness of development.

MIDAS applications are written in the "C" programming language using X-windows version 11, Release 5 (X11R5), and the Motif widget set. Also used is Gensym's G2 expert system shell. The applications currently run on the SUN (OS 4.1.3 version of UNIX) Sparc1+ and Sparc2 machines, Masscomp workstations, and DEC stations.

Acknowledgments

The MIDAS Project is sponsored by the Automation and Robotics Division, Intelligent Systems Branch, with funding from the Orbiter Projects Office, Code VA of JSC. The NASA Project Manager for this task is Ginger L. Pack/ER2. Programming support is performed by the NASA Engineering Support Contractor, Lockheed Engineering and Sciences Corporation (LESC). The

programmers for this task are Jane Falgout, Joe Barcio, Bryan Kubena, and Charles Smith, all of LESC. The technical lead is Louis Flores of LESC.

References

¹D. J. Wright, "Forecasting Irregularly Spaced Data: An Extension of Double Exponential Smoothing," *Comput. & Indus. Engng*, Vol. 10. No. 2, pp 135-147, 1986.

- ²Ku-Band Radar Self Test Application Requirements (internal document only), April 1993.
 ³Steve Schnurg: Trand Analysis: Application Evaluation
- ³Steve Schnurer, *Trend Analysis: Application Evaluation and Recommendation* (internal document only), November 1993.

A Prototype Supervised Intelligent Robot for Helping Astronauts

J. D. Erickson, K. A. Grimm, and T. W. Pendleton Johnson Space Center/ER

Abstract

The Extravehicular Activity Helper/Retriever, a prototype supervised intelligent robot, is being developed for the space applications of (1) helping the crew of a spacecraft such as the Space Station with various tasks such as holding objects and retrieving/replacing tools and other objects from/into storage, and (2) retrieving detached objects, such as equipment or crew that have become separated from their spacecraft. In addition to applications in the low-Earth-orbiting spacecraft environment, certain generic aspects of the technology have potential application to robotic tasks in other environments.

Robotic hardware, software architectures, and artificial intelligence were evaluated. Computer simulations of software performance were run, and KC-135 parabolic flights (to simulate weightlessness) were made to test hardware performance. Results show it is feasible to use the KC-135 environment for evaluation of dexterous grasping based on real-time visual sensing of freely rotating and translating objects.

Introduction

Numerous facets contribute to achieving robotic intelligence. This paper, based on a more complete article to be published in the *International Journal of Applied Intelligence*, describes many of these facets and attempts to relate them to the central theme of a software architecture that enables a sufficient level of robotic intelligence, and thus, real work in real environments under supervision by exception.

The essence of intelligent systems is that they are capable of collecting and applying knowledge of the situation gained at execution time and correlating it with previous knowledge to take effective actions and achieve goals. Intelligent systems are composed of sensors for perceiving both the external and internal environments, effectors for acting on the world, and computer hardware and software systems providing intelligent connection between the sensors and effectors.

Part of the processing by these computer systems is symbolic in a nonnumeric sense and thus enables practical reasoning, or the behavior which in humans we call intelligent. The intelligent system we address here, the Extravehicular Activity Helper/Retriever (EVAHR), is a supervised intelligent, mobile robot with arms and end effectors. Intelligent robots of this nature are required for long-term operations in space and are mandatory for space exploration to improve safety, reliability, and productivity, while enabling large cost savings through minimizing logistics.²

Problem Statement

Long-term space operations such as the Space Station require capabilities for rescue of EVA crew and retrieval of equipment. A space station cannot chase separated crew or equipment, and other vehicles such as the Space Shuttle will not usually be available. In addition to the retrieval of drifting objects, another need is for robotic help to EVA crewmembers in various tasks such as holding objects; retrieving and replacing tools and other items from and into storage; performing inspections; setting up and dismantling work sites; performing servicing, maintenance, and repairs; and deploying and retrieving payloads. Modeling, simulation, and analysis studies of space exploration missions have shown that supervised intelligent robots are enabling for human exploration missions.^{3,4}

The free-flying, supervised intelligent robot called EVAHR is being developed as a prototype crew helper and retriever of detached crew and equipment. EVAHR is a technology test-bed for evaluating and demonstrating the following capabilities:

- Robotic retrieval of objects which become detached from their spacecraft; e.g., astronauts adrift from the Space Station
- 2. A robotic crew helper in such roles as inspector, "gofer," holder, maintainer, servicer, tester
- A generic prototype supervised intelligent autonomous robot for mobility on planetary surfaces by such means as wheels or tracks and for terrestrial applications through appropriate adaptations

Early supervised intelligent robotic systems with initial capabilities to meet real needs are beginning to emerge from laboratories and manufacturers. It is now possible, in our opinion, to construct robots capable of accomplishing several specific high-level tasks in unstructured real world environments.

The ability to acquire and apply knowledge and skills to stated goals in the face of variations, difficulties, and complexities imposed by a dynamic environment with significant unpredictability is our working definition of "robotic intelligence." This ability does not require a broad-based general intelligence or common sense in the robot. However, doing the work needed to accomplish goals does require, in general, both mobility and manipulation in addition to reacting, or deciding "intelligently" at each step what to do. Further, supervised intelligent robots are required for human-robot teams where supervision is most naturally provided by voice.

Certain aspects of the EVAHR technology which provide the capability for specified tasks in a low-Earthorbiting spacecraft environment can be viewed as generic, thereby offering insight into intelligent robots for other tasks and environments. This is because the design of the software architecture, which is the framework for integrating the separate functional modules into a coherent system, is dictated in large measure by the tasks and nature of the environment. And because both the goalachieving tasks and the partially unpredictable nature of the environments in space are similar to those on Earth. the software architecture can be viewed as generic—as can many of the software modules, such as the artificial intelligence (AI) planner, world model, and natural language interface. Other software is bundled with certain hardware. This leads to the concept of an enduser-customized robot, composed of modules with standard interfaces,⁵⁻⁷ yet maintaining real-time response.

Approach

The goal of intelligent space robot development is one or more operational robots as part of human-robot teams in space. Prior to that, an evaluation of performance in space will be required.

To achieve our goal, we use a systems engineering approach with an iterative, three-ground-phase requirements prototype development, tested in both ground and aircraft simulations of space, followed by evaluation testing of a flight test article in space. We adapt and integrate existing technology solutions.

The EVAHR ground-based technology demonstration was established to design, develop, and evaluate an integrated robotic hardware/software system which supports design studies of a spaceborne crew rescue/equipment retrieval and crew helper capability. Goals for three phases were established. The Phase I goals were to design, build, and test a retriever system test-bed in which supervised retrieval of a fixed target could be demonstrated. Phase II goals were to enhance the test-bed subsystems with significant intelligent capability for arbitrarily oriented target retrieval while avoiding fixed obstacles. The objectives for Phase III, which is currently in progress, are to more fully achieve supervised intelligent, autonomous behavior by demonstrating grasp of a moving target while avoiding moving obstacles and by demonstrating crew helper tasks. Phase III is divided into two parts. Phase IIIA goals are to achieve real-time complex perception and manipulator/hand control sufficient to grasp moving objects, which is a basic skill both in space retrieval and in the transition between flying and attaching to a spacecraft. The Phase IIIB goal is to achieve a software architecture for manipulation and mobility, with integrated sensing, perception, planning, and reacting, which guarantees safe, robust conduct of multiple tasks in an integrated package while successfully dealing with a dynamic environment.

Our overall testing approach is short cycle run-breakfix with increasing integration and more relevant environments; such an approach finds design and implementation problems early when the cost to fix them is lowest.

The performance characteristics of the EVAHR hardware enable (or defeat) the intelligent behavior of the robot as animated by the software. We are testing only a subset of the Phase IIIB hardware in Phase IIIA. The hardware subset includes a seven-degree-of-freedom (DOF) arm (Robotics Research K807i), a five-DOF, compliant, force-limited dexterous hand, a laser range imager (Perceptron), a stereo video camera system (Teleos Prism 3), a pan/tilt unit, a 700 Megaflop computational engine employing i860s and transputers, and an inertial measurement unit (IMU) of accelerometers and gyros.

During Phase IIIA we are using a subset of our reaction plan architecture. We are exploring two new approaches to the software architecture for Phase IIIB. The first is a version of the 3-tiered, asynchronous, heterogeneous architecture for mobile robots⁸⁻¹⁰ adapted to include manipulation. The second is a version of the SOAR architecture¹¹ applied to robots.¹² SOAR is of interest because of its capabilities in learning, including recent work in situated, interactive natural language instruction.¹³ For each approach we are conducting evaluation testing of minimal prototype architecture implementations to obtain some evidence of their strengths and weaknesses for our tasks before selecting one for larger scale implementation in Phase IIIB.

Safety is a major issue in human-robot teams, especially in space. Since robotic motion control programs cannot be considered safe unless they run in hard real time, an approach which addresses this issue in a different manner from that of the 3-tiered architecture is needed for comparative evaluation. We are pursuing the development of one such approach.¹⁴

The pivotal problem in successfully coupling symbolic reasoning with the ability to guarantee production of a timely response is that the timing of actions taken by a real-time system must have low variances, so that the effects of those actions on unfolding processes can be predicted with sufficient accuracy. But intelligent software reserves the option of extended searching, which has very high variance. Therefore, when building a system that must act as well as reason in real time, one can choose one of the following categories of approach.

- Subject the AI component of the system to hard deadlines. This effectively embeds the AI reasoner within the real-time system, and under time pressure, results in loss of intelligent function.
- Refuse to subject the AI component of the system to hard deadlines, and have the real-time subsystem do its best with whatever commands the AI subsystem can generate in time. This effectively embeds the real-time subsystem within the AI system, and under time pressure, results in loss of timely control.

3. Refuse to subject the AI component of the system to hard deadlines, but let the AI components "negotiate" with the real-time subsystem to obtain a feasible schedule for task execution. This does not embed either subsystem within the other, and with proper selection of the real-time executive's task schedule, has the promise of remaining functional under time pressure. The 3-tiered approach is a category three approach, whereas we interpret SOAR to be a category two approach.

We can now summarize the state of the art. Simple control systems can get away with seeming to be fast enough, but that approach becomes potentially very dangerous in more complex systems, particularly in intelligent systems where the set of tasks being executed changes over time. In a system that may perform any subset of N possible tasks, there are 2^N possible combinations of tasks, and it becomes impossible to test the performance of each combination by hand when N is large. Therefore, it becomes imperative to have automated support for obtaining a guarantee that the system can always perform in hard real time.

Three-Tiered Software Architecture

Combining all prior knowledge with that sensed during a task requires that planning in advance provide only guidance, with control decisions postponed until the situation is being sensed and the task is being executed. This is the essence of Agre and Chapman's theory of plans-as-advice, ¹⁵ and is a design principle underlying the 3-tiered approach. The three tiers are the planner, the sequencer, and the reactive controller. The responsibility of the planning layer is to determine which tasks would accomplish the goal, and in what approximate order. Thus, the planning layer forms a partially ordered set of tasks for the robot to perform, with temporal constraints. The Al planner which we are evaluating for this application is the AP Planner. ¹⁶ It may be possible to use SOAR for this application.

The sequencing middle layer is responsible for controlling sequences of primitive physical activities and deliberative computations. Operating asynchronously from the planner, yet receiving inputs from that layer, the sequencer expands the sketchy plan based on the current situation. Thus, the hierarchical plan expansion happens at execution time rather than at the deliberative stage. To implement the sequencer, data structures called reactive action packages (RAPs) are used to represent tasks and their methods for executing.⁹

At the lowest level, the reactive controller accepts sensing data and action commands, sensorimotor actions that cannot be decomposed any further, from the sequencer. For example, "move," "turn," or "grasp" are all action commands that are passed on to the hardware. The reactive controller also monitors for success or failure of these commanded activities.

Phase IIIA Results to Date

Results from Phase II have been reported previously.¹⁷ Some preliminary results from Phase IIIA have also been reported.¹⁸⁻²³

SOAR Evaluation for Phase IIIB—SOAR was selected for study as a promising candidate for the EVAHR planning system. SOAR is a symbolic AI architecture which emphasizes problem-solving, planning, and learning.

One major advantage of SOAR is its ability to learn from a new experience by saving the sequence of steps to the goal as a "chunk." This chunk is in the form of a set of production rules, and if the same scenario is encountered in the future, the associated chunk will execute without the system's having to search for the correct sequence as it did initially.

From our experience with Hero-SOAR, a subset of SOAR for a Hero robot, we know that the reactivity of SOAR is an important capability needed to respond to the environment quickly. SOAR may be seen as a system with a planner which plans in the traditional sense yet with no actual data structure produced, a mechanism to execute the plan, and a fast replanning ability.

Phase IIIA Computer Simulation Results—Software modules for grasping free-floating objects in a zero-g 6–DOF environment have been described in previous sections. Results are given here of performance testing of these modules as subsystems, and of the same modules integrated and tested in our orbital and KC-135 simulations.²⁴

Search is the first visual function to be performed when there is no knowledge about the location of an object of interest. It is carried out as follows EVAHR's front hemisphere is divided into concentric rings, and each ring is further divided into sectors, each of which is enclosed by the FOV of the sensor. Each search starts from the center ring and spirals outward until an object is found.^{25,26}

Algorithms for image-based pose estimation have been implemented. Several objects were chosen for testing. These objects include some orbital replaceable units (ORUs), a star tracker, a jettison handle, and some wrenches. To test the robustness of the software, 500 tests were run on each object with actual poses of the object randomly oriented using a random number generator in (simulated) images. Noise was added to the range component of the image to test the sensitivity of the algorithms to noise. Test results indicate that (1) most estimation errors are less than 5° (with up to 3 percent noise in range), (2) the performance of the pose estimation software gradually degraded with increasing noise in range measurements.

The rotational state estimator uses intermittent delayed poses from the pose estimator software to provide the arm trajectory planner with current estimates of the target's rotational state at the rate of 100 Hz. The estimator utilizes

an extended Kalman filter because of the inherent nonlinear nature of rotational dynamics. The effects of various parameters on the performance of the standalone rotational state estimator have been reported in Hewgill.¹⁹ Testing on the integrated rotational state estimator shows it converges within 4 pose estimates (about 4 sec) and maintains error estimates of less than 3°, which meets requirements.

The relative translational state estimator used for the KC-135 experiment does not use an inertial coordinate system. The equations describing the dynamics are nonlinear. Therefore, the estimator design is based on an extended Kalman filter. The results of its performance in the KC-135 simulator show an accuracy similar to that for the orbital case.²⁷

Integrated software testing in the orbital simulation has concentrated on and produced results in two areas: (1) determining the overall system performance against grasping different moving targets with random initial states and (2) determining the computational requirements for the pose estimation software, using rate and delay as parameters. Grasp impact dynamics calculations are made to verify that the target is not knocked away during the grasp or by a prior collision with the arm. Under these conditions, the system has achieved a >70 percent successful grasp rate for both objects tested. The state estimates have less than 1 inch and 5° of error. Results from the second suite of tests show that pose estimation rate and delay also have a direct effect on the time-tograsp in successful tests. Assuming pose estimation rate and delay of 0.1 sec, we were able to estimate that six i860 processors would be sufficient to achieve these rates and delays.

Aircraft Reduced Gravity Environment

Some microgravity research can be conducted inside an aircraft simulating space by flying vertical parabolic flight paths, but only for very limited amounts of time. During Phase IIIA we are flying a subset of the EVAHR Phase IIIB hardware and software aboard the NASA Reduced Gravity Program's KC-135 aircraft. This aircraft flies a series of parabolic trajectories resulting in approximately 15 sec of near microgravity (<.01-g) in the cabin during each parabola. The robotic arm, hand, vision sensor with pan/tilt system, and IMU are attached to the floor of the aircraft. During microgravity, an object is released, tracked by the vision system, and grasped by the hand. All of these objects have a complex construction with multiple graspable points.

On several KC-135 preliminary flights, data characterizing the reduced gravity were collected from an IMU placed on the cabin floor. Video recordings also were made of objects floating during the reduced gravity interval. The vertical acceleration fluctuated significantly about zero-g. Fluctuations between 75 mg and -75 mg were commonplace. These fluctuations caused the released object to accelerate toward either the ceiling or floor of the airplane.

Lateral accelerations were also observed and were due to air turbulence, flight path corrections, or other effects.

Trajectory duration was determined during 38 parabolas. A test interval started when the target was released and continued until the target hit the inside of the airplane fuselage, or was touched by personnel, or left the field of view of both video cameras. The results indicate that two-thirds of the parabolas have 4 seconds or less of usable microgravity.

These results, especially the trajectory durations, do not match well with the extrapolation to the KC-135 of time-to-grasp results from the orbital simulation presented above.

In a separate flight of the KC-135, we tested the unintegrated hardware subsystems (except the stereo cameras) independently because all of this hardware is designed to operate in a one-g environment and might behave differently in the KC-135 in microgravity or after the 1.8-g pullout at the bottom of the parabolas. Motions and operations representative of those that will be used in later object tracking and grasping evaluations were used in these tests. All equipment was determined to operate without measurable changes in behavior from that expected.

Conclusions

The need for crew help and retrieval of detached crew and equipment in space has been identified. Evaluation of the practical realization of a potential solution has passed several successful milestones, but is still ongoing, with many of the critical developments yet to come. We have described here an initial attempt to build and understand a prototype of a supervised intelligent robot for use in space. Its software architecture is also potentially useful for many U.S. economy-related robot applications on the ground.

Both our Phase II and Phase IIIA results demonstrate that manipulation requires greater accuracy of sensing and perception than does mobility. Integrated testing with our Phase IIIA computer simulation has not only shown that we have a workable software design, but has also afforded us systems engineering analyses supporting computer hardware design for achieving real-time complex perception processing (sensor to percept) and grasp control (percept to action) for freely moving objects.

Our plans are first to complete the metrology of the manipulator and joint calibration of both vision-systemmanipulator pairs. We are recoding the laser scanner pose estimation software to run in real time on the i860 network. The tracker and translational state estimator are currently running in real time on i860s. The manipulator trajectory controller and grasp planner are running in real time on the transputer network. Grasp testing using targets mounted on the object-motion unit is being conducted in preparation for the KC-135 vision-guided grasping flights. Then we have several moving object

grasp evaluation flights to conduct. Phase IIIB developments are dependent on the selection of a final software architecture from the preliminary prototyping efforts which are underway using a set of crew helper tasks, scenarios, and computer simulation environments with human-injected unpredictable events to assess the value of the many goal-planning and real-time reaction aspects of the supervised intelligent robot design.

References

- ¹Erickson, J. D., et al., "An Intelligent Space Robot for Crew Help and Crew and Equipment Retrieval," *International Journal of Applied Intelligence*, accepted for publication in 1994.
- ²Erickson, J. D., et al., "SEI Planet Surface Systems Humans/Automation/ Robotics/Telerobotics Integrated Summary," internal document JSC-45100, Johnson Space Center, Houston, TX, Mar. 1991.
- ³Erickson, J. D., "Needs for Supervised Space Robots in Space Exploration," 1992 World Space Congress, IAF-92-0800, International Astronautical Federation, Paris, France, Aug. 1992.
- ⁴Erickson, J.D., et al., "Some Results of System Effectiveness Simulations for the First Lunar Outpost," 1993 AIAA Space Programs and Technology Conf., Huntsville, AL, Sept. 1993.
- ⁵Bonasso, R. P., and Slack, M. G., "Ideas on a System Design for End-User Robots," *Proc. SPIE 1829 Cooperative Intelligent Robotics in Space III*, Nov. 1992, p. 352.
- ⁶Ambrose, R. O., Aalund, M. P., and Tesar, D., "Designing Modular Robots for a Spectrum of Space Operations," *Proc. SPIE 1829 Cooperative Intelligent Robotics in Space III*, Nov. 1992, p. 371.
- ⁷daCosta, F. et al., "An Integrated Prototyping Environment for Programmable Automation," *Proc.* SPIE 1829 Cooperative Intelligent Robotics in Space III, Nov. 1992, p. 382.
- *Gat, E., "Integrating Planning and Reacting in a Heterogeneous Asynchronous Architecture for Controlling Real-World Mobile Robots," AAAI-92, *Proc. 10th Natl. Conf. on AI*, San Jose, CA, July 1992.
- ⁹Firby, R. J., "Adaptive Execution in Dynamic Domains," Ph.D. Thesis, Yale University, 1989.
- ¹⁰Bonasso, R. P., "Using Parallel Program Specifications for Reactive Control of Underwater Vehicles," *Jour. of Applied Intelligence*, June 1992.
- ¹¹Laird, J. E., Newell, A., and Rosenbloom, P. S., "SOAR: An Architecture for General Intelligence," *Artificial Intelligence*, Vol. 33, No. 1, pp. 1-64, 1987.
- ¹²Laird, J. E., et al., "RoboSOAR: An Integration of External Interaction, Planning, and Learning Using SOAR," *Robotics and Autonomous Systems*, Vol. 8, 1991.
- ¹³Huffman, S. B, and Laird, J. E., "Learning Procedures from Interactive Natural Language instructions," *Proc. 10th Intl. Conf. on Machine Learning*, June 1993.

- ¹⁴Schoppers, M., "Ensuring Correct Reactive Behavior in Robotic Systems," AIAA/NASA JSC Workshop on Automation and Robotics '93, NASA Johnson Space Center, Houston, TX, Mar. 24, 1993.
- ¹⁵Agre, P., and Chapman, D., "Pengi: An Implementation of a Theory of Activity," *Proc. AAAI*, 1987, pp. 268-272.
- ¹⁶Elsaesser, C., and MacMillan, T. R., "Representation and Algorithms for Multiagent Adversarial Planning," MTR-91W000207, MITRE Corp, McLean, VA, Dec. 1991
- ¹⁷Erickson, J. D., et al., "Technology Test Results from an Intelligent, Free-Flying Robot for Crew and Equipment Retrieval in Space," *Proc. SPIE 1612, Cooperative Intelligent Robotics in Space II*, Boston, MA, November 1991.
- ¹⁸Littlefield, M. L., "Adaptive Tracking of Objects for a Mobile Robot Using Range Images," *Proc. SPIE 1829, Cooperative Intelligent Robotics in Space III*, Boston, MA, Nov. 1992, pp. 433-443.
- ¹⁹Hewgill, L., "Motion Estimation of a Freely Rotating Body in Earth Orbit," *Proc. SPIE 1829, Cooperative Intelligent Robotics in Space III*, Boston, MA, Nov. 1992, pp. 444-457.
- ²⁰Grimm, K. A., et al., "Experiment in Vision-Based Autonomous Grasping Within a Reduced Gravity Environment," *Proc. SPIE 1829, Cooperative Intelligent Robotics in Space III*, Boston, MA, Nov. 1992, pp. 410-420.
- ²¹Chien, C. H., "A Computer Vision System for Extravehicular Activity Helper/Retriever," *Proc. SPIE Conference on Sensor Fusion and Aerospace Applications*, Orlando, FL, Apr. 1993.
- ²²Norsworthy, R. S., "Performance Measurement of Autonomous Grasping Software in a Simulated Orbital Environment," *Proc. SPIE 2057, Telemanipulator Technology and Space Robotics*, Boston, MA, Sept. 1993.
- ²³Anderson, G., "Grasping a Rigid Object on Zero-G," Proc. SPIE 2057, Telemanipulator Technology and Space Robotics, Boston, MA, Sept. 1993.
- ²⁴Norsworthy, R. S., "Simulation of the EVAHR/KC-135 for Software Integration/Testing," *Proc. AIAA/NASA Conf. on Intelligent Robotics in Field, Factory, Service, and Space*, Houston, TX, March 1994.
- ²⁵Littlefield, M. L., "Real-Time Tracking of Objects in a KC-135 Microgravity Experiment," *Proc. AIAA/NASA Conf. on Intelligent Robotics in Field, Factory, Service,* and Space, Houston, TX, March 1994.
- ²⁶Huber, E. L., and Baker, K., "Object Tracking with Stereo Vision," *Proc. AIAA/NASA Conf. on Intelligent Robotics in Field, Factory, Service, and Space*, Houston, TX, March 1994.
- ²⁷Hewgill, L., "Motion Estimation of Objects in KC-135 Microgravity," *Proc. AIAA/NASA Conf. on Intelligent Robotics in Field, Factory, Service, and Space*, Houston, TX, March 1994.

A Reactive Navigational Controller for Autonomous Mobile Robots

Scott Hawkins
Johnson Space Center/ER

Abstract

Autonomous mobile robots must respond to external challenges and threats in real time. One way to satisfy this requirement is to use a fast low-level intelligence to react to local environment changes. A fast reactive controller has been implemented which performs the task of real-time local navigation by integrating primitive elements of perception, planning, and control. Competing achievement and constraint behaviors are used to allow abstract qualitative specification of navigation goals. An interface is provided to allow a higher-level deliberative intelligence with a more global perspective to set local goals for the reactive controller. The reactive controller's simplistic strategies may not always succeed, so a means to monitor and redirect the reactive controller is provided.

Introduction

The effectiveness of an intelligent agent is judged on both the appropriateness and timeliness of its actions. These two attributes of intelligence are not separable in many contexts, since an action must often take place within a limited time window in order to be appropriate. Reactive systems improve the time response of an intelligent system by providing reflexive responses to changes in the environment of the agent. Reactive control software that operates in conjunction with a higher-level intelligence (such as a global path planner) was developed to provide fast intelligent control for a mobile robot.

Reactive control is the process of trying to achieve an abstract goal (a plan step) while attempting to comply with a set of environmental constraints. Changes in the environment do not necessarily mean that the goal must be changed. As long as the goal is sufficiently abstract, the reactive controller may be able to cope with simple environmental changes within the context of achieving the goal. In other words, if an obstacle moves into the path of the robot, the reactive controller may be able to deal with the situation without help from the planner.

Reactive Controller Context

A reactive controller can be considered minimally intelligent, in that it combines primitive elements of perception, planning, and control. These elements of reactive controller intelligence must be fast, so they won't necessarily use the most sophisticated methods available. The reactive controller has a local perspective, so it needs to be given abstract goals by some higher-level intelligence with a more global perspective (Fig. 1).

It is likely that some goals may not be achievable by the reactive controller without further decomposition, so there must be a monitoring function that can interrupt the reactive controller and trigger replanning in the higher-level intelligence.² Simple constraints on achieving a goal, such as time-outs, could be used by the reactive controller to trigger a request for replanning, but a more intelligent appraisal of progress toward the goal would require longer deliberation. Therefore the monitoring functionality should probably reside in the higher level intelligence.

The focus of the reactive controller is not on using classical control laws, per se, but rather on producing concrete primitive actions from an abstractly specified goal. It is appropriate to have at least one level of conventional control that executes these primitive actions. The controllers that execute these primitive actions will be designated low-level controllers.

Reaction to stimuli perceived in the environment is based on raw or minimally processed sensor data. Sometimes it might be necessary to rely on higher level perception from another source, but these data should be delivered at a fast enough rate that the reactive controller does not have to wait to make a decision.

Competing Behaviors

The reactive navigational controller was implemented using competing behaviors. Behaviors are procedures that transform a set of inputs composed of goals and sensor data to outputs that are used to determine the actions that will be taken by the robot. Competing behaviors that produce actions based on different criteria

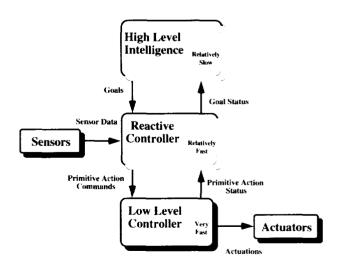


Figure 1. Reactive controller system context.

may be combined using mediation techniques to produce emergent behaviors. Behaviors are prioritized to allow behaviors with critical functions to override less critical behaviors. The outputs of competing behaviors share the same data structure so that the behavior mediation may be performed generically.

Behavior Output

The output data structure of the behaviors should be appropriate for the information and the actions that are available to the intelligent agent. The agent that the reactive controller was developed for is a mobile robot with a ring of sonar, infrared, and tactile proximity sensors. The robot may rotate both the sensors and the steering independently of translation. The configuration of the robot suggested a data isomorphism in which a continuum of candidate directions in the horizontal plane are available to move. This continuum of directions was discretized into beams that correspond to arcs of coverage by individual proximity sensors. A set of beams that make up a behavior output is called a beam array.

Each beam is composed of direction, action, constraint, desire, and achievability components. The beam direction is a preferred direction to move within the beam. This direction will usually be the center of the beam arc, but a more specific direction may be provided for fine tuning of a goal direction. The action component is the distance that behavior would like to move, if this beam were chosen as the direction to move in. Constraint is the limit that this behavior places on movement within the arc of the beam. Desire, specified on a normalized scale of 0.0 to 1.0, is a subjective measure that indicates the value of moving in a particular direction. The degree of desire doesn't necessarily correspond directly to the constraint or action for the beam. Achievability is a measure of how much the action can be actualized within the imposed constraints and is determined during behavior mediation.

Behavior Mediation

Suppose that there is a set of outputs produced by competing behaviors B_1 to B_m , and for each behavior B_i there is weight w_i that corresponds to the priority for that behavior. Each behavior B_i is divided into beams b_{i1} to b_{in} , with directions f_{i1} to f_{im} , actions a_{i1} to a_{in} , constraints c_{i1} to c_{in} , desires d_{i1} to d_{in} , and achievabilities q_{i1} to q_{in} . The behaviors are combined to produce a single beam array output with directions f_1 to f_n , actions a_i to a_n , constraints c_1 to c_n , desires d_1 to d_n , and achievabilities q_1 to q_n .

The first step in behavior mediation is to propagate the constraints. The constraints from all of the behaviors are considered for each beam and the most pessimistic constraint is adopted as the combined constraint for that particular direction. So

$$c_{j} = MIN(c_{1j}, \ldots, c_{mj})$$
 (1)

The next phase of behavior mediation is to constrain each action according to the worst case constraint that was discovered for the beam that contains the action:

$$\mathbf{a'}_{ij} = \mathbf{MIN}(\mathbf{a}_{ij}, \mathbf{c}_{j}) \tag{2}$$

where a'_{ij} is the constrained action. This ensures that no proposed action will violate an absolute constraint. Of course, the constraints are only as accurate as the information that is available from the sensors.

If a beam action is derated because of a constraint, then achievability for the beam is set to the proportion of the constrained action to the full proposed action, so

$$q_{ij} = \begin{cases} \frac{a'_{ij}}{a_{ij}} & \text{if } a'_{ij} < a_{ij} \\ ... & 1.0 & \text{if } a'_{ij} \ge a_{ij} \end{cases}$$
(3)

For example, if the action specifies moving 5 meters, but there is an obstacle detected within the beam at 2 meters, then achievability would be set to 0.4. However, if the constraining obstacle were sensed beyond the proposed movement, say at 7 meters, then achievability would be set to the full 1.0.

The combined action chosen for a particular beam direction is the greatest constrained action for that direction:

$$a_{i} = MAX(a'_{1i}, \dots, a'_{mi})$$
 (4)

Selection of the greatest constrained action for a beam results in an ambitious but safe action to be proposed. The direction, f_j , is chosen from the beam in the behavior with the maximum constrained action.

The final step in behavior mediation is to combine the desire components. The combined desire will be a function of the desire generated by each behavior, the priority for each behavior, and the achievability of the original proposed actions:

$$d_{j} = \sum_{i=1}^{m} w_{i} d_{ij} q_{ij}$$
(5)

Action Selection

The result of behavior mediation is a beam array in which each beam contains a preferred direction, a constrained action, and a desire to move in that direction. A specific beam must be chosen from the beam array from which the resultant action will be determined. Simply choosing the resultant beam with the greatest desire is the fundamental method. However, this may not be an adequate solution for some systems.

Simply picking the direction with the greatest desire may not be adequate, partly because of inefficiencies due to "smoothness" of control issues. For example, suppose that the low-level controller pauses every time it receives a new command before executing the command. It is desirable to run the reactive controller at a fast control rate so that changes in the environment may be accommodated, but if the changes result in relatively insignificant fine tuning of the robot's movement, it may be inefficient to interrupt the progress that is already being made. So there would need to be some hysteresis in the reactive controller. This hysteresis could be resistance to choosing a new beam when there would be no significant change in desire. The hysteresis could also take the form of not issuing a new command unless the action or direction changes by some arbitrary amount.

Another potential problem is with oscillations due to interactions with the environment. This type of problem can cause the robot to be stuck in some type of repeating behavior. Once again, hysteresis can be inserted in the system to help dampen out the oscillations. Alternatively, actions could be smoothed over time using a filtering technique.

Implementation

Navigation Behaviors

Three competing behaviors are used to provide constraint, achievement, and optimization in the reactive navigational controller. They are, in order of priority, Keep Safe Distance, Follow Vector, and Persist.

Keep Safe Distance is primarily a constraint behavior that makes decisions based on maintaining a margin of safety around the robot. This is the highest priority behavior, with a weight of 0.55. The inputs to Keep Safe Distance are the safety margin to be maintained, the proximity sensor data, and the maximum sensor range. The sensor data include fused sonar, infrared, and tactile proximity.

Sensor fusion is accomplished by discriminating between redundantly oriented sensors based on confidence ranges. Sonars are believed at medium and long distances (0.5 to 3.0 meters). Infrared is utilized at close range (less than 0.5 meters). Tactile bumper switches override the other sensors to indicate collision. Fused proximity sensor data is provided at a finer granularity by dividing the sensor arcs into smaller arcs and using the same proximity values for each subdivided arc that were used for the original arc.

Constraints generated by Keep Safe Distance indicate how far the robot could move radially within a safety margin. If the margin of safety is violated for some unexpected reason, Keep Safe Distance will generate desires and actions to reestablish the safety margin.

Follow Vector is an achievement behavior whose only criterion for making decisions is to try to reach a goal represented as a two-dimensional relative

displacement vector. Follow Vector is weighted to have a medium priority of 0.35. The maximum desire and action are generated in the direction of the goal, varying with the cosine of the direction so that they reach minimum values in the direction opposite to the goal. The minimum values can be tuned, but are nominally zero. The shape of the desire and action lobes can be focused more sharply toward the goal by varying the values with the cosine raised to a fractional power, such as that of the square root.

Persist is an optimization behavior that is used to add energy to the behavior of the robot to try to break out of local minima. Persist is the lowest priority behavior at 0.10. Desires and actions in Persist are generated by the same algorithm used by Follow Vector, except that the goal vector for Persist is one that attempts to maintain the heading of the robot. In other words, the Persist behavior resists any change in direction. Persist uses a strategy which is often contradictory to Follow Vector; thus this behavior is activated only when the robot has not made any new progress toward the goal in an arbitrarily specified amount of time. This time-out is called the amount of patience and it is typically set to 1 minute.

Interface

The interface to the reactive navigational controller is minimal at this time. A goal can be set or removed. The reactive controller provides a notification when the goal has been achieved. There are currently no built-in criteria for failing to achieve the goal, so there is no notification of failure to achieve the goal. The reactive controller is eternally optimistic and will happily continue to try until it achieves the goal, the goal is replaced by another goal, or the goal is removed. In fact, even when the goal is achieved the controller remains reactive, so it will attempt to maintain the safety margin and the state of being at the goal.

Sample Reactions

Two sample reactions of the robot are shown in Figures 2 through 5. These reactions are from data obtained from running the robot in the hallway of an office building. The first reaction demonstrates goal seeking behavior. The second reaction demonstrates obstacle avoidance behavior.

Obstacle Map Display—Obstacle maps created as informational displays for a human operator are shown in Figures 2 and 4. The reactive controller does not use this information, but the map allows a human to understand the robot's perceived environment. The obstacle map is an occupancy grid created over time by proximity data from the sensors. It is important to note that the immediate sensor image won't match the occupancy grid image exactly. The robot's position is indicated in the occupancy grids by a circular icon with two radial lines inside. The longer radial line indicates the robot's steering

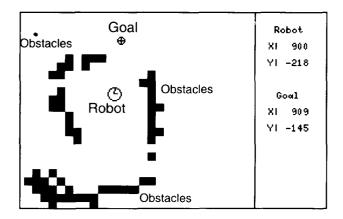


Figure 2. An occupancy grid depiction of the robot's environment showing a clear path between the robot and the goal.

azimuth. The shorter line shows the orientation of the sensor turret. The goal is an abstract point in two-dimensional space indicated by a circular icon with cross-hairs. Obsta-cles are shown in the occupancy grid as black squares.

Behavior Output Display—The displays in Figures 3 and 5 show the fused proximity sensor data, the output of the individual behaviors, and the result of combining the competing behaviors using behavior mediation. In the center of each box in the display is an icon representing the robot. Each icon has a heading bar that indicates the orientation of the robot steering. All references to direction are in degrees, with the origin at 3 o'clock and with angular measure increasing in the counterclockwise direction.

The box labelled Proximity Data shows the robot icon surrounded by a curve obtained by connecting the end points of proximity readings from the sensors. This proximity data is from a single frame of sensor data.

The Persist box in Figure 3 shows that the behavior has not been activated. Persist has been activated in Figure 5, since the reactive controller has run out of "patience." Desire is shown as a continuous lobe of values represented by a curve filled with a dot pattern. It can be seen that for the Persist behavior in Figure 5, the greatest

desire is in the direction of robot motion, or at a heading of about 200°. The end points of the action vectors are shown as small black rings around the robots.

The Follow Vector box in Figure 3 shows a lobe of desire that points directly toward the goal shown in Figure 2. The action end points have a distribution similar to that of desire.

The Keep Safe Distance box shows a constraint curve that indicates how far the robot could move in a radial direction while maintaining a margin of safety a little less than the robot radius. The Keep Safe Distance is capable of generating desire and actions when the margin of safety is violated. This is shown in Figure 5, where an obstacle at an azimuth of 45° is too close to the robot, generating a strong desire to move in the reciprocal direction. The action end point for this move is very close to the robot at the point where the margin of safety would be reestablished.

The Result box shows the result of behavior mediation. In Figure 3 the Result box indicates the strongest desire is to move directly toward the goal, so the reactive controller exhibits goal seeking behavior. The desire is reduced from that of Follow Vector because the components from Persist and Keep Safe Distance were zero. The actions shown are not limited in the direction of the goal, but are limited to the left and right of the robot by the constraints provided by Keep Safe Distance.

The Result box in Figure 5 shows goal avoidance behavior that occurs when the desires and constraints generated by Keep Safe Distance swamp out any other desires. Some vestigial desire to move laterally toward 135° can be seen, but all desire to move toward the goal is cancelled out by the disappointment that none of the proposed action can be achieved in that direction.

Discussion

The reactive controller uses a simplistic numerical method of local path planning. I expected that there would be difficulties with local minima and numerical instabilities. I was correct. I was able to correct most problems by first understanding the problems dynamically. I tried at first to understand the problems with textual data dumps, but this approach did not help much. After I developed the explanation displays shown in

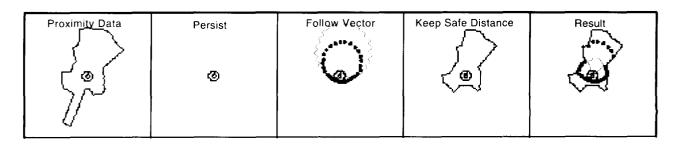


Figure 3. An explanation display showing the goal seeking behavior that is stimulated in the reactive navigational controller in response to the environment shown in fig. 2.

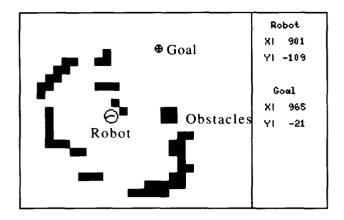


Figure 4. An occupancy grid depiction of the robot's environment showing a dangerously close obstacle between the robot and the goal.

Figures 3 and 5, then the problems usually became immediately obvious.

Discouragement

One of the first observed anomalous behaviors had intriguing similarities with my own behavior. I observed that when the robot was a long distance from the goal, would become easily discouraged and would wander off in the wrong direction. The Follow Vector behavior was given the full distance to the goal as the vector to follow. The Keep Safe Distance behavior was given a parameter that specifies the maximum range of the sensors so that it set the constraint for action at no further than the maximum sensor range. The problem was that when the range to the goal was significantly farther than the maximum sensor range, achievability would be low for an action in that direction. This meant that lateral directions and lower priority actions in other directions took precedence, so that if the robot turned away from the goal, Persist would tend to keep it going in that direction.

I solved this problem by limiting the length of the input vector to Follow Vector. After the length was

limited to the maximum sensor range, the robot did not become so easily discouraged. This unexpected result seems like my own tendency to wander from the task at hand when the goal seems to be too difficult. However, if I can set shorter term goals for myself that still move in the right direction, then I do not become so easily discouraged.

Persistence and Patience

Another problem observed in the behavior of the robot was a tendency to become trapped in local minima, such as large flat or concave obstacles with the goal directly behind the obstacle. I reduced this problem by adding the Persist behavior, which added more energy to the control strategy so that the robot would have more of a tendency to continue moving toward the periphery of the obstacle. However, the solution became a problem when the robot would sometimes persist in moving away from the goal when a fairly direct path was available. I tried solving this by further adjusting the behavior priorities, but it soon became apparent that the Persist strategy was not appropriate in most cases.

The Persist behavioral strategy was needed only when the robot was stuck in local minima and not making any progress toward the goal. This analysis prompted the policy of activating the Persist behavior only after no progress had been made for a certain period of time. Once again, I couldn't resist comparing it to my own behavior of trying to achieve a goal using a straightf-orward strategy until it was clear that I was not making any progress. Eventually I would lose patience and try a different strategy. So I named this time-out parameter the amount of patience.

Achievability

One of the admirable attributes of this reactive controller is the smoothness of its actions compared with those of another reactive controller that was developed in our lab using Rex³ and GAPPS.⁴ The other reactive controller also uses mediated behaviors, but each behavior requires only a single decision instead of a continuum of alternatives. Perhaps one reason for any apparent

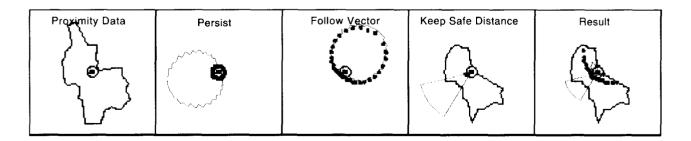


Figure 5. An explanation display showing the obstacle avoidance behavior that is stimulated in the reactive navigational controller in response to the environment shown in Fig. 4.

smoothness in the current reactive controller is that a large set of prioritized alternative actions is produced by the behaviors. This alone is not enough, however, since an effective method for sorting through the possible actions must be used. It seems that the key to this method is the achievability component produced during behavior mediation. This component encourages using actions that can be most fully actualized over those that must be severely limited. The result is that moving toward the goal and moving through open areas are co-optimized.

Conclusions

The reactive navigational controller developed here is rich in behavioral and motivational metaphors. Concepts such as goal, action, desire, constraint, achievement, persistence, and patience combined with the pulsating and seemingly organic explanation displays make the reactive controller almost seem to be alive. Some differences between expected behavior and actual behavior are simply bugs or overly simplistic strategies, but many of the discovered problems have had compelling psychological analogs.

One of the best ways to explain the use of this reactive controller is to compare it to riding a horse. The horse avoids obstacles and will attempt to follow simple goals directional cues from the rider or environmental cues such as pathways. The benefits of autonomous behaviors such as these can be very useful in many cases, but the rider must also be vigilant that the horse doesn't follow its own agenda to the detriment of the rider. For example, the horse might decide to move toward a clearing when the rider wants to plunge directly into the forest.

It is important to remember that this reactive controller is not a global path planner. It works best when it has local goals that should be easily accomplished in the perceived environment. It will, however, make quick and reasonable decisions when the perceived environment changes unexpectedly. It could be given more sophisticated planning capabilities, but the speed of execution should not be reduced to the point where the reactive controller no longer reacts fast enough to changes in the environment.

This reactive navigational controller is still very primitive in its capabilities and interfaces. Further work

will include adding qualitative behaviors such as following a hallway from one location to another. Qualitative behaviors will require qualitative success criteria, such as following the hallway until an intersection is reached. Also, the higher level intelligence should be able to fully specify the members of a set of competing behaviors, including parameters such as priority and margin of safety.

Acknowledgments

I would like to thank the other members of the SodaPup autonomous mobile robot project for their support while I experimented with this approach. I would especially like to thank Bob Goode and Jeff Kowing, whose work was most directly impacted by any problems with the reactive controller. Besides being patient, they also offered many valuable suggestions and discovered several bugs.

During the initial conception of the reactive controller, I examined my own behavior closely and applied metaphors that I had discovered in the course of learning a martial art called Aikido. I thank Morihei Ueshiba, the founder of Aikido, for laying the foundation for my understanding of movement and motivation when it really matters.

References

- ¹Kaelbling, L. P., "An Architecture for Intelligent Reactive Systems," *Reasoning About Actions and Plans: Proceedings of the 1986 Workshop*, Morgan Kaufmann, Los Altos, California.
- ²Ambros-Ingerson, J., and Steel, S., "Integrated Planning, Execution, and Monitoring," *Proceedings of the* Seventh National Conference on Artificial Intelligence, AAAI Press, Minneapolis-St. Paul, Minnesota, 1988.
- ³Kaelbling, L. P., "Rex: a Symbolic Language for the Design and Parallel Implementation of Embedded Systems," *Proceedings of the AIAA Conference on Computers in Aerospace*, Wakefield, Massachusetts, 1987.
- ⁴Kaelbling, L. P., "Goals as Parallel Program Specifications," *Proceedings of the Seventh National Conference on Artificial Intelligence*, AAAI Press, Minneapolis-St. Paul, Minnesota, 1988.

Reengineering Legacy Software to Object-Oriented Systems

D. Braley, E. Fridge, C. Pitman, M. Izygon*, B. Mears*, and A. Plumb**

Johnson Space Center/PT

*I-NET, Inc.

**LinCom, Inc.

Introduction

Like many other organizations, NASA has a legacy of complex software systems that were developed during the past three decades and are still being used today. These systems are critical to NASA's mission; they represent an enormous investment; and they are very expensive to use, maintain, and enhance. Methods and tools to help modernize these software systems so that they are easier to use, maintain, and enhance are becoming increasingly important. NASA and all other organizations facing the same situation cannot afford to rebuild all of these systems from scratch. Furthermore, the actual code of these older systems is often the only place that crucial information and/or system requirements are captured, and such information/requirements must be extracted from the old code before it is replaced. Thus, instead of rebuilding from scratch, modernizing these millions and millions of lines of code by reengineering them using object-oriented technology (and other modern software engineering principles and tools) is often the best way for NASA and industry to decrease operations and maintenance costs.

Definition of Reengineering

Reengineering terminology is not always used in the same way by different authors, and so it is best to begin with brief definitions of some terms. Forward engineering refers to the usual direction of software development (whether a waterfall, spiral, incremental, or rapid prototyping process): begin with requirements, then design, and deliver code. In contrast, reverse engineering refers to starting with code and recovering from it the essential syntax and semantics (i.e., in preparation for translation into a new language), or the design of the old code (i.e., design recovery), or the requirements of the old code and design (i.e., requirements recovery). Reengineering is NOT synonymous with reverse engineering. Reengineering is the combination of reverse engineering (either syntax and semantics recovery, design recovery, or requirements recovery) followed by forward engineering into the new, modernized software system. Note that reengineering that goes all the way back to requirements recovery before going forward again is very similar to rebuilding the software system from scratch, but the difference is that the reverse engineering portion of the reengineering process helps to ensure that all of the critical requirements which are captured only in the old code will appear in the new system.

Background of Work at JSC

The Software Technology Branch (STB) has been developing and testing reengineering methods and tools for several years. The first project involved a large orbital mechanics program named the Orbital Maneuver Processor (OMP). The project recovered the design of the OMP FORTRAN code, modified the design into an object-based one, and then implemented the new design in Ada. Several tools that aid in the recovery of the design from FORTRAN code (e.g., COMMON block structures, calling trees, etc.) were used and enhanced for this and following projects; these tools were originally developed by JSC during the period of development of the Space Shuttle flight planning software.

Work on support environments for reengineering has resulted in the Reengineering Applications (REAP) environment, which provides a uniform presentation and invocation of reengineering tools and a suggested sequence for their use. The STB is providing reengineering support to other projects: a command system (Mission Operations Computer), a database reconfiguration system (Recon-figuration Tools), and a solar thermal analysis and optimization system (in conjunction with the University of Houston, for Sandia National Laboratories). The STB has developed training, enhanced support tools, and refined and extended methodologies.

Reengineering Methods Used on the ROSE Project

Another of the more significant reengineering projects with which the STB is associated is the Reusable Objects Software Environment (ROSE). This project is seeking to recover the requirements from the Flight Analysis and Design System (over 2 million lines of FORTRAN code), enhance the requirements for reuse if necessary, and then redesign the system into an object-oriented one and implement it in C++. The first-year phase of this four-year project will be concluded in January, 1994; so far, very promising results have been obtained.

On the ROSE project, the reverse engineering method used for FORTRAN design recovery was developed over the course of a few years and then tailored to the ROSE project. Several Computer-Aided Software Engineering (CASE) tools are used to facilitate this process, such as data and control structure analysis tools, complexity metrics tools, and restructuring/refining tools (to a limited extent). The forward engineering part of the

ROSE reengineering project is using the object modeling technique (OMT), an object-oriented analysis and design (OOAD) method developed by James Rumbaugh, et al. OMT is excellent for analysis, providing the basis for communication and clarification of the problem to be solved and of the requirements. However, this is still a manual-intensive phase of reengineering.

Lessons Learned

One of the most important lessons learned over the past two decades of software development and maintenance at JSC is that the design must never be allowed to diverge from the code during maintenance and enhancement; i.e., the design must be kept closely tied to the code. For the ROSE project, it was discovered that, during design, OMT must be supplemented and extended to permit a closer tie between the design and the C++ code that will eventually implement it. Another very important lesson learned is that it is critical to provide appropriate training in the methods, processes, tools, and language used for the project, before the project team members are expected to meet project deadlines and deliverables. The ROSE project adopted this approach and it is paying off. The STB was asked to help coordinate the ROSE training and to provide initial training in the OMT method.

Future Directions: Integration Technology and Data Models

As one of its more forward-looking research projects, the STB has also been investigating integrated reengineer-

ing environments. Today, many companies are working on integrated support environments for forward engineering, but the requirements for a reengineering environment are very similar. An integrated environment should provide presentation, data, control, and process integration. The National Institute of Standards and Technology (NIST) and the European Computer Manufacturers Association (ECMA) have proposed a standard model for discussing such an integrated environment. The STB, in conjunction with IBM, has been working to develop a reengineering data model for a repository, which would provide data integration in a reengineering environment based on the NIST/ECMA model. Much good initial work has been done to date, but this is a challenging problem and much work still remains. Nevertheless, the objective is to produce the REAP II environment, based on this integration work, within one to two years.

Conclusion

The STB has been researching and developing reengineering of legacy software systems for many years, and it has pulled together some methods, training, and tool products that can greatly facilitate the tasks associated with reengineering legacy software. These products and services are proving useful for JSC software systems, and can be useful for reengineering software in other scientific and technical domains as well. The STB is committed to applying and transferring this reengineering technology to other projects, including those in industry.

Virtual Reality in Medical Education and Assessment

Stewart Michael Goza, Laurie A. Sprague*, Brad Bell*, Tim Sullivan*, Mark Voss*, and
Dr. Andrew F. Payer, Ph. D.**

Johnson Space Center/ER

*LinCom Corporation

**University of Texas Medical Branch

Abstract

JSC, LinCom Corporation, the University of Texas Medical Branch at Galveston (UTMB), and the Galveston Independent School District (GISD) have teamed up to develop a virtual visual environment display (VIVED) that provides a unique educational experience using virtual reality (VR) technologies. The VIVED end product will be a self-contained educational experience allowing students a new method of learning as they interact with the subject matter through VR. This type of interface is intuitive and utilizes spatial and psychomotor abilities which are now constrained or reduced by the current twodimensional (2D) terminals and keyboards². The perpetual challenge to educators remains the identification and development of methodologies which conform the learners' abilities and preferences. The unique aspects of VR provide us with an opportunity to explore a new educational experience.

Endowing medical students with an understanding of the human body poses some difficult challenges. One of the most difficult is to convey the three-dimensional (3D) nature of anatomical structures. The ideal environment for addressing this problem would be one that allows students to become small enough to enter the body and travel through it—much like a person walks through a building. By using VR technology, this effect can be achieved; when VR is combined with multimedia technologies, the effect can be spectacular.

Introduction

Medical students, interns, residents and physicians spend a significant amount of their time identifying and organizing data and information based on their educational programs or interactions with patients. It is important that they effectively organize this data and identify any issues that they need to learn about. Many of these "learning issues" can be accessed through the computer. The use of computers to process medical information, known as "Medical Informatics," is becoming more frequently used. This technology has advanced to 3D renderings of human anatomy on a 2D computer screen. Even with this technology and other classic methods, such as dissection of cadavers, there are times when it would be helpful for the user to be able to be placed into the anatomical environment to better understand the true 3D relationships that exist in that particular region of the

body. This leads to the need for VR experiences in anatomical imaging. Studying images on a 2D computer screen can be compared to looking at fish through a glass-bottom boat^{1,3}, whereas VR allows one to put on the scuba equipment and enter the water, interacting with the surroundings without getting wet. This type of learning experience would be an excellent addition to the currently available methods.

With inevitable improvements in imaging for VR and in digital gloves, it is not difficult to visualize future applications for this technology. The practice of general medicine can be compared to activities of an airline pilot. whereby while each deals with many routine landings and takeoffs, both also have to be prepared for emergency situations. We have the means to simulate the environment for the pilot allowing him to develop specific skills in routine and emergency situations. Imagine a physician putting on a VR helmet and digital gloves for a clinical simulation. When the computer is activated, the physician sees the operating room, equipment, staff and patient. The physician holds out a hand, feels a scalpel being placed in it and begins a surgical procedure allowing him to practice the procedure and evaluate any possible problems before opening up the patient.

Fidelity of the images produced is of utmost importance when applied to medical education. Magnetic resonance imaging (MRI), computerized axial tomography (CT) scans and <1 millimeter cadaver sections all provide acceptable levels of image quality. The National Library of Medicine is using these methods of data acquisition to build a nationally accessible database of information on human anatomy. This project, know as the Visible Human Project, will provide an invaluable source of data for VR work in medical education.

JSC has used VR to expand its training capabilities, specifically by providing a means to incorporate extravehicular activities (EVAs) with remote manipulator system (RMS) task training. This same VR technology is being transferred by way of the VIVED project for use in medical education. This is the subject of this paper.

Background

In 1990, Dr. Andrew F. Payer was invited to experience a VR prototype for astronaut training that used wire frame models of the Shuttle and Space Station. He was placed in the VR module and allowed to translate around objects under his own control. After the experience, he

was asked if he thought there were any possible applications to medical education. This was the beginning of an exciting project called the VIVED project.

Discussions with potential commercialization partners identified the need for the project to have applications broader than just the medical school environment (there are only 137 medical schools in the US). It was decided that a joint plan would be identified that would allow the VR prototypes to be tested for effectiveness in educational arenas including elementary schools, high schools, colleges, and professional schools. Thus a Memorandum of Understanding was developed between JSC, UTMB, and GISD so that prototypes could be tested in a variety of educational environments.

The human skull was chosen as an initial specimen due to readily available methodology, namely CT scans, of obtaining imaging data for bony structures. A second model of a heart specimen was created using MRI data.

Early models generated for VR did not meet the quality requirements of the project. After using newer CT scanners of higher resolution, and improvements in VR software, the skull image now nears the quality of an actual human skull. Because of the amount of image data, interactive fly-throughs into the skull are not currently possible. However, prescribed fly-throughs are being generated in digital and video formats to utilize multimedia technology.

The short-term goal of VIVED is to integrate prescribed fly-throughs of the skull with other interactive multimedia (audio, video, etc.) capabilities.

Methods: Creating Stereo Sequences Of the Human Skull

File Conversion and Data Preparation

Scans of a human skull were performed resulting in a data set consisting of over 120 slices through the skull and 60 slices through the mandible (jaw). The first attempts used 2.5-mm-slice thickness and a low resolution scanner resulting in poor image quality. The last scan used a newer high-resolution scanner and a slice thickness of 1.5 mm, improving the quality tremendously (figs. 1 and 2).

The data files obtained from the scan were transferred to JSC IGOAL (Integrated Graphics, Operations, and Analysis Laboratory) for further processing. The skull was held in place during the CT scan by a foam band, thus creating extraneous data. The scans were then cropped to eliminate as much extraneous data as possible without losing any critical information. The final stage of data file preparation required using a tool developed in the IGOAL called "ctimager" to remove unwanted noise and extraneous data from each slice.

An MRI scan of a human heart was performed resulting in a data set consisting of 200 slices. In order to use the image tools developed to process the skull data, the data for the heart was converted to the same format as the



Figure 1. First skull attempts using CT data.

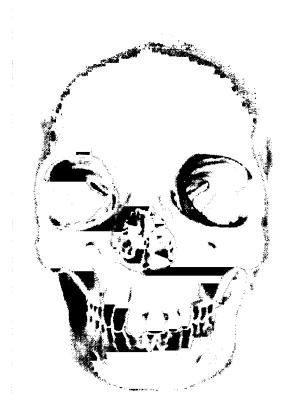


Figure 2. Current 3D Skull Model.

skull data. Ctimager was then modified to automatically remove the noise from each scan.

Data Filtering and Conversion of Volume Data to Polygonal Data

A tool called "dispfly" was developed in the IGOAL to convert volume data into a form that could be displayed directly by the computer. Dispfly used multiple filtering

algorithms to prepare the CT and MRI data for conversion to polygonal form. Anatomical models are generated based on the marching cubes algorithm developed by W. E. Lorensen and H. E. Cline. This technique generates surfaces based on the density of the imaging data. It generates a polygonal surface based on a "logical" cube cre-ated from eight data points on two adjacent slices of data. The algorithm determines how the surface of a selected density intersects this cube. A table lookup is performed to determine which triangles describe the surface. The normals are then determined using gradients computed directly from volume data.

The raw data set contains noise from the CT or MRI scanning process, so data is filtered before generating the polygonal model. The filtering process typically consists of thresholding the data to eliminate most of the noise. A low pass filter is used to minimize the high-frequency noise that would produce an irregular bumpy surface when input to the algorithm. This filtering process produces a relatively smooth surface that approximates the scanned specimen and reduces the number of polygons generated due to noise. A unique filter was created for the heart data which only smoothed the data between scans; no other filtering was needed (fig. 3). Due to the large number of slices in both heart and skull data sets, several models were made, each of which represented a small number of slices. To improve display performance a meshing algorithm was developed (meshit), that converted the raw collection of triangles into efficient strips. The triangle strips averaged over 100 triangles in size.

Generating Stereo Images

After the models were made, stereo sequences were rendered. To generate the sequences, a tool developed by IGOAL called OOM (object orientation manipulator) was used. OOM (available through COSMIC) rendered each frame to disk. The images used red and blue color separation for representing stereo images. Once the sequence was recorded to disk it was converted frame by frame to Macintosh ".pict" format and transferred to a Macintosh (full color image sequences were also transferred to the Macintosh for non-stereo viewing).

Macintosh - Stereo Images and Multimedia

The Macintosh was selected because it is a relatively affordable platform and has a wide base already installed in the school systems. It is a leading engine of desktop multimedia and has a wide array of software and hardware available for this task, though more is needed.

Once on the Macintosh, the images were edited to produce the desired effect, such as digitized cadaver overlays or text inserts describing what is being viewed. By using Apple's QuickTime extension, the images were then converted into QuickTime movies for animation on the Mac. The movies can also be edited on the Mac. To



Figure 3. 3D heart model from MRI data.

be able to view the stereo effects, the user must wear red/ blue 3D glasses.

A Hypercard interface (a simple tool for creating prototypes) is being created to house the Educational Experience on the Mac. Other hypertext programs have been investigated and will eventually replace the Hypercard interface. Many forms of multimedia will be considered and then incorporated into the finished product including, but not limited to, a VR head-mounted display (HMD) or boom system, CD ROM, laser disc, audio, video, digital imagery, and 3D.

The VIVED application will contain lectures, supplemental text, graphics, digital movies, notes, pop quizzes, references, exams, virtual reality experiences of anatomy, student comments, bookmarks, qualitative analysis of student performance, summations, and program evaluations.

Conclusions

The VIVED project is at a point where CT-scanned medical images of bone (e.g., the skull) can be generated into high-quality VR imaging for prescribed fly-throughs on the Macintosh computer using an HMD or boom system. The project team is in the process of working on a heart VR model that has been generated from MRI data. Preliminary results indicate that a high-resolution model can be developed using this type of imaging data. The project has been able to maintain its goal of high quality of VR imaging. This has led to some problems because

of the amount of data the computer needs to deal with even during frame-by-frame sequencing of the prescribed fly-throughs. Alternative hardware and software options are being explored to deal with this problem.

Another problem has been the current status of technology for the display systems for HMDs. The LCD displays do not have the resolution needed to maintain a high-quality VR experience. The CRT displays are reaching the resolution needed for the project, but the cost is prohibitive for multiple education platforms.

The next goal for the project include improving the software and hardware for generating VR images, developing prescribed fly-throughs and incorporating multimedia into the VR fly-throughs. Other anatomical imaging data will be obtained from CT scans, MRI, and cadavers to develop VR imaging of anatomical regions that contain different tissues with different data densities.

References

- ¹Brooks, F. P. "Grasping Reality Through Illusion— Interactive Graphics Serving Science." *Proceedings AMC SIGCHI.*, 1988.
- ²Fuchs, H., Levoy, M., and Pizer, S. M. "Interactive Visualization of 3D Medical Data." *IEEE Computer*, August, 1989.
- ³Furness, T. "Designing in Virtual Space." Chapter in W.B. Rouse and K.R. Boff, eds., *System Design: Behavioral Perspectives on Designers, Tools, and Organizations.* North Holland, 1987.

Virtual Reality Library (VRL)

Tim Sullivan,* Brad Bell,* and S. Michael Goza
*LinCom Corporation
Johnson Space Center/ER

Abstract

To further develop the specifics of virtual reality (VR) applications, a VR Library (VRL) was created by the IGOAL lab at NASA JSC to hide the details of the hardware and communication environment. The objective of the library is to provide a VR application framework for building multiprocess, multimachine VR applications which are easily modified.

Introduction

The VRL allows reconfiguration during runtime, easier porting of VR applications across platforms, and unlimited network connections and/or processes across machines, thereby allowing full utilization of resources available to the application. The VRL is based on methods used in the Model Support Library (MSL), which has produced such applications as Solid Surface Modeler (SSM), and Object Orientation Manipulator (OOM), currently available through COSMIC. The VRL library provides a high level interface to process control, communication (process and network), device drivers, and data filters and predictors which automatically configure the systems to the VR applications. The VRL is designed to be extendible, allowing the user to add more devices or filters to the library. Processes can run asynchronously and do not limit an application to wait for a response unless one is desired. The VRL does not have to be recompiled to enable additional processes to communicate with each other. One of the major strengths of the VRL is that it provides a few routines rather than hundreds to control complex interaction, thereby making it easy to learn and use.

Method

Process and Sensor Configuration

The VRL supports flexible configuration requirements through the use of a configuration file. The file specifies symbolic names for the different processes and the host names they will run on. It also specifies sensor mapping, displays which need updated graphics information, helmet list, and defaults for head-mounted displays and gloves. The following is an example configuration file.

```
PROCESS LIST
      VR PTT
                         sam
      VR CHAIR
                         cheers
      VR_VIEW
                         rebecca
      VR MAGIK
                         sam
      VR_MAGIK_UDF
                         sam
      VR_CONTROLLER
                         marian
      VR_LEFT_EYE
                         robinhood
      VR RIGHT EYE
                          marian
      VR_CONTROLLER2
                         rebecca
      VR_LEFT_EYE2
                         cliff
      VR TEST
                         erin
      VR FT
                         erin
      VR BIKE
                          rebecca
   }
   SENSOR_LIST
                   VR FT RIGHT_PALM
      VRD FT 1
      VRD FT 2
                   VR FT LEFT_PALM
      VRD_FT_3
                   VR_FT HEL
      VRD_FT_4
                   VR_FT CYB
   }
   HELMET_LIST
   VR_HELMET VR_LEFT_EYE
VR CONTROLLER VRH
   CYBER VR_LEFT_EYE VR_RIGHT_EYE
CYBERI
   }
   PERSON_LIST
   VRH LEFT_PALM RIGHT_PALM
"file location" TIM
   CYBERI LEFT_PALM RIGHT_PALM
      "file location" BRAD
   DISPLAY LIST
      VR LEFT EYE
      VR_RIGHT_EYE
      VR_VIEW
   }
```

The "PROCESS_LIST" section specifies all processes that may be executed during the simulation. In this section there are two columns: the first specifies a symbolic name representing a particular process, while the second specifies the host name of the machine the process is to run on. To facilitate process registration, each program initializes itself by calling the VRF_Init-("symbolic_name") library function. This function does several things. First it reads the configuration file to see if the process was executed on the intended machine; if not, it attempts to move the process to the proper machine. Next it sets up a shared memory block, if one is not already set up, to facilitate communication with other processes on the same machine; then it initializes sockets for communication to all other processes.

The "SENSOR LIST" section specifies all the sensors involved in the simulation. In this section there are three columns: the first specifies the type of sensor, the second specifies the symbolic name of the driver process, and the third specifies a symbolic name used internally by other processes as a method for mapping a specific sensor to something in the environment. Sensor data are automatically collected into an array indexed by an identification number based on the symbolic name in the third column. The function VRF_GetSensorID-("symbolic name") returns the index into the sensor array for that item. Initially all sensors are turned off. The library function VRF_ActivateSen-sor(sensor_id) activates the sensor. The VRF_Update-Sensors() function is used to update the sensor array. To facilitate a method for extending the library to support future sensors, the VRF_InstallSensor() function is provided. This function allows users of the library the ability to add support for new sensing devices without needing access to the library source.

The "DISPLAY_LIST" section specifies all of the processes which need to be notified when the graphics are updated. For instance, when an object is grabbed in the simulation, all processes in the display list would be notified. For simultaneous updates, a VRF_SendAllDisplays("INFO") function sends the information to the displays at the same time. Also, because all send notices are nonblocking, the information may be put into a queue so that it will not be lost.

The "HELMET_LIST" section specifies the helmets which are going to be used in the simulation, which processes are going to drive each helmet, and a symbolic name for the helmet.

The "PERSON_LIST" section specifies the users of the simulation, which helmet and other sensors they will be using, and the location of their default data for these sensors. These data include such things as eye separation and glove calibration.

Process Communication

The library functions VRF_Send(process to receive, data to send) and VRF_Recv(process to receive from,

data to receive) were created to minimize the time used for process communication and network programming. These functions hide the underlying protocol of the communication code, allowing the VR application code to remain machine independent. If a process sends data to or receives data from another process on the same machine, shared memory is used; otherwise, sockets are used for the communication. Since socket communication times are longer than shared memory communication times, it is preferable to use shared memory whenever possible. Overhead added by these high-level send and receive functions is minimal. VRF_Send and VRF_Recv do not block; therefore, the processes can continue to execute after requesting a send or a receive.

Filters and Predictors

A modifiable filter is included in the VRL to eliminate spikes and to smooth sensor data. Values which can be modified are the maximum value change before ramping, the number of values to include in the filtering, and the maximum percentage of change from one value to the next, until a preset number of values above some threshold has been reached. This filter gives the user the flexibility to smooth noisy sensor data.

Since computer processing delays are inevitable, a predictive filter has also been added which uses the velocity and acceleration of a sensor to predict the position of that sensor at a determined time. The predictive filter allows the VR application to better synchronize hand or head movement with the rendering of the scene. This allows the user in the VR application to move more naturally, instead of using slow or predicted motions. This becomes increasingly important in complex graphical applications where the update rate drops.

Current Limitations and Future Work

Currently the VRL includes drivers for the Polhemus Fastrack, the Polhemus 3SpaceTracker, VPL datagloves, Virtual Research Flight helmet, and the Leep Cyberface 2 helmet. A driver for the EXOS exeskeloton is being developed currently. The VRL is still in the early stages of development, but has been integrated into the VR applications currently used in the lab. The ease of adding new processes and sensors has made developing new VR applications or modifying current applications easier and faster. The use of shared memory on the machines with multiple processes has allowed those machines to run at peak efficiency by keeping traffic off the ethernet. While the initial library has been designed to run on Silicon Graphics workstations, porting the library to run on other UNIX Systems should not be difficult.

The next feature to be added to the library is generic rule-based constraint support through a rule-based constraint language that the library could parse and use to determine behavior of a particular system. The capability

would allow for automatic handling of simple gesturebased operations like opening a door. Other possibilities include the modeling of more complex systems in which the constraints change over time. An example of such change would be the removal of a cable whose motion is completely constrained until the connector holding it is turned to some specified angle, at which time the cable takes on certain degrees of freedom and behaves as though it had been disconnected. It is our belief that this library will make the development process easier by eliminating some details common to all VR applications.

Medical, Life, and Space Sciences

The Effect of Gravitational Acceleration on Ventricular Filling: Diastolic Ventricular Function in Weightlessness and One-g—Preliminary Results

John B. Charles, George M. Pantalos,* Barbara S. Bennett†, Scott D. Everett,

* M. Keith Sharp,* Thomas E. Bennett,** Thomas Schurfranz,**

Johnson Space Center/SD

*The University of Utah

**Bellarmine College

†KRUG Life Sciences

Introduction

The recognition and understanding of cardiovascular adaptation to spaceflight has advanced substantially in the last several years.^{1,2} In-flight echocardiographic measurements of astronaut cardiac function on the Space Shuttle have documented a 15% reduction in both left ventricular volume index and stroke volume when compared to preflight values with a compensatory increase in heart rate to maintain cardiac output.3 To date, the reduced cardiac size and stroke volume have been presumed to be the consequence of the reduction in circulating fluid volume following diuresis and other physiological processes that act to counter a perceived condition of hypervolemia (i.e., expanded central volume) within a few days after orbital insertion. However, no specific mechanism for the reduced stroke volume has been elucidated. The following investigation utilizes a physical modelling of the cardiovascular system to examine the possibility that the observed reduction in stroke volume may, in part, be biophysical in origin.

Many biophysical factors influence the filling of the heart during diastole (Fig. 1). These factors include (1) the atrial pressure, (2) the inertia energy of the blood as it enters the ventricle, (3) the transmural pressure gradient, (4) the diastolic compliance of the myocardium and the passive, elastic recoil attributed to the "parallel elastic element" connective tissue mesh around the myofibrils, 4.5 and (5) the gravitational accelerationdependent hydrostatic pressure difference, DP, that exists in the ventricles due to their size and anatomic orientation. This investigation is limited to an examination of left ventricular function although the same concepts apply to right ventricular function. Hence, only the hydrostatic pressure difference in the left ventricle, DP_{1,v}, will be considered in this report (Fig. 2). This hydrostatic DP_{1 v} linearly increases the intraventricular pressure when progressing from the ventricular base to apex. Consequently, the linearly increasing DP_{1,v} acts to augment the diastolic filling of the heart by increasing the elongation of the elastic, contractile, and viscous elements of the ventricular wall. The hydrostatic $DP_{i,v}$ is the product of the blood density ($r_{blood} = 1.06 \text{ gm/cm}^3$), gravitational acceleration constant ($g = 980 \text{ cm/sec}^2$), and the change in fluid column height from the reference point, Dh, cm, (Fig. 2). Magnetic resonance imaging

(MRI) scanning data have indicated that a typical Dh_{LV} for an average adult male left ventricle is approximately 7 cm. This Dh_{LV} results in a ventricular base-to-apex DP_{LV} of ≈ 7300 dynes/cm² (≈ 5.5 mm Hg) for an average effect of between 2 to 3 mm Hg. Consequently, based purely on fluid mechanical considerations, in the absence of gravity where DP_{LV} becomes zero, one would predict a rightward shift of the ventricular function curve of approximately 2 to 3 mm Hg. The investigators have hypothesized that the absence of this gravitation-dependent contribution to the ventricular filling process in the weightless

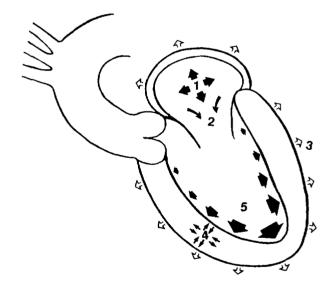


Figure 1. Biophysical factors that contribute to the filling process of the natural left ventricle are schematically depicted. These factors include (1) the atrial filling pressure, (2) the inertia of the blood as it flows into the ventricle, (3) the transmural pressure gradient, (4) the diastolic compliance of the myocardium and the passive elastic recoil of the connective tissue mesh surrounding the cardiac myocytes (modeled as the parallel elastic element), and (5) the gravity-dependent, intraventricular pressure difference.

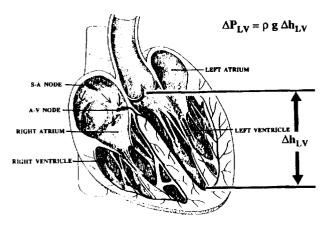


Figure 2. The intraventricular hydrostatic pressure difference, DP_{Lv} , arises from the difference in height between the left ventricular base and apex as indicated by Dh_{Lv} . This pressure difference is calculated using the equation: $DP_{Lv} = rgDh_{Lv}$, where r is the blood density $(r_{blood} = 1.06 \text{ gm/cm}^3)$, g is the gravitational acceleration constant $(g = 980 \text{ cm/sec}^2)$, and Dh_{Lv} is the change in fluid column height from the reference point in cm.

environment of spaceflight may account, in part, for the 15% reduction in stroke volume reported for astronauts while in orbit.

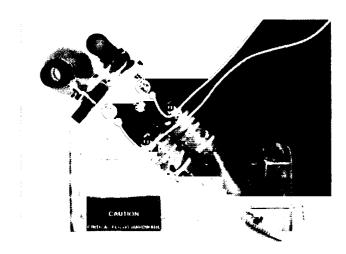
Access to the weightless environment to test this hypothesis was obtained on board the NASA KC-135 aircraft. This aircraft, which is based at Ellington Field near the NASA Johnson Space Center, makes experimental flights using parabolic flight profiles to create approximately 20 seconds of weightlessness while coasting over the top of each parabola. The opportunity to fly a hydraulic model of the left ventricle and systemic circulation (devoid of reflex and neurohumoral responses) on board the NASA KC-135 aircraft provided the environment in which the investigators could test the hypothesis stated above by determining the effect of the presence and absence of the gravitational accelerationdependent hydrostatic DP, v on ventricular function. Since the ventricular model used in the experiments is a preload-sensitive device and is controlled to reach the same end-systolic volume while operating at a fixed heart rate, any changes observed in the cardiac output would indicate a change in the stroke volume via an effect on diastolic function.

Methods

The experimental apparatus consisted of a pneumatically actuated, elliptical artificial ventricle (UTAH-100 human version left ventricle, 6.7 5cm x 6cm x 10cm) with prosthetic mitral and aortic valves (Medtronic HallTM, Medtronic, Inc.) and a highly compliant, pumping diaphragm. The inflow and outflow ports were located at the superior end of the long-axis of the ventricle to approximate the anatomy of the natural left ventricle

(Fig. 3). A compliant artificial atrium (Penn State⁸) was attached upstream of the inflow port of the ventricle. The ventricle was connected to a closed-loop, hydraulic circulation simulator (an adapted version of the Penn State mock circulation⁸) with compliance and resistance elements to create physiologic pressure and flow conditions (Fig. 4). The mock circulation was filled with a blood-analog fluid of 40% glycerin in water to approximate the viscosity of whole blood (3.4 cP @ 115 sec⁻¹). This mock circulation was fixed to a stainless steel tray (1m x 1.5m x .1m) which was bolted to a floormounted support frame.

The ventricle was instrumented with high fidelity, acceleration-insensitive, catheter-tip pressure transducers (Millar Instruments) in the apex and base to determine the instantaneous ventricular pressures and DP_{1,y} across the



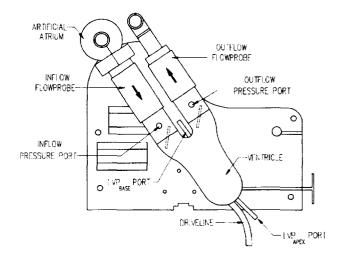


Figure 3. The artificial left ventricle used in these experiments is shown (above) positioned in the 45°, one-g anatomic orientation. The schematic (below) indicates the location of the flow probes and pressure catheter introducer ports and other details. The arrows indicate the direction of flow through the ventricle.



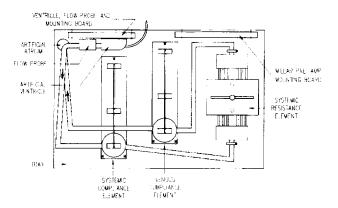


Figure 4. The hydraulic circulation simulator is shown mounted in the KC-135 aircraft (above). The schematic (below) indicates the location of the resistance and compliance elements as well as the artificial atrium and ventricle. The arrows indicate the direction of flow through the circulation simulator.

left ventricle (LVP_{apex} - LVP_{base}). When the ventricle was positioned at 45° to the horizon to mimic the anatomic orientation of the human left ventricle, the Dh_{LV} for the UTAH-100 left ventricle was 6.3 cm, resulting in a calculated base-to-apex DP_{LV} of 4.9 mm Hg. The ventricle was also instrumented with flow probes (Transonic Systems) and pressure transducers (Millar Instruments) immediately upstream of the mitral valve (inflow) and downstream of the aortic valve (outflow, see Fig. 3). Pressure transducers and flow probes and their calibration signals were calibrated against reference standards prior to shipment of the hardware to Ellington Field where the NASA KC-135 is based and upon return to Salt Lake City. The electrical calibration reference

signals were used for in-plane checks of probe calibration. The shearing rate profile of the glycerine/water blood-analog fluid was also verfied prior to departing Salt Lake City using a cone-and-plate viscometer (Brookfield Engineering, Model LVTDV-IICP).

The associated recording equipment and heart controller were rack-mounted in a chassis that was fixed to the aircraft floor. The equipment in the chassis included a sixteen-channel digital data tape recorder (TEAC, Model RD-200T), a two-channel flow meter (Transonic Systems), eight transducer pre-amplifiers (Gould), an eight-channel thermal pen recorder (Gould), and an artificial-heart controller (CardioWest Technologies) with a regulator and two tanks of compressed air. Accelerometers (PCB Piezotronics, Kistler) to measure the verticle axis (G_7) acceleration were mounted on the instrumentation chassis and the circulation simulator tray.

The in-flight test protocol specified the examination of ventricular function with the heart rate fixed at 90 beats per minute to correspond to the elevated heart rates reported for orbital flight. The percentage of the cardiac cycle spent in systole was 43 and the ventricular driveline pressure delivered to inflate the diaphragm was 190 mm Hg. This driveline pressure was sufficient to fully eject whatever stroke volume the preload conditions created while the ventricle pumped against a mean afterload pressure of 95 mm Hg during stable, one-g flight. Since this mode of artificial ventricular control (referred to as partial-fill, full eject) results in the same end-systolic volume at a fixed heart rate, any changes in the cardiac output are due to a change in stroke volume and, therefore, diastolic function. The circulating fluid volume of the mock circulation could be adjusted to create different preload conditions on the ventricular function curve. In flight, the initial circulating fluid volume was adjusted to establish a stable, one-g baseline near the peak of the ventricular function curve. After each set of 10 parabolas, 60 ml of the blood-analog fluid was withdrawn from the circulating fluid volume to establish a new, lower preload condition. The pressure, flow, and acceleration signals were continuously recorded to document the hemodynamic changes during the transition from one-g to weightlessness, during the period of weightlessness, and during the transition from weightlessness back to one-g (including the period of ≈ 1.8-g hypergravity). The mock circulation system stabilized at a new operating condition in approximately 5 seconds, so stable system function was achieved for the majority of the 20 second duration exposure to weightlessness. Postflight ground tests repeated the inflight test conditions in a stable, one-g environment with the ventricle positioned in the diagonal 45°, one-g anatomic orientation and in the horizontal 0°, nulled-g orientation which eliminates the ventricular base-to-apex Dh_{1 v} and, thus, DP_{1 v}. Data from 10 consecutive beats at stable test conditions were used to create ventricular function curves for all of the test conditions as well as to

examine the end-diastolic pressure difference between the left ventricular base and apex. A shift of the ventricular function curve to the right would substantiate the hypothesis of this experiment.

Preliminary Results and Discussion

Ventricular function data were gathered during two missions on the NASA KC-135 aircraft with four preload conditions being explored on each mission. Data were also collected postflight during ground-based experiments with the ventricle positioned in the 45° "one-g anatomic" orientation and in the 0° null-g orientation. The typical hemodynamic response in-flight to transitioning from the ≈ 1.8-g environment to the weightless environment was a reduction in cardiac output (outflow) and stroke volume concurrent with an increase in preload (inflow) pressure, as shown in Fig. 5. Consistent with the increased preload pressure, LVP_{hase} also increased while LVP_{anex} decreased as the two pressures equilibrated in the absence of an intraventricular hydrostatic DP_{1 v}. These hemodynamic changes were reversed in transition from the weightless environment back to the ≈ 1.8-g environment during aircraft pullout on the downslope of the parabola. Corresponding changes were seen in the ground-based measurements during transitioning from the 45° "one-g anatomic" ventricular orientation to the 0° null-g ventricular orientation and back, as shown in Fig. 6.

Elimination of the intraventricular hydrostatic DP_{1.V} between the ventricular base and apex by ventricular operation in the weightless environment or horizontally aligning the ventricle resulted in the predicted rightward shift of the ventricular function curve (Figs. 7 and 8). The measured intraventricular DP_{LV} was consistent (within preliminary evaluation measurement error) with the values predicted for the four acceleration environments (Fig. 9) investigated (weightless, "nulled-g," one-g, and ≈ 1.8-g. The rightward shift of the ventricular function curves from both in-flight and ground-based data provided initial evidence to support the hypothesis that the gravitational acceleration-dependent, intraventricular hydrostatic DP_{1 v} contributes to the ventricular filling process and its absence, therefore, results in reduced ventricular filling and stroke volume. Though not quantitatively identical, the rightward shift of the ventricular function curves from the in-flight and groundbased data is substantial (≈ 3 mm Hg) and results in stroke volume reductions of up to 50% in the physiologic range. This reduction in stroke volume is greater than the values reported from measurements in orbit. Since the hydraulic circulation simulator is devoid of reflex and neurohumoral responses, our initial interpretation of this result is that this change in stroke volume is the maximum change that could occur if only biofluid mechanical effects were influencing cardiac function. One can then speculate that the reflex and neurohumoral responses and the cardiac myocyte biomechanics limit the extent of the actual stroke volume reduction. It is important to

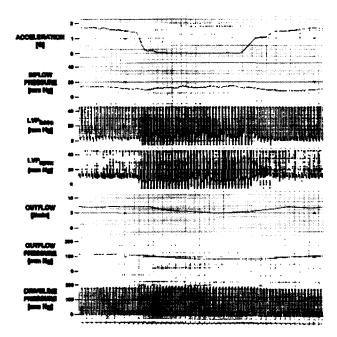


Figure 5. An example of the in-flight pressure and flow tracings for one parabola sequence is presented going from the \approx 1.8-g pull-up, through the period of weightlessness (m-g) and finishing with the \approx 1.8-g pull-out.

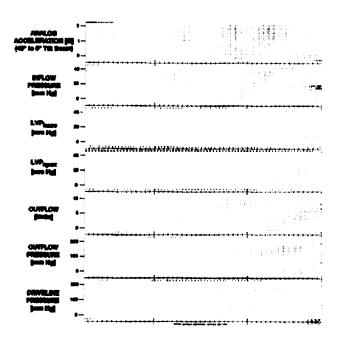


Figure 6. An example of the ground-based pressure and flow tracings for one sequence going from the 45° one-g anatomic orientation to the 0° null-g orientation and back is presented.

recognize that the filling rate for the artificial ventricle is limited, for a given transmural pressure, by the viscous resistance experienced by the air exhausting from under the diaphragm and flowing out the pneumatic driveline. The filling rate of the natural heart is similarly limited by tissue viscous resistance to elongation of the ventricular

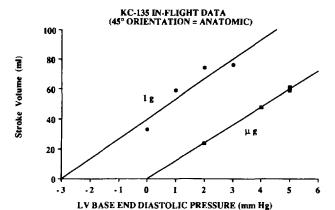


Figure 7. In-flight ventricular function graphs from the second day of in-flight experiments are presented for the one-g and weightless (m-g) environments. The linear regressions for each graph are based on steady-state measurements at four different preload conditions. [For one-g: $SV = 13.3 \times LVEDP_{base} + 39.6$, $R^2 = 0.88$; For weightlessness (m-G): $SV = 12.0 \times LVEDP_{base}$, $R^2 = 0.99$]

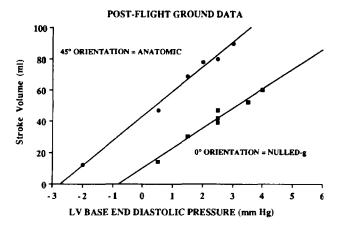


Figure 8. Ground-based ventricular function graphs are presented for the 45° one-g anatomic ventricular orientation and the 0° null-g ventricular orientation. The linear regressions for each graph are based on steady-state measurements at seven different preload conditions. [For 45° one-g anatomic orientation: SV = $15.8 \times \text{LVEDP}_{\text{hase}} + 42.9, \, \text{R}^2 = 0.99$; For null-g orientation: SV = $12.7 \times \text{LVEDP}_{\text{hase}} + 9.7, \, \text{R}^2 = 0.97$]

wall, but also by elastic elements that constrain the ventricular end diastolic volume and reduce the rate of ventricular filling near the end of the diastolic period. These elastic elements, which have no analog in the artificial heart operated in the partial-fill mode (since its diaphragm is of extremely high compliance), would tend to reduce the augmentation effect of the DP_{LV} on ventricular filling.

KC-135 IN-FLIGHT AND GROUND DATA

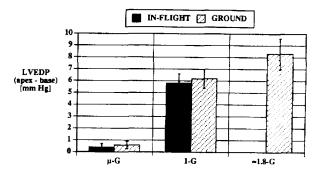


Figure 9. The in-flight determination of the intraventricular pressure difference [LVEDP $_{\rm apex}$ -LVEDP $_{\rm base}$] from the second day of in-flight experiments for the weightless (m-g), one-g and \approx 1.8-g environments are presented in the stippled bars. The ground-based determination of the intraventricular pressure difference for the 45° one-g anatomic orientation and 0° null-g orientation are presented in the solid bars. All values for [LVEDP $_{\rm apex}$ -LVEDP $_{\rm base}$ -l were at the levels predicted within measurement error.

These findings may provide a biofluid mechanical explanation for changes in stroke volume with changes in subject posture and for the reduced stroke volumes in Space Shuttle astronauts while in orbit, as documented by echocardiography. Although the existence of the intraventricular hydrostatic DP has been documented to clarify the interpretation of cardiac catheterization data,9 we are not aware that the potential contribution to cardiac diastolic function of the intraventricular hydrostatic DP has been previously recognized. Therefore, it warrants further consideration and investigation. Additional KC-135 in-flight investigations with expanded protocols and a refined circulation simulator are being pursued in preparation for in-orbit measurements in the extended duration, higher quality microgravity environment of the Space Shuttle as a Get Away Special experiment package. Further correspondence to echocardiographic and hemodynamic data from human cardiac catheterization subjects in the supine and upright postures will also be explored. Based on these preliminary findings, the investigators conclude that this experiment has demonstrated that the absence of small hydrostatic pressure differences may influence physiologic adaption to spaceflight and that physical modelling of the cardiovascular system can be a useful adjunct for the examination and understanding of in vivo data obtained during manned spaceflight.

Acknowledgments

The investigators would like to gratefully acknowledge the generous contributions by the many people and organizations that made this project possible. Since the inception of this project, students at Bellarmine College and the University of Utah have played a major role in the development of the experiment. These students include Max Barton, Tom Schurfranz, Scott Everett, Bill Shaw, David Johnson, Jason Lyddane, Mike Brown, Scott Tucker, and Robert Wessel. Dr. Frederick T. LaRochelle of the Space Biomedical Research Institute at NASA JSC was instrumental in obtaining approval and sponsorship for this experiment. Preflight and in-flight assistance was received from Linda Billica and Bob Williams of the Reduced Gravity Office at NASA JSC and Lynette Bryan of KRUG Life Sciences, each of whom patiently guided us through all of the preflight manifest requirements. Additional assistance was received from the staffs of the University of Utah Artificial Heart Research Laboratory and the Rocky Mountain NASA Space Grant Consortium. We also thank the following individuals and their organizations for support given to this project: Pat Patterson (Space Dynamics Laboratory, Utah State University), Sandy Vanderploeg (Universities Space Research Association), Jay Giles (TEAC America, Inc.), Lenny Leuer and Dave Scott (Medtronic, Inc.), Lauren Ostergren and Margo Sosa (Transonic Systems, Inc.), Jim Lally (PCB Piezotronics, Inc.), Jim Donachy (Division of Artificial Organs, Pennsylvania State University), Michelle White (Millar Instruments, Inc.), Steve Parnis (Texas Heart Institute), Steve Langford (CardioWest Technologies, Inc.), Jim Peck (Astro-Med, Inc.), Boris Osojnak (Aero Tech Manufacturing, Inc.), Rick Burr and Bob Bohle (Kistler Instrument Corporation), and Norm Nowalk.

Bibliography

¹ Charles, J.B, Lathers, C.M., "Cardiovascular Adaptation to Spaceflight," *J Clin Pharmacol*, Vol. 31, 1991, pp. 1010-1023.

- Bungo, M.W., "The Cardiopulmonary System, Space Physiology and Medicine, edited by A.E. Nicogossian, C.L. Huntoon, and S.L. Pool. 2nd ed., Lea & Febiger, 1989, pp. 179-201.
- ³ Bungo, M.W., Charles, J.B., Riddle, J., Roesch, J., Wolf, D.A., Seddon, R., "Echocardiographic Investigation of the Hemodynamics of Weightless," *J Am Col Cardiol*, Vol. 7, No. 2, 1986, p. 192A.
- Yellin, E.L., Sonnenblick, E.H., Frater, R.W.M., "Dynamic Determinants of Left Ventricular Filling: An Overview." *Cardiac Dynamics*, edited by J. Baan, A.C. Arntaenius and E.L. Yellin, Martinus Nijhoff Publishers, 1980.
- Sonnenblick, E.H., "The Structural Basis and Importance of Restoring Forces and Elastic Recoil for the Filling of the Heart," *Euro Heart J*, Vol. 1(A Supplement), 1980, pp. 107-110.
- Robison, P., Pantalos, G., Olsen, D., "Pneumatically Powered Blood Pumps Used as a Bridge to Cardiac Transplantation," *Critical Care Nursing Clinics of North America*, Vol. 1, No. 3, 1989, pp. 485-494.
- White, R.K., Pantalos, G.M., Olsen, D.B., "Total Artificial Heart Development at the University of Utah: The Utah-100 and Electrohydraulic Cardiac Replacement Devices," *Cardiac Mechanical Assistance Beyond Balloon Pumping*, edited by S. Quad, Mosby-Year Book, 1992, pp. 181-193.
- Rosenberg, G., Phillips, W.M., Landis, D.L., Pierce, W.S., "Design and Evaluation of the Pennsylvania State University Mock Circulatory System," *ASAIO J*, Vol. 4, No. 2, 1981, pp. 41-49.
- ⁹ Rubal, B.J., Gantt, D.S., Bird, J.J., Wilkens, T.A., "Effects of Transition from Supine to Upright Position on Central Hemodynamics in Patients with Chest Pain Syndrome," *Physiologist*, Vol. 32(1 Suppl), 1989, pp. 533-534.

Alternative Methods for Measuring Calcium Absorption and Kinetics in Humans Exposed to Microgravity

H.W. Lane, L.E. Nyquist, S.M. Smith,* C.-Y. Shih,** J.L. Nillen,* H. Wiesmann**

Johnson Space Center/SD and SN

*KRUG Life Sciences

**Lockheed Engineering and Sciences Company

Abstract

Calcium and bone homeostasis are significantly affected by exposure to microgravity. Studies of calcium absorption and kinetics are needed to characterize this process. Calcium absorption typically is estimated using two isotopes, one administered orally and one intravenously. Stable (nonradioactive) isotopes are ideal for such studies; however, isotope costs are often prohibitive. We sought to develop techniques that would allow calcium absorption and kinetics to be estimated from µg doses of isotopes instead of the more common mg doses. 43Ca and 46Ca were selected because very small amounts of these isotopes can be measured precisely and accurately by the thermal ionization mass spectrometer (TIMS) at this facility. After sample preparation procedures were developed for serum, urine, saliva, and feces samples, subjects received 80 (subject 1) or 160 µg (subject 2) of ⁴³Ca orally in water with a capsule of 250 mg unlabeled calcium (i.e., natural abundance) as CaCO,. Samples were collected over 96 hrs and analyzed for Ca isotopes by TIMS. The enrichments found in the 96-hr samples (18.4 E for subject 1, 41.1 E for subject 2) were well above the precision of the TIMS (≈ 1 E for ⁴³Ca analyses). Enrichment data are expressed as epsilon where $E = [(^{43}Ca;^{44}Ca]_{\text{sample}}/[^{43}Ca;^{44}Ca]_{\text{natural abundance}})-1]x$ 10,000. Other studies of absorption and kinetics are under way using oral ⁴³Ca and intravenous ⁴⁶Ca doses. We believe that the reduction in tracer costs permitted by this method will allow calcium absorption and kinetics to be studied in more subjects at lower cost.

Introduction

Spaceflight results in negative calcium balance and loss of bone calcium.^{3,4} Space crew members need calcium in their diets to maintain health during long missions.^{1,2} Ideally, studies of calcium and bone homeostasis should not require the use of radioisotopes.

Previous studies of calcium absorption in humans have used either radioisotopes of calcium or high doses (i.e., 2500 μ g) of stable isotopes of calcium. The cost of stable isotopes in general, and calcium isotopes in particular, is often prohibitive. Here we describe efforts to develop methods for estimating calcium absorption using much smaller doses (e.g., < 200 μ g) of stable isotopes of calcium, specifically ⁴⁶Ca and ⁴³Ca. These isotopes were selected because they can be analyzed precisely and accurately with the TIMS at this facility.

Calcium homeostasis requires a balance between absorption and excretion. Calcium is absorbed from foods consumed (i.e., from the gastrointestinal (GI) tract to the bloodstream); however, calcium is also secreted from the bloodstream into the GI tract and is excreted in both urine and feces. To account for endogenous secretion of calcium, two isotopes are needed to estimate calcium absorption and homeostasis in humans. One isotope is administered orally and the other intravenously. The ratio of the two stable isotopes in a biological sample (e.g., blood, serum, urine) is calculated after a suitable equilibration period, thus allowing the calculation of fractional absorption (percent of dietary calcium absorbed). Thus, if the blood pool of calcium is spiked with a known amount of calcium, any loss of absorbed calcium (e.g., to the GI tract, urine, bone, or other tissues) will be reflected by the injected tracer (which will also be lost to the GI tract, urine, etc.). The key assumptions in this technique are that both isotopes enter the exchangeable calcium pool at the same time, and that both are subject to the same physiological processes (i.e., the two tracers act the same as each other as well as the calcium present in the body). Fractional absorption is calculated as follows:

Calcium kinetics and whole body turnover are calculated using nonlinear regression to determine the nature of the decay curve after the labeled calcium is administered.

Statement of Problem/Task

Measuring calcium absorption requires radioisotopes or expensive stable isotopes. We sought to determine whether microgram doses of ⁴³Ca (administered orally) could be detected in biological samples of blood, urine, saliva, and feces.

Methods

One man (subject 1) and one woman (subject 2) received oral doses of 80 (subject 1) or 160 µg (subject 2) of ⁴³Ca in dilute HCl with a carrier dose of 250 mg of natural abundance calcium as CaCO₃ (i.e., not isotopically enriched) and polyethylene glycol (a fecal marker). Blood samples were collected before dosing; 1, 2, 4, 8, and 24

hours after dosing; and twice a day on the following 4 days. All urine was collected for the first 24 hours, and then at the same time as the blood samples. Saliva samples were collected at the same time as blood samples; one additional saliva sample was collected 12 hours after dosing. Fecal samples were collected for 4 days after dosing.

After the samples were digested in nitric acid, calcium isotope ratios were determined using TIMS techniques. The ratio of ⁴³Ca:⁴⁴Ca was determined. The natural abundance ratio of ⁴³Ca:⁴⁴Ca was determined through multiple analyses of National Bureau Standards. Enrichment data are expressed as epsilon (E), where:

$$E = [({}^{43}Ca: {}^{44}Ca]_{sample} / [{}^{43}Ca: {}^{44}Ca]_{natural abundance}) - 1]x 10,000$$

In addition, total and ionized calcium were measured in serum, as were endocrine indices of bone/calcium homeostasis. Endocrine indices included osteocalcin, calcitonin, and parathyroid hormone (measured with both mid-molecule and intact assays).

Data/Results

The body pool of calcium was enriched quickly in both subjects (Fig. 1). Peak enrichment of serum and urine was approximately 150 E for subject 1 and 75 E for subject 2. The enrichment in the 96-hr serum sample (18.4 E for subject 1, 41.1 E for subject 2) was well above the precision of the TIMS (\approx 1 E for ⁴³Ca analyses).

Serum and Urine 43Ca Enrichment

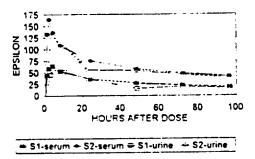


Figure 1. Enrichment of serum and urine samples after an oral dose of ⁴³Ca in two subjects.

Endocrine markers in serum are shown in Fig. 2. All results fell within normal limits, including the expected diurnal variation. Serum total and ionized calcium (Fig. 3) also were unremarkable.

Conclusions

The stable isotope doses in this study seem to be adequate for studying calcium absorption and kinetics in humans and represent a significant cost savings. Further studies with both ⁴⁶Ca and ⁴³Ca are required to determine nominal dosing and sample collection protocols for absorption and kinetic studies. These studies are currently under way.

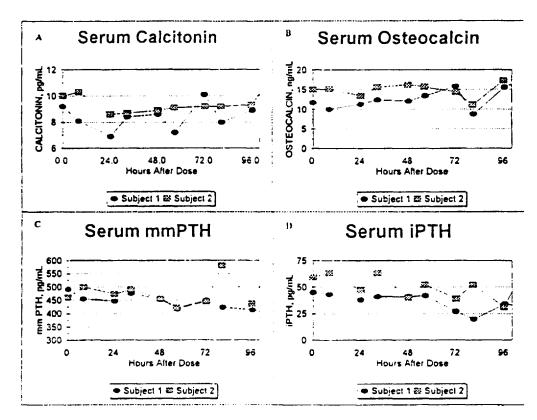


Figure 2. Serum endocrine profiles in subjects receiving an oral dose of ⁴³Ca. mmPTH = assay of mid-molecule parathyroid hormone; iPTH = assay of intact parathyroid hormone.

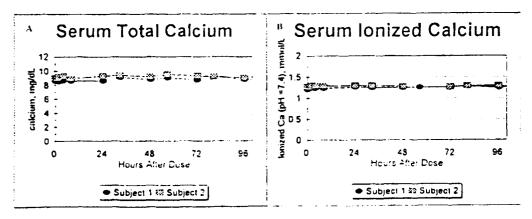


Figure 3. Serum total (A) and ionized (B) calcium profiles in subjects receiving an oral dose of 43Ca.

This technique, involving small doses of nonradioactive isotopes, expands NASA's in-flight research capability. This technique can also be used on Earth for research studies involving infants, children, pregnant women, and the elderly.

References

¹Lane, H.W., Rice, B.L., and Wogan, C.F., "Nutritional Requirements for Space Station Freedom Crews," Report of a panel discussion sponsored by the Biomedical Operations and Research Branch, Medical Sciences Division, Johnson Space Center, Houston, TX, February 1991, Washington, DC: NASA Conference Publication 3146, 1992.

Lane, H.W., LeBlanc, A.D., Putcha, L., and Whitson, P.A., "Nutrition and Human Physiological Adaptations to Space Flight," Am J Clin Nutr, 58:583-588, 1993.
Smith, M.C., Rambaut, P.C., Vogel, J.M., and Whittle, M.W., "Bone Mineral Measurement (Experiment M078)." In: Biomedical Results of Skylab, NASA-SP-377, R. S. Johnston and L. F. Dietlein, Eds., Washington, DC: NASA, pp. 183-190, 1977.
Whedon, G.D., Lutwak, L., Rambaut, P.C., Whittle, M.W., Smith, M.C., Reid, J., Leach, C., Stadler, C.R., and Sanford, D.D., "Mineral and Nitrogen Metabolic Studies, Experiment M071." In: Biomedical Results from Skylab, NASA SP-377, R.S. Johnston and L.F. Dietlein, Eds., Washington, DC: NASA, pp. 164-174, 1977.

Characterization of Spacecraft Humidity Condensate

R. L. Sauer, S. M. Johnson,* J. R. Schultz*
Johnson Space Center/SD
*KRUG Life Sciences

Abstract

When Space Station construction reaches the permanent human presence stage, plans call for recycling distilled urine, spent hygiene water, and humidity condensate to reclaim potable water. To help identify inorganic and organic compounds that could present health risks to the crew and also to help direct the proper design and operation of the potable water processor, we collected samples of humidity condensate on two Shuttle missions: STS-45 and STS-47. A variety of analyses were conducted to identify and quantify inorganic and organic components of these samples. Comparison of Shuttle cabin condensate with condensate from various Spacelabs and ground-based experiments demonstrates the importance of testing condensate collected from an environment close to that of the proposed Space Station.

Introduction

Proper design and operation of the potable water processor aboard Space Station at permanent human presence will depend on the identification and quantification of the organic and inorganic components of the raw wastewaters. Incomplete or inaccurate identification of these components may allow trace contaminants to pass through the potable water processor and into the water distribution system.

Problem Statement

Characterizing wastewaters generated in space requires representative samples. The lack of availability of such samples has deterred characterization in the past. Earlier attempts to characterize such samples have included condensate generated during ground-based tests and several Spacelab missions. Detailed Supplemental Objective (DSO) 317 was performed on Space Shuttle missions STS-45 and STS-47 to gather additional information on contaminants in wastewaters representative of those to be encountered on Space Station. This DSO resulted in the first in-flight collection of Shuttle cabin condensate for ground-based analysis.

Methods

Sample Collection Procedure

The DSO 317 flight hardware was designed to collect samples of cabin humidity immediately after condensation but before storage in the Shuttle's wastewater tank. Figure 1 shows the location of the

sampling port on the Shuttle water system. Because refrigerated storage was not available, all condensate samples were stored under ambient temperatures until return to Earth.

Analytical Procedures and Methods

The DSO Shuttle cabin condensate and the four Spacelab condensate samples (SLS-1, IML-1, USML-1 and SL-J) were analyzed for chemical composition by the Water and Food Analytical Laboratory at JSC. Figure 2 graphically depicts the scheme and various methods that were used to analyze the organic compounds in the condensate samples.

Results and Discussion

The data sets collected from analysis of the Shuttle and Spacelab samples were compared with each other. When possible, the data from condensate collected in space were then compared with other data collected by Marshall Space Flight Center using its ground-based enduse-facility (EUF) to collect the samples.³

Total organic carbon (TOC) in the cabin condensate samples was measured at 82 to 230 mg/L and 169 to 239 mg/L in the Spacelab samples. The TOC from the DSO sample was significantly greater than that from the EUF sample which had a reported maximum TOC of 16.3 mg/L.

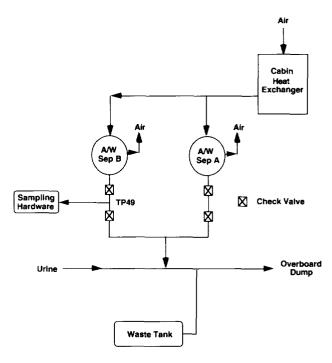


Figure 1. Condensate sample-port location.

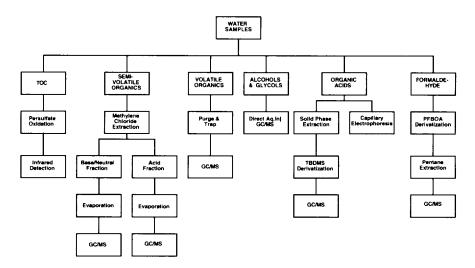


Figure 2. TOC accountability.

When individual compound concentrations were used, the measured TOC in the STS-47 condensate was 75% accounted for and in the STS-45 condensate was 50 to 59% accounted for. Figure 3 shows a graphical presentation of the TOC contribution from various classes of compounds. The Spacelab condensate samples had TOC accountabilities in the 50 to 80% range. In the space-collected condensate samples, the compounds contributing most significantly to the TOC were alcohols and propylene glycol; in the ground-based samples, 3 organic acids made the largest contribution. The high alcohol content in the Shuttle and Spacelab condensates probably resulted from the routine use of disinfectant alcohol wipes inside the Shuttle and Spacelab.

Zinc was the predominant metallic compound in condensate collected in space. Generally, the zinc concentration of the cabin humidity condensate was greater than that of the Spacelab samples (10 to 20 mg/L vs 3-14 mg/L). USML-1 was the notable exception (40.5 mg/L). Zinc was found in the EUF condensate samples but at a considerably lower concentration (0.003 mg/L). The source of the zinc in the Shuttle and Spacelab condensate samples was attributed to the heat exchangers.

Ammonium was the predominant nonmetallic cation in both the Shuttle and Spacelab condensate samples; concentrations ranged from 7.6 to 18.4 mg/L.

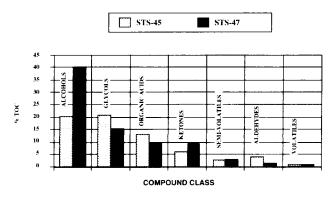


Figure 3. Analytical scheme for organic components.

GC/MS analysis of semivolatile compounds in the Shuttle and Spacelab condensate samples revealed the presence of phenol (10 to 146 mg/L). Phenol is of concern because of its reactivity toward iodine. The GC/MS data did not indicate the presence of any iodinated phenols.

Conclusions

Analysis of the humidity-condensate samples collected from the Shuttle cabin and the various Spacelabs shows that significant differences exist between component concentrations and condensate collected from ground-based experiments. This finding supports the view that humidity-condensate samples need to be taken under conditions that resemble as closely as possible those expected aboard Space Station. Further work is needed to refine the methods used to analyze the organic portion of the condensate samples so that for future water samples, the accountability of component compounds in the measured TOC regularly reaches or exceeds 80%.

References

Carter, D.L., Cole, H., Habercom, M., Griffith, G., and Slivon, L., "Determination of Organic Carbon and Ionic Accountability of Various Waste and Product Waters Derived from ECLSS Water Recovery Tests and Spacelab Humidity Condensate," 22nd International Conference on Environmental Systems, SAE Technical Paper Series #921313, Seattle, WA, July 1992.

²Verostko, C.E., Recovered Waste Water Impurity Characterization, Johnson Space Center internal report, 1986.

³Holder, D.W. and Bagdigian, R.M., "Phase III Integrated Water Recovery Testing at MSFC: Closed Hygiene and Potable Loop Test Results and Lessons Learned," 22nd International Conference on Environmental Systems, SAE Technical Paper Series #921117, Seattle, WA, July 1992.

Decompression Gas Phase Formation In Simulated Physiological Null Gravity

Michael R. Powell, Ph.D., James Waligora, M.S., William Norfleet, M.D., and K. Vasantha Kumar, M.D.*

Johnson Space Center/SD

*KRUG Life Sciences

Abstract

There is a reduced reported incidence of joint pain decompression sickness (DCS) encountered in microgravity by both astronauts and cosmonauts, compared with an expected incidence with similar protocols of decompression performed on test subjects in Earth-based laboratories (unit gravity). One origin of this difference is postulated to be traceable to micronuclei formation processes or stress-assisted nucleation in microgravity. Doppler bubble detection, in a crossover experimental design, indicated a considerable reduction in the Spencer precordial grade in the lower extremities in subjects in simulated microgravity (bed rest) as compared to themselves when ambulatory in unit gravity (chi square test. precordial Grades III and IV differed in the two groups at the p = 0.05 level). The results are in accord with an explana-tion of a decompression gas phase which grows on micro-nuclei possessing short lifetimes, probably only hours.

Introduction

DCS can occur when individuals are subjected to a reduction in ambient pressure and the sum of the partial pressures of dissolved inert gases in certain tissues exceeds that of ambient pressure.¹⁻³ Both astronauts and cosmonauts have reported a lower incidence (0% reported) of DCS during extravehicular activity (EVA) than would be predicted (20 - 30% mild DCS expected) from decompression studies performed in ground-based laboratories.⁴

Joint pain DCS (the "bends") occurs in movable joints and, in the last several decades, kinetic activity has been implicated as playing a major role in the genesis of gas phase transitions.⁵⁻⁷ The conclusion is that musculoskeletal motion, in its ability to produce temporary reductions of pressure in localized microvolumes of tissue, assists statistical fluctuations in the creation of voids in a liquid (embryos) which can be stabilized by surfactants and the inward flux of dissolved gas from the surrounding fluid to form nuclei.⁸⁻¹⁰ There is a predilection for joint pain DCS to occur in the lower extremities, and a reduction in activity of the legs in microgravity, especially with respect to weight bearing, would lead to a lower incidence of joint pain DCS.¹¹⁻¹³

Description of the Problem

Ground-based laboratory studies⁴ conducted with human volunteers over a wide range of tissue pressure

ratios have delineated both the incidence of DCS to be expected and the degree of whole-body gas phase formation that occurs. From this work, the expected incidence of DCS can be calculated for any number of EVAs. The probability f(x) of completing x successful, i.e. "bends free," decompressions in n EVAs with a given failure rate, p, is given by the Bernoulli (binomial) distribution:

$$f(x) = {}^{n}C_{x} p^{x} (1-p)^{n-x} \text{ for } x = 1,2,...,n$$

From this, it can be calculated that there is currently an approximately 17% probability of *not* having encountered a severe joint pain DCS problem during 37 EVAs. If one examines the experience of Russian cosmonauts (no severe DCS/73 trials), then for no severe DCS, $P_{\text{success}} = 1.5\%$. The probability of successfully completing the entire series without severe joint pain DCS by both groups (N = 110) is even less ($P_{\text{success}} = 0.26\%$). Mild DCS statistically should have been encountered on the basis of Earth-based results ($P_{\text{success}} < 10^{-6}$).

Biophysical Mechanisms for the Reduction of DCS in Microgravity

The production of a gas bubble (a void or cavity) in the fluid is known as "cavitation." To fracture pure water, the theoretical limit requires that the gas supersaturation be on the order of 1300 atmospheres [atm]. 14-17 Phase transformations proceed more easily when assisted in real systems by the presence of either impurities or mechanical forces. 18-23

There currently exist three fundamentally different concepts involving gas phase formation in supersaturated in vivo systems. The first process termed the metastable limit, a time-invarient stability of supersaturation, was first used by J. S. Haldane in 1908² for the calculation of his decompression tables. For purposes of schedule calculation, Haldane proposed that a two-phase, gasliquid system would not form if:

$$P_{\text{dissolved inert}} < P_{\text{metastable limit}}$$

Thus, an inert gas partial pressure falling between the metastable limit (which was a fixed partial pressure) and the saturation pressure would not separate and produce DCS.

The second process, random nucleation on a hydrophobic surface, was advanced by B. A. Hills²³ in the thermodynamic model. He proposed that whenever

$$\mathbf{P}_{\text{ambient}} < \mathbf{P}_{\text{inert}} + \mathbf{P}_{\text{CO2}} + \mathbf{P}_{\text{O2}} + \mathbf{P}_{\text{H2O}}$$

gas phase separation would occur within a time frame applicable to the decompression time. The stable, time invariant levels of supersaturation of Haldane were not thought realistic; Hills proposed that the gas phase would separate from the dissolved state on aqueous-hydrophobic interfaces. These interfaces functioned to lower the energy needed and aid a reaction with an unfavorable entropy change. The effects of continued exercise under unit gravity stress on tissue gas phase formation would not appear in this type of analysis.

The third process, stress-assisted nucleation, allows for the qualitative understanding of decompression gas phase formation, and it helps explain the large difference between in vivo and in vitro gas bubble formation. Formation of a free gas phase in pure liquids (i.e., bubble free) requires supersaturations of 100 atmospheres (carbon dioxide in water) to 400 atmospheres (helium in water) before bubbles form. 24, 27,30 The stress-assisted model proposes that in vivo viscous adhesion^{29, 30} supplies the energy required to overcome the surface tension of the microbubble. The need for considerable reduced activity of the lower extremities in microgravity results in a greatly reduced production of micronuclei and therefore fewer tissue bubbles formed during decompression. The gas micronuclei so produced probably have a lifetime of several hours.

Once a spherical bubble has been formed, the conditions for stability are given by the Young-Laplace equation:

$$\Delta P = P_{gas} - P_{ambient} = 2 \gamma / R$$

where $P_{\rm gas}$ is the pressure of the gas within the bubble, γ is the surface tension of the fluid medium, and R is the radius of the bubble. Because of the effect of surface tension, the internal pressure of a gas bubble of R=0.01 micron at 25°C is 143 atmospheres; small, nascent bubbles (embryos) would have considerably higher internal pressures. Some mechanism must deposit sufficient energy into a microvolume to bring the bubble embryo through the formative process to a radius that can be stabilized by the inward diffusion of dissolved inert gas, water vapor, carbon dixoide, and oxygen. Work W must be done on the system before a gas bubble of critical radius R can be formed. The work to form a cavity (bubble) in a fluid medium is given by:

$$W = (16/3) \pi \gamma^3 / (P_{gas} - P_{ambient})^2$$

Using a kinetic approach, cavitation results from statistical fluctuations in molecular positions of water molecules. The rate of bubble production was Q and required a critical energy E_c described by a Boltzmann distribution^{32,33}

$$O = Z e^{(-Ec/kT)}$$

The energy of bubble formation E is given by

$$E_a = 4\gamma \pi r^2 + (4/3)\pi r^3 P_B (ln[P_B/P_a])$$

for a spherical bubble of radius $\, r \,$ in a medium whose surface tension is $\, c \,$ and with a gas pressure of $\, P_{B} \,$ within the bubble and one of $\, P \,$ in the fluid. For the de novo creation of vaporous cavities, recourse has been made to the rate of nucleation $\, J \,$ in the metastable region. This yields mathematical relationships of the type: 31

$$J = BP_{0} \exp\{-[16\pi\gamma^{3}v^{2}]/([3kT]^{3}[ln(P/P_{0})])\}$$

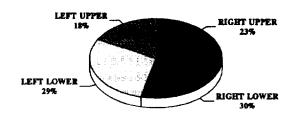
where v is the molecular volume, P/P₀ is the supersaturation (other terms have their conventional meaning in physical chemistry). However, the calculated results are too high for decompression. On the basis of activation energy kinetics, the probability of bubble formation from embryos is small unless the partial pressure considerably exceeds ambient pressure and the surface tension is small. Thus, the pure metastable-state concept has been largely abandoned as an explanation for the appearance of DCS. It has been hypothesized that the relative inactivity of the lower extremities in microgravity results in a greatly reduced concentration of micronuclei and therefore fewer tissue gas micronuclei during decompression. Negative hydrostatic forces, or some other form of "stress assisted" mechanism, must be present to aid the growth of the embryos in the water structure.

Tissue gas micronuclei may exist prior to decompression and be created by several mechanisms. These nuclei would have lifetimes probably on the order of hours (and possibly a day). Tribonucleation can effect the formation of a gas phase when two surfaces are brought into contact with one another and then separated. In a process termed "tacky adhesion" or "viscous adhesion," negative forces (tensions capable of overcoming the tensile strength of water) are generated when adjoining surfaces are separated; the forces during withdrawal can be considerable. The formation of a gas tissue micronucleus has been attributed to the presence of microbubble embryos capable of serving as "seeds" from which nuclei grow by these processes; with surfactants, these are stable and will later grow during decompression.

The reduction in DCS is thus the result of the reduction in activity (hypokinesia) in space and the lack of weight-bearing loads (adynamia) on the legs. This we have termed the abaroferric hypothesis, coined from "a" (the negative), baros (weight, pressure), and fereix (to carry, bear).³⁴

Project ARGO Methods

The subjects of these altitude studies were men and women, 25 - 55 years old. Exercise was performed in an altitude chamber at a similar average level as that measured during EVA. Bubble formation was monitored



Upper: Shoulder, Elhow, Wrist Lower: Hip, Knee, Ankle

Figure 1. Sites of decompression bubbles.

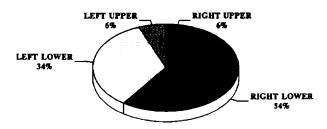


Figure 2. Sites of decompression pain.

in the pulmonary artery by a Doppler-shift ultrasound apparatus. A retrospective analysis was also performed on the results from altitude chamber decompressions conducted at JSC over the past decade to determine both the sites of joint pain DCS and the extremities from which gas bubbles could be found (Figs. 1 and 2).

The hypokinesia study consisted of 3 days of reduced activity of the postural muscles followed by a hypobaric decompression on the fourth day. The bed rest group "crossed over" and remained ambulatory for at least 2 weeks. The subjects were randomly assigned either to Group A (bed rest) or Group B (ambulatory controls); one half of all test subjects began as "bed rested" with the remainder as "controls." A minimum of 2 weeks intervened between the repeat appearance of a subject in one group or the other. The groups are as follows:

Group A. Bed rest: Hypokinetic and adynamic and experiencing cephalic fluid shifts, -6° head down.

Group B. Ambulatory controls: These will be individuals from group A who have crossed over. They would, therefore, be normokinetic and normodynamic individuals undergoing normal activities for daily living.

Four days later, one bed rested and one ambulatory subject at a time were exposed to a reduced pressure of 6.5 psi for 3 hours in a hypobaric chamber by direct decompression (no pre-breathe period). The bed rested subjects were transported into the chamber via a stretcher. Upper body exercise consisted of crank turning, torque wrenches, and rope pulling.

Results

DCS and Decompression Bubbles

Of the anatomical sites for DCS incidence, the legs (predominantly knees) were the joints primarily involved (73/88 DCS cases = 83%). In all cases of pain resulting in impairment of performance, where the subject was removed from the test, the pain was in a lower extremity. In all NASA JSC tests, this predominance of DCS in the lower extremities exists even when the exercise was performed with the upper body. On Earth, naturally, lower body activity is a natural consequence of the activities of daily living.

Decompression Sickness in the ARGO Study

There was one reported case of mild joint pain DCS in the bed rested subject, as could be expected from the tissue ratio. Among the ambulatory subjects, there was one case of neurological DCS involving a paresthesia in the left leg (resolved upon repressurization to site level).

Decompression Bubbles in the ARGO Study

When gas bubbles were heard in both ambulatory and bed rested subjects, the bubble grade (Fig. 3) and/or duration (Fig. 4) was less for rested than ambulatory. The NASA data are such that Doppler-detectable bubble incidence as a function of decompression tissue ratio can be described by power functions of the type:

$$\mathbf{f}(\mathbf{x}) = \mathbf{A} \ \mathbf{x}^{\mathbf{B}}$$

In the case of individuals ambulating in unit gravity, the Doppler gas volume from all four extremities together is given by

^{All}GV_{Doppler} =
$$(8.84 \times 10^{-3}) [TR_{360+520}]^{3.97}$$

and correlation coefficient r = 0.81. We found that there was a greater reduction in the tendency toward gas phase

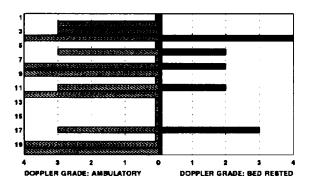


Figure 3. Spencer precordial doppler grade for ambulatory and bed rest.

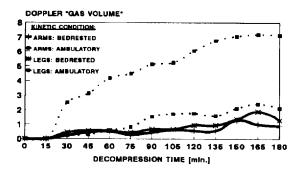


Figure 4. Decompression stress in ambulatory versus hypokinetic individuals.

formation in the lower extremities than the upper as would be expected.

Discussion

Statistical Differences

As evident from this study, there was a difference between the tendency to form a Doppler-detectable decompression gas phase in bed rested subjects compared to ambulatory individuals. By a chi-square test, after grouping the Doppler bubble detection results into Grades 0 - II and III - IV, we find the difference between being ambulatory and bed rested is significant at the p=0.05 level.

It is postulated that the primary reason for the mitigation of the signs and symptoms of DCS is the reduction in the concentration of tissue gas micronuclei, the agents responsible for the loss of supersaturation. These will modify both the volume of gas produced at the tissue level during decompression and the number of moles of gas lost from a microregion during decompression.

Tissue Gas Micronuclei

Under unit gravity conditions, we imagine the continual formation of tissue micronuclei. Stable nuclei probably cannot exist since that would imply viscoelastic properties not found in living tissue and/or that the organic "skin" would be impervious to the diffusion of gas.³⁶ In the latter case, such an entity could not grow by the inward diffusion gas since the boundary would be impermeable. Therefore there must be a finite lifetime t for the gas micronucleus. Fox and Hertzfeld³⁹ have shown that, with no undersaturation, the dissolution time t for a bubble of radius a and surface tension s is

$$\mathbf{t} = (\mathbf{a}^2/3\mathbf{D}\alpha)(1 + [\mathbf{p}_a/2\sigma])$$

If we take the case for a gas bubble situated in a collagenous tendon (semiaqueous tissue) and assume reasonable values for the diffusion coefficient D and solubility of nitrogen, we might estimate bubble lifetimes are thus on the order of 8 to 12 hours when gravitational

forces are removed. There would be a gradual change in size of tissue micronuclei with time. These would attain a new radius r_{0g} which is controlled by muscular activity or tissue constituents, although it is not clear why constituents would change in null gravity. The change in radius of a nucleus from its unit gravity value r_{1g} to the zero-g value of r_{0g} with the passage of time t would then be given by

$$\mathbf{r}_{0g} = \mathbf{r}_{1g} + (\mathbf{r}_{0g} - \mathbf{r}_{1g})(1 - \exp[-\lambda_r t])$$

where k_r is the inverse of the time constant for the change in diameter of all nuclei. More probably, but with a different formulation, we might consider essentially the complete elimination of one species, viz. r_{lg} , and the formation of a new species, viz. r_{0r} according to

$$\mathbf{r}_{n} = \mathbf{r}_{1g}(\mathbf{e}^{-(\mathbf{k}'t)}) + \mathbf{r}_{0g}(1 - \mathbf{e}^{(-\mathbf{k}''t)})$$

More probably, the problem might be represented as a change in the concentration of micronuclei n, possibly of the same size, \mathbf{r}_{lg} when in zero g. The distribution of these sizes and numbers and concentrations is not currently known. In the varying permeability model of Yount, different radii influence different exposures (pressures). The distribution is estimated to follow

$$n = N_{1e} e^{[-\xi r]}$$

where ξ is a constant. In null gravity, $N_{\theta g}$ replaces $N_{1g}.$ Further we postulate that

$$N_{0e} \ll N_{1e}$$

Operational Significance of the ARGO Study

One must consider that we have a large number of decompressions in space (N = 110) with which to compare the results of the ARGO study. The experience of U.S. astronauts alone is considerable in indicating that some protective effect is occurring, either from the diminished musculoskeletal activity before decompression or, as some Russian scientists have suggested, the reduction in musculoskeletal activity during depressurization in the suit. Russian cosmonauts have sustained an even higher tissue ratio ($TR_{360} = 1.85$) and have reported good experience.

The ARGO study seeks to define a possible biophysical mechanism and then to use the information to generate new DCS risk estimates since in-suit Doppler measurements are not available. If we had at our disposal the in-suit Doppler bubble grades, the answer of "estimated risk" would appear quite quickly. Lacking this data, we then compare the ARGO results with the considerable operational experience of the on-orbit decompressions by the U.S. and Russia.

From data collected in earlier NASA/JSC tests, it is possible to determine the degree of in vivo gas phase

formation released into the venous return and measured by means of precordial Doppler methods. It can be determined that a gas volume of 0.303 (that calculated as produced by the bed rested test subjects in the ARGO study) would be produced by a tissue ratio ($t_{1/2} = 360$) of 1.27 (by subjects in unit gravity). From Conkin et al.,⁴ that ratio (1.27) would produce an incidence of mild DCS of:

$$^{\text{\#DCS}} = \frac{[TR_{360} - 0.78]^{4.24} \times 100}{[(TR_{360} - 0.78)^{4.24} + 2.16]}$$

$$^{\text{\#DCS}} = 2.4$$

The probability of *not* encountering minor problems of DCS in 37 decompressions is calculated from the binomial theorem as 41% (from a single DCS incidence = 2.4%). If one enters the Soviet experience (and credits the same success probability), we have a combined total of 110 EVAs and a probability of successful completion of all missions as 6.9%. A similar calculation (Conkin et al., 1987) for severe DCS (joint discomfort sufficient to cause aborting the altitude chamber test) gives DCS = 0.98%. The probabilities of *not* encountering severe DCS in U.S. and combined U.S./U.S.S.R. experience are, respectively, 69% and 34%.

Statististically, one could expect a zero incidence (at the p = 0.95 level) of all, even minor, problems of DCS if the true incidence of even minor DCS in both ground-based and microgravity environments were equal to 0.2%. This clearly is considerably less than the 20% encountered at NASA JSC or the 2.4% predicted for this "effective" tissue ratio in this ARGO study. A predicted incidence of DCS of 0.2% would have an associated (predicted, cf. Conkin et al., 1987) tissue ratio (in the compartment $t_{1/2}$ = 360) of 1.06 as determined from

$$TR = [2.16 (DCS)/(1 - (DCS)]^{1/4.24} + 0.78$$

This work is consistent with the hypothesis that a large measure of the reduction in null gravity can be attributed to a reduction of nuclei. Confirmation must await an in-suit bubble detection system for use on orbit; construction of suitable devices is a portion of other NASA JSC studies.

References

- ¹Elliott, D.H., and E. P. Kindwall, "Manifestations of the Decompression Disorders," *Physiology and Medicine of Diving*, 3rd Edition. Eds. Bennett P.B., Elliott D.H. Bailliere Tindall, London (1982).
- ²Boycott, A.E., G.C.C. Damant, and J. S. Haldane (1908). The prevention of compressed air illness. *J. Hyg.* (Camb), 8, 544.
- ³Ferris, E. B., Jr. and G. L. Engel, "The Clinical Nature of High Altitude Decompression Sickness," Decompression Sickness edited by J.F. Fulton, Saunders, Philadelphia, 1951.

- ⁴Conkin, J., B.F. Edwards, J.M. Waligora, and D. J. Horrigan, Jr., "Empirical Models for Use in Designing Decompression Procedures for Space Operations." NASA TM 100456, 1987.
- ⁵Harvey, E. N., "Physical Factors in Bubble Formation," *Decompression Sickness*, edited by J.F. Fulton, Saunders, Philadelphia, 1951.
- 6Harvey, E.N., D.K. Barnes, W.D. McElroy, A.H. Whitely, D.C. Pease, and K.W. Cooper, "Bubble formation in animals. I. Physical factors," *J. Cell Comp. Physiol.*, 24, 1, 1944.
- ⁷Harvey, E.N., K.W. Cooper, A.H. Whitely, "Bubble formation from contact of surfaces," *J.A.C.S.* 68:2119-2120, 1946.
- 8Harvey, E.N., A.H. Whitely, W.D. McElroy, D.C. Pease, and D.K. Barnes, "Bubble formation in animals. II. Gas nuclei and their distribution in blood and tissues," *J. Cell Comp. Physiol.*, 24, 23, 1944.
- ⁹Harvey, E.N., W.D. McElroy, A.H. Whiteley, "On cavity formation in water," *Journal of Applied Physics*, 18:162-172, 1947.
- Harvey, E.N., W.D. McElroy, A.H. Whitely, G.H.
 Warren, and D.C. Pease, "Bubble formation in animals.
 III. An analysis of gas tension and hydrostatic pressure in cats," *J. Cell Comp. Physiol.*, 24, 117, 1944.
- "Whitaker, D.M., L.R. Blinks, W.E. Berg, V. C. Twitty, and M. Harris, "Muscular activity and bubble formation in animals decompressed to simulated altitudes," *J. Gen. Physiol.*, 28, 213, 1944.
- ¹²Kumar, K.V., J.M. Waligora, and M.R. Powell," Epidemiology of decompression sickness under simulated space extravehicular activities," *Aviat. Space Environ. Med.* Vol. 64, 1993, pp. 1032-1039.
- ¹³Krutz, R.W., G.A. Dixon, "The effects of exercise on bubble formation and bends susceptibility at 9,100 m (30,000 ft; 4.3 psia)," *Aviat. Space Environ. Med.*, 58 (9 Suppl.) A 97, 1987.
- ¹⁴Benson, S.W., E. Gerjuoy, "The tensile strengths of liquids. I. thermodynamic considerations," *Journal of Chemical Physics*, 17:914-918, 1949.
- ¹⁸Blander, M., J.L. Katz, "Bubble nucleation in liquids," Al. Che. Journal., 1-32, 1979.
- ¹⁶Blander, M., "Bubble nucleation," Advances in Colloid and Interface Science, 21:833-848, 1975.
- ¹⁷Zheng, Q., D.J. Durben, G.H. Wolf, C.A. Angell, "Liquids at large negative pressure; water at the homogeneous nucleation limit," *Science*. 254:829-832, 1991
- ¹⁸Daniels, S., K.C. Eastaugh, W.D.M. Paton, and E.B. Smith, "Micronuclei and Bubble Formation: A Quantitative Study Using the Common Shrimp, *Crangon crangon," Proceedings, VIII Symposium on Underwater Physiology,* A.J. Bachrach and M. M. Matzen, eds., Undersea Medical Society, Bethesda, MD, 1984.
- ¹⁹Apfel, R.E., "The role of impurities in cavitationthreshold determination," *Journal of the Acoustical*

- Society of America, 1179-1186, 1970.
- ²⁰Evans, A, and D.N. Walder, "Significance of gas micronuclei in the aetiology of decompression sickness," *Nature*, 222, 251, 1969.
- ²¹Harris, M., W.E. Berg, D.M. Whitaker, and V.C. Twitty, "The relation of exercise to bubble formation in animals decompressed to sea level from high barometric pressures," *J. Gen. Physiol.*, 28, 241, 1944.
- ²²Hemmingsen, E. A., "Bubble Nucleation Mechanisms,"
 The Physiological Basis of Decompression, ed. R. D.
 Vann, UHMS Publication Number 75 (Phys) 6-1-89, 9,
 Undersea Medical Society, Bethesda, MD, 1989.
- ²³Hills, B. A., *Decompression Sickness: A Kinetic and Thermodynamic Approach*, Libraries Board of South Australia, Adelaide, 1966.
- ²⁴Fisher, J.C., "The fracture of liquids," *Journal of Applied Physics*, 19:1062-1067, 1948.
- ²⁵Turnball, D., "Kinetics of heterogeneous nucleation," *Journal of Chemical Physics.*, 18:198-203, 1950.
- ²⁶Zettlemoyer, A. C. (ed)., *Nucleation*, Marcell Decker, 1969.
- ²⁷Speedy, R.J., "Stability-limit conjecture: an interpretation of the properties of water," *Journal of Physical Chemistry*, 86:982-991, 1982.
- ²⁸Weathersby, P.K, L.D. Homer, and E.T. Flynn, "Homogeneous nucleation of gas bubbles in vivo," *J. Appl. Physiol.*, 53, 940, 1940.
- ²⁹Campbell, J., "The tribonucleation of bubbles," *Brit. J. Appl. Phys.* (J. Phys. D), Series 2, 18, 1085, 1968.
- ³⁰Banks, W. H. and C.C. Mill, "Tacky adhesion a preliminary study," *J. Coll. Sci.*, 8, 137, 1953.

- ³¹La Mer, V.K., "Nucleation in phase transitions," Industrial and Engineering Chemistry, 44:1270-1277, 1952.
- ³²Fürth, R., "On the theory of the liquid state," Proceedings of The Cambridge Philosph. Society, 37:252-290, 1941.
- ³³Volmer, M., "Über Keimbildung und Keimwirkung als Spezialfalle der heterogenen Katalyse," *Ztschr. Electrochem.*, Vol 35, pp. 555-561, 1929.
- ³⁴Powell, M. R., J.M. Waligora, W.T. Norfleet, and K.V. Kumar, "Project ARGO Gas Phase Formation in Simulated Microgravity," NASA TM 104762, July 1993.
- ³⁵Hayward, A. T. J, "Tribonucleation of bubbles," *Brit. J. Appl. Phys.*, 18, 641, 1967.
- ³⁶Hayward, A.T. J., "The role of stabilized gas nuclei in hydrodynamic cavitation inception," *J. Phys D.*, 3:574-579, 1970.
- ³⁷Johnson B.D. and R.C. Cooke, "Generation of stabilized microbubbles in seawater," *Science*, 213:209-212, 1981.
- ³⁸Liebermann, L., "Air bubbles in water," *Journal of Applied Physics*, 28:205-211, 1957.
- ³⁹Fox, F.E. and K.F. Herzfeld, "Gas bubbles with organic skin as cavitation nuclei," *J. Acoust. Soc. Amer.*, Vol. 26, 1954, pp 984- 989.
- ⁴⁰Weinke, B.R., "Reduced gradient bubble model," *Int. J. Biomed. Comput.*, 26, 237, 1990.

Longitudinal Study of Astronaut Health: Mortality in the Years 1959-91

Leif E. Peterson, Larry J. Pepper,* Peggy B. Hamm,** and Susan L. Gilbert**
Kelsey-Seybold Clinic and University of Texas
*Johnson Space Center/SD
**KRUG Life Sciences

Abstract

We conducted a historical cohort study of mortality among 195 astronauts who were exposed to space and medical sources of radiation between 1959 and 1991. Cumulative occupational and medical radiation exposures were obtained from the astronaut radiation exposure history database. Causes of death were obtained from obligatory death certificates and autopsy reports that were on file in the medical records. Of the 20 deaths that occurred during the 32-year follow-up period, 16 were due to accidents. The all-cause standardized mortality ratio (SMR) was 181 (95% confidence interval 110 279). There was one cancer death in the buccal cavity and pharvngeal ICD-9 rubric whose occurrence was significantly beyond expectation. Mortality for coronary disease was 53% lower than expected (2 deaths; SMR=47; 95% confidence limit 5 168). The crude death rate for 12 occupationally related accidents was 445 deaths per 100,000 person-years and was an order of magnitude greater than accidental death rates in the mining industries. The SMR of 1346 for fatal accidents was significantly beyond expectation (16 deaths; 95% confidence limit 769 2168) and was similar to SMRs for accidents among aerial pesticide applicators. The 10-year cumulative risk of occupational fatalities based on the exponential, Weibull, Gompertz and linear-exponential distributions was 10%. Mortality from motor vehicle accidents was slightly higher than expected, but was not significant (1 death; SMR=165; 95% confidence limit 2 922). Radiation exposures from medical procedures accounted for a majority of cumulative dose when compared with space radiation exposures. Overall, it was found that astronauts are at a health disadvantage as a result of catastrophic accidents.

Introduction

Thirty years have passed since the Space Radiation Study Panel was convened by the National Academy of Sciences (NAS). The charge to the panel was to develop radiation protection guidelines and identify biologic responses for human exposure to space radiation. In 1967, the panel published its first review of radiation protection issues in the report *Radiobiological Factors in Manned Space Flight*, edited by Wright Langham.¹ The report addressed philosophical considerations, early and delayed radiobiological responses in man, recommendations for additional research and formed the foundation for the

NAS guidelines that were published later in 1971.² Recently, NASA adopted recommendations of the National Council on Radiation Protection and Measurements (NCRP) for its career and ancillary limits for protection.³ The as low as reasonably achievable principle is followed in radiation protection in the U.S. space program and for terrestrial workers. However, the selection of dose limits for manned spaceflights is complicated by the fact that space missions are high-risk endeavors that include accidental death apart from any risks incurred by exposure to densely ionizing radiation.

The space radiation environment is markedly different from those in which terrestrial workers are exposed. During the low Earth orbit (LEO) missions flown in Shuttle, Skylab, Gemini, and Mercury, crews were mostly exposed to geomagnetically trapped protons whose energies ranged from 30-500 MeV. To a lesser extent, another source of radiation is the highly energetic (30) MeV - 10 GeV) charged galactic cosmic rays (GCR) that interact in spacecraft materials and crew members' bodies causing secondary fragmentation particles. A third but infrequent source of radiation is the energetic charged proton and helium ions associated with solar particle events. Radiation doses received by astronauts on Shuttle have been in the low dose range and have averaged 1.31 mGy (131 mrad) per mission. During the Skylab program,4 mission skin dose equivalents were much higher and ranged from 0.03 to 0.18 Sv (3 to 18 rem) to the skin and from 0.02 to 0.08 Sv (2 to 8 rem) to the hematopoietic organs. Projected radiation dose equivalents for a 90-day Space Station mission indicate skin and depth dose equivalents of 0.09 Sv (9 rem) and 0.075 Sv (7.5 rem), respectively.⁵ A more detailed description of the space radiation environment and the dosimetric methods used for monitoring ambient dose is given in NCRP Report 98.3

NASA has used thermoluminescent (LiF-100) dosimeters (TLDs) on all manned flights to date. In addition, plastic nuclear track-etch dosimeters, tissue-equivalent proportional chambers, and charged particle directional spectrometers have been developed and flown recently as part of a new dosimetry program for the Space Station. Despite the new dosimetry, the common denominator has been the use of TLDs to establish the dose of record for each crew member. Astronauts also undergo radiodiagnoses for screening during the selection process and routine health care. Occasionally they volunteer as participants of studies in which microcurie amounts of radioactively labeled compounds are used.

Although worker protection does not generally include the monitoring of medical exposures, NASA takes the additional step of conducting routine surveillance of all medical exposures to ensure an added level of safety. Since Project Mercury, NASA has maintained a computerized database containing space and medical radiation exposure information for each astronaut. Reports containing whole body doses from TLD, organ dose equivalents, effective doses, and site-specific lifetime cancer risks can be generated for space activities and medical procedures.

In consideration of the radiation risk factors mentioned above, it is of interest to conduct periodic hazard identification studies that address disease morbidity and mortality in the astronaut population. This study also addresses the hypothesis that astronauts are at increased risk of malignant neoplasia as a result of occupational radiation exposure and augments primary design criteria of the longitudinal study of astronaut health (LSAH). We report for the first time cause-specific mortality among astronauts employed between 1959 and the end of the 1991 fiscal year.

Methods

Study Population

A listing of the subjects' birth dates and dates of hire was abstracted from the LSAH database and Astronaut Fact Book.⁶ No astronauts were hired and then laid off, and there were no periods of interrupted service in the course of employment. Therefore, the final list contained information for astronauts who worked from the date of the first selection class (April 15, 1959) until the common closing date of September 30, 1991.

Ascertainment of Vital Status

The LSAH database contains International Classification of Diseases (ICD) codes for morbidity and mortality for all astronauts and is updated daily. Causes of death were obtained from obligatory death certificates and autopsy reports that are kept in vault storage at JSC. For this analysis, underlying causes of death were coded according to the 9th revision of the ICD⁷ and arranged alphabetically by name into a list that included dates of birth, hire, and death.

Standardized Mortality Ratios

Cause-specific mortality was analyzed using the MONSON computer program which calculates the expected number of deaths based on indirectly standardized rates of the U.S. population, adjusted for age, race, sex, and calendar year. SMRs were calculated by dividing the observed deaths, O, by the expected, E, and multiplying this ratio by 100. The expected number of deaths was based on the sum product of the 5-year age

and time-specific follow-up time in person-years and the 5-year age-time-sex-cause-specific mortality rates. It is assumed that the observed number of deaths is Poisson distributed with mean E and that under the null hypothesis the ratio of O to E is unity. Confidence intervals (95%) for the SMR were calculated using a computer program devised by Rothman and Boice in which the observed number of deaths are bounded by limits and the expected number of deaths are held constant. Person-years used in SMR calculations were counted beginning with the date of hire until death or the end of the study (September 30, 1991), whichever occurred first.

Parametric Survival Analysis

To estimate the cumulative risk for occupa-tional fatalities, we calculated the hazard and survivorship functions for the exponential, Weibull, Gompertz and linear-exponential distributions with an iteratively reweighted least squares computer program. Cumulative risks at the 10th year of follow-up were approximated by the cumulative distribution function at 10 years, F(10), which was obtained by subtracting S(10) from unity. Tests of significance for the maximum likelihood estimates (H_{α} : B=0) and model goodness of fit were based on the log-likelihood ratio, score, and Wald tests. ¹⁰

Radiation Exposure

A listing of each subject's cumulative radiation dose from space activities and medical procedures was obtained from the astronaut radiation exposure database.¹¹ The listing included the whole-body dose from each spaceflight and the sum of the organ doses from diagnostic X-ray examinations¹ and nuclear medicine studies¹² weighted by the ratio of the site-specific to total lifetime mortality risk for radiation-induced cancer (see table 5.18 of ref. 3).

Results

Demographics and Actuarial Analysis

The computer listing contained the vital status of 195 astronauts. Of these 195 entries, there were 20 deaths and 79 annuitants. At the time of follow-up, the remainder of the astronaut corps consisted of 96 active members. Table 1 shows the demographic characteristics of the entire astronaut population. There was a total of 2700 person-years of follow-up with a mean follow-up time of 13.8 years. There were 20 deaths among the cohort that occurred before September 30, 1991, and cause of death was obtained for all but one individual. Table 2 gives the actuarial parameters for the cohort; Table 3 gives the percentage distribution of deaths by major cause; and crude accidental fatality rates for the astronauts are given in Table 4.

Table 1. Distribution of astronauts employed between 1959 and 1991 by sex and vital status on September 30, 1991

_	S	ex
Vital status	Male	Female
Known alive		
Active	79	17
Retired or resigned	77	2
Known dead	19	1
Total	175	20

Table 2. Actuarial parameters for the astronaut cohort

neter	Estimate
n-years of follow-up	2699.1
t size	195
ge follow-up time	13.84
ge age of entry	33.11
ige year of entry	1976.12
ge age of death	41.75
ge year of death	1978.97
	,

Table 3. Number of deaths and percentage by major cause for astronauts, 1959-1991

Cause of death category (ICDa)	Deaths(%)
Malignant neoplasm (140-209)	1 (5)
Circulatory disease (390-458)	2 (10)
All accidents (800-998)	16 (80)
Unknown causes (799)	1 (5)
Total	20 (100)

^a International Classification of Diseases, 9th revision.

Table 4. Crude fatal accident rates for astronauts (deaths per 100,000 person-years)^a

Cause of death	Rate (95% CI)
All accidents (16 deaths)	593 (329, 857)
Spacecraft (8 deaths)	296 (100, 492)
T-38 trainer jets (4 deaths)	148 (6, 290)
Spacecraft and T-38 trainer jets (12 deaths)b	445 (210, 679)
Military aircraft (5 deaths)	185 (28, 343)
Private aircraft (1 death)	37 (0, 109)
Commercial aircraft (1 death)	37 (0, 109)
Motor vehicles (1 death)	37 (0, 109)

^a Rates calculated with relationship (number of deaths)/ (2699.1 person-years) x (100,000 person-years).

Comparison of Mortality with U.S. Population

The SMRs for specific causes of death are given in Table 5. The all-cause SMR was higher than expected and was statistically significant. There was one cancer death for the oral cavity and pharyngeal rubric (ICD-9 140-149) for which the number of expected deaths was 0.09. Motor vehicle accidents produced a slight though not statistically significant increase in risk. Modeling results of fitting the hazard function for 12 occupational fatalities to the exponential, Weibull, Gompertz, and linear-exponential distributions resulted in a 10-year risk of 10%, all of which had statistically significant log-likelihood ratio, score, and Wald tests.

Table 5. Standardized mortality ratios (SMRs) for selected causes of death among astronauts followed from 1959-1991

Cause of death (ICD ^a)	O/E	SMR (95% CI)
All causes (001-999)	20/11.06	181 ^b (110, 279)
Circulatory disease (390-459)	2/4.28	47 (5, 168)
Ischemic heart disease (410-414)	2/3.14	64 (7, 230)
All external causes (800-998)	16/2.01	796 ^b (454, 1292)
All accidents (800-949)	16/1.18	1346 ^b (769, 2186)
Motor vehicle accidents (810-825)	1/.60	165 (2, 922)

^a International Classification of Diseases, 9th revision.

Radiation Exposures

The radiation encountered and average mission radiation doses for the various space programs are given in Table 6. The mean mission dose during the Mercury program was 0.07 mGy (7 mrad), and doses during the Gemini program were a little higher. The Apollo lunar missions resulted in a mean mission dose for which there was more contribution of GCR and was a little higher than previously recorded mean mission doses. Doses during the Skylab program were much greater than previous doses since these involved much longer mission durations. Last, the Apollo-Soyuz Test Program and Shuttle program resulted in lower average doses because of the short mission durations. There was a high degree of correlation between mission average dose and mission duration (r=0.9966).

Average per capita cumulative radiation doses are given in Table 7. The occupational career doses from space activities were less than cumula-tive doses from medical procedures. This was especially true for selection classes 1 through 7. Although a similar trend was found for selection classes 8 through 13, the ratio of medical to space career doses was much lower. Figure 1 shows the mean cumulative radiation doses for all astronaut classes selected between 1959 and 1991. As

b Considered to be occupationally related.

b p-value < 0.05

Table 6. Average mission radiation doses for various U.S. space programs^{a,b}

Program	Radiation encountered	Missions flown	Average duration (days)	Average mission dose (mGy)
Mercury	Trapped protons	6	0.37 ± 0.20	0.07 ± 0.04
Gemini	Trapped protons	10	4.04 ± 1.22	1.24 ± 0.66
Apollo	GCR, trapped protons,			
	electrons	11	9.47 ± 0.65	4.05 ± 0.85
Skylab Apollo-	Trapped protons, GCR	3	57.17 ± 13.24	4.32 ± 13.55
Soyuz	Trapped protons	1	9.00 ± 0.00	1.06 ± 0.00
Shuttle ^C	Trapped protons	43	6.28 ± 0.31	1.31 ± 0.26

a Correlation coefficient between average duration and average mission dose is 0.9966.

noted in Table 7, class-specific cumulative doses from diagnostic X-ray examinations exceeded in all cases the career doses from space activities. After selection class 8, the contribution of diagnostic X-ray exposures to total cumulative dose drops off precipitously. Also notable in figure 1 is a peak in the cumulative doses from in vitro nuclear medicine studies which occurred during the Apollo program.

Discussion

The astronaut cohort experienced an increase in allcause mortality when compared with the U.S. population primarily because the number of observed accidental deaths greatly exceeded the number expected. It is unusual to find elevated all-cause SMRs in a healthy working population whose overall SMR should, according to the healthy worker effect, be less than 100. An explanation for this is the high *force of mortality* of fatal accidents since they accounted for 80% of all deaths.

The hypothesis that astronauts have increased cancer mortality is not supported by the results, although neither the numbers of person-years of follow-up nor the radiation doses experienced would lead one to expect a significant excess in these data. A previous analysis of astronaut career risks from exposure to space radiation and medical procedures indicated that the estimated cancer risk from medical procedures was 13 times greater

Table 7. Average per capita cumulative radiation doses for astronauts selected during 1959-91

Per capita cumulative dose (mSv) b

Selection class ^a	Selection date	Space activities	Diagnostic X-Ray	Nuclear medicine
1 (4,6,3)	April 1959	3.91 ± 2.24	45.54 ± 12.31	6.48 ± 3.60
2 (7,7,4)	September 1962	8.67 ± 3.34	45.84 ± 10.87	4.15 ± 1.24
3 (9,9,6)	October 1963	8.96 ± 4.38	48.89 ± 8.00	3.87 ± 0.85
4 (4,4,4)	June 1965	33.63 ± 14.96	45.72 ± 16.51	6.86 ± 1.01
5 (14,14,12)	April 1966	18.67 ± 6.93	85.21 ± 9.94	8.09 ± 2.19
6 (7,7,4)	August 1967	2.28 ± 0.10	50.85 ± 10.60	2.92 ± 0.46
7 (7,7,2)	August 1969	2.82 ± 0.10	61.52 ± 8.36	2.51 ± 0.11
8 (23,23,0)	January 1978	3.50 ± 0.48	13.10 ± 3.50	-
9 (15,15,1)	January 1980	2.41 ± 0.50	9.88 ± 1.74	1.60 ± 0.00
10(12,13,0)	May 1984	1.13 ± 0.28	6.13 ± 1.52	-
11(8,10,0)	June 1985	0.87 ± 0.32	4.75 ± 1.06	-
12(8,13,0)	August 1987	0.91 ± 0.35	3.69 ± 0.59	-
13(0,16,0)	January 1990	-	2.88 ± 0.55	-

a Numbers in parentheses represent astronauts with non-zero career doses for space activities, diagnostic X-ray and nuclear medicine procedures.

b Statistical uncertainty represented by standard error of mean.

^c Average Shuttle dose based on STS-1 through STS-48.

b Statistical uncertainty represented by standard error of mean.

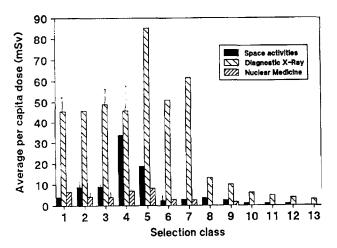


Figure 1. Average per capita dose equivalents (mSv) from space activities, diagnostic X-ray examinations, and radioisotope studies for astronaut classes selected between 1959 and 1991. (Weighted dose equivalents for medical procedures are based on organ doses weighted by organ-specific lifetime mortality risks in table 5.18 of NCRP Report 98, ref. 3).

than that incurred from space activities. 11 Krain conducted an extensive review of the literature and reported that high-altitude aviators are at increased risk for cancers of the skin (squamous and basal cell and malignant melanoma), and cancer of the testes, bladder and thyroid sites.¹³ In a morbidity study on hospitalization rates among U.S. Navy pilots, aircrew officers, unrestricted line officers and staff officers, it was discovered that pilots and aircrew members had the highest admission rates for neoplasms and Hodgkin's disease, and interestingly, were at twice the risk of being admitted for cancer of the testes, when compared with the other nonflying groups.14 The Band et al. study15 of Canadian airline pilots was not etiologic in terms of radiation exposure, but the findings nevertheless indicated a statistically significant elevated risk for rectal cancers (SMR=439; 90% confidence limit 120 1120) and brain cancers (grade IV astrocytomas; SMR=417; 90% confidence limit 140 950). A biologic reason was elucidated for the increase in rectal cancers, which was explained in part by a combination of high-fat diet and effect modification by constipation. Exposure to chemicals and ionizing and non-ionizing radiation were suspected etiologic factors contributing to the increased incidence and mortality of brain cancers.

Epidemiological studies in the nuclear industry suggest an increased risk of leukemia, ^{16,17} multiple myeloma, ^{18,19} and lymphopoietic and unspecified brain cancers. ²⁰ Wilkinson reviewed several epidemiologic studies of U.S nuclear workers and reported an increased risk of leukemia, lymphopoietic cancers, and solid cancers. ²¹ Although a majority of the epidemiologic research that has been conducted is based on low linear-energy-transfer (LET) corpuscular radiation, ^{22,25} of primary interest is the wealth of information available from space-related research on bioeffects of low- and

high-LET particulate radiations.²⁶ Results of the U.S. Air Force Delayed Effects Colony study of 358 rhesus monkeys exposed to proton radiation indicate statistically significant increases in brain cancer (55 MeV proton group) and endometriosis.^{27,28} Other radiobiologic studies on high-LET particulate radiations have reported elevated risks for the inhibition of spermatogenesis,²⁹ cell survival,³⁰ oncogenic transformation,³¹ cataractogenesis,^{32,33} and mutagenesis.34-36 Mutation induction studies with moderate to high LET-charged particles suggest that, when compared with low-LET radiation, a substantial proportion of the mutations induced by densely ionizing radiation at the tk locus involves large-scale genetic changes.³⁴ In a recent study by Brenner and Hall, it was postulated that the inverse dose-rate effect could enhance the bioeffects of trapped protons in LEO and that little enhancement would be expected for GCRs.37

The low SMRs for coronary disease were expected since they are generally low among nuclear workers. 16-21,38,39 McMichael has shown that, for occupational cohorts, SMRs for coronary disease are usually less than 100 because the referent population includes sick individuals.40 The high SMRs for external causes and accidents suggests that astronauts are at an increased risk. Epidemiologic studies in occupational settings have shown increased fatality rates among workers in the agricultural, construction, mining, manufacturing and transportation industries. 41,42 The crude accidental death rate of 445 deaths per 100,000 person-years for the 12 occupationally related deaths (Table 4) was an order of magnitude higher than accidental death rates in the mining industries (34-41 deaths per 100,000 personyears). The finding of an SMR of 1346 for all accidents was in consonance with the SMR of 1168 (95% confidence limit 1046 1301) for fatal accidents (other than motor vehicles) among aerial pesticide applicators⁴³ and Canadian airline pilots (15) (SMR=2129; 95% confidence limit 1460 3020). The 10% cumulative risk of occupationally related fatal accidents for the cohort is, when compared with the "safe industries" with lifetime risks of 3 to 5%, more cause for concern and carries a greater social toll.

Cumulative occupational radiation doses during the Shuttle program have been in the low dose range. The peak in career doses from space activities was attributable to three astronauts in selection class 4 who flew on the long-duration Skylab missions and whose mean crew doses were substantially higher than those of other missions (Table 6). The finding that cumulative medical doses outweighed career space doses corroborates the results of a previous study we conducted¹¹ and is explained by the fact that active astronauts train for 2 to 3 years for each mission and receive medical exposures in the interim. Retired astronauts, most of whom are voluntary participants in the LSAH, on occasion receive diagnostic X-ray examinations during their annual follow-up physicals. Thus, they may be increasing their cumulative medical dose at a time when they can no longer, by

definition, be occupationally exposed to radiation. Before 1978, there were many cases in which active astronauts had routinely undergone X-ray examination of the chest and abdomen as part of the required annual flight physical. A primary reason for the reduction of dose from diagnostic X-ray examinations over the years is attributable to the increase in collimation and correlation of the beam to field size, which reduced the number of wasted X-rays. The marked reduction in cumulative medical exposures after 1978 (selection class 8) was the direct result of a Presidential recommendation to reduce unnecessary medical exposures in Federal agencies. In 1982, the JSC Clinic started using rare-earth screens for all X-ray examinations, which resulted in a substantial reduction of skin entrance exposure.

The above findings suggest that occupational and medical sources of radiation should be considered when assessing the risks of radiation exposure in the LSAH. Moreover, emphasis should be placed on the continued monitoring and surveillance of radiodiagnoses of astronauts. It is expected that radiation doses from space activities will increase substantially during the Space Station era, namely because of the extended mission durations. A recently developed internal standard (control) population is now being used for comparing disease morbidity and mortality between astronauts and their frequency matched controls. As the LSAH matures in size, the use of its internal standard will prove useful as a bias reduction technique in the study of low-dose effects of human exposure to low- and high-LET ionizing radiation.

Conclusions

The purpose of this study was to estimate and measure the presence of risk involved in space activities. Special attention was paid to occupational radiation exposure and likely adverse health effects. Emphasis was placed on the risks to which astronauts are exposed and their rights to full information of the risks. The findings of the study do not indicate that astronauts are at increased risk of cancer, but there are several reasons why this does not obviate the need for further surveillance. First, radiation dose profiles in space are not the same as those for ground-based radiation workers: the source remains turned on for 24 hours a day to the extent that space crews are exposed in their sleep. Second, the planned 90-day, 180-day, and annual radiation dose equivalents incurred during Space Station work will exceed in most cases the 50 mSv (5 rem) annual limit for ground-based radiation workers, who seemingly may be at increased risk of cancer. Finally, there is unambiguous evidence that high-LET radiation results in a higher transformation efficiency when compared with low-LET radiation. Although this is based largely on studies using experimental animals and rodent cell lines, it has strong implications for assessing hazards from human exposure to high-LET space radiation.

The risk of death due to heart disease was 53% lower than that expected in a sample of the U.S. population with an identical age-sex-race distribution. Occupationally related death rates were a factor of 10 greater than accidental death rates in the mining industries. The SMR for fatal accidents was similar to the SMR for accidents among aerial pesticide applicators. The cumulative risk of accidental death over a 10-year career was 10%. Cumulative doses from medical procedures are generally greater than those from space activities because astronauts train for 2 or 3 years for each mission and receive medical exposures in the interim. In addition, retired astronauts may undergo X-ray examination during their annual LSAH follow-up physical when they are no longer occupationally exposed. The major finding of this investigation demonstrates that astronauts are at a health disadvantage because they are exposed to a high level of risk for catastrophic accidents.

Acknowledgments

The authors are grateful to Drs. Robert Hardy and Barry Davis of the University of Texas, School of Public Health, for their helpful comments on survival data analysis. The valuable advice of the reviewers is also appreciated.

Footnotes

1. L.E. Peterson, M. Rosenstein, *Computer Program for Tissue Doses in Diagnostic Radiology*. Technical Report, Center for Devices and Radiological Health, Food and Drug Administration, Rockville, 1989.

References

- ¹National Academy of Sciences, Report of the Space Radiation Study Panel of the Life Sciences Committee, Space Science Board. In: *Radiobiological Factors in Manned Space Flight* (Langham, W.H., Ed.), Publication 1487. National Academy of Sciences, Washington, D.C., 1967.
- ²National Academy of Sciences, Radiation Protection Guides and Constraints for Space-Mission and Vehicle-Design Studies Involving Nuclear Systems. National Academy of Sciences, National Academy Press, Washington, D.C., 1970.
- ³NCRP, *Guidance on Radiation Received in Space Activities*, NCRP Report 98. National Council on Radiation Protection and Measurements, Bethesda, 1989.
- ⁴J.V. Bailey, R.A. Hoffman, R.A. English, Radiological Protection and Medical Dosimetry for the Skylab Crewmen. In: *Biomedical Results from Skylab* (Johnston, R.S., Dietlein, L.F., Eds.). NASA SP-377. National Aeronautics and Space Administration, Washington, D.C., 1977.

- F.A. Cucinotta, W. Atwell, M. Weyland, A.C. Hardy, J.W. Wilson, L.W. Townsend, J.L. Shinn, R. Katz, Radiation Risk Predictions for Space Station Freedom Orbits. NASA Technical Paper 3098. National Aeronautics and Space Administration, Washington, D.C., 1991.
- NASA, Astronaut Fact Book, NASA Publication (JSC) PMS-011B. National Aeronautics and Space Administration, Houston, 1989.
- ⁷WHO, International Classification of Diseases: Manual of the International Statistical Classification of Diseases, Injuries, and Causes of Death, 9th Revision. World Health Organization, Geneva, 1977.
- ⁸R.R. Monson, Analysis of relative survival and proportionate mortality. *Comp. Biomed. Res.* 7, 325-332, 1974.
- ⁹K.J. Rothman, J.D. Boice, Epidemiologic Analysis with a Programmable Calculator. NIH Publication No. 79-1649. Department of Health and Human Services, Washington, D.C., 1979.
- ¹⁰J.C.W. Rayner and D.J. Best, Smooth Tests of Goodness of Fit. Oxford University Press, New York, 1989.
- ¹¹L.E. Peterson, D.S. Nachtwey, Radiological health risks to astronauts from space activities and medical procedures. NASA Technical Memorandum 102164. National Aeronautics and Space Administration, Washington, D.C., 1990.
- ¹²ICRP, Radiation Dose to Patients from Radiopharmaceuticals. ICRP Publication 53. Ann. of the ICRP, Vol. 18 (1-4). International Commission on Radiological Protection, Pergamon, Oxford, 1988.
- ¹³L.S. Krain, Aviation, high-altitude, cumulative radiation exposure and their associations with cancer. *Med. Hypoth.* 34, 33-40, 1991.
- ¹⁴A. Hoiberg, C. Blood, Age-specific morbidity among Navy pilots. *Aviat.*, *Space & Envir. Med.* 54, 912-918, 1983.
- ¹⁵P.R. Band, J.J. Spinelli, T.Y. Vincent, J. Moody, R.P. Gallagher, Mortality and cancer incidence in a cohort of commercial airline pilots. *Aviat.*, *Space & Envir. Med.* 61, 299-302, 1990.
- ¹⁶G.M. Kendall, C.R. Muirhead, B.H. MacGibbon, J.A. O'Hagan, A.J. Conquest, A.A. Goodhill, B.K. Butland, T.P. Fell, D.A. Jackson, M.A. Webb, R.G.E. Haylock, J.M. Thomas, T.J. Silk, Mortality and occupational exposure to radiation: first analysis of the National Registry for Radiation Workers. *Br. J. Med.* 304, 220-5, 1992.
- ¹⁷S. Wing, C.M. Shy, J.L. Wood, S. Wolf, D.L. Cragle, E.L. Frome, Mortality among workers at the Oak Ridge National Laboratory: Evidence of radiation effects in follow-up through 1984. *JAMA*. 265, 1397-1402, 1991.
- ¹⁸E.S. Gilbert, S.A. Fry, L.D. Wiggs, G.L. Voelz, D.L. Cragle, G.R. Petersen, Analysis of the combined mortality data on workers at the Hanford Site, Oak Ridge National Laboratory and Rocky Flats Nuclear Weapons Plant. *Radiat. Res.* 120, 19-35, 1989.

- ¹⁹H. Inskip, V. Beral, P. Fraser, M. Booth, D. Coleman, A. Brown, Further assessment of the effects of occupational radiation exposure in the United Kingdom Atomic Energy Authority mortality study. *Br. J. Indus. Med.* 44, 149-160, 1987.
- ²⁰G.S. Wilkinson, G.L. Tietjen, L.D. Wiggs, W.A. Galke, J.F. Acquavella, M. Reyes, G.L. Voelz, R.J. Waxweiler, Mortality among plutonium and other radiation workers at a plutonium weapons facility. *Am. J. Epid.* 125, 231-250, 1987.
- ²¹G.S. Wilkinson, Epidemiologic studies of nuclear and radiation workers: an overview of what is known about health risks posed by the nuclear industry. In: *Occupational Medicine: State of the Art Reviews.* Vol. 6, 715-724. Hanley and Belfus, Philadelphia, 1991.
- ²²R.E. Shore, Occupational radiation studies: status, problems, and prospects. *Health Physics*. 59, 63-68, 1990.
- ²³National Research Council, Committee on the Biological Effects of Ionizing Radiations, Health effects of exposure to low levels of ionizing radiation-(BEIR V). National Academy of Sciences National Research Council, National Academy Press, Washington, D.C., 1990.
- ²⁴United Nations Scientific Committee on the Effects of Atomic Radiation, 1988 Report, Annex F: *Radiation Carcinogenesis in Man*. I. General Considerations -Sources of Data. United Nations, New York, 1988.
- ²⁵ICRP, 1990 Recommendations of the International Commission on Radiological Protection. ICRP Publication 60. Ann. of the ICRP, Vol. 21 (1-3). International Commission on Radiological Protection, Pergamon, Oxford, 1991.
- ²⁶NASA, Radiation Health Research, 1986-1990. NASA Technical Memorandum 4270. National Aeronautics and Space Administration, Washington, D.C., 1991.
- ²⁷D.H. Wood, Long-term mortality and cancer risk in irradiated rhesus monkeys. *Radiat. Res.* **126**, 132-140, 1991.
- ²⁸J. Fanton, J.G. Golden, Radiation-induced endometriosis in Macaca mulatta. *Radiat. Res.* 126, 141-146, 1991.
- ²⁹W. Schimmerling, E.L. Alpen, P. Powers-Risius, M. Wong, R.J. DeGuzman, M. Rapkin, The relative biological effectiveness of 670 MeV/A neon as a function of depth in water for a tissue model. *Radiat. Res.* 112, 436-448, 1987.
- ³⁰F.A. Cucinotta, R. Katz, J.W. Wilson, L.W. Townsend, J. Shinn, F. Hajnal, Biological effectiveness of highenergy protons: target fragmentation. *Radiat. Res.* 127, 130-137, 1991.
- ³¹ T.C. Yang, L.M. Craise, M.T. Mei, C.A. Tobias, Dose protraction studies with low-and high-LET radiations on neoplastic cell transformation in vitro. *Adv. Space Res.* 6, 137-147, 1986.
- ³²B.V. Worgul, G.R. Merriam, Jr., C. Medvedovsky, D.J. Brenner, Accelerated heavy particles and the lens. III. Cataract enhancement by dose fractionation. *Radiat. Res.* 118, 93-110, 1989.

- ³³J.T. Lett, A.C. Lee, A.B. Cox, Late cataractogenesis in Rhesus monkeys irradiated with protons and radiogenic cataract in other species. *Radiat. Res.* 126, 147-156, 1991.
- ³⁴A. Kronenberg, J.B. Little, Molecular characterization of thymidine kinase mutants of human cells induced by densely ionizing radiation. *Mutat. Res.* 211, 215-24, 1989.
- ³⁵K. Tsuboi, T.C. Yang, D.J. Chen, Charged-Particle Mutagenesis. I. Cytotoxic and mutagenic effects of high-LET charged iron particles on human skin fibroblasts. *Radiat. Res.* 129, 171-176, 1992.
- ³⁶T.K. Hei, D.J. Chen, D.J. Brenner, E.J. Hall, Mutation induction by charged particles of defined linear energy transfer. Carcinogenesis 9, 1233-6, 1988.
- ³⁷D.J. Brenner, E.J. Hall, The inverse dose-rate effect for oncogenic transformation by neutrons and charged particles: a plausible interpretation consistent with published data. *Int. J. Radiat. Biol.* 58, 745-758, 1990.
- ³⁸H. Checkoway, N. Pearce, D.J. Crawford-Brown, D.L. Cragle, Radiation doses and cause specific mortality among workers at a nuclear materials fabrication plant. Am. J. Epid. 127, 255-266, 1988.
- ³⁹L.D. Wiggs, C.A. Cox-DeVore, G.L. Voelz, Mortality among a cohort of workers monitored for ²¹⁰Po

- exposure: 1944-1972. *Health Physics*. 61, 71-76, 1991.
- ⁴⁰A.J. McMichael, Standardized mortality ratios and the "Healthy Worker Effect": Scratching beneath the surface. *J. Occ. Med.* 18, 165-168, 1976.
- ⁴¹A. De Bock, Surveillance for accidents at work. In: Surveillance in Health and Disease (Eylenbosch, W.J. and Noah, N.D., Eds). Oxford, New York, 1988.
- ⁴²J.F. Kraus, Fatal and nonfatal injuries in occupational settings. *Ann. Rev. Pub. Hlth.* 6, 403-418, 1985.
- ⁴³K.P. Cantor, C.F. Booze, Mortality among aerial pesticide applicators and flight instructors. *Arch. Env. Hlth.* 45, 295-302, 1990.
- ⁴⁴D.W. Johnson, W.A. Goetz, Patient exposure trends in medical and dental radiography. *Health Physics*. 50, 107-116, 1986.
- ARA, Radiation Protection Guidance to Federal Agencies for Diagnostic X-Rays, Recommendations Approved by the President Presidential Documents. *Federal Register*, 43(22), February 1, 1978. National Archives and Records Administration, Washington, D.C., 1978.

Microgravity Encapsulation of Drugs

Dennis R. Morrison, Benjamin Mosier,* and John Cassanto**
Johnson Space Center/SD4
*Institute for Research, Inc.
**Instrumentation Technology Associates

Abstract

A new liquid-liquid diffusion process has been developed for microgravity formation of unique microcapsules that contain both aqueous and hydrocarbon soluble drugs in alternating layers of multilamellar microcapsules. Flight experiments on Consort 4 and 5 sounding rockets and Shuttle missions STS-52 and STS-56 produced multilamellar microcapsules containing both an antitumor drug (Cis-Platinum) and a radiocontrast medium (IPO, iodinated poppy seed oil), surrounded by a low molecular weight polymer skin. Microcapsules also were formed containing amoxicillin (antibiotic) or urokinase (a clot-dissolving enzyme), co-encapsulated with IPO, and some are still intact after two years. Multilayered microcapsules, with both hydrophobic and hydrophilic drug compartments, permit diffusion of complimentary drugs from the same microcapsule; e.g., cytotoxic drugs and interferon-gamma to treat tumors, antibiotics and immuno-stimulants to treat resistant infections, or multiple fibrinolytic drugs to dissolve emboli. Co-encapsulation of adequate amounts of radiocontrast medium permits confirmation of the delivery of antitumor microcapsules to target tumors using computerized tomography and radiography that track the distribution of microcapsules after release from the intra-arterial catheter. These microcapsules could have important applications in chemotherapy of certain liver, kidney, brain, and other tumors. Using certain formulations, microcapsules were formed with the drug so concentrated that crystals formed inside; these microcapsules can provide maximum sustained release rates (zero order release kinetics) until the crystals are dissolved, whereupon first order release rates would begin.

Introduction

Encapsulation of drugs or biological therapeutics into liposomes or liquid microcapsules can enable delivery to target organs where the bioactive drug can be released directly to the target area by diffusion. The size and shape of the microcapsules is critical for the distribution and drug delivery in the tissues. Typically, microcapsules of 1 to 5 microns diameter are optimum for intravenous administration, whereas 200- to 300-micron diameter microcapsules are used for intra-arterial delivery. Perfect microcapsules are needed for maximum packing densities and maximum drug payload delivery to target organs or tumors. The disadvantages of using conventional liposomes or microcapsules include

manufacturing methods that require many batch process steps to 1) form the liposomes, 2) remove unwanted organic solvents and detergents, and 3) harvest the proper size microparticles for optimum pharmacologic efficacy.² Also, conventional liposomes often use natural lipids and lecithins (from eggs, soybeans, and other inexpensive sources) which attract certain phagocytic immune cells that rapidly remove the liposomes from the circulatory system before they arrive at the target tissue. This creates variable dose-responses which greatly complicate the pharmacokinetics and make calculations of therapeutic doses very difficult.3 New formulations of "stealth" liposomes have been made with lipids that are less detectable by immune cells in an attempt to avoid phagocytosis4; however, new types of microcapsules are needed to exploit the various unique applications of this type of drug delivery.

Microcapsules specifically designed for intravascular delivery require the appropriate size and durability that can withstand the shear forces of intravascular injection and flow through the blood vessels until they reach the target site. The outer lipid bilayer or microcapsule matrix must also be designed for drug diffusion at appropriate release rates once the microcapsule has reached the target tissue. One of the authors (Mosier) has invented a new method of preparing microcapsules by liquid encapsulation and solid-phase entrapment wherein the water-soluble drug is dispersed in a solid matrix material.⁵ This method involves dissolving the aqueous drug and the matrix material in an organic solvent, in which they are mutually soluble, then dispersing this mixture in a second organic solvent to form an emulsion that is stable enough for intravascular injection. Dispersion of finely divided solids and dense materials in liquids or microemulsions can be achieved with similar techniques; however, successful formulations depend upon the interparticle behavior in the suspensions. For example, when powdered Cis-Platinum (antitumor drug), in saline solution, is dispersed in alcohol solution containing a lipid and surfactant, dense microspheres will form. The aqueous phase causes the solid to be preferentially wet, thereby causing sticky collisions of the solid owning to the interfacial tension between the two liquid phases. The sedimentation rate of the microspheres is quite high compared with that of the original suspension.

Statement of Problem

Liposomes and other encapsulation systems cannot meet all of the requirements for delivery of a wide range

of hydrophilic or hydrophobic drugs, especially at the same time. Many immiscible liquid systems offer great promise as combined drug delivery systems; however, gravity-driven phase separation results in horizontal stratification with very small interfacial surface area between bulk liquids. When conventional surfactants and mixing are used to increase the number of micelles formed, the micelle size is variable and too small (< 1 μ diameter) for many medical applications. New formulations and studies are needed to explore special combinations of immiscible liquids, surfactants, cosurfactants and tracer compounds that can be used to form unique micro-capsules, especially those designed for chemoembolization.

Current methods of forming liposomes are based on mechanisms wherein phospholipids arrange themselves into bilayers, entrapping an aqueous core, when they are dispersed in an excess of water above a critical transition temperature. Drugs that are soluble in organic solvents are usually limited to those that bind inside the hydrophobic region of the liposome bilayer. However, most drugs are dissolved in the aqueous phase which is entrapped when the liposome forms and the drug is either incorporated into the aqueous core or electrostatically binds to the polar regions of the bilayer. Some drugs are insoluble and are not associated with the bilayer and therefore have very low encapsulation efficiencies. Major difficulties with commercial preparation of microcapsules often involve density-driven phase separation of the immiscible carrier fluids, especially when trying to encapsulate multiple drugs.

Microcapsule formation by liquid-liquid dispersion of aqueous drugs and organic solvents typically produces water-in-oil (W/O) type liposomes, which then require the organic solvent to be removed (evaporated) to form reverse-phase evaporation vesicles (rev) or stable plurilamellar vesicles (splv). Multilamellar vesicles (mlv) are rarely formed by these methods, but usually require film casting with organic solvents, hydration, and sizing using filtration through inert membrane filters.² Methods of forming multilayered microcapsules often require emulsification of the aqueous phase into organic carrier solutions by mechanical shear, bubbling, or sonication. Sophisticated, multistep emulsion technology is required, and yields of uniform type and size are often very low.

Approach

Production of multilayered microcapsules with alternate hydrophobic and hydrophilic drug compartments opens up the possibility of developing multiple-therapy microcapsules which can allow sequential diffusion of two or more drugs out of the same microcapsules once they arrive at the target tissues. In some applications, the organic phase can include a tracer compound or radio-contrast medium to provide the additional advantage of real-time imaging of the microcapsules with computerized tomography scanning as they are released from the

catheter and travel to the target tissue. Practical applications of immiscible, liquid-liquid microcapsule formation are limited, however, because of density-driven phase separations resulting in the necessity to use multistep batch processing with solvent evaporation phases and mechanical mixing, which often is not practical. These restrictions led to the design of several microgravity experiments to explore the utility of this process during short duration space flights. The microgravity experiments led to the development of a new liquid-liquid microencapsulation process that involves use of surfactants and co-surfactants in the aqueous phase, and co-surfactant alcohols and high molecular weight lipids in the organic phase, which also contain polymers that can form a tough outer "skin" on the final microcapsules. In microgravity a single-step dispersion produced unique multilamellar microcapsules containing various aqueous drugs co-encapsulated with iodinated poppy seed oil (a radiocontrast medium with an sp gravity =1.35). Subsequent ground control experiments produced unique microcapsules and confirmed that the one-g process could be improved to yield usable microcapsules by using different formulations or electrostatic deposition to add the polymeric outer coating.

Methods

Immiscible liquid formulations and simplified liquidliquid dispersion methods were developed in 1988 for microgravity experiments for space missions using the materials dispersion apparatus (MDA) mini-lab developed by Instrumentation Technology Associates, Inc. The MDAs consist of an upper and a lower block that contain chambers (500 µl) for each sample fluid. The blocks are misaligned at launch so that the chambers are not in contact with each other. Upon activation in microgravity, the blocks are moved to align the chambers so that the fluids can mix by liquid-to-liquid diffusion. For some experiments, a single-step, magnetic-mixing technique was utilized to accelerate the process. Some of the experiments were conducted with a single-step fluid mixing, and some were done with a two-step fluid mixing technique which allows diffusion of a third fluid or sample into the mixture of the first two fluids while still in the microgravity environment. The Consort sounding rocket flights produced only 6.5 minutes of microgravity conditions, but this was adequate to form the unique microcapsules in a single step. Experiments on the Space Shuttle permitted 10-minute dispersion times followed by curing of the outer polymer skin for 8 days under microgravity conditions. New formulations were tested on Shuttle STS-52, using only aqueous-soluble drugs, polymers, and surfactants, and on STS-56 using alcohols as a solvent and co-surfactant.

Microgravity experiments on sounding rockets used liquid-liquid dispersion of aqueous drug solutions, surfactants, and polyethylene glycol dispersed in alcoholic co-surfactant solutions containing soluble

polyglycerides. Image analysis of the microcapsules was made possible by co-encapsulation of standard size fluorescent beads. Single-pass mixing, under microgravity conditions, using finely dispersed iron particles drawn through the immiscible interface by a small magnetic field, was also used to form microcapsules containing hydrophilic drugs, microbeads, and hydrophobic components. After 6.5 or 10 minutes of liquid dispersion, the reservoirs were separated automatically.

Results

The Consort experiments produced multilamellar liquid microcapsules (concentric spheres within spheres) comprised of three or more alternating immiscible layers of oil/water and polymer/water/oil. Microcapsules were formed in the ranges of 1-15 μ , 40-50 μ , 110-130 μ , and 160-230 μ diameters. Digital analysis of fluorescent images taken with a fluorescent microscope showed that the aqueous-soluble drugs were often encapsulated within the inner aqueous core and the outermost aqueous shell of the microcapsules. This typical distribution is illustrated in Figure 1, where the left image is a photomicrograph and a fluorescent photomicrograph (lower right) of the same multilamellar microcapsule. The polyglyceride skin is clearly shown in the normal-light photomicrograph (upper left).

Multilamellar microcapsules were formed which contained relatively large amounts of IPO in discrete lamella or vesicles. Figure 2 (left side) shows a microcapsule heavily loaded with IPO, which often comprised up to 38% of the total volume. Often small hemispheres of IPO were also found clinging to the outer surface of the large inner (aqueous) sphere or adhered to the outer polymer skin of the microcapsule as also shown in Figure 2 (upper center). Microcapsules formed by almost all of the formulations survived >15 g's, severe vibrations, and turbulent mixing during the reentry of the experiment capsule, and have remained intact for 2 years after recovery from space. These multilayered microcapsules are similar to liquid-filled, thin-skinned microballoons which are flexible enough to be manipulated on a microscope slide without collapse. The microcapsules formed in just 6.5 minutes of microgravity retain their spherical shape and appear tough enough to survive the extensive physical manipulations and fluid shear encountered during intravascular injection.

Microencapsulation experiments on Consort 4 and 5 and STS-56 used mixtures of aqueous-soluble drugs, IPO, C3-C8 alcohols and polyglycerides that are insoluble in aqueous solutions. Experiments on STS-52 co-encapsulated Cis-Platinum with IPO by forming microcapsules from water-soluble polymers using special formulations of aqueous, nonalcoholic solvents. Polyvinyl pyrolidone (PVP) and a commercial lecithin (Centrolex-F TM, a lecithin produced by Central Soya, Inc.) were used to form the multilamellar microcapsules at 20-28 °C.



Figure 1. Photomicrographs of multilamellar microcapsules.



Figure 2. IPO-loaded microcapsules.

Fluorescent beads and fluorescent labeled drugs were co-encapsulated to permit drug distribution measurements within the various vesicles and lamella, using fluorescence microscopy and digital image analysis at the Johnson Space Center. The final microcapsules were suspended and recovered in either aqueous solutions, IPO or mineral oil. The microcapsules produced by these formulations were similar to those made using alcoholsoluble polyglycerides.

Another unique type of microcapsule was formed during these experiments that was characterized by drug crystals formed within the inner aqueous core of the multilamellar microcapsules. Figure 3 shows an example of a microcapsule which is packed (approximately 65% of the aqueous compartment) with crystals of Cis-Platinum, antitumor drug. Figure 4 shows two microcapsules containing crystals of amoxicillin that were formed in the STS-52 experiments. These illustrate that aqueous-soluble drugs can be encapsulated at very high concentrations near the solubility limit of the drug. After the microcapsules are formed, the drug can become further concentrated to form large crystals which can be more stable than the dissolved drug during prolonged storage.

The STS-56 experiments again produced multilamellar liquid microcapsules (multiple concentric spheres within spheres) comprised of alternating immiscible layers. Using fluorescent 6.4-μ beads and image analysis, it was found that the most interesting microcapsules were formed in the range of 10-15 μ , 40-50 μ , $50-100 \,\mu$, and $160-230 \,\mu$ diameters. More microcapsules were formed containing numerous crystals of Cis-Platinum or amoxicillin which were formed after encapsulation. Several microcapsules were formed that contained a single large tetrahedral crystal of Cis-Platinum which so completely filled the inner sphere that only about 15% of the inner volume remained as a liquid. One encapsulated Cis-Platinum crystal was measured at 50 μ across within a 57-μ diameter microcapsule (data not shown). After formation, some of the microcapsules were dispersed in an external oil phase (either IPO or mineral oil) and allowed to cure for 8 days

Figure 3. Cis-Platinum microcapsules.

before return to Earth. Microcapsules formed with hydrocarbon soluble polymers on STS-56 were tougher than those formed on STS-52 using only water soluble polymers.

Conclusions

Our space experiments are the first to demonstrate that multilamellar, alternating-phase microcapsules can be formed during short exposures of immiscible liquid phases when special drug and solvent formulations are used. Microgravity permits the encapsulation of drugs into unique microcapsules by liquid-liquid dispersion and spontaneous emulsification using alcohol/water/oil mixtures, appropriate surfactants, and co-surfactants.7-10 Spontaneous formation of multilamellar microcapsules containing alternating layers of aqueous and hydrophobic solvent compartments is largely dependent on the interfacial tension and less on the amount of mixing between immiscible liquid phases. Once formed, these microcapsules remain spherical due to the predominant surface tension of the internal phases. High molecular weight polymers and polyglycerides can be included to form flexible, permeable "skins" around the liquid microcapsules as they are created by phase-partitioning mechanisms. The microcapsules can be formed and cured without deformation by contact with container walls. This offers new possibilities for using electrostatic fields to form the microcapsules or deposit additional coatings. The flexible microcapsules formed in microgravity have more uniform size distributions than those formed in one g, largely due to the absence of thermal convection and instabilities that occur at the immiscible interfaces. These

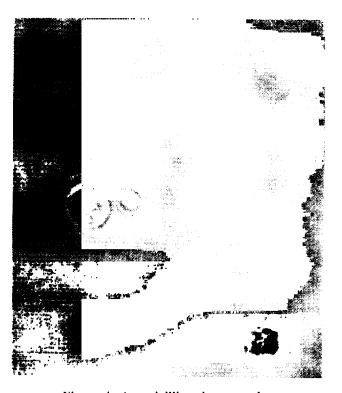


Figure 4. Amoxicillin microcapsules.

methods permit formation and harvesting of unique microcapsules which are durable enough to be removed from the external solvent without disruption or destruction of the internal phases. These microcapsules have several advantages over conventional liposomes and are better suited for chemoembolization therapy.

Co-encapsulation of an aqueous-soluble, antitumor drug (Cis-Platinum) and a radiocontrast medium (IPO) in microgravity has produced a unique drug delivery system that can be visualized by radiology or computerized tomography scanning to ensure that the cytotoxic drug is delivered directly to the target tumor. Multilayered microcapsules have been developed which can provide a new intravascular delivery system for targeted tissues and sequential, sustained release of multiple antitumor drugs. This method has formed perfect microcapsules and more uniform sizes, which can provide maximum packing densities and maximum drug delivery to target organs or tumors. This opens up more possibilities to treat highly vascular tumors (liver and kidney) with chemoembolization, where the microcapsules (100-200 μ) are injected via an arterial catheter to form artificial emboli which block the blood supply to the tumor. The reduced blood volume that flows past the tumor becomes loaded with the antitumor drug that diffuses out of the microcapsules, thus increasing the chemotherapeutic dose to the tumor cells.

The use of multiple drugs within the same microcapsule can provide an opportunity to design microcapsules specifically for multiple modality cancer treatments. Multiple-drug microcapsules could be used to deliver first a chemotherapeutic drug which would kill tumor cells, and secondly an immuno-adjuvant (e.g., tumor necrosis factor) or immuno-stimulant (e.g., Interferon-g) that would enhance the patient's immune response to the tumor. These microcapsules can also be used to deliver combinations of antitumor drugs or simultaneous delivery of two different types of drugs, e.g. Cis-Platinum and Diaziquone, to high grade malignant brain tumors.¹¹ The Cis-Platinum is chemically toxic to the tumor cells and the Diaziquone acts as an adjuvant to enhance the effects of radiation therapy.

Multilayered microcapsules could also be used to treat deep infections that are resistant to systemic antibiotics. In these applications, one or more antibiotics and an immune stimulating cytokine (Interleukin-1) could be delivered to the site of the infection for sequential release. Multilayered microcapsules also can be designed to protect active forms of urokinase and other thrombolytic enzymes until they are delivered and entrapped at the local site of a blood clot, where therapeutic doses of the enzyme can diffuse out of the microcapsules to dissolve the unwanted embolism. The

types of potential multiple drug combinations is quite extensive, limited only by the drug solubility in each carrier phase within the microcapsule and by the drug diffusion rates through the outer layers and semipermeable outer skin.

References

- ¹Rhoerdink, F. H., *et al*, "Therapeutic Utility of Liposomes," *Drug Delivery Systems*, Vol. 1, edited by J. G. Lloyd-Jones and P. Johnson, Ellis Horwood, Chichester, UK, 1987, pp. 66-80.
- ²Talsma, H., and Crommelin, D. J. A., "Liposomes as Drug Delivery Systems, Part I: Preparation," *Pharmaceutical Technology*, October 1992, pp. 96-106
- ³Allen, T. M., "Interactions of Drug Carriers with the Mononuclear Phagocytic System," *Liposomes as Drug Carriers*, edited by G. Gregoriadis, John Wiley & Sons Ltd., New York, 1988, pp.37-50.
- ⁴Allen, T. M., Mehra, T., Hansen, C., and Chin, Y.C., "Stealth Liposomes: An Improved Sustained Release System for 1-b-D-Arabinofuranosylcytosine," *Cancer Res.*, Vol. 52, 1992, pp. 2431-39.
- ⁵Mosier, B., "Method of Preparing Microspheres for Intravascular Delivery," U.S. Patent, 4,492,720, 1985.
- ⁶Bhargava, H. N., Narurkar, A., and Lieb, L. M., "Using Microemulsions for Drug Delivery," *Pharmaceutical Technology*, March 1987, pp. 46-54.
- Morrison, D. R., and Mosier, B., "Microencapsulation of Drugs, Microbeads and Radio-opaque Contrast Medium: Consort 4 Sounding Rocket Experiments in the Materials Dispersion Apparatus," NASA-JSC internal report (unpublished), December 1991.
- ⁸Microencapsulation Experiments on Consort 4 Sounding Rocket, Minilab I, *Earth Space Review*, July -September, 1992.
- Morrison, D.R., and Mosier, B., "Preliminary Results of the STS-52 Experiments on Microgravity Encapsulation of Drugs," NASA-JSC internal report (unpublished), November 28, 1992.
- ¹⁰Morrison, D.R., Mosier, B., and Cassanto, J.M., "Microencapsulation of Anti-tumor, Antibiotic and Thrombolytic Drugs in Microgravity," *Proceedings of the Technology 2003, National Technology Transfer Conference*, Anaheim, CA., Dec. 7-10, 1993, available NTIS, Washington, DC., (in press).
- ¹¹Kimler, B. F, *et al.*, "Combination of Aziridinylbenzoquinone and Cis-platinum with Radiation Therapy in the 9L Rat Brain Tumor Model," *Int. J. Radiation Oncology Biol. Phys*, Vol. 26, 1993, pp. 445 450.

Radiation Damage to Internal Organs from Low Energy Galactic Cosmic Ray Particles

Honglu Wu and Chui-hsu Yang* KRUG Life Sciences *Johnson Space Center/SD

Abstract

The relation between biological damage to human internal organs and the energy of galactic cosmic rays (GCRs) on free-space missions is investigated in this report. In particular, the number of GCR particles stopped in the lung and the absorbed dose due to the stopped particles are estimated. It is found that for the lung, the percentages of the particles halted in the organ and of the dose due to the stopped particles are as high as 20% for iron ions. The results indicate that the low energy particles stopped in the organ may not be neglected in assessing the radiation damage.

Introduction

Space radiation damage to internal organs of astronauts is one of the safety concerns for manned spaceflight. We know that charged ions of different energies have different stopping powers and thus produce different biological effects. Low energy particles with small range are likely to be stopped in the organ and may produce qualitatively different damage than the particles that penetrate the organ. However, the damage due to the stopped particles may be neglected if the fraction of the particles is small enough. The purpose of this report is to quantify the number of the energetic particles stopped in internal organs of astronauts and the absorbed dose due to the stopped particles in free-space missions.

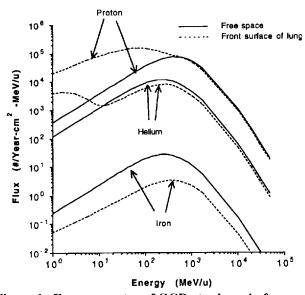


Figure 1. Energy spectra of GCR at solar min for proton, helium, and iron. Solid lines represent the spectra in free space, and dashed lines represent the spectra at the front surface of the lung.

From the critical human organs identified by the National Council on Radiation Protection and Measurements,¹ the lung is selected in this study because the lung has the highest sensitivity to space radiation for men and the second highest for women. The mission scenario considered here is a free-space flight at solar minimum activities, and the astronauts are protected by a 10 g/cm² aluminum shield of the spacecraft. In free-space missions, astronauts are constantly bombarded by GCR and infrequently by the particles emitted from large solar particle events. Radiation from solar particle events is not considered in this report. The energy distributions for proton, helium, and iron (three components of GCRs) are shown in Fig. 1.

Problem Statement

An internal organ in free space is protected not only by the spacecraft but also by the shield of the human body. At JSC, the body shield areal density is generated by the computerized anatomical man (CAM) and computerized anatomical female (CAF) models.^{2,3} The CAM and CAF represent a 50th percentile US Air Force male and a 50th percentile US Air Force female, respectively. The average shield areal density of the lung from distributions of five locations is presented in Fig. 2 for a 50th percentile US Air Force male.

High-energy-charged particles interact with both electrons and nucleons as they propagate through the

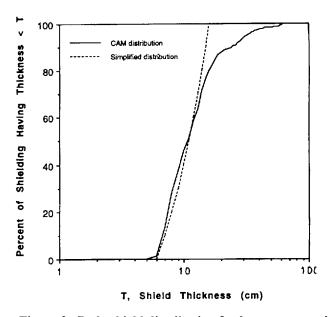


Figure 2. Body shield distribution for lung, generated from CAM (solid line) and slab (dashed line) models.

target. The interaction with electrons results in a slow-down of the primary particles, and the energy is deposited in the target. The nuclear interaction may produce particles of different charge and mass—known as secondary particles. Computer models of atomic and nuclear reactions are used to construct transport codes that compute the absorbed energy in a target from a modeled radiation environment. Transport of GCRs through materials is performed with the computer code (HZETRN, developed at NASA Langley Research Center).⁴

Because of the irregular shape of a human lung, we replaced the geometry of the lung with a slab to simplify our computation. Under the simplification, the body shield areal density is now replaced by the dashed line in Fig. 2. As shown in Fig. 3, GCR particles from the left penetrate through the shields of the spacecraft and the human body to reach the front surface of the lung. The damage of the particles to the lung is now fully determined by the energy distribution at the front surface of the organ. The thickness of the slab (which represents the lung) is taken as the cubic root of the volume of the lung. Since the volume of a male lung is about 1000 cm³ (with air excluded), the thickness is 10 cm. The shield for the center of the slab is determined by the thickness of the 50th percentile of CAM distribution. The body shield thickness in front of the lung is 6 cm.

Method

The energy spectrum of the particles at the front surface of the lung is computed with HZETRN by transporting the free-space GCR through the shield of 10 g/cm² Al and 6 g/cm² H₂O. The spectra for protons, helium, and irons are shown as dashed lines in Fig. 1. The number of particles stopped in the lung and the dose due to the stopped particles may be calculated with the following formulas. The number of primary particles stopped in the lung is given by:

$$n_j^{stop} = \int_0^{E_j(r_0)} f_j(E) dE$$
 (1)

where $f_j(E)$ is the energy distribution of j-type particles at the front surface of the lung, $E_j(r_0)$ is the energy of j-type particles having a range of $r_0(r_0 = 10 \text{ cm})$. The total number of j-type particles at the front surface of the lung is given by:

$$N_j^{tot} = \int_0^\infty f_j(E) dE$$
 (2)

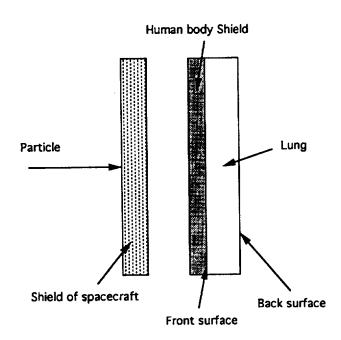


Figure 3. Simplified geometry of lung.

Since the stopped particles lose all their energies in the organ, the dose due to the particles is calculated from:

$$D_j^{stop} = \int_{0}^{E_j(r_0)} E f_j(E) dE$$
 (3)

Similarly, the dose due to higher energy primary particles may be evaluated from

$$D_{j}^{non-stop} = \int_{E_{j}(r_{0})}^{\infty} \left[E - E_{j}[r_{j}(E) - r_{0}] \right] f_{j}(E) dE$$
 (4)

where $r_j(E)$ is the range of j-type particles having energy

These formulas are derived without taking into account the secondary effect.

Results and Discussion

Listed in Table 1 are numbers of particles at the front surface of the lung and numbers of particles stopped in and penetrating through the lung. Among the three kinds of particles, iron has the largest percentage of particles stopped in the lung. The smallest percentage is 4.6% for helium. Doses due to the particles stopped and not stopped are shown in Table 2. The percentage of the dose

Table 1. Number of GCR Particles

Particle	# of stopped particles	# at front surface	% of stopped particles	# of non-stopped particles	# at back surface (HZETRN)
Proton	1.49x10 ⁷	1.60x10 ^s	9.3	1.45x10 ⁸	1.57x10 ^x
Helium	4.52×10^5	9.88x10°	4.6	9.43x10°	7.48x10°
Iron	1.33×10^3	$6.21x10^3$	21.0	4.88x103	1.50×10^3

Table 2. Absorbed Dose (RAD/Year) in the Lung From GCR Particles

Particle	Stopped particles	Non-stopped particles	Total	% of stopped particles
Proton	1.53	6.49	8.02	19
Helium	0.20	1.70	1.90	11
Iron	0.036	0.121	0.157	23

due to particles stopped in the lung ranges from 11 to 23% among proton, helium, and iron particles.

The number of particles (with secondary particles included) at the back surface of the lung are also computed with HZETRN. These numbers, listed in the last column of Table 1, are compared with the numbers of particles not stopped. The differences between the last two columns in the table are small for protons and helium but large for irons. More protons appear in the last column because secondary protons are generated from heavier particles. Less iron is found at the back surface (with secondary effect considered) because iron is broken into lighter pieces due to nuclear reactions, and the production of iron ions from heavier particles is negligible.

Dose equivalent, which differs from absorbed dose by a quality factor, takes into account the biological response to the radiation and is sensitive to linear energy transfer (LET) at high LET. At the end of a particle trajectory, a charged particle deposits a large amount of energy (known as Bragg peak), and the value of the quality factor is higher. As a result, the percentage of dose equivalent due to the stopped particles in an organ is expected to be larger. However, dose equivalents are not estimated in this report because only the average LET may be used in formulas in the last section, and the Bragg peak effect will be lost.

Conclusion

We have computed the percentages of GCR particles stopped in the lung and of the dose due to the stopped particles. The percentage of dose contributions from stopped particles to total dose recovered ranges from 4 to 23% among proton, helium, and iron particles and is non-negligible. Hence, low energy particles stopped in internal organs must be included in the radiation risk assessment.

References

- ¹National Council on Radiation Protection and Measurements (NCRP), "Guidance on Radiation Received in Space Activities," NCRP Report No. 98, Bethesda, MD, 1989.
- ²Billings, M.P. and Yucker, W.R., Summary of Final Report: "The Computerized Anatomical Man (CAM) Model," Report MDC G4655, McDonnell Douglas Astronautics Company, Huntington Beach, CA, 1973.
- ³Yucker, W.R., "Computerized Anatomical Female Body Self-Shielding Distributions," Report MDC 92H0749, McDonnell Douglas Space Systems Company, Huntington Beach, CA, 1992.
- ⁴Wilson, J.W., Chun, S.Y., Badavi, F.F., Townsend, L.W., and Lamkin, S.L., "HZETRN: A Heavy Ion/Nucleon Transport Code for Space Radiations," NASA TP-3146, 1991.

Radiation Studies on Chromosomal Aberrations in Human Lymphocytes

Chui-hsu Yang, Kerry George,* and Honglu Wu*
Johnson Space Center/SD
*KRUG Life Sciences

Abstract

For health risk assessment, direct measurements of space radiation damage in the human body are essential. Using the fluorescent in situ hybridization (FISH) technique, we studied the induction of chromosomal aberrations by low dose and dose rate of gamma rays. A linear relationship between the dose and the number of chromosomal aberrations per cell or the number of cells with chromosomal aberration was observed.

Doses from 16 to 65 cGy were used; and translocation, deletion, and ring of chromosomes #2 and #4 were scored as aberrations. The slope of the dose response curve was about 2.8x10-4 aberrations per cGy. We also conducted split-dose experiments to determine the sublesion repair. Experimental results showed no repair in lymphocytes which were incubated at 37°C for 3.25 hrs between doses. The dose-response curve for high doses and dose rate was curvilinear.

Introduction

Conducting radiation safety research and applying such measures to space vehicle crews is an important part of space biology, medicine, and clinical medical safety in flight. Accurate measurements of biological damages induced by space radiation are important for crew health risk assessment.1 Space radiation is a complicated spectrum of particles with various energies and charges, which determine relative biological effectiveness in causing acute and late effects.2 There are active and passive dosimeters for monitoring space radiation. However, these monitors do not provide complete information on charges and energies of all particles found in space. For health risk assessment, it is critical to know the organ doses, which are calculated by using transport codes and quality factors. At present, the transport codes have significant uncertainty, and the quality factors are not well known. Furthermore, there are potential effects of microgravity on radiation responses of cells in vivo. Direct measurements of radiation damage in the human body and other biological systems are, therefore, very much needed. Chromosome aberrations in human lymphocytes have been used as biodosimetry to determine the radiation exposure of radiation workers and atomic bomb survivors.^{3,4,5} For these reasons, we initiated studies to evaluate the effects of ionizing radiation on chromosomal aberrations in human lymphocytes.

Problem Statement

The basic goal of this investigation was to quantitatively determine the radiation-induced biological changes at cellular and molecular level under microgravity. The specific objectives were to measure chromosomal aberrations in human lymphocytes induced by radiation in the space environment and to correlate the measured biological damages with physical doses for health risk assessment. In this report, experimental results from ground studies with gamma rays are presented. These data are essential to this project, since they serve as the baseline information for spaceflight experiments.

Methods

Peripheral blood samples were collected from human subjects and irradiated with gamma rays at room temperature. Each sample consisted of 10 to 20 ml of blood drawn into a heparin-treated container coded with an ID number. Immediately after irradiation, the heparinized blood sample was cultured for 48 to 72 hrs in an RPMI 1640 medium containing 20% fetal calf serum and stimulated to proliferate with phytohemagglutinin (0.15 mg/ml). Colcemid was added to the cultures after 48 to 72 hrs for 4 hrs, and metaphase spreads were prepared by the standard hypotonic treatment method.

The FISH technique was used to determine chromosome translocation and deletion frequency. Metaphase spreads were stained with probes for two different chromosomes and then examined under a fluorescence phase microscope. All spreads were scored as normal if they showed two pairs of large fluorescence-stained chromosomes. Structural aberrations were recognized as bicolor chromosomes.

For dose rate studies, peripheral blood samples were irradiated by gamma rays at 0.13 cGy/min or 1000 cGy/min. Samples were kept at room temperature during irradiation.

Results and Discussion

Figure 1 shows the experimental results of low-dose rate studies. Human lymphocytes were irradiated at room temperature by gamma rays at 8 cGy/hr or 0.133 cGy/min. The longest exposure was 8 hrs. Holding cells at room temperature for 8 hrs had no observable effect on the viability of control lymphocytes. After irradiation, lymphocytes were grown in culture for 72 hrs before

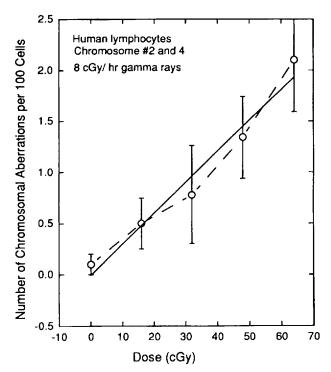


Figure 1. Dose-response curve for human lymphocytes exposed to gamma rays at low dose rate, 8 cGy/hr or 0.133 cGy/min, at room temperature. Solid line is a regression fitting and has a slope of 2.8x10-4 aberrations per cGy.

mitotic cells were harvested. FISH was performed for chromosomes #2 and #4, and chromosome aberrations were scored under a fluorescent microscope. Over 800 mitotic cells were scored for 0, 16, 48, and 64 cGy, and about 300 mitotic cells for 32 cGy. Most chromosomal aberrations observed were deletion and interchromosomal translocation. The dose-response curve for this dose range appears linear. A least square regression fitting of these data give a slope about 2.8x10-4 aberrations per cGy. These results indicate that by increasing the number of cells scored, it will be possible to detect chromosomal effects of a dose as low as 10 cGy.

The potential of human lymphocytes to repair radiation-induced chromosomal damages was studied by conducting a split-dose experiment, and results are shown in Fig. 2. Human lymphocytes were exposed to single or split doses of gamma rays at high dose rates (1000 cGy/min). For determining the repair of subchromosomal injuries, cells were kept at 37°C for 3.25 hrs between two irradiations. The dose-response curve for single exposures appears curvilinear with no significant difference between single- and split-dose irradiated cells.

Conclusions

These experimental results suggest that human lymphocytes are sensitive to ionizing radiation with little or no repair capability. In combination with the molecular biology technique, FISH can be very useful as a biodosimetry for measuring cellular damages in crew

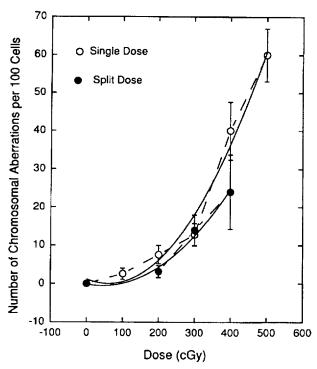


Figure 2. Dose-response curves for single- and split-dose irradiation. Human lympocytes were kept at 37°C for 3.25 hrs between two split doses. Solid line is a regression fitting.

members exposed to space radiation. Because for low doses a large number of mitotic cells must be scored to get good statistical data, development of automated systems for chromosome analysis is essential and has been initiated.

References

¹Nachtwey, D.S. and Yang, T.C., "Radiological Health Risks for Exploratory Class Missions in Space," *Acta Astronautica*, 23:227-231 (class missions in space), 1991.

²Yang, T.C., Craise, L.M., Mei, M., and Tobias, C.A., "Neoplastic Cell Transformation by Heavy Charged Particles," *Radiat. Res.*, 104:S-177-S-187, 1985.

³Evans, H.J., Buckton, K.E. Hamilton, G.E., and Carothers, A., "Radiation-Induced Chromosome Aberration in Nuclear-Dockyard Workers," *Nature* (London), 277:531-534, 1979.

⁴Lucas, J., Tenjin, T., Straume, T., Pinkel, D., Moore, D., Litt, M., and Gray, J., "Rapid Determination of Human Chromosome Translocation Frequency Using a Pair of Chromosome-Specific DNA Probes," *Int. J. Radiat. Biol.*, 56:35-44, 1989.

⁵Lucas, J.N., Awa, A., Straume, T., Poggensee, M., Kodama, Y., Nakano, M., Ohtaki, K., Weier, U., Pinkel, D., Gray, J., and Littlefield, G., "Rapid Translocation Frequency Analysis in Humans Decades After Exposure to Ionizing Radiation," *Int. J. Radiat. Biol.*, 62:53-63, 1992.

Sharps Container

Angelene M. Lee Johnson Space Center/SE

Abstract

Many of the missions flown on the Space Shuttle involve metabolic experiments which require that blood samples be obtained from the crew members on orbit. Taking such samples is not difficult, but disposing of the used syringes and used needles can present problems in microgravity. The sharps container developed for use in space safely holds the entire needle assembly in a closed container and prevents potential harm associated with taking blood samples in microgravity.

Introduction

Sharps containers for used hypodermic needles are well known. Hospitals, for example, provide disposal boxes to receive different types of medical refuse. One special class of items for disposal is commonly referred to as "sharps" and includes items such as used hypodermic needles or broken glass vials and pharmaceutical containers. After use, these articles may be unsanitary and potentially dangerous. Some of the articles may be coated with blood, carry residual quantities of drugs, or be contaminated in other ways. In addition, there is danger of physical injury to hands or fingers from the sharp points or edges. Although attempts have been made to provide disposal containers for such items, existing containers suffer from various disadvantages when used in microgravity.

Problem Statement

The object of this project was to provide an improved container that addresses these problems. The commercially available sharps containers used in hospitals and laboratories to guard against the accidental use of used needles typically use devices that cause the needle to be broken off at the end of the syringe, or act as a receptacle for the needle assembly or as a receptacle for both the needle and syringe. Currently available sharps containers are gravity-dependent in that the disposed item is dropped or inserted into the container and falls to the bottom of the container. In a space environment and the absence of gravity, there are some problems in introducing and retaining a disposable item in the presently available sharps containers. Plastic containers present an off-gassing and flammability problem.

Method

The design of the in-flight sharps container includes small volume, gravity independence, flight-quality materials, and a one-way entrance. The container (Figures 1 through 5) basically consists of a lid and a waste cup, which are machined from aluminum and are alodined gold. Aluminum is a standard flight-approved material and is lightweight. Alodining the aluminum helps prevent corrosion and presents no known toxic hazards due to off-gassing. After use, the unit can be emptied, cleaned, and reused.

The waste cup of the container has a conical taper to a narrower bottom, which allows storage of several

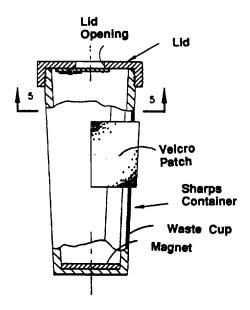


Figure 1. Sharps container.

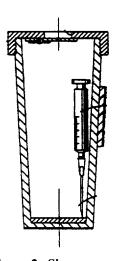


Figure 2. Sharps container.

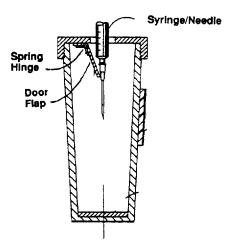


Figure 3. Sharps container.

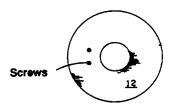


Figure 4. Sharps container.

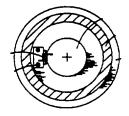


Figure 5. Sharps container.

disposable units. The narrower diameter of the cup prevents the larger needle assemblies from moving or reorienting their direction toward the lid in the absence of gravity. The larger needle assemblies are entered needle first and remain in a needle-first position in the waste cup. A magnet is attached to the bottom of the waste cup to attract the smaller needles away from the opening. A hook and loop fastener (such as a Velcro fastener patch) is placed on the outside of the waste cup so the device can be attached to a wall or workbench. The lid of the container is threaded so it will screw onto the top of the cup. Attached to the underside of the lid is a spring hinge assembly with a flap member, which performs a one-way entry to the container. The flap member of the spring hinge assembly is constructed of 304 stainless steel, which has greater resistance to corrosion and scratching than aluminum. The impact resistant material prevents undue wear when used needles are frequently in contact with the door flap member. The hinge assembly is anchored to the lid by two screws, which causes the spring in the hinge to be placed in tension. The diameter of the door flap member is greater than that of the opening of the lid, and the tension in the spring keeps the flap member firmly pressed against the underside of the lid. Pressure on the door flap member from the outside of the container will force the flap member to swing into the waste cup. Once the pressure is released, the tension of the spring snaps the flap member shut again. Pressure from the interior only pushes the flap member more firmly against the underside of the lid.

Results

The sharps container was successfully used on the STS-40 (Spacelab Life Sciences-1), STS-55 (D-2), and

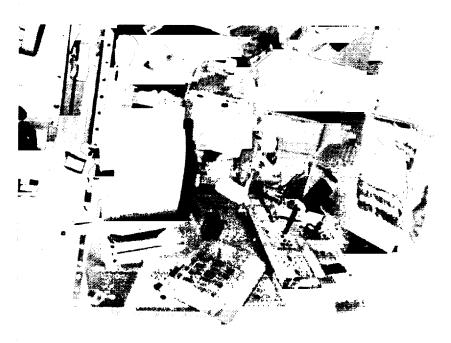


Figure 6. In-flight operational stowage of three sharps containers on the SLS-1 workbench.

STS-58 (Spacelab Life Sciences-2) missions. Figure 6 illustrates the in-flight operational stowage of three sharps containers on the SLS-1 workbench. All three crews commented that the sharps container worked very well in space.

Conclusion

The sharps container is practical, safe, and convenient for disposing of used hypodermic needles in

space. Astronaut crews have successfully used the sharps containers on orbit and found them to be very effective. The device will continue to be used on future missions.

References

Lee, Angelene M., Sharps Container, U. S. Patent No. 5,145,063, dated 9/8/92.

Spacecraft Applications of Thermoelectric Refrigeration

Dan DeMonbrun, Robert Deutschman, and Walter Hanby*
Martin Marietta Services, Inc.
*Johnson Space Center/SE

Abstract

Meeting the science objectives of many space flight programs requires refrigeration of samples and supplies. Specific requirements vary between missions, with the primary variables being temperature, stowage volume, and rate of cooling. The approaches to satisfying these requirements have included many technologies encompassing vapor compression, acoustic, and Stirling cycle refrigeration. Each approach yields specific benefits and performance trades. Thermoelectric systems have seen application in meeting specific requirements since the inception of the space program. Recently this technology has undergone reevaluation with greater systems engineering emphasis. The results have been efficient and economical solutions to the specialized requirements of current and future life sciences experiments.

Introduction

Thermoelectric refrigeration units based on the Peltier effect have been available commercially since the early 60's. The typical device consists of a sandwich with ceramic surfaces separated by a series of doped Bismuth conductors arranged in a series string of alternating dopant material types. When the mechanical arrangement of this series string is such that the P-N junctions are on one face, and the N-P junctions are on the opposite face, heat will flow from one face to the other, controlled by

the polarity and amplitude of the current flow. A Thermoelectric Stack is illustrated in figure 1. Although not as efficient as the more conventional vapor compression refrigeration systems, thermoelectric systems offer several unique advantages. A properly engineered thermoelectric refrigerator is small, lightweight, and free of chlorofluorocarbons and other pressurized gases; requires few moving parts (normally the only moving parts consist of fans associated with the hot and cold side heat exchangers); and exhibits a rugged insensitivity to physical and electrical abuse.

Early in 1993, the Life Sciences Programs Division (LSPD) of the NASA Johnson Space Center committed to develop a prototype refrigeration unit designed specifically to fulfill the needs of life sciences experimenters. This prototype, the Thermoelectric Refrigerator Freezer (TERF), was to be built as a "protoflight" model which would be of a quality and construction that would not preclude the eventual evaluation of the prototype as a class D flight article (figure 2).

Problem Statement

Many life sciences experiments require the use of refrigeration and freezing of materials and samples not only while the experiment is being conducted but also for storage of samples for postflight analysis. In many cases it is necessary to initially cool a sample, perform a

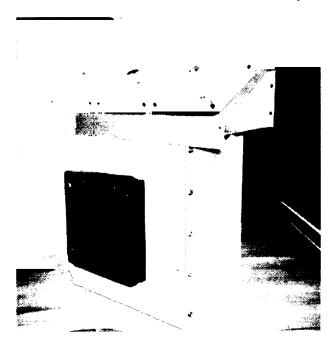


Figure 1. Thermoelectric stack.

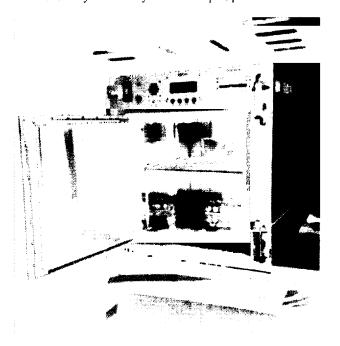


Figure 2. Thermoelectric freezer (TERF).



procedure or process, and then freeze the sample for later evaluation. Experience with similar systems has shown that an internal volume of approximately 0.028 to 0.057 cubic meters is a minimum usable space for experiments normally carried out in the span of one Shuttle flight. In addition, it may be necessary to freeze blood or urine samples of up to 500 milliliters in a maximum of 1 hour. The heat of fusion for conversion of these samples to ice requires in excess of 45 watthours.

For an air-cooled refrigerator to function adequately over the period of time required, provisions must be made for moisture removal and forced convective flow within the cold volume. A desiccant provision must be included in the inlet air path prior to the cold side heat exchanger to perform the task, and a fan and internal baffle are required to ensure that air is circulated to all areas of the cold volume. To provide the necessary experiment and operator functions, a system controller and data acquisition subsystem capable of sensing, recording, controlling, and transferring data is desirable. An interactive control panel was necessary to allow crew monitoring and modification of the system status and function. Data storage requirements exist both locally and through transfer of data via the standard interface rack (SIR) general purpose interface bus (GPIB) data path.

Approach

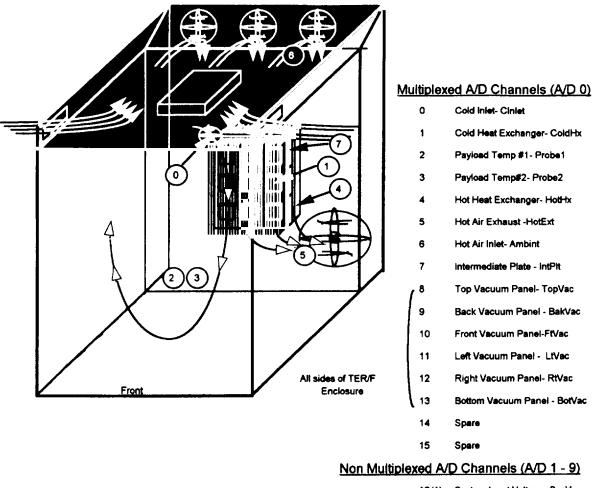
As is true of most engineering decisions, the design of a thermoelectric refrigeration unit is an exercise in compromise. Starting with a basic set of requirements, the parameters are traded to produce an applicationspecific design. In the case of TERF, the physical limitations were constrained by the operating environment and the vehicle. LSPD has undertaken to standardize many payload and data systems configurations by adopting an SIR environment which provides mechanical, power, data, and cooling interface standards for payloads flown aboard Spacelab, Spacehab, and Shuttle Mir. To conform to this standard, the TERF was designed to use the maximum internal volume of an SIR 12-panel unit (12PU) rack enclosure. Power and data accommodations were also configured for compatibility to SIR. Weight was minimized within the limitations of the rack support structure. Power requirements, a maximum of 400 watts, were established to provide the maximum cooling afforded by the power and cooling air available from the rack power system. The thermoelectric heat pump, an inhouse two-stage design, was optimized to accommodate 66 watts of heat at the desired freezer temperature of -22°C. Heat transfer from the hot side of the heat pump was maximized by a heat exchanger incorporating over 1.86 square meters of surface area. Because of the reduced pumping capacity of thermoelectric devices as compared to gas compression/expansion techniques, minimization of heat leak is critical. The TERF addresses this heat leak in two areas and through two design approaches.

Heat enters the cold volume through the walls from ambient. The degree of insulation afforded to the walls significantly affects the overall heat leak. The approach to insulation of the walls incorporates an enclosed vacuum space similar to that of a ThermosTM bottle. Unlike a glass-enclosed vacuum, these panels (AuraTM panels manufactured by Owens Corning) are enclosed by a thin sheet of stainless steel. A core material of fused glass fiber maintains structural integrity by preventing implosion of the cover material. Panels of this construction cover four sides and the door of the TERF.

The door, which allows access to the storage volume, presents a particular problem. The door seal, a common source of leakage, consists of a fitted, air-filled silicone rubber "P" extrusion. A secondary gasket is located outboard of this primary seal to complete the closure and preclude transport of moisture to the cold surfaces of the primary gasket. The mechanical structure of the door incorporates a fiberglass barrier between the metal surfaces of the inner liner and the outer skin.

TERF operation is controlled by user input and software. The software operates on a Little Board[™]/386. The Little BoardTM/386 is a scaled-down version of an IBM-compatible desktop personal computer (PC) with two serial ports, one parallel port, and a small computer system interface (SCSI). The computer is augmented with a MiniModuleTM/488 GPIB board, PCMCIA removable card drive, ITC-232A data acquisition and control and a liquid crystal display (LCD). The GPIB board can be used to downlink data within the SIR, via the standard interface rack controller. The PCMCIA card drive is connected to the central processing unit via the SCSI interface and is used as the boot device for the PC. The PCMCIA memory card contains the MS-DOS operating system and the executable control software for the TERF. The PCMCIA card can also be used to archive data collected during TERF operations. The ITC-232A is an interface board controlled through one of the PC's RS-232 ports. The ITC-232A contains three 8-bit digital input/output (DIO) ports (A, B & C), one 4-bit port (D), a 10-channel analog-to-digital (A/D) converter, and pulse width modulation (PWM) circuitry. The ITC-232A design was modified in-house with multiplexing circuitry on the first channel of the A/D converter, expanding the number of A/D channels to 25. The multiplexing circuit is controlled using four DIO bits on port C. The other DIO ports are used for monitoring the keypad, as well as control of other hardware within the TERF. The PWM is used to control the temperature of thermoelectric devices. The LCD is controlled through the PC's parallel port and is used to display messages and allow the user to control the operation of the TERF.

Upon power up, the PC boots from the PCMCIA card drive and loads the MS-DOS operating system and TERF control software. The TERF software then initializes by loading two configuration files. The TERF uses the configuration files to define its operational parameters. The first file contains the experiment identification, the



- 16(1) System Input Voltage -SysV
- 17(2) Peltier Drive Voltage- PeltV
- 18(3) Peltier Drive Current- PeltC

Figure 3. TERF A/D Channel Assignments.

information for the GPIB interface, telemetry buffer size, and telemetry buffer output rate. The configuration file also contains information regarding the RS-232 port configuration, baud rate, and number of data bits. The second configuration file contains the A/D number of channels, various default set points, and the names of the A/D channels and their calibrations (figure 3). The file also contains the index of TERF control sensors relative to the list of A/D channels and two fields that indicate whether disk archival and GPIB transmission will be performed. Both configuration files are text editable. The configuration files were designed so that the operating parameters of the TERF could be changed at will without changing the executable code.

Once the initialization sequence is complete, the user is presented with various input screens. These screens allow the user to select the refrigerator (REF), freezer (FRZ), or manual (MAN) modes of operation. Screen selections are made by the user pressing one of the four keys located beneath the selections on the LCD. Under REF and FRZ modes, the TERF begins operating using

the default temperature set point for the selected mode. Under MAN mode the user can set the operating temperature of the TERF. The MAN mode screen also allows the user to view the temperatures at various locations of the TERF and set the default temperature sensor on Normal, EX1, or EX2.

In operating mode, the thermoelectric devices and internal fan are turned on and the periodic TERF control processing is enabled. The thermoelectric devices are controlled by using the PWM on the ITC-232A. A 200-Hz square wave signal is generated with a duty cycle ranging from 1 to 99 percent. As the percentage of the duty cycle increases, the voltage supplied to the thermoelectric devices increases, thus making the TERF colder. Once per second, the software reads the temperature from the selected temperature sensor and, if necessary, makes the adjustment to the PWM output. If either GPIB transmission or disk archival is enabled and the time period has expired for the buffer processing, the specified A/D signals and a status word are assembled into a buffer and processed accordingly.

Results

The first example of the TERF is currently approaching completion. The thermoelectric heat pump subassemblies are complete and tested. The control and data systems are complete and tested. The power supplies and displays are complete. The mechanical structure which makes up the cold volume of the unit is complete and currently being installed in the SIR 12PU chassis. It is expected that full functional testing will begin early in 1994. At this time all test results indicate that TERF will meet or exceed the goals established at the onset of the program.

Conclusions

Thermoelectric refrigeration, when combined with state-of-the-art insulation and seal technology, represents a viable alternative to conventional refrigeration methods. Systems level design, which addresses the issue of efficiency while maintaining the many advantages of thermoelectric cooling, enables performance with unsurpassed reliability. Since the inception of the TERF, several additional cooling tasks based on thermoelectrics have emerged. Experience and techniques developed on the prototype have proved valuable in extending the scope and understanding of this technology.

Continuous Blood Pressure Monitor

Vaughan Clift, M.D.,* and Walter Hanby
*Martin Marietta Services, Inc.
Johnson Space Center/SE2

Abstract

A plausible method for measurement of carotid artery blood flow and blood pressure is being developed for the purpose of crew monitoring.

Introduction

Central blood pressure (BP) is a term used to describe the pressure inside the arteries of the body during the heart cycle of filling and emptying. Peripheral pressure is that measured on the small (few millimeters or less) arteries in the distal portion of the limb. The small arteries have muscular walls, and the pressure inside them is directly controlled by the autonomic nervous system and to some extent varies independently of the central BP. For short periods of time under controlled conditions, peripheral BP can give trend information about central BP.

Central BP is that in the vessels from the heart down to but not including the muscular arteries mentioned above. Measurement of central BP can be performed in two basic ways. The most common is noninvasive and involves a pressure cuff which is placed around a limb and inflated above the pressure in the underlying arteries. As the pressure is released, the pressure in the arteries overcomes the constriction and blood begins to flow turbulently into the distal vessel. This blood flow is detected by either the sound (auscultatory) or vibration (oscillometric) methods. At best this method is intermittent with repetitions approximately every minute. However, over prolonged use the cuff is uncomfortable and the system is very sensitive to noise and vibration, so the limb must be kept still. It cannot be used on the neck or chest vessels for obvious reasons. The second and less common method is to place a catheter into the artery and extend the catheter to the point where the measurement is to be made. This method is invasive and can only be safely used under very controlled conditions. There is a great clinical need for the development of a noninvasive system which can measure beat to beat or continuous BP and which, if possible, could be applied to more centrally located vessels.

Exposure to the space environment produces profound changes in human physiology. One area known to be affected is the distribution of body fluid and control of blood pressure.

A combination of factors such as lowered autonomic nervous system response, depleted blood volume, and loss of muscle mass predisposes the crew to potentially dangerous alterations of BP during the critical phase of reentry into the Earth's atmosphere. As the crew reenters, the body is subjected to the force of gravity while in a sitting position. The warmth of the reentry suit and pooling of venous blood decrease the return of blood to the heart and head. The addition of subdued autonomic nervous system response and any vasovagal (syncopal) stimuli could lead to further decrease in cerebral profusion.

Problem Statement

At present there is no way to monitor blood flow to the brain or BP in the carotid arteries, the main cerebrovascular supply, without insertion of potentially dangerous intra-arterial catheters. Present noninvasive blood flow measurement systems, such as Doppler ultrasound probes, are very sensitive to vibration and are effectively useless during reentry or clinically in an ambulatory patient.

Approach

In order to provide a mechanism to monitor carotid artery blood flow and BP in such a difficult environment, new methods had to be sought. A potential system for measuring carotid artery blood flow was designed using a modified form of Doppler ultrasound. A search of the literature did not identify such a system in commercial or research use. A proposal was presented to test the feasibility of such a device as the first phase of the development of a carotid artery BP measurement system.

A second component of the system is based on the principle that if an accurate (and continuous) measurement of blood flow could be made and a known force could be exerted onto the column of blood in the artery, then the change in blood velocity produced by this force would provide a measurement of BP.

A number of possible ways of producing this force were considered, and details of the present method being explored are subject to NASA patent application.

Results

In both components of the concept, production and environment of a force on the column of blood and measurement of flow in the space, there has been significant progress.

Production of Reference Force on the Column of Blood

Calculations showed that by using the selected method a measurable force can be exerted on the column of blood. This is done intermittently and for only a brief period to provide frequent measurements of the change in velocity produced but without grossly upsetting the flow of blood to the carotid sinus, one of the body's BP sensors.

It is difficult to construct an accurate laboratory model on which to test this system because of the complexity of the skin and subcutaneous tissue; therefore, further development will have to wait for clinical tests.

Measurement of Blood Flow in the Space Environment

The measurement of blood flow in the presence of low frequency vibration (0.1–1000 Hz) has proven extremely difficult in all medical and physiology research. This problem also plagues measurement of BP in exercise physiology studies. The system that has been designed is a modified version of the ultrasonic Doppler blood flow method.

It is very difficult to construct an ex vivo model of blood flowing through an artery because of the peculiar rheological properties of blood and tissue. Also, the red cells act as ideal ultrasound reflections, and this is difficult to mimic with particles in suspension. The equipment used is an approved, commercially available, ultrasonic blood measurement device.

The modifications to the equipment do not alter the basic Doppler principle used in making measurements on the radial and carotid arteries of adult volunteers. By providing random or constant movement to the probes along the line of the artery, it was possible to mimic what would happen during exercise or reentry. Up to an amplitude of several millimeters, the modified ultrasound flow sensor was able to provide a clear analog signal of the blood flow which is completely lost to similar but unmodified measurement devices.

This demonstrated that it is feasible to measure blood flow in an artery even in the presence of reasonable vibration in a direction parallel to the flow of blood. This has been the most disruptive form of vibration as it is technically equivalent to synchronous noise.

In the proposed clinical version, three such modified devices will be placed over an artery side by side. The three sets of signals will then be compared and the strongest signal selected. This is proposed for two reasons. First, it allows for some inaccuracy in initial placement of the probe over the artery. The probe can then be adjusted so that the strongest signal comes from the middle of the three sensors. Second, vibration which is at right angles to the artery can now be allowed for (up to a specific amplitude related to the physics of the sensor

heads) because the blood flow is now being measured by a bar-like region rather than a single point.

The experimental version being used at present has only a single sensor, but tests indicate this version can tolerate vibration across the artery of up to 1 mm in amplitude. In addition, experiments to date have shown surprisingly little sensitivity to movement toward and away from the artery up to an amplitude of about 2 mm. This is probably due to the geometry of the system with an increasingly diffused ultrasound beam which is 3–4 mm in diameter approaching the artery at a 45-degree angle. Small movements toward and away from the artery do not greatly alter the position of the column of blood in the beam until the movements become several millimeters or more.

Review of Literature and Industry

A more detailed review of the literature has failed to find any method similar to this. It was not possible to find a research device which could achieve this end. So-called noninvasive blood flow measurement devices fell into three distinct groups:

- New infrared laser diode Doppler devices, which use pulsed infrared light to measure blood flow in the capillary bed.
- Vascular probes, which are magneto hydrodynamic systems clipped around a vessel. Though reasonably sensitive and useful in animal research, they are invasive in that they must be surgically inserted around an exposed vessel.
- Ultrasound devices. Though most commercially available systems use the Doppler principle and are truly noninvasive, one device uses "transit" time and requires a reflector placed behind the far wall of the vessel.

None of these methods were practical for our purposes. Other methods have been described, such as electrical impedance and thermal dilution, but none are reliable or practical.

For the purposes of reentry monitoring, invasive methods were considered inappropriate. These methods, such as thermal dilution, gas diffusion, and optode devices, were reviewed but not studied in detail.

One observation made from the literature review was the great benefit the device being developed here may have to clinical medicine. In the areas of stroke and limb ischemia, quantifying the significance of a blockage to arterial flow is difficult when it is based on the immobile patient. A more relevant marker of intermittent claudication can be made using a blood flow measurement device on a mobile patient. Similarly, carotid artery occlusion may only become significant in the erect, active patient.

Planned Research and Devices Under Construction

A series of practical models for the flow sensor system are under construction. The present research experiment is limited by the fact that the ultrasound crystal transducers are connected directly to electronic circuitry through a bulky plastic housing. The bulk of this device prevents easy fixation to the skin over the carotid or radial artery. In addition, the mass of the sensor head contributes phase delay and secondary oscillations to the test bed. In order to overcome this, and approximating the planned sensor device, a modified sensor head is being constructed using the present transducers and electronics by the Imex Corporation. The new sensors will have a low mass, small volume ultrasound probe about the size of a pen top attached by 2-3 inches of cable to the electronic component. This will enable more clinically relevant research.

Planned studies include using the device to measure blood flow in the radial artery during exercise on the ergometer cycle and carotid artery flow during KC 135 and T38 flights. The development of a sensitive reliable blood flow measurement is critical to subsequent tests of the BP measurement method. In addition, the blood flow measurement device is of great clinical and research use on its own.

Three phases of the research are scheduled.

<u>Phase I.</u> Development of radial artery and carotid artery blood flow sensors capable of functioning in 0.1–1000 Mz vibration up to 2 mm in amplitude in any direction. This will require the construction of the low mass sensor head and subsequently the three head array sensor head system. Both of these will provide valuable information and contribute to the final design.

<u>Phase II.</u> Construction of the definitive flow sensor and testing of the force production method for blood

pressure measurement. The method requires the construction of a control circuit which has not been commenced. The appropriate design for the control circuit, frequency, duty cycle, etc. will need to be determined by direct experimentation.

<u>Phase III.</u> This is not anticipated until the third year and consists of the construction of clinical research devices based on the previous research prior to clinical trials (FDA phase I trials).

Conclusion

The research to date has identified a strong need for both a method to measure blood flow in a space environment where vibration is present and a device to measure carotid artery BP. It has also identified that no device exists which is adequate for these purposes.

Initial results using off-the-shelf systems have demonstrated the feasibility of the modified Doppler design to measure blood flow in the presence of reasonable vibration as may be encountered during reentry and exercise. Also, an experimental model has shown unusual levels of force produced on a column of similar fluid using the selected principle. With development of "purpose-built" research hardware, this concept should continue to show promising results and lead to development of a practical and useful device for NASA research and clinical medicine.

References

The list of articles reviewed was obtained through Medline and are publicly available. Details of the literature search and review are subject to a NASA patent application and are not, therefore, included.

Design Considerations in the Development of the Life Sciences Spacelab Refrigerator/Freezer or Why Spaceflight Refrigerators Are Different From Your Domestic Refrigerator

David R. White Johnson Space Center/SE3

Abstract

After studies of a number of different refrigeration systems, including thermoelectrics, for use in storing medical specimens on Spacelab, the decision was made to pursue the development of a vapor compression type (Carnot cycle thermodynamic model) similar in principle to the type used in the commercial industry. This decision was based on, one, a system that would meet the scientific requirements for cooling biomedical specimens and, two, availability of inflight resources (power, etc.). However, use of the vapor compression type of refrigeration system imposed constraints associated with safety and reliability, such as the application of a twophase fluid system in the microgravity environment of space and the use of a toxic fluid (Freon). A Spacelab refrigerator/freezer was developed and delivered that met the requirements and satisfied the constraints. The Spacelab units have successfully supported the first and second dedicated Spacelab Life Sciences missions (SLS-1 and SLS-2), the first International Microgravity Laboratory mission (IML-1), and the Japanese Spacelab mission (SL-J); in addition, a unit has been delivered in support of the second International Microgravity Laboratory mission (IML-2), which will be flown in 1994.

Introduction

In the early 1980s, the Life Sciences Project Division (LSPD) at JSC initiated development of a refrigerator that would store and preserve biomedical specimens taken during life sciences experiments conducted on Shuttle space flights. Because neither the Shuttle nor the European Space Agency (ESA)-provided Spacelab module had provisions for refrigeration of biomedical specimens, a standalone refrigerator to be installed as needed was required. The basic requirement for refrigeration of biomedical specimens in space is the same as that for the ground-based domestic refrigerators and freezers utilized by investigators in the storage and preservation of specimens. Typical refrigeration setting is 4°C with freezer settings ranging from -70°C to -20°C. For this development (as explained below), the upper freezer range selected was -22°C. Cooling capacity specification was based on, first, a target 1°C/min cooling rate for a 500 ml body temperature specimen; second, reasonable cooldown, starting at ambient temperature (30 min to 4°C and 1 hr to -22°C); and third, reserve capacity to handle

frequent additions of specimens to the cool volume without raising the temperature of samples already in storage. Cooling capacity specification was established at 400 BTU/hr at 4°C and 1000 BTU/hr (later reduced to 700 BTU/hr) at -22°C. The temperature range (minimum) setting for the 0.071 cubic meters of internal storage volume was established as 10°C (refrigerator) to -22°C (freezer).

The initial efforts at developing a standalone refrigeration system were directed toward the use of thermoelectric (Peltier effect) cooling. A concern was use of a thermoelectric unit to support the relatively high temperature lift, as a freezer would require cascaded thermoelectric devices, thereby reducing reliability and requiring excessive power consumption. A request for proposal based on the above specifications was released in July 1981 through the LSPD support contractor, the General Electric Management & Technical Services Company (MATSCO). Two proposals, both based on the use of thermoelectric devices, were received in September 1981. In an attempt to meet flight cooling requirements, the most favorable of the proposals required the use of a large thermal capacitor, a large battery, and a liquid coolant loop operating at a maximum of 20°C. The proposed units were expensive, marginal in cooling capacity, and higher in power consumption, and thus were considered unacceptable for meeting the life sciences refrigeration requirements. The thermoelectric effort was put on hold, and a detailed test objective (DTO) was initiated to prove that a modified commercial off-the-shelf vapor compression refrigeration system utilized in the boating industry could successfully operate in the microgravity environment of space.

Statement of Task

A vapor compression refrigerator has a coefficient of performance (ratio of input power to cooling power output of a refrigeration system) that is typically 10 times that of a thermoelectric refrigerator. However, performance of a two-phase Freon refrigeration system in microgravity was in question, and safety concerns associated with the use of Freon had to be addressed. To prove this concept, a small single-head vapor compressor refrigerator, designed and built by Mvis Corporation in Italy, was modified by General Electric in Houston and successfully demonstrated the ability of this design to perform in microgravity as DTO No. 467 on the Shuttle STS-4 flight in June 1982. A task order was issued to

MATSCO in August 1982 for the delivery of a certification unit and five Spacelab flight units to meet the specified refrigeration requirements.

Approach

Design objectives in the selection of a vapor compressor refrigeration system included the following.

- A compressor design that could tolerate or avoid liquid "sługging" in the microgravity environment of space.
 The migration of liquid refrigerant through a vapor phase compressor during operation could lock up and/ or damage the compressor.
- 2. No oil in the refrigerant. Most domestic vapor compression refrigeration systems have an oil mixed with the refrigerant to provide lubrication to the compressor during operation. In microgravity, this oil forms a film on all interior surfaces of the condenser and evaporator, thus reducing cooling capacity.
- Evaporator and condenser systems that would provide effective boiling and condensation in the absence of gravity.
- 4. Protection of the flight crew from exposure to dangerous toxic levels of Freon.
- 5. Insensitivity to orientation to ensure proper operation during launch and in microgravity.

The Spacelab refrigerator/freezers (Figure 1) have met these objectives and have satisfied performance requirements, but not without constraints to the operational use of the units.

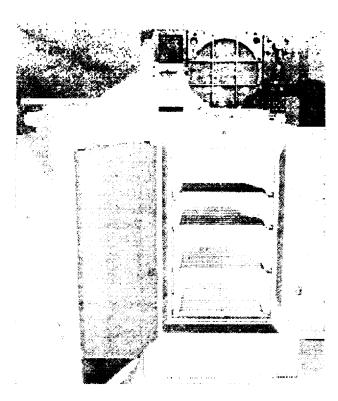


Figure 1. Spacelab refrigerator/freezer.

The selection of a diaphragm-driven compressor satisfied the first two design objectives. The elastomer diaphragms (Neoprene W), driven by a free piston, could tolerate occasional passage of liquid through the compressor. Pumping action of the diaphragms was accomplished by the action of the free piston (driven by an eccentric crankshaft with sealed bearings) pushing the diaphragm externally, and the Freon pressure on the inlet (suction) side of the compressor keeping the diaphragm in contact with the piston during its travel. This design feature emphasizes the importance of Freon suction pressure on compressor performance.

With this free piston design, and the use of Freon 12 for the single stage DTO vapor compression refrigerator, the lowest operating temperature was -17°C, and the cooling capacity was less than half of that required for the larger Spacelab units. Several iterations in compressor design to meet temperature and cooling capacity requirements resulted in a two-stage, four-headed compressor (duplicated copies of the single-head unit) that used Freon 502 as the refrigerant. The shaft of each of the four free-floating pistons rests on an independent cam bearing whose outer races do not move with respect to their respective piston ends. This unique camshaft arrangement solved previous mechanical failure problems at the interface between the pistons and their cam bearing interfaces.

The replacement of Freon 12 by Freon 502 provided a cooling capacity improvement of 76% and improved inlet compressor pressure levels to exceed the requirement for the -22°C operating temperature range. The toxic issue associated with the use of Freon provided one of the most challenging aspects of this design.

Because of the toxic nature of Freon, the amount of Freon allowed in the refrigerator/freezers could not exceed the maximum spacecraft allowable concentration levels. For Freon 12 and 502 the level is 100 ppm and calculates to 36 g of Freon for a refrigerator/freezer used in Spacelab. To exceed this value would create the potential for a catastrophic hazard, necessitating a twofailure-tolerant design (i.e., one wherein three failures are required to expose the crew to unsafe conditions). In the case of the vapor compression refrigerator/freezers, this requirement would impose triple containment of all refrigerant components. Considering that heat transfer is a vital process in refrigeration systems, imposition of this requirement would have made the development of these units impractical. The DTO vapor compression refrigerator held 36 g of Freon, which was contained only by the refrigerant components (single containment). The Spacelab refrigerator/freezer also used a maximum of 36 g. However, since two refrigerator/freezers (one operating at 4°C and the other at -22°C) were to be flown in Spacelab on SLS-1, double containment was imposed on this design. While not as severe a constraint as triple containment, the design caused problems in maintainability of the units and providing adequate heat removal from the compressor, condenser, and evaporator.

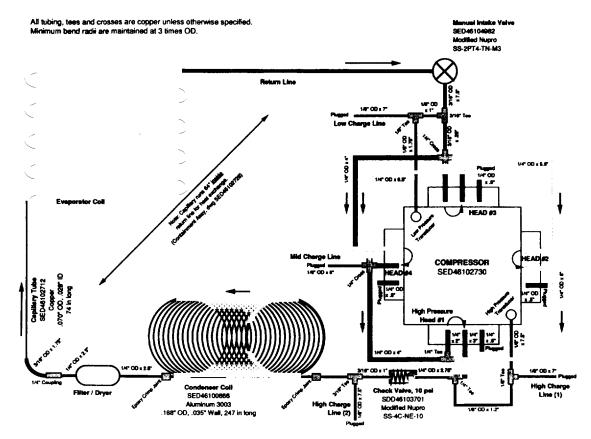


Figure 2. Spacelab refrigerator/freezer freon flow diagram.

Meeting the constraint of 36 g of Freon, approximately one-sixth of the amount used in domestic refrigerators, required very careful selection of refrigerant components (see Figure 2 for diagram of the components). Because of this, a capillary tube rather than an expansion valve was selected as the Freon expansion device. (Since the Spacelab refrigerator/freezer had to function as either a refrigerator at 4°C or a freezer -22°C, an expansion valve would have been the logical choice). The use of the capillary tube simplified the design and reduced the amount of Freon required. Selection of the capillary tube, in conjunction with the relatively small amount of Freon, imposed stringent requirements in assembly of the units. Variation in capillary internal diameter of more than 0.025 mm or a Freon charge variation greater than 0.5 g could greatly affect cooling performance.

After assembly, loss of Freon over time due to very small leaks or permeation though the Neoprene W diaphragms would cause loss in cooling performance. This is particularly important for the Spacelab refrigerator/freezer as it is delivered approximately 1 year prior to launch to allow for integration into the Spacelab rack. Detection and correction of very small leaks and the reduction of loss of Freon through diaphragm permeation became critical design and operational goals. These goals were accomplished in the following ways: leak detection tests during fabrication and assembly of subsystems; after assembly, extended monitoring of the secondary

containment for any rise in pressure levels; and incorporation of a system which isolated the Freon from the diaphragms during inactive periods for the refrigerator.

In domestic refrigerators, removal of heat from the refrigerator during cooling is accomplished primarily through natural convection of the heated air. In microgravity there is no natural air convection, and heat removal must be accomplished through conduction (use of a coolant loop), forced air convection, or a combination of both. The original concept for heat removal from the Spacelab refrigerator/freezers was through the use of the Spacelab avionics air or a water coolant loop. Limited resources for the SLS-1 mission eliminated these options. Instead, internal fans were incorporated into the units for circulating cabin air across the refrigerator/freezer condenser and electronics. Incorporation of these fans generated other design issues associated with cabin debris and an increase in acoustic noise. These were addressed and subsequently resolved.

Results

The Spacelab refrigerator/freezers have been successful on all missions (SLS-1, IML-1, SL-J, SLS-2) they have supported. One unit has been delivered in support of the upcoming IML-2 mission, scheduled for late 1994.

This paper has primarily addressed the design associated with the refrigeration system itself, with the emphasis on considerations for using vapor compression refrigeration in the microgravity environment. There were many other difficult issues that had to be resolved.

Conclusions

The limited life nature of the Neoprene W diaphragms necessititates refurbishment of each refrigerator after each mission. Refurbishment of these units is difficult and is complicated by the double containment and critical nature of the design. It is vital that the Freon loop be maintained at a high cleanliness level and free of any moisture. Frequent tear-downs and reassembly in the refurbishment process jeopardize these protocols. This fact, along with the requirement that future programs such as the joint United States/Russia space activities and the Space Station program will require a refrigeration system which can operate continually for years, has prompted the Life Sciences program to relook at state-of-the-art technology. This includes thermoacoustic refrigeration, thermoelectric refrigeration, a linear compressor as a replacement for the diaphragm compressor, and Stirling cycle refrigeration. The experience and lessons learned in the successful

development of the Spacelab vapor compression refrigerator/freezer will go a long way in ensuring the success of whichever refrigeration technology is selected for these future programs.

Acknowledgments

Numerous people from NASA, General Electric, CALSPAN Corporation, and Martin Marietta Services contributed to resolution of these problems and the successful development of this Refrigerator/Freezer.

References

Additional information may be found in the following documents.

- 1. Mosinskis, G. J.; "Advanced Refrigeration System," AiResearch Manufacturing Company, report no. 76-12715; NASA CR-161974, May 1976.
- Cox, J. E., et al., "Characterization of Heat Transfer in Nutrient Materials," University of Houston, NASA CR-134383.
- 3. Hye, A., "The Design and Development of a Vapor Compression Refrigerator/ Freezer for Spacelab, "SAE technical paper 831091, 1983.

2-51

Gas Analyzer Systems To Support Life Sciences Experiments

Floyd Booker, Jeff Bahr,* Charlie Davis*, and Steve Mai*
*Martin Marietta Services, Inc.
Johnson Space Center/SE

Abstract

This paper describes the first and second generation gas analyzer mass spectrometer developed to support space flight experiments investigating cardiovascular/cardiopulmonary (CV/CP) function in the microgravity environment of space. Included is a brief developmental history, a description of the experiment hardware, and a brief summary of the equipment's performance on space missions.

Introduction

Medical researchers have long suspected that the absence of gravity would affect the function of the human CV/CP systems. In an attempt to determine these effects, medical researchers proposed the use of a noninvasive method to first evaluate the changes in the CV/CP systems using respiratory gas mixtures for the test subject to breathe, and then to analyze the inhaled and exhaled gases to determine their interaction in the blood flow to the heart and lungs. Measurements are made on the test subjects preflight, during flight, and postflight to compile an adequate database and to ensure that changes are actually a result of microgravity during flight. Results are subsequently evaluated to determine how microgravity affects the performance of these human systems. To provide researchers with the necessary tools to measure gas species, NASA Johnson Space Center (JSC) initiated a development effort for a flight gas analyzer mass spectrometer (GAMS) to support a variety of spaceflight experiments.

In 1978, NASA initiated an Announcement of Opportunity for medical research experiments to be flown on dedicated Life Sciences Spacelab missions. One cardiopulmonary and two cardiovascular experiments were chosen for the Spacelab Life Sciences-1 (SLS-1) and SLS-2 missions. JSC initiated a development program in 1979 for a flight-qualified GAMS to support these experiments. The GAMS was designed and built by Perkin-Elmer Corp. in Pomona, California. The GAMS development technology was based upon a four-channel analyzer developed and flown on Skylab. Two GAMS units were flown on STS-40 (SLS-1) and STS-58 (SLS-2) in 1991 and 1993, respectively. Changes in the breathing gas requirements for future missions coupled with the age of the original GAMS required a new gas analyzer development effort in 1993 for a replacement unit that could provide more flexibility for life sciences investigations. The second generation gas analyzer, the gas

analyzer system for metabolic physiology (GASMAP), is currently being developed by Marquette Electronics, Inc., in Milwaukee under a Martin Marietta contract for NASA JSC.

Description

Gas Analyzer Mass Spectrometer

Two flight units and one qualification unit, built by Perkin-Elmer, were delivered to JSC in 1982-83. The GAMS is a magnetic sector device with the capability of measuring the partial pressures of 10 gas species simultaneously and providing corresponding analog signals to the experiment hardware for processing and downlink. The gas species selected were nitrogen, oxygen, carbon dioxide, helium, argon, acetylene, water vapor, nitrous oxide, isotope of carbon monoxide, and a wide channel for total hydrocarbons (50-100 atomic mass, unified mass units [AMU]). Response time of the instrument had to be sufficient to accommodate breath-by-breath analysis during heavy exercise conditions. Housekeeping parameters were also generated in analog and digital format for processing by the experiment hardware. The GAMS unit mounts in a 48.26-cm Spacelab rack and is approximately 0.085 cubic meters in volume and weighs approximately 40.82 kg. Figure 1 depicts the GAMS front panel indicating functional switch locations and output display light emitting diode (LED). An ion pump was used to maintain a vacuum pressure of approximately 10⁻⁶ Torr in the analyzer to permit ionization of the gas sample and collection of ion species for analog signal generation. The instrument is also plumbed to the Spacelab vacuum port for on-orbit analyzer and inlet roughout should these tasks be required. The GAMS gas sample inlet connects to the experiment breathing apparatus through a 2-m-long capillary tube to provide breath-by-breath partial pressures of inhaled and exhaled gases.

Gas Analyzer System for Metabolic Analysis Physiology

The GASMAP is a commercial miniature quadrupole mass spectrometer system designed and modified by Marquette Electronics to meet NASA and Mir spaceflight requirements. The system consists of an analyzer module residing in an 8-panel unit (8PU) x 60.96-cm-long standard interface rack (SIR) drawer and a calibration module residing in a 4PU x 60.96-cm-long SIR drawer. Figure 2 depicts the proposed GASMAP front panel

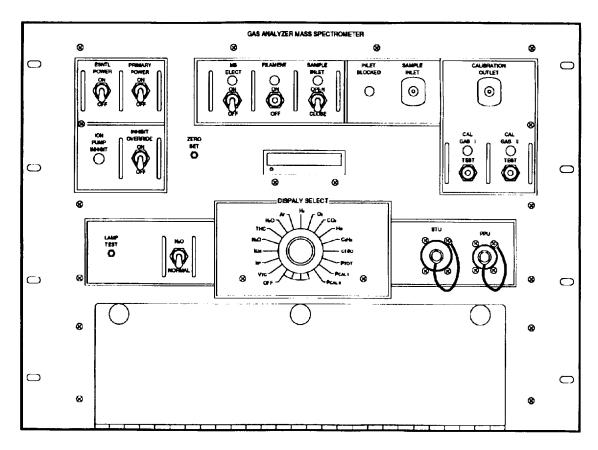


Figure 1. GAMS front panel.

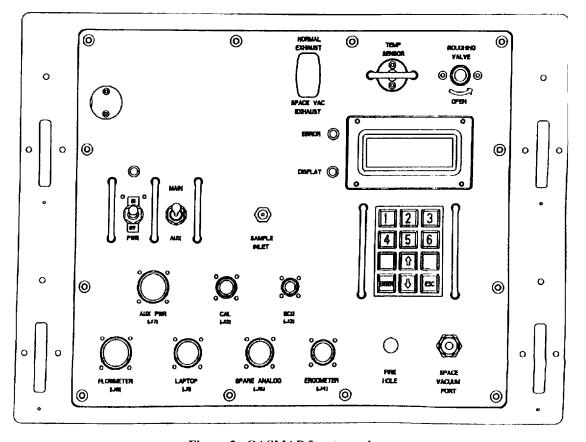


Figure 2. GASMAP front panel.

indicating functional switch locations and output liquid crystal display (LCD). The GASMAP is being designed to fulfill the following three modes of operation:

- 1. Generic Gas Analyzer—The GASMAP produces analog signals proportional to gas concentration for use with other experiment hardware. Gas concentrations can be displayed at the 8PU front panel LCD. Basic maintenance and diagnostics can be performed on the mass spectrometer from the front panel controls.
- 2. Mir Gas Analyzer—A laptop computer can be connected to an RS-232 port at the 8PU front panel of the GASMAP to provide a more complete user display and interface. In this mode, a complete metabolic stress test can be performed, and processed breath-by-breath data are stored to disk on the laptop computer.
- 3. NASA Metabolic Analyzer—The GASMAP can be mounted in the SIR. In this mode, a complete metabolic test can be performed. The GASMAP transfers all raw signals as well as processed breath-bybreath data to the SIR controller via the SIR IEEE-488 bus. A laptop computer is optional.

The analyzer module has a piezoelectric controlled inlet valve, an efficient ionizer, a quadrupole mass filter, a solid-state electrometer, and an ion pump. The inlet valve maintains constant ionization pressure regardless of pressure changes outside the mass spectrometer. When the valve is closed and/or the power is removed from the system, the valve seals well enough to maintain vacuum for 30 days or more. The inlet system uses a catheter for gas transfer rather than a fixed-length capillary. The ionizer is a unique in-line design that provides excellent sensitivity and stability in gas measurement. The GASMAP employs a quadrupole mass filter as opposed to a magnetic sector device. The filter is controlled by a unique RF/DC drive system which allows it to detect any gas over a mass range of 1 to 250 AMU, with 1 AMU resolution at 100% transmission. The gas peaks, observed during a sweep of the spectrum, have flat tops which indicate the 100% transmission and provide the excellent stability of the instrument. The quadrupole concept uses a single solid-state electrometer which can detect gas concentration down to 100 parts per million with a response time of less than 100 ms. Thus a gas can be tuned and measured in 1 ms. This speed is necessary for reproducing respiratory waveforms. The 20 liter/second ion pump maintains vacuum in the system, and its power supply delivers up to 200 mA in a pulsed mode for initial pumpdown during roughing. Power can be removed from the system for extended periods of time (months), and vacuum can be restored by the ion pump. No roughing pump is attached to the instrument. However, a quick disconnect is available at the front panel to provide interface to space vacuum or roughing pump should roughing be required. Analog and digital data are available through the two rear data connectors. Input power can be applied to the instrument from the rear

power connector or from the front panel auxiliary power connector. A 4-line x 20-character LCD also exists on the front panel to provide visual feedback to operate the GASMAP as a generic gas analyzer when a laptop computer is not connected to the system. A 4 x 3 keypad mounted on the front panel allows the user to make menu selections. Both the LCD and the keypad are controlled by the interface shell computer which resides in the 8PU drawer and is the heart of the GASMAP. Changes to the gas list monitored or sample flow rate can be modified through software rather than hardware. The gas analyzer module weighs approximately 55.34 kg and occupies 0.117 cubic meters in volume (48.26 cm wide x 76 cm deep x 35.48 cm high).

The calibration module is a passive 4PU drawer which contains three calibration gas tanks, analog pressure gauges, regulators, and the necessary plumbing to allow the interface shell computer to control which gas is to be sampled during the calibration process. The tanks are filled to 5515.81 kilos Pascal (kPa), and the regulators reduce this pressure to 206.84 kPa. The output of each regulator is connected with tubing to a solenoid which opens to a common manifold. The outputs of the manifold are connected to a single output on the front panel of the drawer. The solenoid drivers reside in the 8PU drawer and connect to the solenoids through a connector at the front panel. When the gas calibration procedure is initiated from the GASMAP 8PU front panel keypad or from the laptop computer, the user will be provided with step-by-step instructions, via the 8PU drawer LCD or the laptop computer display, on how to perform the calibration. Refill ports are accessible at the back of the drawer. The calibration module is being designed with adequate mechanical restraint and relief valves to be two-failure tolerant. The calibration module weighs approximately 20.412 kg and occupies 0.058 cubic meters in volume (48.26 cm wide x 76 cm deep x 17.7 cm high).

The GASMAP can also accept heart rate (TTL or analog signal proportional to heart rate) and analog ergometer input signals, via the 8PU front panel connections, for metabolic stress test analysis. The GASMAP is capable of providing the following outputs for downlink: 10 analog gas signals, 0 to 10 volts; 8 TTL status signals, 0 to 5 volts; and 6 single-ended differential analog signals, -0.5 to +0.5 volts. The system also has a serial RS-232 port and a parallel IEEE-488 bus to provide additional data transfer/downlink. The new GASMAP consumes 135 W of power and provides researchers with many additional capabilities for spaceflight experimentation.

Approach

Because of the criticality of the GAMS in support of three CV/CP human experiments, two GAMS units were flown on SLS-1 and SLS-2 to provide backup capability should one unit fail. The two units were selectable through the CV/CP interface panel with outputs routed to each experiment system for processing. Experiment requirements began changing after SLS-1, and modifications were required on the GAMS to measure sulfuric hexafluoride (SF6), which is a heavy tracer gas and beyond the AMU range of the original GAMS design. The total hydrocarbons channel was used to measure fractions of the SF6 gas. The new GASMAP unit will be rack-mounted in an SIR to support CV/CP studies being planned for future Spacelab, Mir, and Space Station missions.

Results

Two GAMS units were flown on both SLS-1 and SLS-2 to support the CV/CP experiments. The data were collected on four to seven crew members four times each mission. Hardware problems occurred during each mission with the flight GAMS. However, since a backup unit was available, no data runs were impacted. Although researchers are still evaluating the science data, they have

concluded that the data collected by the flight GAMS unit are good and will provide an insight into the experiment studies. Experiments similar to those flown on Spacelab are being proposed for the Space Station and the joint U.S.-Russian program. The new, more flexible GASMAP will support the future experiments to determine how long-term spaceflight affects the CV/CP systems.

Conclusions

The GAMS unit provided excellent data to the CV/CP researchers on the SLS-1 and SLS-2 missions. However, the frequency of changes in experiment requirements led to the conclusion that future Life Sciences laboratory equipment must be extremely versatile and flexible to minimize costs and scheduling for upgrading reflown hardware. GASMAP should be capable of providing flexibility for Spacelab, Space Station, and other medical research missions in the future.

2-55

A Passive and Rapid Intravenous Infusion for Use in Spaceflight Experiments

Charles Buntin, Ashok Desai,* Dean Mento,* Kevin Lee,*
Chad Airhart,* James Zografos,* and Omkar Dalal*
Johnson Space Center/SE
*Martin Marietta Services, Inc.

Abstract

The Infusion Cuff Assembly (ICA) was developed by the NASA Life Sciences Project Division and the Biomedical Dynamics Corporation for use aboard the joint Germany and United States Spacelab Shuttle mission known as Die Deutsche Spacelab mission or simply as D-2. The primary requirements for the infusion system were that it should have the capability to deliver a volume of 20 ml of saline per kilogram of body mass over 20 minutes into a large vein in the arm of an astronaut subject. Pressure and flow data were collected for air bladder pressures ranging from 30 to 80 mm Hg when using an 18-gauge catheter and from 30 to 180 mm Hg using a 20-gauge catheter. Due to the wide range of saline volumes required for infusion, both 1- and 2-liter bags were used in the evaluation of the system. The results indicate that the pressure-flow profiles are linear. The flow-time profiles indicate that the ICA maintains a constant flow until "bag empty" using both 1- and 2-liter saline bags.

Problem Statement

In response to NASA Research Announcement of Opportunity, AO-84, a study known as Cardiovascular Regulation at Zero Gravity was proposed and subsequently selected to be flown on Spacelab mission D-2 in April 1993. The study was conceived by Dr. C. Gunnar Blomqvist, et al., of the University of Texas Southwest Medical Center in Dallas. The purpose of the study was to examine in detail the hemodynamic, regulatory, and structural characteristics of cardiovascular responses to microgravity. The major goals of the study included defining the cardiovascular responses to acute changes in the distribution of intravascular volume and cardiac preload before, during, and after spaceflight. The principal in-flight objective was to define cardiovascular responses to intravenous volume loading with isotonic saline. To facilitate the study, NASA Johnson Space Center personnel developed several hardware items that included a passive, rapid infusion device known as the ICA. The ICA was developed by NASA and the Biomedical Dynamics Corporation. Scientific requirements established for the infusion device included the ability to infuse a volume of 20 ml of saline/kilogram body mass over a period of 20 minutes into a large vein in the arm of an astronaut subject. The system had to be compatible for use by any member of the United States Astronaut Corps.

Design parameters for the Corps include individuals from the fifth percentile Asian female to the ninety-fifth percentile Caucasian male of the general population. This corresponds to 46.4- to 95.6-kg body mass.1 Hence, for use in infusing the full range of the astronaut population, the system had to be capable of delivering flows from 46 to 95 ml/min with an accuracy of ±5 ml. This requirement implied that the flows had to be adjustable. To ensure the system delivered an accurate volume of fluid into a subject, the system had to be capable of maintaining a constant flow to complete emptying of the bag. With this assurance, a specified flow could be established and terminated at the appropriate time to deliver the volume of saline required. To accommodate this wide range of fluid volumes, the infusion system had to be capable of utilizing commercially available 1- or 2-liter saline bags. Additional requirements levied on the design of the system were that it be passive (requiring no power for operation) and that it be of minimal weight and volume.

Description

Figure 1 depicts the construction of the ICA. Internally the ICA consists of two air bladders, which are heat bonded together along the length of the air bladders. The bladders themselves are made of nylon/urethane laminate material which is joined together using heat bonded seams. The two bladders are contained within a polyester outer netting, which prevents bulging of the air bladders, thereby maximizing the pressure applied to the

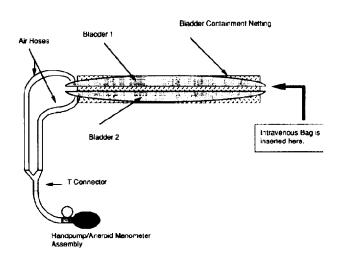


Figure 1. Construction of the ICA.

saline bag. The bladders receive air via a plastisol Y-tube enabling both bladders to be inflated simultaneously by a single source. A 30-cm-long polyvinylchloride (PVC) tube is attached to the Y-tube and enables the bladders to be connected to an external air source. The unattached side of the PVC tube is fitted with a Luer-Lok connector. A calibrated Tycos hand pump/manometer is used to inflate the bladders and is attached to the external PVC hose. The cuff is deflated by opening the inflate/bleed knob on the hand pump and manually squeezing the pressure bulb. A specified pressure is maintained by observing the manometer. For remote infusions, a 61-cmlong Viton tube can be attached between the PVC tube and the hand pump. A cylindrical Nomex cover with zipper closures at the opposite ends encloses the air bladders. This cover provides flammability protection as required by NASA for space-qualified hardware and also provides a measure of fluid leakage protection. The zipper closures facilitate simple insertion and extraction of a 1- or 2-liter saline bag. The saline bag is inserted through the front opening of the ICA and positioned by inserting one's hand through the rear ICA opening. The saline bag is prefitted with an intravenous (IV) tube before insertion. The front-end side of the ICA has two zippers, which serve as a pass-through for the IV tube as well as securing the IV tube spike, preventing it from being inadvertently pulled out of the saline bag. The extraction of the saline bag is accomplished by unzipping the front of the ICA and pulling the saline bag out. Four square hook velcro patches are equally spaced along the long bottom Nomex panel to aid in attaching the ICA to a crew member's clothing or some fixed object in Spacelab. A belt is also provided for securing the cuff on the crew member's upper thigh during infusion. The belt is adjustable for comfort by way of two D-rings located on the side of the cuff. Figure 2 illustrates how the crew member dons the ICA in flight.

Methods

The evaluation of the ICA was performed using a 1-and 2-liter PVC bag (Baxter, Inc.) filled with distilled water and an 18- and 20-gauge catheter (Becton Dickinson Vascular Access) for each volume. The preliminary NASA protocol called for the smaller individuals to use the 20-gauge catheter and a 1-liter bag while the larger individuals used the 18- or 20-gauge catheter and a 2-liter bag. Before conducting the evaluation, the dry and wet weight of each PVC bag was determined using a calibrated digital balance (Mettler model PM 30), which is accurate to 1 gm. Distilled water was used, which has a density of 1 gm/cm³. The mass was converted to volume by the conversion factor 1 gm = 1 cm³. The 1- and 2-liter PVC bags were filled with 1000 ± 1.0 and 2000 ± 1.0 gm of distilled water, respectively.

The test setup is illustrated in figure 3. A PVC bag was inserted into the infusion device, and a specially constructed IV tube having no drip chamber was attached



Figure 2. Donning the ICA in flight.

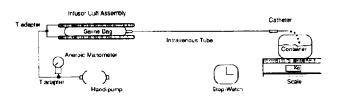


Figure 3. ICA test setup.

to the filled PVC bag. Flow through the IV tube was controlled by a roller clamp on the tube. The test setup was placed on a level work surface that was perpendicular to the force of gravity and then secured. The digital balance and an effluent container were positioned to receive the fluid expelled from the catheter during the test. The balance was zeroed with the container in place so the container's weight would not be considered.

Pressurization of the system was attained using a hand pump (Tycos, Inc.) with a calibrated pressure gauge accurate to 1 mm Hg. A 3-foot length of Viton tubing was used to provide air flow from the hand pump to the infusion system under test. A small, positive pressure (less than 20 mm Hg) was applied to the infusion system under test, and the roller clamp was opened to purge residual air from the PVC bag and tubing. The roller clamp was closed when all the air bubbles were eliminated. The mass of the water ejected during purging was recorded, and the air bladder(s) were then pressurized

as required using the hand pump. The time of fluid flow was determined using a quartz crystal stopwatch (Hamilton, Inc.), which was accurate to the second. Data recording began with the opening of the roller clamp on the IV tube.

A pressure-flow profile was constructed for the ICA to illustrate the linearity of the system. The initial and final pressures selected for constructing the profile corresponded with the calculated flows necessary to infuse the fifth percentile female and the ninety-fifth percentile male. For consistency with NASA protocols,² a 20-gauge catheter was used in conjunction with both the 1-and 2-liter PVC bags while the 18-gauge catheter was used only with the 2-liter PVC bag. The flow was plotted for pressures ranging from 30 to 80 mm Hg for the 18-gauge catheter. Another plot was made in similar fashion using the 20-gauge catheter. In this case the pressure range was extended and varied from 30 to 180 mm Hg. The procedure was repeated three times, and the points were plotted for each run. For all runs, pressure was incremented 10 mm Hg. Flow was calculated from volume measurements determined over time.

Another series of tests was conducted to determine ability of the ICA to sustain a predetermined flow for 20 minutes for both catheter sizes. The system was evaluated using both 1- and 2-liter bags. The 1-liter bag was used in conjunction with a 20-gauge catheter, while the 2-liter bag was used in conjunction with both 18- and 20-gauge catheters. The infusion systems were pressurized to 80 and 50 mm Hg corresponding to the use of the 18- and 20-gauge catheters, respectively. These pressures were arbitrarily selected on the basis of achieving an adequate flow necessary to infuse a 70-kg individual. Mass measurements were recorded at 1-minute intervals over a 20-minute period. Flow was later calculated from volume measurements determined over time.

Results

A representative graph of the pressure-flow profile using a 2-liter saline bag and an 18-gauge catheter can be seen in figure 4. The pressure-flow profiles (not shown)

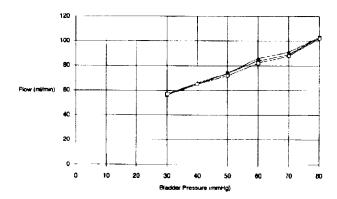


Figure 4. Pressure-flow profile using a 2-liter saline bag and an 18-gauge catheter.

using a 2-liter PVC bag and 20- and 18-gauge catheters illustrate similar results. The graph illustrates that the pressure-flow profiles are linear for the ICA with a correlation coefficient near 1.0.

Figure 5 illustrates the ability of the ICA to maintain a constant flow until the bag has emptied for a 2-liter saline bag and an 18-gauge catheter. The flow-time profiles used a 2-liter saline bag and an 18-gauge catheter and a 1-liter PVC bag and a 20-gauge catheter. It is seen from the curve that the ICA maintains constant flow until the bag has emptied (flow dropped to zero immediately following the 20-minute mark).

Discussion

The flow-time profiles demonstrate that flow remains constant to the point of emptying the saline bag. This is an important characteristic, demonstrating that the volume of fluid delivered can be accurately predicted regardless of the volume of the fluid remaining in the bag during an infusion. The pressure-flow profiles for both the 18- and 20-gauge catheters indicate that the relationship between pressure and flow is linear throughout the entire range of pressures necessary to the United States Astronaut Corps. These two operating characteristics permit the construction of a look-up table for saline volume delivery based on the weight of the subject.

The maintenance of desired infusion bladder pressure requires momentary squeezing of the hand pump at 2- to 3-second intervals, which was determined to be acceptable for experiment performance. Due to the ease of operation of the ICA, the astronaut subjects aboard D-2 were able to monitor the manometer and operate the hand pump during infusion. This allowed the test operator to monitor other medical equipment in order to observe subject responses to fluid loading.

Acknowledgments

Special thanks to Matthew Bellin, John Trine, Susan Brunsvold, and Biomedical Dynamics, Inc., of Minneapolis, Minnesota.

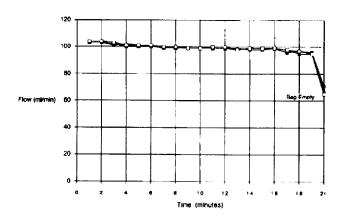


Figure 5. ICA flow constancy until bag empties.

References

¹Anthropometric Source Book, Anthropometry for Designers, Vol. 1. National Aeronautics and Space Administration Scientific and Technical Information Office, 1978.

²Human Research Master Protocol for Experiment US-1: Cardiovascular Regulation at 0-G, June 13, 1989.

Refrigerator/Freezer Based on Stirling Cycle Cooler

Kelly McDonald and Don Schmalholz*
Martin Marietta Services, Inc.
*Johnson Space Center/SE

Abstract

Cooling and storing biological samples are a critical part of Spacelab Life Sciences missions. To meet this need, the Life Sciences Project Division has designed two kinds of vapor compression refrigerator/freezers. While these units have worked successfully, they are not without problems. In order to address acoustic, environmental, and reliability issues, a new Space Shuttle Orbiter refrigerator/freezer was developed based on the Stirling cycle.

Introduction

For years, vapor compression refrigeration has been the standard in home and commercial cooling applications. Based on the Rankine cycle, these machines approach efficiencies of 35%, and nearly all use some form of FreonTM as the working fluid. FreonTM was originally thought to be an ideal fluid: it is inexpensive and nontoxic to humans, and oil is immiscible in it. However, in recent years the ozone-destroying potential of chlorofluorocarbons (CFCs) has become known. To protect the ozone layer, the Montreal Protocol called for the phaseout of CFCs by the end of the century. Existing refrigerator/freezers use Freon 502TM, and because of the sophistication of the system, a direct replacement of the working fluid is not easily accomplished.

The existing refrigerator/freezers have long been a source of acoustic noise that has been an irritation to the

Figure 1. Stirling Orbiter refrigerator/freezer.

crew. Although by 1992 significant time and effort had been spent to reduce the noise from these units, further improvement was still desired.

During a study of some of the major refrigeration cycles by General Electric's corporate research and development organization, the Stirling cycle emerged as the best candidate. Among other things, the study weighed cycle efficiency, technology maturity, and cost. Stirling machines are being designed for commercial and home refrigeration, electronics cooling, satellite cooling, automotive engines, and low temperature experimentation.

In October 1992, Martin Marietta Services and the Life Sciences Project Division established a program to design and develop an Orbiter refrigerator/freezer (OR/F) based on a Stirling cycle cooler. OR/Fs are used in the Shuttle middeck to store experiment samples (primarily blood and urine).

Problem Statement

The Stirling Orbiter refrigerator/freezer (SOR/F) had to meet the requirements as detailed in Specification and Assembly Drawing LS-30106. In general, the unit was to be no bigger than two middeck lockers, offer 0.034 cubic meters of cooled volume, cool contents from 10°C to 22°C, and meet payload acoustic specifications.

Approach

The SOR/F (Figs. 1 and 2) uses a horizontally opposed Stirling cooler designed by Sunpower, Inc., of

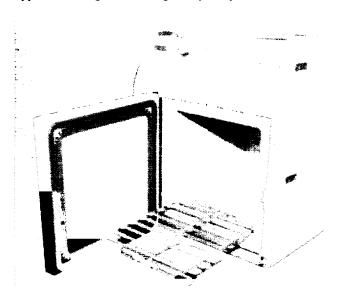


Figure 2. Stirling Orbiter refrigerator/freezer.

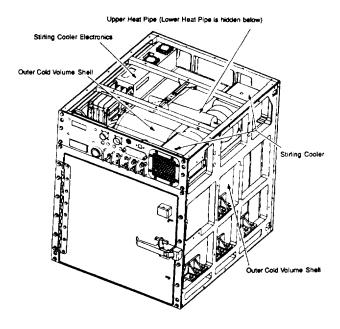
Athens, Ohio. The cooler is lightweight and efficient, and uses helium as the working fluid instead of a CFC. The operation of the cooler is deceptively simple. During the entire cycle, the displacer floats on a layer of gas—the gas bearing. The piston, made of ferrous material, is held in position by the linear motor's magnetic field. The linear motor moves the piston in a simple harmonic motion. The displacer has a different mass from that of the piston, so its response to the changes in pressure generated by the motion of the piston is out of phase with the piston motion. This creates the pattern of two constant volume steps alternated with two constant temperature steps that comprises the Stirling cycle. A fan for the warm heat exchanger and a small electronics package to control the linear motor complete the system.

Two acetone heat pipes, designed and built by Thermacore, Inc., of Lancaster, Pennsylvania, are used to transfer heat from the cold volume to the cooler where it is rejected to cabin air. The finned evaporator sections of the heat pipes are located in the cold volume air duct. A fan circulates air from the cold volume over the fins and back into the box. The condenser end of the heat pipes attaches to the cold heat of the Stirling cooler (Figure 3). The heat pipes work using natural forces and do not require a pump or electronics, which helps to keep the overall system simple and efficient.

The SOR/F also uses a new insulation: precipitated silica. The insulation packets are layered around the inner cold volume, made of LexanTM, and then surrounded by a second LexanTM piece. The configuration is not unlike that of a picnic cooler and greatly reduces heat leaks. The improved insulation allows for a reduction in cooler size.

Results

The SOR/F has a total lift of greater than 85 W (net lift 55 W) at -22°C and uses 80 W input power. In addition to meeting its thermal specifications, the SOR/F meets another primary design goal: acoustic noise reduction. At this time, the unit has over 300 hours of run time and is installed in SpaceHab 2 for flight on STS-60 in early 1994. The SOR/F represents the first practical application of a Stirling cooler at standard refrigeration temperatures.



Note: Outer skins and poured foam removed for clarity

Figure 3. Stirling Orbiter refrigerator/freezer systems.

Conclusions

Based on the results of the STS-60 flight, the SOR/F design could be used to replace existing OR/Fs. In addition, the Stirling cooler could be packaged as a Spacelab refrigerator/freezer, a quick-chill unit, or a cryocooler.

Acknowledgments

This work was performed by Martin Marietta Services under contract NAS9-19800 for the NASA Life Sciences Project Division.

References

Specification and Assembly Drawing for the Stirling Orbiter Refrigerator/Freezer, LS-30106.

Standard Interface Rack (SIR)

Bill Davis, Walter Hanby, Claude Chambellan, Tommy Martin,* Chris Griffin,* Janet Rush,* and Tim Gadd* Johnson Space Center/SE *Martin Marietta Services, Inc.

Abstract

The standard interface rack (SIR) is an integration system that is currently being developed in the Life Sciences Project Division at the NASA Johnson Space Center. The SIR integration system contains a set of standard experiment mechanical, data, video, power, and cooling interfaces, which will reduce payload development costs and increase the flexibility in placement and maintenance of rack-mounted experiment hardware in the SIR. The integration system is designed for use in experiment racks on Spacelab, Spacehab, Mir, and Space Station missions.

Introduction

The objective of the SIR program is to provide a standard set of interfaces that will simplify the hardware development and integration process for the experiment developer. The experiment data interfaces are based on open standards commonly used in commercial laboratories. A mechanical interface has been developed that allows the installation or removal of the experiment drawers from the racks without the use of tools or threaded fasteners. This drawer installation and removal were successfully demonstrated on the second Spacelab Life Sciences mission, STS-58. The rack-mounted hardware and the experiment chassis have been verified to be structurally acceptable for Spacelab, Spacehab, and Mir.

The SIR, when used on the Space Station, Spacehab, and Mir missions, will provide the same experiment-to-rack interface as Spacelab, but the Space Station SIR will potentially have some additional capabilities. The SIR rack controller (RC) will have unique configurations to accommodate specific avionics data system interfaces. The unique configurations will be transparent to the experiment developer using the various space carriers.

Background and Advantages

Historically, integration of experiments into the Spacelab has required many individual pieces of hardware to install each experiment. The installation was a unique process with experiment-specific mechanical and cooling hardware as well as special power, data, and video interface cabling. This approach has been adequate for the relatively short duration Spacelab missions, but if extended to Space Station and Mir, will result in many inefficiencies and restrictions.

For Space Station and Mir, the ability to install and remove experiment drawers at less than the full rack level is a necessity for most scientific disciplines. Standardization of experiment-to-rack interfaces on Spacelab and Spacehab missions also offers many advantages.

Use of the SIR data and video intrarack network allows the experiment developer to develop hardware systems using commercial, off-the-shelf electronics. Since all of the data and power are distributed over a fixed data and power bus network in the rack, the rack can be reconfigured in a very short time to accommodate a different set of experiment hardware with the data flow managed through the RC module. The ability to reroute data within a rack through software control rather than making hardware changes offers significant possibilities.

One of the advantages of providing standard interfaces in Spacelab, Spacehab, Mir, and Space Station experiment racks is that the same experiment hardware or common laboratory equipment can be used in all four environments. One experiment design could be used on Spacelab or Spacehab, providing a seamless transition to Space Station or Mir. The opportunity to develop and test Space Station hardware on Spacelab or Mir is a distinct benefit.

The SIR provides simplification of the experiment-to-spacecraft interface to be designed by the experiment developer. The video and data interface circuits interfacing with the present Spacelab subsystems have unique requirements that have caused verification and integration problems for many experiments. This development program provides data and video interfaces that are based on accepted industry and scientific standards, which reduce development time and costs.

An important spinoff has evolved from the SIR program in the area of experiment checkout and verification. With standard interfaces and automated equipment programmed to test interfaces, the experiment chassis can be tested quickly, consistently, and reliably. This improvement in experiment verification and checkout allows rapid progress of an experiment assembly through extensive testing processes. Both design and testing timelines are shortened for testing new science or technology in space.

In summary, the SIR development program is creating a set of standard experiment-to-spacecraft rack interfaces that simplify the mechanical, cooling, and power interfaces between the experiment and the racks in the Spacelab, Spacehab, Mir, and Space Station. The following section describes these interfaces in more detail.



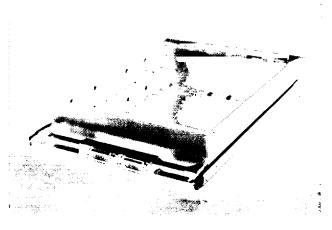
Figure 1. Spacelab single-width rack.

General System Design

The basis for the design of the mechanical hardware is a set of slide guide assemblies at four-panel-unit (17.78 cm) spacing attached to each side and to the center post of a flight rack. At the back of the rack and attached to the mechanical slide guide is a connector bar with a pair of rack and panel connectors: one for power and one for data. Each power connector in the rack has the same contact assignment for power, and each data connector in the rack has the same contact assignment for the data bus network.

A Spacelab single-width rack with the standard interface integration hardware installed is shown in figure 1. This series of identical mechanical, data, power, and cooling interfaces, spaced along the height of the rack, allows any experiment module to be "plugged in" to any of the "slots" in the Spacelab, Spacehab, Mir, or Space Station rack.

The experiment chassis or drawer design requires that the mechanical slides, the front panel latches, and the electrical connectors be placed at controlled locations. However, the remainder of the chassis design is at the discretion of the experiment developer. The experiment drawers can be any height from three panel units (13.335 cm) to the full rack experiment height. The drawer can also be any depth up to the allowable rack experiment volume depth dimension. Figure 2 shows an experiment drawer using the full 60.96-cm depth of the Spacelab rack and a drawer configuration that does not require the full 60.96 cm. The less-than-60.96-cm



(a) Standard interface experiment drawer with connector bar.



(b) Full-length experiment drawer.

Figure 2. Experiment Drawers.

drawers require the use of a connector bar to properly position the data and power connectors. The four-panel-unit spacing of the connector bar and slide guides in the rack makes the use of drawers in four-panel-unit increments optimum.

The data distribution within the SIR is managed over a set of fixed digital and analog data buses that are interfaced to the experiment through a rack-and-panel blind mate connector. The data routing between experiment drawers, and from the experiment drawers to the Spacelab, Spacehab, or Mir data system, is managed by an RC module. The RC, which is a four-panel-unit-high plug-in module, supports both high- and low-rate digital as well as analog (dc to 5 MHz) data as shown in figures 3 and 4. Low-rate digital data transfer is provided by a general purpose interface bus according to the IEEE STD 488.2-1987 specification. The high-rate digital data transfer will be provided by a fiber distributed data interface (FDDI) local area network (LAN). The FDDI LAN still requires development.

The analog bus provides three inputs and three outputs for each connector bar. Those inputs and outputs are

routed to any other chassis in the same rack or routed to external analog lines by the signal interconnect matrix, which is part of the RC. Analog interconnections between chassis can of course be provided by experimentunique front panel connectors and cables.

The RC also serves as a data gateway between the standard interface environment in the rack and the spacecraft data systems, transferring data between the standard interface data buses and the spacecraft data systems.

As the Mir and Space Station are equipped with experiment racks, the racks can be outfitted with SIR hardware and RCs, which provide the same data environment inside the rack that is used on Spacelab, with external interfaces to the Space Station data systems. Comparing the data interfaces for Spacelab, Spacehab, and Space Station in figures 3, 4, and 5, respectively, illustrates this interchangeability.

Results

A Spacelab single rack was outfitted with SIR hardware on STS-58. The SIR flight stowage drawers were intended primarily to carry stowage items for the mission experiments. Two of the drawers were outfitted with an electrical switch and indicator light on the front panel. These switches were turned on by the crew member after the drawers had been removed and reinstalled into the rack in different locations. The inflight objective was to demonstrate that experiment modules could be easily deintegrated and reintegrated into experiment racks on orbit, and still provide reliable

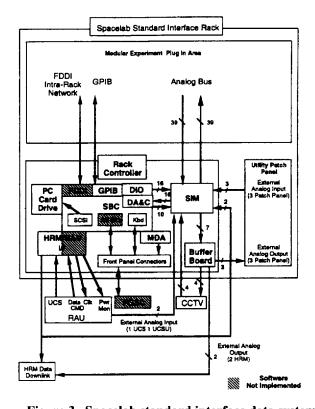


Figure 3. Spacelab standard interface data system.

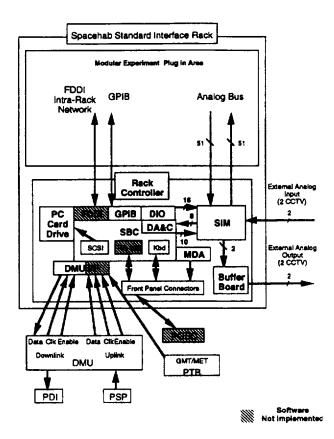


Figure 4. Spacehab standard interface data system.

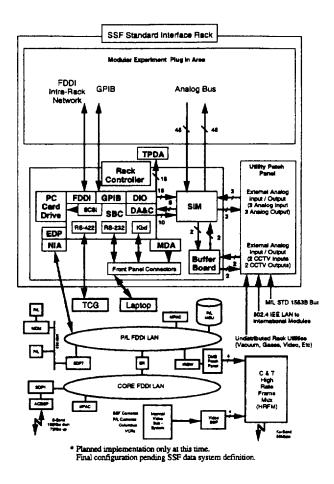


Figure 5. Space Station standard interface data system.

mechanical, data, and power interfaces. The STS-58 pilot, Rick Searfoss, performed the drawer changeout on flight-day 5 of the mission. He said, "The operation was extremely easy, surprisingly easy – twice as easy to perform in flight as it was on the ground. There were no forces or friction, and the electrical continuity checks worked fine."

Conclusions

With a common standard interface environment on Spacelab, Spacehab, Mir, and Space Station, experiments, laboratory equipment, and test equipment designed for Spacelab can be moved to Mir or Space Station without modification.

References

LS-60077, Standard Interface Rack Specification 320014-02 NI-488, Functions for C Languages 320282-01 NI-488-2, MS-DOS Software Reference Manual

Thermoelectric Freezer

Dave Lawson, Rand Nichols, and Walter Hanby*
Martin Marietta Services, Inc.
*Johnson Space Center/SE

Abstract

The recent success of the Second Spacelab Life Sciences mission, supported by the Life Sciences Project Division, has elevated the importance of biomedical experimentation in a microgravity environment. To collect accurate data from the biological samples taken in orbit, the samples are cooled to a temperature dictated by the experiment procedures to be performed on the samples. Various refrigeration designs and techniques have been implemented to carry out this task, and one such design employs a thermoelectric heat pump as the element of refrigeration. The unit is called the Thermoelectric Freezer (TEF) and is currently under development for the Shuttle/Mir Science Project.

Introduction

In 1985, a prototype TEF was developed for cooling samples stored in test tubes. The prototype refrigerator was flown later that year, and its initial tests provided outstanding technical results. The data gathered from the flight proved that thermoelectric techniques could be implemented as a viable source of refrigeration. The Mir

science experiments require a device that is capable of refrigerating and freezing biological samples stored in test tubes. The TEF provides the two modes of operation necessary for the Mir experiments and can accommodate 24 sample test tubes of various diameters. In addition to being small and lightweight, the TEF has minimal moving parts and requires no pressurized gases for operation. This increases the reliability of the device and eliminates the possible hazard of gases leaking into the Mir environment.

Task Description

One mode of operation for the TEF is to cool blood samples to +4°C. Once the samples have reached that temperature, they are placed in a centrifuge for processing according to experiment procedures. The second mode of operation for the TEF is to freeze blood and urine samples to -22°C. This aids in delaying the natural decay of the cellular matter. A sample holder has been designed to house 10 mm and 15 mm diameter test tubes in any mixed configuration (Figs. 1 and 2). The test tube holder required the versatility to adapt to the changes in experiment requirements without being cumbersome for

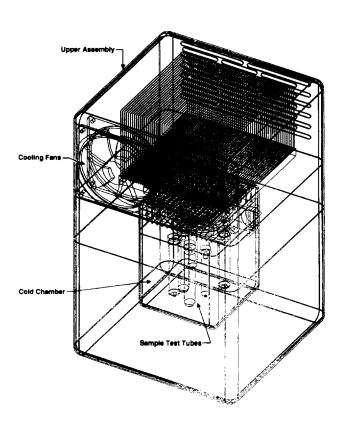


Figure 1. Isometric view of the TEF.

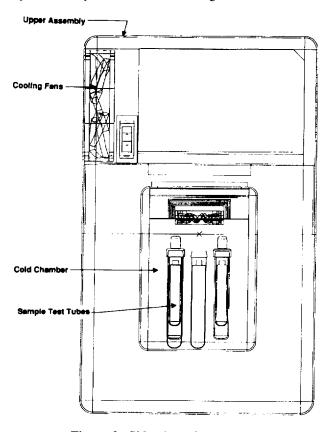


Figure 2. Side view of the TEF.

the astronauts to operate. The overall volume of the sample chamber is 0.002 cubic meters; this small volume creates a more efficient and even air flow to the surfaces of the test tubes. Because of the small sample volume, the test samples frozen at -22°C will be placed in a larger TEF for storage. The TEF will be able to freeze 24 samples in approximately 40 to 60 minutes, depending on the overall volume of liquid in the test tubes.

Methods

For an outer structure, the TEF (Figs. 1 and 2) uses an aluminum box measuring 25.4x25.4x25.4 cm; an equally proportional inner aluminum box assembly, measuring 12.7x12.7x12.7 cm, is used for the cold volume chamber. The TEF is separated in the middle using latches and an insulation barrier. This allows easy access to the sample chamber. All of the front panel controls, electronic circuitry, fans, and the thermoelectric heat pump will be housed in the top portion of the assembly. The bottom half of the TEF will consist of the outer shell and the inner cold chamber assembly.

The test tube sample holder will be mounted to the bottom half of the cold chamber assembly. A small 7.08 liters per second fan is mounted in the cold chamber to provide air circulation, and two larger 42.48 liters per second fans are housed in the upper portion of the TEF to provide cooling to the thermoelectric heat pump. The inner cold volume will be insulated from the outer assembly by using an expanding foam and silicone rubber gasket material that will act as an insulation barrier

between the two halves of the TEF. Front panel controls will consist of a power connector, circuit breaker, and power switch. The TEF is designed to operate on the 28 Vdc power system supplied by the Mir. A liquid crystal display panel meter is used to display temperature, and a toggle switch is used to change between the freeze and refrigerate modes of operation. The electronic circuitry (Fig. 3) consists of a proportional controller used to duty cycle the thermoelectric heat pump when in the refrigerate mode and a thermal sensor to measure the temperature of the sample chamber. A light emitting diode indicator on the front panel will light when the samples reach the appropriate temperature. In the freeze mode of operation, the thermoelectric heat pump will operate at full capacity. The top portion of the TEF will be latched to the bottom half during operation, and upon reaching the appropriate sample temperature, the top of the TEF will be removed to gain access to the test samples. The small size of the TEF allows the unit to be stowed in one of the Mir storage lockers when not in use.

Conclusion

Although the TEF is still in the development stage, we have gained valuable knowledge about thermoelectric elements and refrigeration systems. We will use this knowledge in the design of the TEF to produce a device that we hope will exceed current expectations. Our goal is to provide a practical and reliable product to support Life Sciences flight experiments and open a gateway to the future of spaceflight refrigeration systems.

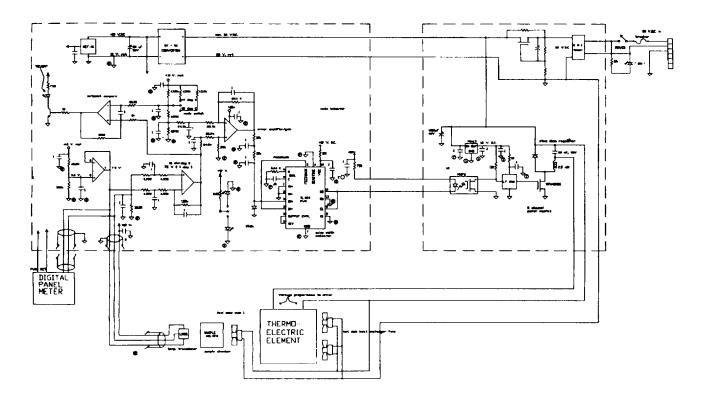


Figure 3. TEC analog controller schematic.

Mir Interface to Payload Systems (MIPS)

Janet Rush and Walter Hanby*
Martin Marietta Services, Inc.
*Johnson Space Center/SE

Abstract

To place NASA's experiments aboard the Mir Space Station, there must be a way for data to be shipped down to Earth or stored on the station. The Mir Interface to Payload Systems (MIPS) was established to perform this task. It provides the American experiments with the interfaces they require, a 1-gigabyte magneto-optical drive for data storage, an interface to Mir for data downlink to the ground, and a notebook computer for data display and processing.

Introduction

Six disciplines (cardiovascular; neurological; behavior and performance; hygiene, sanitation, and radiation; metabolic; and microgravity sciences) may fly several experiments on the Mir Space Station, and the MiPS will provide the experiments with data interfaces, downlink, and on-orbit storage capability. The MIPS involves a notebook computer, a magneto-optical drive, and a MIPS controller.

Problem Statement

A system was needed to provide NASA's experiments with a data interface for data downlink and on-orbit storage. The system has to communicate with the Mir Space Station, and it must be able to store a large amount of data quickly since data downlink to the ground can occur only about 10 minutes per hour. Because of this limitation, a notebook computer is required to display data and determine that an experiment is working correctly. Martin Marietta Services, in conjunction with the Life Sciences Project Division, developed this system to fly on the first Mir mission in the core module of the station.

Approach

The MIPS controller design is based on the Standard Interface Rack Controller design. Much of the rack controller design was used to save time and money and to promote compatibility. The MIPS architecture is shown in Fig. 1.

The MIPS controller provides the following data interfaces.

- 32 analog-to-digital channels (ADCs) differential input to the MIPS controller
- 2 digital-to-analog channels (DACs) output
- 16 digital lines input to the MIPS controller

- RS-232, 2 channels
- Small computer system interface (SCSI)
- Modified interrange instrumentation group B (IRIG-B) output
- Ethernet interface
- User clock signal (UCS) output
- High rate multiplexer (HRM) input from the experiments
- Mir telemetry system interface
- Mir timing system interface
- · Mir environmental system interface

The architecture of the MIPS controller is based on an Intel 386 processor and the personal computer-advanced technology (PC-AT) bus. A commercial single board computer (SBC) provides control, a parallel port, two RS-232 ports, and an SCSI port. A data acquisition and control board provides the ADC, DAC, and digital lines. The modified IRIG-B signal and the ethernet are provided by commercial boards as well. The UCS clock, HRM receiver, and three Mir interfaces are provided on custom boards that were designed in-house. A PC card drive substitutes for a floppy drive and holds the programming for the MIPS controller. The PC card is a solid state memory card, the size of a credit card, that can be changed out on orbit.

The MIPS controller is powered by 28 Vdc from the Mir. The input power is switched through a 10-amp circuit breaker and then filtered. DC-to-DC converters provide ±5 Vdc and ±12 Vdc to the passive backplane. All secondary voltages are regulated. External filtering reduces ripple to <3 mV peak-to-peak. Two utility power connectors provide 28 Vdc after the electromagnetic interference (EMI) filter.

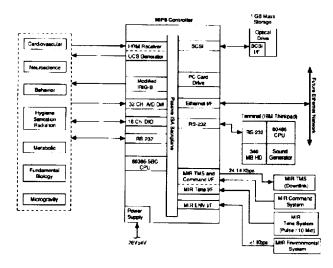


Figure 1. MIPS architecture.

The MIPS controller is a sheet metal chassis with a front panel. An isometric drawing of the chassis is shown in Fig. 2. The front panel contains data and power connectors and two handles. The PC card drive is located on the right side of the chassis. The chassis contains a card cage which holds eight full-length PC-AT size cards that plug into an Industry Standard Architecture passive backplane. A power stack, EMI input filter, thermal cutoff switch, and backup battery for the SBC memory are also included in the chassis. The card cage is mounted on a plate for easy assembly. Two fans on the left side of the chassis pull air from a vent in the top right side of the top cover. The fans run off of 12 Vdc and are thermostatically controlled.

The size of the MIPS controller is 45.72 cm wide by 35.56 cm deep by 15.875 cm high. Velcro strips will be placed on the back and the bottom of the chassis for

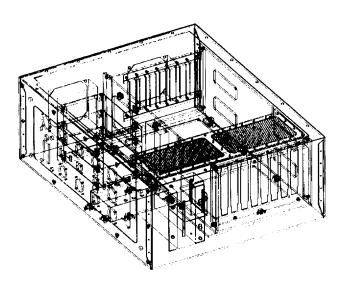


Figure 2. MIPS controller chassis.

mounting in the Mir Space Station. The estimated weight of the MIPS controller is 13.61 kg.

A ruggedized optical drive was selected for data storage. It operates from an SCSI interface on the MIPS controller. The 1-gigabyte optical disks that store the data will be replaced at predetermined intervals.

The notebook computer is an IBM Thinkpad 750C. It has been modified to accept 28 Vdc, and its battery has been removed for safety considerations. It connects to the MIPS controller through RS-232.

Results

The MIPS controller design is complete, and the mechanical parts are being fabricated. All electrical parts have been ordered. The controllers will be assembled by the middle of February, tested, and shipped to Russia in May 1994.

Conclusion

This MIPS will interface NASA's experiments to the Mir Space Station and provide for data downlink and storage on orbit. It will provide a notebook for data display and processing. This should facilitate the integration of American experiments on the Mir Space Station.

Acknowledgments

Engineering and technical support were provided by Martin Marietta Services and the Standard Interface Rack Development Group.

References

The Standard Interface Rack Specification, LS-60077. Spacelab Payload Accommodations Handbook, Appendix B, SLP/2104-2.

Estimate of Cancer Risks From Low Earth Orbit Flights

Honglu Wu, William Atwell,* Alva C. Hardy,** and Chui-hsu Yang⁺ KRUG Life Sciences

- *Rockwell International
- **Johnson Space Center/SN
- +Johnson Space Center/SD

Abstract

One of the risks associated with long-term spaceflight is cancer incidence resulting from chronic exposure to space radiation. The space radiation exposure received by each Space Shuttle astronaut is measured by a thermoluminescent dosimeter worn during every mission. The dosimeter measures the absorbed dose to the skin, but the dose to internal organs is required for estimating the cancer risk induced by space radiation. Using human anatomical models and transport codes, a method has been developed to extrapolate these skin dose measurements to realistic organ-specific dose estimates. Probabilities of cancer incidence and cancer mortality are evaluated for the critical organs identified by the National Council on Radiation Protection and Measurements for several low Earth orbit Shuttle missions.

Introduction

Federal regulations require the monitoring and measurement of personnel radiation exposures in a known enhanced radiation environment for both ground-based nuclear workers and astronauts working in space. During every Space Shuttle mission, astronauts wear a thermoluminescent dosimeter (TLD) which measures their absorbed skin dose. Since one of the many risks associated with manned spaceflight is cancer incidence due to space radiation exposure, the National Council on Radiation Protection and Measurements (NCRP) has identified the most radiosensitive body organs and has assigned cancer incidence and mortality risk coefficients for these body organs. These critical organs include the lung, female breast, thyroid, esophagus, stomach, colon, liver, pancreas, kidney/bladder, and the blood-forming organs (BFO). Extremely detailed male and female anatomical computer models have been developed and are used to describe the body self-shielding about these critical body organs.2.3

Table 1. Space Shuttle Mission Summary Data

Shuttle	Launch		Inclin.			Crew Skin Measurement (mrad)			
Mission	Date	(Km)	(deg)	M/F	Min	Max	Avg		
STS-31	4/24/90	617	28.5	4/1	722	1100	830		
STS-40	6/5/91	287	39.0	4/3	56	68	62		
STS-48	9/12/91	565	57.0	5/0	251	329	283		

An analytical method has been developed to extrapolate the skin dose measurements to realistic organ-specific dose estimates and is discussed in detail. In this paper, we report on the results from Space Shuttle missions STS-31, 40 and 48. These missions were selected based on the variety of altitudes, inclinations, durations, and crew/gender numbers. The profiles for the three flights are listed in Table 1. The Privacy Act of 1974 prevents the disclosure of individual crew member exposures; therefore, only average values for males are reported for STS-31.

Anatomical Models

The computerized anatomical man (CAM) and computerized anatomical female (CAF) models have been developed to perform detailed analyses of the body selfshielding about any point in the human body. 2.3 The CAM represents a 50th percentile US Air Force man and was used as a starting point for developing the CAF. The CAF was prepared by removing the male organ (genitals) models and replacing with female organ (uterus, ovaries, and breasts) models. In addition, a scaling capability was incorporated to account for the smaller stature of the female. In general, the scale factor is 92% of the CAM; however, a variable scaling feature was added since the female pelvic region is larger than the male. Using the body organs listed in NCRP Report 98,1 shielding distributions have been computed for the male and female. These organs and their cancer risk coefficients can be found in reference 1.

Analytical Approach

The space radiation risk to astronauts emanates from three sources. The naturally occurring space radiation environment, which is dominated by the approximate 11-year solar cycle, consists of the Van Allen (trapped) radiation, galactic cosmic radiation (GCR), and solar particulate radiation. The trapped radiation consists of high-energy protons and electrons trapped in the Earth's magnetic field. GCR consists of extremely high-energy nuclei ranging from hydrogen (proton) to uranium. Solar minimum and maximum models of the trapped and GCR environment have been developed. The proton AP-8 MIN and MAX and the electron AE-8 MIN and MAX models^{4,5} are the most recently developed models of the trapped radiation. The Badhwar model⁶ is currently being used to compute the GCR spectra. Since solar

proton emission is very unpredictable, no adequate model exists. The National Oceanic and Atmospheric Administration Solar Forecast Center, Boulder, Colorado, provides real-time Shuttle mission support to the NASA Space Radiation Analysis Group (SRAG).

Figure 1 shows a flow diagram of the analytical approach for calculating the radiation exposure, and subsequent risk, to astronaut critical body organs. A mission trajectory profile in 1-minute intervals which contains time, latitude, longitude, and altitude is received by the SRAG prior to each flight. The AP-8 and AE-8 models contain maps of particle flux as a function of B, L, and E, where B (gauss) is the geomagnetic field strength, L (Earth radii) is the physical distance to the magnetic field line, and E (MeV) is the particle energy. The trajectory point (latitude, longitude, and altitude) is converted to its corresponding B, L point, and the particle flux is obtained for each trajectory point. The magnetic field model IGRF 1965, epoch 1964,7 is used with AP-8 and AE-8 solar minimum models; the US C&GS 19708 is used with the solar maximum models. The particle flux as a function of energy is summed over the mission trajectory to obtain a particle spectrum.9

To compute the radiation exposure (absorbed dose or dose equivalent), the spectrum is attenuated through a shielding model(s) to the dose point of interest. Using combinatorial geometry, an analytical shielding model was developed for the Space Shuttle. More recently, shielding models of SPACELAB and SPACEHAB have been developed. These models are used with the CAM and CAF models to calculate exposure to critical body organs.

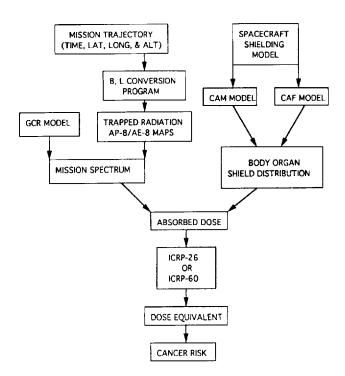


Figure 1. Flow diagram for calculating space radiation exposure and cancer risks.

Organ Dose Extrapolation Method

We have recently developed a simple technique to compute realistic critical body organ doses by normalizing to the crew passive dosimeter (CPD) measurement obtained during a given Space Shuttle mission. The basic assumption is that the CPD is a measurement of the astronaut's skin dose at the center of the astronaut's chest. Using the computed Shuttle mission trapped proton spectrum and the body self-shielding skin distribution for a point at the center of the chest, a spherical shell thickness is computed. This is then the shielding thickness that the input proton spectrum must penetrate and be attenuated to produce the CPD dose measurement. As mentioned above, shield distributions for each CAM and CAF critical body organ have been calculated. The spherical shell thickness is added to each body organ shield distribution, and the corresponding dose computation is made.

The GCR at the Space Shuttle orbital regime is less dependent on altitude and more dependent on orbital inclination due to the geomagnetic field. Using the latest version of the HZETRN program, ¹⁰ absorbed dose and dose equivalent vs shield thickness computations have been made as a function of orbital inclination. A database was generated using three orbital inclinations: 28.5°, 57.0°, and 90.0°. A semi-log interpolation is used for intermediate inclination values (such as 39° for STS-40).

We have incorporated the option of computing the quality factor based on ICRP-26¹¹ or ICRP-60.¹² In this paper we have used ICRP-26, since ICRP-60 has not yet been officially adopted.

Organ Risk Estimate Results

The absorbed dose equivalents at the critical organs are shown in Fig. 2 for 50th percentile US Air Force male and female subjects. The skin dose is taken as the average

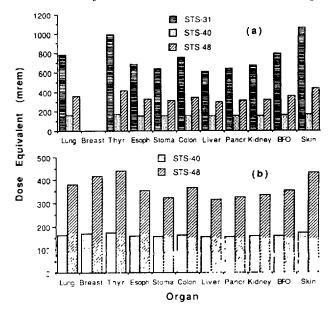


Figure 2. Organ-specific dose equivalent for (a) male and (b) female astronauts.

TLD measured value at the center of the astronaut's chest. The variation of doses in different organs is the consequence of effective body shield thicknesses for the organs. Shown in Tables 2, 3, and 4 are the risks of cancer incidence and cancer mortality for the critical organs per 1000 people. The risks are derived from

 $Risk = Coefficient \times D/D0$

Table 2.
(a) STS-31, excess cancers per 1000 people

SEX	AGE@EXP.	LUNG	BREAST	THYROLO	ESOPHA	STOMACH	COLON
M	25	0.073	0.000	0.025	0.004	0.031	0.030
M	35	0.050	0.000	0.016	0.002	0.016	0.014
м	45	0.035	0.000	0.011	0.001	0.010	0.008
М	55	0.026	0.000	0.006	0.002	0.010	0.008
		LIVER	PANCREAS	KLONEY/ BLADDER	NON-CL LEUKEMIA	ALL OTHER CANCERS	TOTAL CANCERS
М	25	0.026	0.018	0.019	0.017	0.073	0.317
M	35	0.009	0.009	0.011	0.018	0.033	0.177
M	45	0.004	. 0.006	0.007	0.020	0.017	0.119
M_	55	0.002	0.006	0.005	0.020	0.014	0.098

(b) STS-31, excess cancer mortalities per 1000 people

SEX.	AGE@EXP.	LUNG	BREAST	THYROND	ESOPHA	STOMACH	COLON
M	25	0.057	0.000	0.004	0.004	0.022	0.017
M	35	0.039	0.000	0.003	0.002	0.011	0.008
M	45	0.028	0.000	0.002	0.001	0.007	0.005
М	55	0.020	0.000	0.001	0.001	0.007	0.004
		LIVER	PANCREAS	KJONEY/ BLADDER	NON-CL LEUKEMIA	ALL OTHER CANCERS	TOTAL DEATHS
M	25	0.025	0.017	0.006	0.013	0.029	0.194
M	35	0.009	0.008	0.003	0.014	0.013	0.110
м	45	0.004	0.005	0.002	0.016	0.006	0.076
м	55	0.002	0.005	0.001	0.016	0.005	0.063

Table 3.

(a) STS-40, excess cancers per 1000 people

SEX,	AGE@EXP.	LUNG	BREAST	THYROID	ESOPHA	STOMACH	COLON
M	25	0.015	0.000	0.004	0.001	0.008	0.006
м	35	0.010	0.000	0.003	0.000	0.004	0.003
м	45	0.007	0.000	0.002	0.000	0.002	0.002
M	55	0.005	0.000	0.001	0.000	0.002	0.002
F	25	0.012	0.053	0.013	0.001	0.011	0.008
F	35	0.010	0.032	0.010	0.001	0.006	0.004
F	45	0.009	0.006	0.007	0.000	0.004	0.002
F	55	0.006	0.003	0.005	0.001	0.003	0.002
		LIVER	PANCREAS	KIDNEY/	NON-CL	ALL OTHER	TOTAL
		1		BLADDER	LEUKEMIA	CANCERS	CANCERS
М	25	0.006	0.004	0.004	0.003	0.012	0.064
М	35	0.002	0.002	0.002	0.004	0.005	0.036
м	45	0.001	0.001	0.002	0.004	0.003	0.024
M	55	0.001	0.001	0.001	0.004	0.002	0.020
F	25	0.008	0.007	0.005	0.002	0.008	0.127
F	35	0.003	0.003	0.003	0.003	0.004	0.079
F	45	0.002	0.002	0.002	0.003	0.003	0.040
F	55	0.001	0.002	0.002	0.003	0.003	0.032

(b) STS-40, excess cancer mortalities per 1000 people

SEX,	AGE PEXP.	LUNG	BREAST	THYROIO	ESOPHA	STOMACH	COLON
M	25	0.012	0.000	0.001	0.001	0.005	0.003
M	35	0.008	0.000	0.001	0.000	0.003	0.002
M	45	0.006	0.000	0.000	0.000	0.002	0.001
M	55	0.004	0.000	0.000	0.000	0.002	0.001
F	25	0.009	0.017	0.001	0.001	0.008	0.004
F	35	0.007	0.010	0.001	0.000	0.005	0.002
F	45	0.007	0.002	0.001	0.000	0.003	0.001
F	55	0.006	0.001	0.001	0.000	0.002	0.001
		LIVER	PANCREAS	KIDNEY/	NON-CL	ALL OTHER	TOTAL
		l		BLADDER	LEUKEMIA	CANCERS	DEATHS
M	25	0.006	0.004	0.001	0.003	0.005	0.041
м	35	0.002	0.002	0.001	0.003	0.002	0.023
M	45	0.001	0.001	0.000	0.003	0.001	0.016
M	55	0.000	0.001	0.000	0.003	0.001	0.013
F	25	0.007	0.007	0.002	0.002	0.003	0.060
F	35	0.003	0.003	0.001	0.002	0.002	0.036
-	45	0.002	0.002	0.001	0.002	0.001	0.021
•	73	0.002					

Table 4.
(a) STS-48, excess cancers per 1000 people

SEX.	AGE PEXP.	LUNG	BREAST	THYROID	ESOPHA	STOMACH	COLON
М	25	0.033	0.000	0.010	0.002	0.015	0.014
М	35	0.022	0.000	0.007	0.001	0.008	0.007
М	45	0.016	0.000	0.005	0.001	0.005	0.004
м	55	0.012	0.000	0.003	0.001	0.005	0.003
F	25	0.028	0.130	0.034	0.002	0.022	0.018
F	35	0.023	0.080	0.025	0.001	0.013	0.009
F	45	0.021	0.014	0.016	0.001	0.008	0.005
F	55	0.018	0.007	0.012	0.001	0.007	0.005
		LIVER	PANCREAS	KIDNEY/	NON-CL	ALL OTHER	TOTAL
		1		BLADDER	LEUKEMIA	CANCERS	CANCERS
z	25	0.013	0.009	0.009	0.007	0.030	0.143
м	35	0.004	0.004	0.005	0.008	0.013	0.080
м	45	0.002	0.003	0.003	0.009	0.007	0.054
м	55	0.001	0.003	0.003	0.009	0.006	0.044
F	25	0.016	0.015	0.011	0.005	0.019	0.300
F	35	0.007	0.006	0.007	0.006	0.011	0.187
F	45	0.003	0.004	0.005	0.007	0.008	0.093
F	55	0.002	0.004	0.004	0.007	0.008	0.075

(b) STS-48, excess cancer mortalities per 1000 people

SEX.	AGE@EXP.	LUNG	BREAST	THYROLD	ESOPHA	STOMACH	COLON
М	25	0.026	0.000	0.002	0.002	0.011	0.008
М	35	0.018	0.000	0.001	0.001	0.005	0.003
М	45	0.013	0.000	0.001	0.001	0.003	0.002
М	55	0.009	0.000	0.000	0.001	0.003	0.002
F	25	0.020	0.041	0.003	0.002	0.017	0.009
F	35	0.017	0.025	0.002	0.001	0.010	0.004
F	45	0.015	0.005	0.002	0.001	0.006	0.003
F	55	0.013	0.002	0.001	0.001	0.005	0.003
		LIVER	PANCREAS	KIONEY/	NON-CL	ALL OTHER	TOTAL
				BLADDER	LEUKEMIA	CANCERS	DEATHS
м	25	0.012	0.008	0.003	0.006	0.012	0.089
М	35	0.004	0.004	0.002	0.006	0.005	0.050
м	45	0.002	0.002	0.001	0.007	0.003	0.035
M	55	0.001	0.002	0.001	0.007	0.002	0.029
F	25	0.015	0.014	0.004	0.004	0.008	0.136
F	35	0.007	0.006	0.002	0.004	0.004	0.083
F	45	0.003	0.004	0.002	0.005	0.003	0.047
-	55	0.002	0.004	0.001	0.005	0.003	0.040

where Coefficient is the cancer risk coefficient listed in reference 1, D is the absorbed dose equivalent in rem, and $D_0 = 10$ rem. In calculating the risks for "all other cancers," the TLD measured dose is used as the upper limit. The ages in Tables 2 through 4 are the age at first exposure to space radiation. For male astronauts, the lung is the most sensitive organ. For female astronauts, the possibility for breast cancer is much higher. Because of breast cancer, the cancer risk due to space radiation for female astronauts is about twice as high as for male astronauts.

Conclusion

The current limit of radiation exposure in space activities is 25 rem of BFO dose equivalent in 30 days and 3% excess cancer mortality risk. The BFO exposures for the three flights and excess cancer mortality risks for the 35-year-old astronauts are compared with the exposure limit and shown in Table 5. The minimum and maximum doses and risks in Table 5 correspond to the minimum and maximum TLD values recorded. It is seen that the radiation exposure and the cancer risk in a single Space Shuttle flight do not exceed the current limit.

Table 5. BFO Dose Equilvalents And Total Cancer Mortality Risks Compared With The Current Limits

Flight/Sex	BFO Dose (mrem)			Excess	Excess Mortality Risk (%)			Career Excess Mortality Limit	
	MIN	AVE	MAX	MIN	AVE	MAX			
STS-31/M	651	749	1001	0.010	0.011	0.015	25 rem	3%	
STS-40/M	145	160	175	0.002	0.002	0.002	25 rem	3%	
STS-40/F	145	160	175	0.004	0.004	0.004	25 rem	3%	
STS-48/M	317	357	415	0.004	0.005	0.006	2S rem	3%	
STS-48/F	314	354	412	0.007	0.008	0.009	25 rem	3%	

References

- ¹National Council on Radiation Protection and Measurements (NCRP): Guidance on Radiation Received in Space Activities, NCRP Report No. 98, Bethesda, MD, 1989.
- ²Billings, M.P. and Yucker, W.R., Summary of Final Report: The Computerized Anatomical Man (CAM) Model, Report MDC G4655, McDonnell Douglas Astronautics Company, Huntington Beach, CA, 1973.
- ³Yucker, W.R., Computerized Anatomical Female Body Self-Shielding Distributions, Report MDC 92H0749, McDonnell Douglas Space Systems Company, Huntington Beach, CA, 1992.
- ⁴Sawyer, D.M. and Vette, J.I., "AP-8 Trapped Proton Environment for Solar Maximum and Solar Minimum," NASA TM X-72605, 1976.
- ⁵Private communication: J.I. Vette, NASA/GSFC, with W. Atwell, 1986.
- ⁶Badhwar, G.D. and O'Neill, P.M., "An Improved Model

- of Galactic Cosmic Radiation for Space Exploration Missions," *Nucl. Tracks Radiat. Meas.*, Vol. 20, No. 3, 1992, pp. 403-410.
- ⁷"International Geomagnetic Reference Field 1965.0," *J. Geophys. Res.*, Vol. 74, 1969, p. 440.
- ⁸L. Hurwitz, et al., "A Model of the Geomagnetic Field for 1970," *J. Geophys. Res.*, Vol. 79, 1974, p. 1716.
- "Gates, M.M., Lewis, M.J., and Atwell, W., "Rapid Method of Calculating the Orbital Radiation Environment," *J. Spacecraft and Rockets*, Vol. 29, No. 5, pp. 646-652, 1992.
- ¹⁰Wilson, J.W., Chun, S.Y., Badavi, F.F., Townsend, L.W., and Lamkin, S.L., "HZETRN: A Heavy Ion/ Nucleon Transport Code for Space Radiations," NASA TP-3146, 1991.
- ¹¹Recommendations of the International Commission on Radiological Protection, ICRP Publ. 26, Pergamon Press Inc., 1987.
- 121990 Recommendations of the International
 Commission on Radiological Protection, ICRP Publ.
 60, Pergamon Press Inc., 1991.

Stability of White Blood Cells in Whole Blood Stored at Room Temperature

Karin C. Loftin, Gerald R. Taylor,* Robert Ferebee,** and Dorothy E. Lewis†
KRUG Life Sciences
*Johnson Space Center/SL
**University of Houston Clear Lake,
†Baylor College of Medicine

Abstract

This ground-based study was conducted to define the requirements for collecting in-flight blood samples of crew members for postflight analysis of the immune function. The stability of total white blood cell (WBC) counts, differential WBC counts, cell viability, and lymphocyte surface antigens was investigated in whole blood with heparin or acid citrate dextrose (ACD) stored upright, slowly rotating, or rocking at room temperature. We tested the hypothesis that blood samples in heparin could be stored upright at room temperature for 3 days without marked changes in the stability of the total WBC, differential WBC counts, and lymphocyte surface antigens. The total WBC count, cell viability, and percentage of neutrophils decreased significantly on Day 3. Conversely, the percentage of lymphocytes increased on Day 3. The conclusion was that heparinized whole blood could be stored upright for up to 2 days at room temperature with minimal changes in the stability of the stated parameters.

Introduction

Present evidence supports the contention that the cell-mediated immune response of crew members is attenuated during both American and Russian space missions.^{1,2} The elements of the immune system that were impaired postflight were the distribution and counts of specific populations of leukocytes, the response of lymphocytes to mitogens, the natural killer cell (K cell) function, and the cytokine production. Changes in the leukocyte populations were neutrophilia, monocytopenia, lymphopenia, eosinopenia, and reduced numbers of helper T-lymphocytes, B-lymphocytes, and natural K cells.³

To reduce the risk of infection, it is expected that the immunocompetence of crew members in flight will be monitored during long-duration missions.⁴ This ground-based study was conducted to define the requirements for collecting in-flight blood samples of the crew for post-flight analysis. Considering the technical resources, limited stowage, and power available in flight, we stored whole blood at room temperature for up to 6 days to investigate the changes in WBC measurements. The critical variables were identified from existing literature.⁵⁻¹⁰

The first experiments in the study compared the effect of two anticoagulants, heparin and ACD, on the storage of whole blood at room temperature. The blood sample tubes were stored under the following three

conditions: rotating slowly in a vertical position, horizontally on a rocker to simulate microgravity condition and to maintain the cells in suspension, or stored upright as the control. Cell viability, total WBC counts, and the differential WBC counts were measured. Once we determined the optimal physical condition and anticoagulant from these experiments, the stability of lymphocyte surface markers was investigated in two subsequent experiments. We tested the hypothesis that heparinized blood samples could be stored upright at room temperature for 3 days without marked changes in cell viability, total WBC counts, differential WBC counts, and lymphocyte surface antigens.

Materials and Methods

Sample Collection and Storage

Subjects donated a 20 ml blood sample that was collected in 5 and 6 ml B-D vacutainer tubes (Becton-Dickinson, Co., Rutherford, New Jersey) containing 72 USP units of sodium heparin (B-D #6481) or 1.0 ml ACD (B-D #4816), respectively. Separate samples were either rotated slowly on a custom-constructed rotary aliquot mixer, rocked on an Ames aliquot mixer (Model 4651 Miles Laboratories, Elkhart, Indiana), or allowed to stand upright between testing. All samples were maintained at room temperature (22°C±2°C) for up to 6 days. Each blood sample was assayed for total WBC counts, percentage of viability, and differential WBC counts.

Cell Counts and Viability

Total WBC counts were measured automatically with a Coulter model Z electronic cell counter (Coulter Electronics, Inc., Hialeah, Florida) and manually with a Spenser Bright Light Hemocytometer (Improved Neubauer Ruling) using standard methods. The percentage of viable WBCs was measured using the Trypan blue dye exclusion method. The WBCs were differentiated on the feathered edge of a stained microscope slide smear of whole blood. The air-dried slides were stained on an automated Hema-Tek slide stainer (Miles Laboratory, Elkhart, Indiana) with Wright hematological stain (Fisher Scientific, Fairlawn, New Jersey). A standard Schillings differential of 100 WBCs total and the percentage of each cell type were recorded.

Immunofluorescence and Flow Cytometry

Subjects donated a 20 ml blood sample containing sodium heparin to determine the percentage of lymphocyte subsets. The 20 ml samples were divided into 4 ml aliquots for storage and testing. The National Committee for Clinical Laboratory Standards guidelines for quality assurance of immunophenotyping peripheral blood lymphocytes by flow cytometry were followed.¹¹⁻¹³

Whole blood was kept at room temperature and aliquoted into tubes containing appropriate monoclonal antibodies (mAb) (Becton Dickinson, Mountain View, California). The mAb were used according to a dual staining protocol with paired groups of antibodies: CD45, CD14; CD3, CD4; CD3, CD8; CD2, CD19; and CD3, CD16/56. 12.13 The CD45, CD14 tube was used to verify that the cells examined for fluorescence had the characteristics of lymphocytes. The rest of the panel allowed the determination of the percentage of T cells, CD4 and CD8 subsets, B cells, and natural K cells, respectively.

The mAb and 100 µl of whole blood per test were incubated for 30 minutes at room temperature. The red blood cells were lysed and fixative was added in a single step using Q prep reagents (Coulter Immunology, Hialeah, Florida). The cells were examined using the Coulter EPICS Profile I with power pac option. The instrument was calibrated daily for both sensitivity and mean channel fluorescence. The percentage positive for each marker was recorded using established gates.

All data were collected and stored in a database (Microsoft Excel Software, Microsoft Corp., Redmond, Washington) and analyzed statistically using one-, three-, or four-factor analysis of variance and post hoc Scheffe F-test (Statview II Software, Abacus Concept, Inc., Berkeley, California). A value of *p*<0.05 was chosen to indicate a significant difference between the groups and rejection of the null hypothesis. CA-Cricket Graph III (Computer Associates International, Inc., San Jose, California) was used to illustrate the figures.

Results and Discussion

The WBC data from three subjects for the three independent variables (i.e., storage days, physical state, and anticoagulant) are summarized in Fig. 1 and demonstrate that all three variables had a significant effect on the Coulter WBC counts (p<0.05, n=3). The data indicate that on Day 4, for both ACD and heparin blood stored upright, the absolute leukocyte counts were markedly reduced (Fig. 1). Slowly rotating both the heparin and ACD blood tubes caused the WBC Coulter counts to be elevated artifactually (Fig. 1). We attributed this elevation to the destruction of erythrocytes by the shearing forces of rotation and clumping of red cell ghosts. In subsequent experiments, we measured the WBC counts by the two procedures described in Materials and Methods.

In one subsequent experiment, we discontinued the use of the rotary aliquot mixer and rocked the samples on

an Ames aliquot mixer to suspend the cells. The blood cells, counted both manually and with the Coulter counter, were stored for 4 days. The four-factor (storage day, physical state, anticoagulant, and counting methods) analysis of variance for storage day indicated that the total WBC counts of the various groups did not differ significantly over 3 days (p>0.05, n=3). However, both the length of storage and the type of anticoagulant had a significant negative effect (p<0.05, n=3) on the percentage of WBC viability (Fig. 2). On Day 3 the viability of WBCs in whole blood was 84% with heparin and only 48% with ACD.

For the final two experiments, we collected blood samples in heparinized tubes and stored them upright for 3 days. Figure 3 illustrates the stability of the absolute and differential WBC counts and cell viability in heparinized blood. When compared to Day 0, the one-factor (storage day) analysis of variance of the data resulted in significant reduction (p<0.05, n=7) of the total WBC count, viability, and percentage of neutrophils on Day 3. Correspondingly, the relative percentage of lymphocytes increased by Day 3. The viability also was significantly reduced on Day 2, but was still very high at 92% dropping to 79% by Day 3. The lymphocyte surface antigens were stable over a 3-day period (Table 1) supporting the hypothesis in part. The extreme variability of the pan

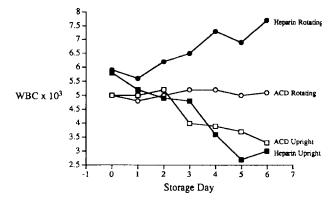


Figure 1. Coulter WBC counts (mean) n=3.

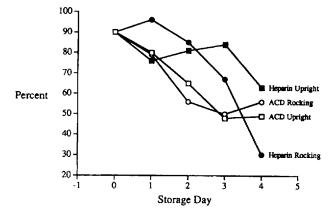


Figure 2. Percentage viability of WBC population (mean) n=3.

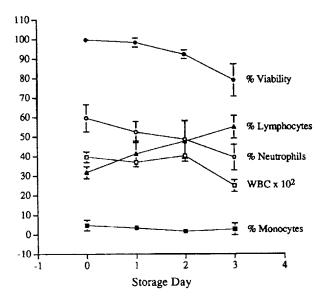


Figure 3. Viability, absolute and differential WBC counts of heparinized blood stored upright (mean \pm SD) n = 7.

leukocyte (CD45) marker on Day 3 indicated that the samples were deteriorating. Others have reported no changes in lymphocyte surface antigens even after 4 days of storage at room temperature.⁷ This may allow blood to be collected from crew members and stored at room temperature during spaceflight for up to 4 days prior to landing.

Conclusions

Whole blood in heparin can be stored at room temperature for 2 days with minimal changes in WBC counts, differential counts, and cell viability, and for 3 days with no changes in lymphocyte surface antigens. Gentle rocking of the blood samples to suspend the cells (as may occur in microgravity) is not detrimental to the WBC counts or viability and suggests that microgravity does not adversely affect the blood samples. Further studies should investigate the stress of microgravity and landing on the cellular functions of blood samples collected in flight.

Acknowledgments

We wish to gratefully acknowledge Joanne Thompson and Lisa Jenks for their technical assistance, Robert P. Janney and Daniel Barineau for constructing the rotary aliquot mixer, and Jackie Reeves for preparing the graphs and for final editing of the manuscript. This work was supported by NASA contract NAS 9-18492.

References

- ¹Taylor. G.R., "Immune Changes During Short-Duration Missions," *J. Leukocyte Biol.*, Vol. 54, No. 3,1993, pp. 202-208.
- ²Konstantinova, I.V., Rikova, M.P., Lesnyka, A.T., Antropova, E.A., "Immune Changes During Long-Duration Missions," *J. Leukocyte Biol.*, Vol. 54, No. 3, 1993, pp. 189-201.
- ³Taylor, G.R., "Overview of Spaceflight Immunology Studies," *J. Leukocyte Biol.*, Vol. 54, No. 3, 1993, pp. 179-188.
- ⁴Couch, R.B., Chairman's Summary of NASA Workshop on Infectious Diseases in Space Station. In: Space Station Infectious Disease Risks, Pierson, D., ed., NASA-JSC, 1986.
- ⁵Dzik, W. and Neckers, L., "Lymphocyte Subpopulations Altered During Blood Storage," *N. Engl. J. Med.*, Vol. 308, 1983, pp. 435-436.
- ⁶Shield, III, C.F., Marlett, P., Smith, A., Gunter, L., Goldstein, G., "Stability of Human Lymphocyte Differentiation Antigens When Stored at Room Temperature," *J. Immunol. Meth.*, Vol. 62, 1983, pp. 347-352.
- ⁷Nicholson, J., Jones, B., Cross, G., McDougal, J.S., "Comparison of T and B Cell Analysis on Fresh and Aged Blood," J. *Immunol. Meth.*, Vol. 70, 1984, pp. 29-40.
- ⁸Weiblen, B., Debell, K., Giorgio, A., Valeri, C.R., "Monoclonal Antibody Testing of Lymphocytes after Overnight Storage," J. *Immunol. Meth.*, Vol. 70, 1984, pp. 179-183.

Table 1. Percentage Lymphocyte Subsets and B Cells of Lymphocyte Population (Mean ±SE)

Storage Day	Pan Leukocyte CD45	T Cells CD2	BCells	CD3 (T3)	Helper (H) CD4 (T4)	Suppressor (S) CD8 (t8)	CD16/56	H:S Ratio
0	98.5 ±0.4	79.5 ±1.8	11.9 ±1.4	69.7 ±3.8	43.1 ±5.3	22.9 ±2.1	10.1 ±2.2	1.9 ±0.2
1	97.1 ±0.3	79.0 ± 1.9	11.9 ±1.6	72.9 ± 3.0	44.6 ± 2.6	24.1 ± 1.4	10.4 ±2.5	1.9 ±0.2
2	97.2 ±0.9	81.8 ± 1.2	9.8 ±1.4	75.2 ± 3.0	48.1 ±2.3	25.3 ± 1.8	15.0 ±6.5	1.9 0.1
3	88.5 ±10.7	83.7 ±1.6	9.3 ±1.8	77.7 ±3.5	49.6 ± 2.2	25.9 ± 2.1	12.3 ± 4.7	2.0 ±0.2

- O'Sherman, M.E. and Dzik, W.H., "Stability of Antigens on Leukocytes in Banked Platelet Concentrates: Decline in HLA-DR Antigen Expression and Mixed Lymphocyte Culture Stimulating Capacity Following Storage," *Blood*, Vol. 72, No. 3, 1988, pp. 876-872.
- ¹⁰Carey, J.L., "Flow Cytometric Immunoanalysis of Leukemia and Lymphoma," *J. Clin. Immunoassay*, Vol. 12, No. 1, 1989, pp. 21-28.
- ¹¹NCCLS, Clinical Applications of Flow Cytometry: Quality Assurance and Immuno-Phenotyping of Peripheral Blood Lymphocytes, NCCLS H42P, Vol. 9, No. 13, 1989, pp. 765-849.
- ¹²Giorgi, J.V., Cheng, H.L., Margolick, L.B., Bauer, K.D., Ferbas, J., Waxdal, M., Schmid, I., Hultin, L.E., Jackson, A.L., Park, L., Taylor, J.M.G., and the Multicenter AIDS Cohort Study Group, "Quality Control in the Flow Cytometric Measurement of T-Lymphocyte Subsets: The Multicenter AIDS Cohort Study Experience," *Clin Immunol. Immunopathol.*, Vol. 55, 1990, pp. 173-186.
- ¹³Lewis, D.E. and Rickman, W.J., "Methodology and Quality Control for Flow Cytometry, Section D: Immune Cell Phenotyping by Flow Cytometry." In: *Manual of Clinical Laboratory Immunology*, Rose, N.R., et al., eds., 4th edition, American Society for Microbiology, Washington, D.C., 1992, pp. 164-173.

Discrimination of Ocean Conditions Using Space Shuttle Polarization Photography

David E. Pitts and Steven A. Israel*
Johnson Space Center/SN
*Hernandez Engineering, Incorporated

Abstract

Space Shuttle and aerial polarimetric imagery were evaluated for discrimination of a variety of sea states over several view/illumination angles. The Space Shuttle experiment was performed using two bore-sighted Hasselblad 70 mm cameras having identical settings and linear polarizing filters aligned orthogonally about the optic axis. The aerial experiment was performed using a single 35 mm Nikon FE2 camera and rotating the linear polarizing filter 90° to acquire both minimum and maximum intensity photographs. Characteristic curves (plot of percent polarization versus b (phase) angle and/or differential azimuth) were created for each cover type and waveband for both aerial and Space Shuttle imagery. Significant differences were found between the data sets, but the ability to discriminate among terrestrial features improved using this technique.

Introduction

Polarimetric observations of celestial bodies have been acquired for most of the 20th Century (Lyot 1929, Wolff 1975). A number of laboratory (Coulson et al. 1965, Egan 1967, and Vanderbilt et al. 1985) and field (Curran 1979 and Walraven 1981) polarimetric experiments have been performed. These articles have also shown that polarimetric information can be used as a measure of surface texture or roughness. However, limited polarimetric experiments have been performed from aerial (Egan 1985 and Stockhoff and Frost 1974) and orbital platforms (Israel and Duggin 1992, Coulson et al. 1986). The relationship between orbital and aerial polarimetry has been discussed only in a handful of articles (e.g., Egan et al. 1992). The percent polarization was determined by using the following equation:

% polarization =
$$\frac{I_{max} - I_{min}}{I_{max} + I_{min}} * 100$$

This analysis is based upon aerial polarization data collected from the Apex Barge spill in Galveston Bay during 3 days in July 1990 and orbital polarization data taken during Space Shuttle mission STS-51A.

Methods

Aerial Photography

Photographs were taken of the Apex Barge oil spill near Texas City, Texas. The spill occurred on the west

side of Galveston Bay near a sand bar called Red Fish Island. Minimum and maximum polarization photographs were taken in rapid succession. Photographs were taken 2, 3, and 5 days after the spill. The oil features of interest were the concentrated spill, sheen, and unpolluted water.

In order to analyze a large number of photographs, photographic densities were taken of each cover type within a scene for both photographs of a given polarization pair. The density values were then converted to intensity measurements. From these intensity values the percent polarization was calculated (equation 1). To determine separability, density values were differenced for the minimum and maximum photographs between different cover types, and the percent polarization was differenced for calculated polarization image. (Density measurements were specifically chosen for differencing because this experiment was initially designed for human perception. Differences in Log intensity values are easier to observe than real intensity values.) Cover type separability was performed for the minimum and maximum reflectance and the percent polarization by waveband for each cover type.

The sun-target and target-sensor differential azimuth was determined for each pair of images by registering the images to maps and knowing the time and date of exposure.

Space Shuttle Photography

For the Space Shuttle experiment, the astronaut rotated the camera mount to obtain the maximum intensity in one camera and the corresponding minimum in the other (figure 1).



Figure 1. Astronaut performing the dual camera polarization experiment aboard STS-51A.

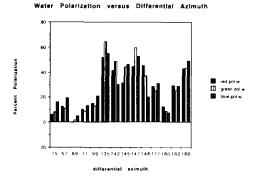


Figure 2. Plot of percent polarization versus differential azimuth (degrees) from the aerial platform.

The targets of interest were Shark Bay in western Australia and the Atolls near Tahiti. These targets were photographed multiple times with varying view/illumination geometry using Kodak black-and-white panchromatic film. The normal albedo of these two oceans was assumed to be similar.

Individual images were digitized and the percent polarization image was generated using equation 1. The polarization images were registered to a map and common areas were sectioned from each polarization image. The view/illumination geometry was determined for each kernel. Characteristic curves of angle versus percent polarization and differential azimuth versus percent polarization were plotted for ocean and barren land areas, angle is the angle in three dimensions between the suntarget vector and the target-sensor vector. Differential azimuth is the projection of the angle onto the plane tangent to the Earth at the target.

Results

General

The value for the degree of polarization was inversely related to surface roughness and albedo. The characteristic



Figure 3. Polarization image of oil spill components.

curves for aerial unpolluted water were similar to the curve produced for Space Shuttle ocean imagery (figs. 2 and 4).

Aerial Platform

For water features, the blue polarization information best separated sheen, concentrated oil, and unpolluted water. The highest values for the degree of polarization were also found in the blue polarization band (figure 3). This result is in contrast to the results obtained from Egan et al. (1992), who found the highest values of the degree of polarization to be the red band for imagery obtained from the Space Shuttle. The addition of the linear polarizing filter increased the separability between subsurface oil types significantly. The minimum image provided better discrimination between subsurface oil, heavily sedimented water, and unpolluted water than either the maximum or polarization image. In these cases, the value for the degree of polarization was low. Though the degree of polarization varied with view/illumination geometry, the separation of cover types for the minimum image was not angle dependent.

Orbital Platform

From Israel and Duggin (1992), panchromatic polarimetric signatures of ocean features are significant to permit their separation. The degree of polarization appears to be most dependent upon differential azimuth than angle for space-based terrestrial observations (figure 4). The addition of linear polarizing filters significantly increases the radiometric separation between terrestrial features.

Conclusions

Polarimetric and reflectance signatures of ocean features are separable and vary with view/illumination geometry from both aerial and orbital platforms. This

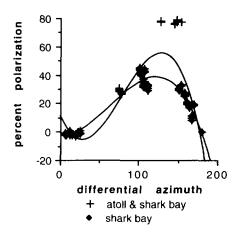


Figure 4. Differential azimuth angle versus polarization for the ocean regions.

relationship between signatures observed from the different platforms varies with wavelength and the target's surface texture. Surface texture information is also resident in nonpolarized photography. Extracting texture is useful in mapping terrestrial features. Future work needs to be performed which can describe the atmospheric interaction and enhance scene information that is in normal photography. The genesis of this work started with Egan et al. (1993) and practical applications for these enhanced views are still being researched.

References

- Coulson, Whitehead, Campbell, "Polarized Views of the Earth from Orbital Altitude," *SPIE*, Vol. 637, *Ocean Optics* VIII, 1986, pp. 35-41.
- Coulson, Bouricius, Gray, "Optical Reflection Properties of Natural Surfaces," *Journal of Geophysical Research*, Vol. 70, No. 18, September 15, 1965, pp. 4601-4611.
- Curran, P. J., "The Use of Polarized Panchromatic and False-Color Infrared Film in the Monitoring of Soil Surface Moisture," *Remote Sensing of the Environment*, 8:249-266, 1979.
- Egan, W.G., Israel, S.A., Sidran, M., Hindman, E.E., Johnson, W.R., Whitehead, V.S., "Optical Properties of Continental Haze, Cumulus, and Orographic Clouds Based on Space Shuttle Polarimetric Observations," *Applied Optics*, Vol. 32, No. 33, November 20, 1993, pp. 6841-6852.
- Egan, W.G., Israel, S.A., Johnson, W.R., and Whitehead, V.S., "High Resolution Space Shuttle Polarimetry for Farm Crop Classification," *Applied Optics*, Vol. 31, No. 10, April 1, 1992, pp.1542-1548.
- Egan, W., *Photometry and Polarization in Remote Sensing*, Elsevier Science Publishing Company, Inc., New York, 1985.

- Egan, W.G., "Polarimetric Measurements of Simulated Lunar Surfaces," *Journal of Geophysical Research*, Vol. 72, No. 12, June, 1967, pp. 3233-3245.
- Israel, S.A., Duggin, M.J., "Characterization of Terrestrial Features Using Space Shuttle Based Polarimetry," *Proceedings IGARSS* '92, Houston, Texas, Vol. 2, May 26-29, 1992, pp. 1547-1559, IEEE #92CH3041-1, Library of Congress #91-72810.
- Israel, S., Duncan, M., Johnson, W., Whitehead, V., "Observations and Analysis of Oil Spills Using Polarized Imagery," *Eighth Thematic Conference on Geologic Remote Sensing*, April 28-May 2, 1991, pp. 945-953.
- Lyot, B., Research on the Polarization of Light from Planets and some Terrestrial Substances, Annales de l'Observatoire de Paris, Section de Meudon, VII, No. 1, 1929. Translated as NASA Technical Translation TTF-187
- Stockhoff, Frost, "Remote Detection of Soil Surface Moisture," 9th International Symposium on Remote Sensing of Environment (University of Michigan), 1974.
- Talmage, D., Curran, P., "Remote Sensing Using Partially Polarized Light," *International Journal of Remote Sensing*, Vol. 7, No. 1, 1986, pp. 47-64.
- Vanderbilt, Grant, Daughtry, "Polarization of Light Scattered by Vegetation," *Proceedings of the IEEE*, Vol. 73, No. 7, pp. 1012-1023, June 1985.
- Walraven, R., "Polarization Imagery," *Optical Engineering*, Vol. 20, No. 1, January/February 1981, pp. 14-18.
- Wolff, M., "Polarization of Light Reflected from Rough Planetary Surface," *Applied Optics*, Vol. 14, No. 6, June 1975, pp. 1395-1405.

In Situ Resource Utilization — Making Oxygen and Ceramics on the Moon

Carlton C. Allen, Thomas A. Sullivan,* and David. S. McKay*
Lockheed
*Johnson Space Center/SN

Abstract

The In Situ Resource Utilization (ISRU) program at JSC is developing technology necessary to "live off the land" on the Moon and planets. Three studies were conducted under this project in FY93. Oxygen was produced from actual and simulated lunar samples by two methods: hydrogen reduction and the sulfate process. A third project focused on the production of ceramics by sintering of simulated lunar soil. The ISRU program also produced a new lunar simulant, in response to requests from scientists and engineers.

Introduction

"Space resources must be used to support life on the Moon and the exploration of Mars. Just as the pioneers applied the tools they brought with them to resources they found along the way rather than trying to haul their needs over a long supply line, so too must space travelers apply their high technology tools to local resources" (McKay et al., 1992). The ISRU program at JSC is actively studying and supporting research in some of the key technologies projected for use by future explorers of the Moon and planets.

We have concentrated our efforts on three research programs. First, we produced oxygen from actual lunar materials and simulants by the method of high-temperature reduction with hydrogen gas. Second, we explored the production of oxygen using the sulfate process, based on proven technology from the chemical industry. Third, we fabricated ceramic "bricks" from lunar soil by a variety of sintering processes. In addition, we have produced a new lunar soil simulant and made it available to the research community.

Problem Statement

Oxygen Production

A future lunar base will need oxygen both for life support and rocket propulsion. Carrying all of this oxygen from the Earth would require a huge investment in propulsion and launch vehicles. Oxygen produced on the Moon could thus be one of the greatest performance-enhancing technologies for round-trip lunar missions.

Twenty different methods have been proposed for producing oxygen from lunar materials (Taylor and Carrier, 1992). Most of these proposals are theoretical, or backed by limited experimental evidence. Research is required to assess which processes are actually feasible,

and provide basic data to support design of flight hardware.

Ceramic Production

A lunar base will require large amounts of dense, strong construction material for thermal and dust control, as well as for radiation protection. The cost of transporting such material from Earth is prohibitive. Lunar soil, a fine-grained mixture of crushed rock and glass, has been proposed to meet this need. By analogy to familiar terrestrial construction techniques, the soil could be piled, bagged, sintered, or cast, depending on the specific need (Toups, 1990). Research is required to determine how these operations could be carried out on the lunar surface using local materials.

New Lunar Soil Simulant

The NASA Workshop on Production and Uses of Simulated Lunar Materials (McKay and Blacic, 1991) concluded: "Simulants of lunar rocks and soils with appropriate properties, although difficult to produce in some cases, will be essential to meeting the system requirements for lunar exploration." Researchers in a variety of scientific and engineering disciplines have called for materials that are well characterized, inexpensive, similar to lunar soils, and available in large quantities.

Approach

Oxygen from Hydrogen Reduction

Reaction of geologic materials in a reducing atmosphere at elevated temperatures converts FeO to iron metal and releases oxygen. This is among the oldest and most technologically mature of the numerous lunar oxygen production methods which have been proposed (Taylor and Carrier, 1992). Our oxygen production research has concentrated on three types of lunar materials: basalt, mare soil, and volcanic glass. In addition, we have investigated oxygen production from lunar simulants and the constituent minerals of lunar soil.

We have studied the release of oxygen by high-temperature reduction using hydrogen gas. Small (< 1 g) samples were reduced in a microbalance furnace, which measured oxygen release as weight loss through the course of each test. Experiments were also scaled up to over 1000-g samples using a newly developed oxygen-production testbed.

Oxygen from the Sulfate Process

This project explored modifications to a commercial process for releasing oxygen from the mineral ilmenite. Lunar simulant rocks and minerals were first dissolved in sulfuric acid. The acid solution was then electrolyzed to yield oxygen. Finally, any remaining insolubles were treated to recover sulfur, which was recycled to sulfuric acid. Each major process step was studied to explore kinetics and yields.

Ceramics from Sintered Lunar Soil

Many methods have been proposed to make construction material from lunar soil. We chose to study the production of ceramics by sintering, wherein compacted lunar soil is heated to the point at which localized melting at grain interfaces produces a strong, porous mass. Research focused on practical methods of sintering to make lunar bricks.

We set out to demonstrate how large, strong, crackfree bricks could be produced using a minimum of mass and energy. Experiments were designed to determine the range of conditions under which sintering takes place, as well as the best methods for compacting and heating the material. Using simulants, we compared the sintering behavior of various types of lunar soil.

New Lunar Soil Simulant

Development of a new lunar soil simulant was undertaken at JSC. The approach was to first locate a suitable deposit of glass-rich volcanic ash. The material was then characterized, ground to match the size of lunar soil, bagged, and made available for distribution.

Results

Hydrogen Reductions

High-temperature hydrogen reduction experiments on terrestrial analogs to lunar minerals, basalt, and glass have been completed. These tests have identified the contributions of all major phases to oxygen yield. They show that ilmenite and glass are the most reactive phases, followed by olivine and pyroxene (Allen et al., 1993).

Tests on actual lunar basalt, soil, and volcanic glass confirm these results (Gibson et al., 1994; Allen et al., 1994a). These first oxygen production experiments using lunar material demonstrated that oxygen yield from rock and soil is determined by the sample's ilmenite content. The oxygen yield from lunar glass is sensitive to both the iron oxide abundance and the reaction temperature. Maximum yields from high-titanium soil and iron-rich glass are 7.3% and 13.5% of the sample's total oxygen, respectively.

Complementary oxygen production experiments, using lunar simulant JSC-1, illustrate the complexity of

scaling up from ≤ 1 g samples to masses of over 1000 g (Allen et al., 1994a). We are continuing our research to determine how kinetics and yield data from tests on lunar samples can be used to support design of a lunar demonstration plant.

Oxygen from the Sulfate Process

We studied in detail the three major steps of the sulfate process, namely digestion, electrolysis, and sulfur recovery. Optimum acid digestion conditions were determined for simulated lunar soil and its individual constituent minerals. The parameters required to produce oxygen by electrolysis of the resultant solution were determined. Finally, several alternatives for the recovery of sulfur from the reaction products were investigated. A patent covering the entire process was recently granted (Sullivan, 1993).

Ceramics from Sintered Lunar Soil

Sintering of full-scale bricks from lunar soil simulants was accomplished by radiant heating to 1100°C for approximately 2 hours, followed by slow cooling. Small-scale precompaction, either by uniaxial pressure or vibration, proved critical for producing uniform bricks. The use of an insulating mold greatly improved product quality by minimizing thermal stress cracking (Allen et al., 1994b).

Sintering was also accomplished using a combination of microwave and radiant heating. This technique was shown to be extremely sensitive to thermal profile and sample configuration (Allen et al., 1994b).

New Lunar Soil Simulant

The JSC-1 lunar soil simulant was developed and fully characterized (McKay et al., 1994). JSC-1 was derived from volcanic ash of basaltic composition, which was ground, sized, and placed into storage. The simulant's chemical composition, mineralogy, particle size distribution, specific gravity, angle of internal friction, and cohesion were shown to fall within the ranges of lunar mare soil samples. The project yielded over 20 metric tons of lunar soil simulant for large-volume uses.

JSC-1 was produced specifically for large- and medium-scale engineering studies in support of future human activities on the Moon. Such studies include material handling, construction, excavation, and transportation. The simulant is also appropriate for research on dust control, space suit durability, and agriculture. JSC-1 is currently being used in studies of oxygen production and sintering. The simulant is available in large quantities to any qualified investigator, for only the cost of shipping.

Next Steps

Oxygen from Hydrogen Reduction

The major goal for FY94 is to determine the potential of a variety of lunar soil and volcanic glass samples for oxygen production. We will complete analyses of the reaction products of our initial tests and publish these results. We will perform additional tests on a wider range of lunar samples, including pyroclastic glass and highland and mare soils. The results will allow accurate prediction of the oxygen potential of any location on the lunar surface, and provide quantitative data for future mission planners.

A second goal is to use our testbed to scale up oxygen output to that of a lunar pilot plant. In the process, material-handling methods and instrument controls will be developed. A particularly important task is to quantitatively recover water from the hydrogen off-gas stream at a minimal cost in energy and complexity.

Oxygen from the Sulfate Process

Laboratory work on digestion, recovery of sulfur from the reactants, and electrolysis of the acid solution to produce oxygen were completed and the process was patented (Sullivan, 1993). No further work will be done on this project.

Ceramics from Sintered Lunar Soil

Laboratory work on lunar-derived ceramics has been completed and the results published (Allen et al., 1994b). No further work will be done on this project.

New Lunar Soil Simulant

Production and characterization of lunar simulant JSC-1 has been completed, and the material made available to the scientific and engineering communities. The results of our efforts have been published (McKay et al., 1994). No further work will be done on this project.

Acknowledgments

The experimental and analytical work described here was conducted at the Johnson Space Center. We are

grateful for the support of personnel from the experimental Petrology and Electron Beam Analysis Laboratories. The work of R.V. Morris and H.V. Lauer in the Mössbauer and Spectroscopy Laboratories was essential to the successful completion of this research. The In Situ Resource Utilization Program is supported by the JSC Director's Discretionary Fund.

References

- Allen, C.C., Morris, R.V., Lauer, H.V., Jr., and McKay, D.S., Microscopic iron metal on glass and minerals—a tool for studying regolith maturity. *Icarus*, 104, 1993, 291-300.
- Allen, C.C., Bond, G.G., and McKay, D.S., Lunar oxygen production—a maturing technology. *Eng.*, *Constr.*, *and Ops. in Space IV*, in press, 1994a.
- Allen, C.C., Graf, J.C., and McKay, D.S., Sintering bricks on the Moon. *Eng.*, *Constr.*, *and Ops. in Space IV*, in press, 1994b.
- Gibson, M.A., Knudsen, C.W., Bruene-man, D.J., Allen, C.C., Kanamori, H., and McKay, D.S., Reduction of lunar basalt 70035—oxygen yield and reaction product analysis. Submitted to *J. Geophys. Res. Planets*, 1994.
- McKay, D.S. and Blacic, J.D., Workshop on Production and Uses of Simulated Lunar Materials, LPI Tech. Rpt. 91-01, Lunar and Planetary Institute, 1991.
- McKay, D.S., Carter, J.E., Boles, W.W., Allen, C.C., and Allton, J.H., JSC-1—a new regolith simulant. *Eng.*, *Constr.*, and *Ops. in Space IV*, in press, 1994.
- McKay, M.F., McKay, D.S., and Duke, M.B., *Space Resources, SP-509*, National Aeronautics and Space Administration, 1992.
- Sullivan, T.A., Method for producing oxygen from lunar materials, U.S. Patent # 5,227,032, 1993.
- Taylor, L.A. and Carrier, W.D., III, The feasibility of processes for the production of oxygen on the Moon. *Eng., Constr., and Ops. in Space III*, Am. Soc. Civil Eng., 1992, 752-762.
- Toups, L., A survey of lunar con-struction techniques. *Proceedings of Space 90*, Am. Soc. Civ. Eng., 399-408, 1990.

An Iterative Technique to Reduce Image Degradation Caused by Lens Defocus and Linear Motion Blur

David Pitts and Ranjit Bhaskar*
Johnson Space Center/SN
*Lockheed

Abstract

Imagery taken of the Space Shuttle is often degraded by lens defocus or image motion blur. Conventional space-domain filtering techniques allow enhancement of some features but also substantially increase noise. Frequency-domain techniques, such as magnitude-phase merging or edge extraction, often induce artifacts that degrade the image further. A procedure was developed at the Video Digital Analysis System (VDAS) Laboratory at the Johnson Space Center to improve on existing methods of image restoration given limited a priori scene information. The procedure approximates the modulation transfer function (MTF) of the input image from edge information within the scene and then utilizes an iterative technique to reduce the amount of blur.

These procedures were applied to a set of test images of the Space Shuttle obtained from film and video cameras at the launch site. Using these two sources gave a range of image quality over which to test the techniques. Separate procedures were developed to deal with linear motion blur and lens defocus. The iterative process allows the user to modify the frequency-domain filtering mechanism to achieve desired results.

Output from these procedures showed a substantial visual improvement in image quality. Moreover, the techniques appeared to work as well on video as they did on film imagery. Future effort will be directed at reducing the ringing artifacts inherent in frequency-domain sharpening procedures.

Introduction

The sources for image degradation can usually be classified under one of three groups: atmospheric blur, camera system blur, and motion blur. One of the topics currently being explored at the VDAS laboratory is whether assumptions of uniformity can be applied in the restoration of such degraded images.

Atmospheric degradation can be attributed to one or more of the following factors: Rayleigh (molecular), Mie (water vapor and dust particles), and nonselective (water droplets) scattering and scintillations. In general, as the optical depth increases between a camera and its target, atmospheric factors play a larger role in image quality. Camera filters that cut off shorter wavelengths can be used to minimize the effects of haze. Other atmospheric effects are not as easily removed.

As the rays from an object pass through a camera, each successive component degrades the output image. System-induced distortions pose a serious problem in

image analysis. A manifestation of such a problem is the simple one of lens defocus. One technique used to solve this problem is generation of an MTF, which requires knowledge of the optical quality of each system component. This metric could then be used to design a filter that effectively removes the induced distortions from the output image. However, accurate MTF information is rarely available to the end user. Other approaches rely on the enhancement of linear features simply by increasing local area contrast. These techniques are limited in that they magnify noise within the region of interest.

The acquisition of moving targets can result in motion blur. If one were able to mathematically describe that motion in terms of image coordinates, the resultant blur could theoretically be removed using spatial filters. In reality, however, if the motion was nonlinear, these procedures would become prohibitively complicated. Conventional space-domain-based techniques would not remove such effects.

Problem Description

The image on a photograph has been degraded by the atmosphere, the camera system lens, internal optics, and film processing and enlargement procedures. The problem for the end user is how to restore the image with little or no a priori information about any of these processes. Also, while procedures that address different causes of degradation exist, most require intensive time on and knowledge of the central processing unit (CPU).

Approach

There are two underlying assumptions in this research. One is that the user does not have prior knowledge of the actual sources of image degradation. The other is that some linear object in the original scene is identifiable on the image. Since this work was initially meant to address the issue of blurred Space Shuttle images, the latter was not a problem.

Typical data analyzed at the VDAS Laboratory are in either film or video format. Thus, examples of each were used as the input images. Three specific cases are presented in this study. One is an actual blurred image of the Space Shuttle that was digitized from a photographic print taken during the STS-37 launch. This image would include all the different types of degradation discussed except noticeable motion blur. The second image is the same as the first except that a motion blur was imparted to it by moving the photograph during the digitization

process. The third image is a single video frame of the external tank. This video was obtained by crew members on STS-57.

Method

This work involved finding a metric to quantify image quality and then implementing it into the restoration filter.

The MTF of the blurred image is generated in the following manner: an assumption is made that the degradation in the image is uniform—that is, the blur is uniform across the region of interest. An edge (along the vehicle) is identified and a digital count profile across that edge is generated. A line spread function (LSF) is calculated by taking the derivative of this profile.

$$LSF(x) = \frac{d(profile)}{dx}$$

Because of the uniform blur assumption, the LSF can be rotated to create a point spread function (PSF).

$$PSF(x) \approx rotated(LSF(x))$$

This PSF is a representation of how much distortion a single point in the scene undergoes. The PSF is then Fourier transformed into the frequency domain to generate the MTF.

$$MTF(f) \Leftrightarrow PSF(x)$$

Now that the metric defining the image blur has been calculated, it can be incorporated into the power spectrum equalization (PSE) restoration filter in image form.

$$PSE = \frac{1}{MTF(f)\sqrt{1 + \left\{1/k \cdot MTF^{2}(f)\right\}}}$$

This filter also utilizes a user-driven constant (k) that defines the estimated signal-to-noise ratio of the image. Checks are then built-in to prevent the denominator from approaching zero.

$$Output(f) = Input(f) * PSE$$

The resultant is then back-transformed into the space domain and viewed as the output image.

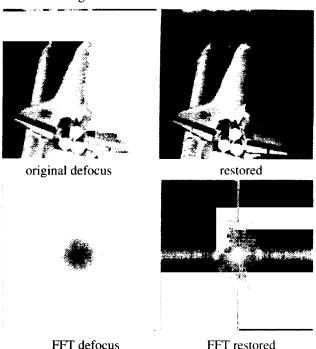
$$Output(x) \Leftrightarrow Output(f)$$

This image is visually compared to the original. This entire procedure is repeated until the results are satisfactory.

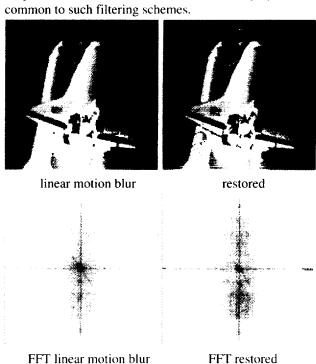
In the case of linear motion blur, the MTF is generated by finding the profile of an edge and projecting this edge along the motion direction instead of rotating it.

Results

The following images show the results obtained by using this iterative approach on each data type. Each input scene was digitized to a single band grey-scale 512 x 512 image.

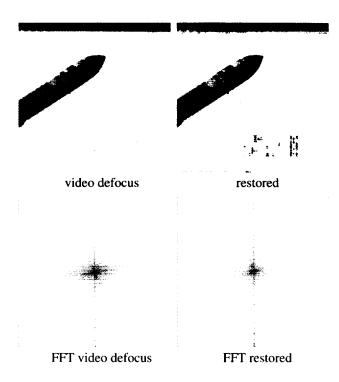


Note the improvement in the restored image. Specifically, the lettering, the flag, and the cockpit windows all appear sharper than they do in the original. The fast Fourier transform (FFT) magnitude of each image is shown to identify the filter's effects on specific frequencies. One detrimental effect is the ringing artifact common to such filtering schemes.



Note the linear blur in the vertical direction in the original image. Compare this to the restored image—especially in those high frequency areas. Now the ringing artifact is displaced by horizontal banding since the frequencies in that direction were the ones that were modified.

Video images have inherent difficulties because of the horizontal banding that results from interleaved frames. The "noise" at the top and bottom of the image is an artifact produced when converting the video image into a standard size (512 x 512 pixel) picture. The following scene displays this artifact.



Conclusions

A substantial improvement in visual quality was obtained on each of the different types of input data. One point that needs to be emphasized is that several improvements to the procedures have been implemented over the course of the past year.

Using subsets of the full images to generate the MTFs has made the process much less CPU-intensive. The iterative procedure allows the user to adjust the signal-to-noise ratio estimate until desired results are achieved.

Future work will attempt to minimize the ringing artifacts with an adaptive frequency-domain filter. Other variations of the power spectrum equalization filter will also be tried.

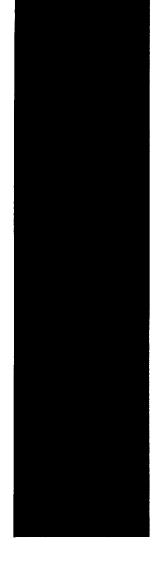
Since one of the initial goals of this research was to make this procedure user-friendly, the next step involves porting the code over to a UNIX platform and generating better graphical user interfaces.

Acknowlegments

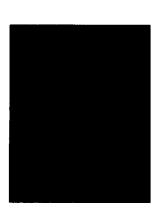
Funding for this work was provided by the Photo/TV Analysis Project of the Space Shuttle Operations Program.

Bibliography

- Bundschuh, Bernhard, "Adaptive Image Restoration and Reconstruction," Proc. Third Int. Seminar Digital Image Process-ing in Medicine, Remote Sensing, and Visual Information, Riga, Latvia, 1992, p. 511.
- Gaskill, J. D., Linear Systems, Fourier Transforms, and Optics, John Wiley & Sons, New York, 1978, p. 554.
- Gonzalez, R. C., and P. Wintz, *Digital Image Processing*, 2nd ed., Addison-Wesley, Reading, Massachusetts, 1987, p. 503.
- James, S., J. Lee, P. V. Budak, C. R. Lin, R. M. Haralick, "Adaptive Image Processing Techniques," *SPIE Intelligent Robots Computer Vision: Sixth in a Series*, Vol. 848, 1987, pp. 255-262.
- Lillesand, T. M., R. W. Kiefer, *Remote Sensing and Image Interpretation*, John Wiley & Sons, New York, 1979, p. 612.
- Mayers, M., L. Wood, J. Hood, "Adaptive Spatial Filtering," *Proc. 1988 ACSM-ASPRS Fall Convention*, Virginia Beach, VA, Sept., 1988.
- Russ, J. C., *The Image Processing Handbook*, CRC Press, Boca Raton, Florida, 1992, pp. 165-275.



Space Systems



An Analysis of the Modes and States for Generic Avionics

D. A. Pruett Johnson Space Center/EK11

Abstract

NASA is entering into a new era of space exploration. Long-term objectives such as returning to the Moon and then on to Mars and beyond remain much the same, but decreasing funding levels dictate that new, more efficient and less costly ways of doing business be implemented. To further the accomplishment of these long-term objectives within funding availability, the Lockheed Engineering and Sciences Company (LESC), under the auspices of JSC's Flight Data Systems Division, developed the Space Generic Open Avionics Architecture (SGOAA) [PRU93], an open systems architecture for design and development of avionics for future space vehicles. (The SGOAA reference model is described in [WRA93].) An extension of the SGOAA development effort is a simulation of the actual dynamic behavior of the SGOAA in a demonstration system design. Modes and states analysis provides a valid approach for the description of dynamic system behavior. Understanding the dynamic behavior of a system by developing a system model in the early stages of a project will eliminate much of the uncertainty now inherent in the design process. This paper presents the results of a study into the definition of modes and states for application to a simulation of space generic avionics.

Introduction

When new space vehicles are developed, typical technical approaches concentrate on defining the functionality needed in those vehicles and the capabilities which must implement the functions. Specifications often describe the avionics processes, inputs, and outputs, but it is often late in the program development before the behavior of the functions and their system/subsystems is addressed, e.g., the definition of which outputs respond to which inputs, when, and under what conditions. Yet the behavior of avionics systems is key to the successful operation of space vehicles, and a more thorough understanding of the space avionics behavior is needed prior to design commitment. Behavior (in this context) is described by the mission, vehicle and system/subsystem configurations and potential interactions; by the scenarios which map out how interactions should proceed; and by the rules set up by developers on what inputs may be given to, and what responses are desired in return from, the avionics systems. This behavior may also be captured in part by descriptions of the modes and states of the system.

Problem Statement

This study had two primary objectives. The first objective was to develop a more precise definition of the modes and states to which generic avionics can be subjected. The second objective was to provide inputs to the development of a computer model for simulation of the behavior of the SGOAA for the entities in flight vehicle core avionics. The modes and states analysis described in this paper was partially based on the modes analysis performed for Space Station Freedom (SSF) before the 1993 restructure.

Approach

Modes and states were defined by studying the interfaces for a space vehicle. The skin of the spacecraft was defined to be the boundary for partitioning between external and internal interfaces. The boundary between modes and states was based on partitioning between activities planned and directly controlled by humans (i.e., a mode) and those activities directed, in response, by the machine (i.e., a state). Some activities were recognized as transcending all boundaries, such as operational procedures. However, even such transcending activities can be implemented by partitioning them along an established boundary; when one does so, then the procedures can be more closely linked with the activities and subsystems defined by that boundary. Such linkages can enable transcending activities to be more clearly understood and implemented.

Results

Presented in this report is a top level overview of the modes and states analysis performed. [RW793] presents a detailed description of the modes and states defined as applicable to space generic avionics.

A mode is a predefined set of hardware and software configurations, and associated procedures used to organize and manage the conditions of operation for an avionics system's behavior, as planned (in advance) or directed by a human. Modes may have several levels of expanding detail. Mode models were developed to define the set of modes and mode transitions governing the behavior of a generic mission or vehicle. Generic mode transition diagrams illustrating mode models are provided in [RW793]. Tailoring of these models to a specific mission or vehicle would require identification of the set of allowable commands and responses for each mode.

States are the activities that a system or subsystem adopts in response to a mode input. A system/subsystem may step though several states in transitioning between one mode and another. The key difference between a mode and a state is that a mode is planned in advance or directed by a human, while a state is the response configuration adopted by a processing controlled system/subsystem. A state may be a complex configuration with many subsets, or it may be a simple configuration at the lowest level consisting of a switch setting such as on-off. State transition models (state transition diagrams) for space generic avionics were developed and are provided in [RW793].

Four types of mode and state models, as illustrated in Figure 1, were defined:

- Mission mode model governing mission element behavior
- Vehicle mode model governing internal vehicle behavior
- Subsystem state model identifying potential subsystem element behavior, with the Avionics Subsystem used as an example
- Function state model identifying potential functional element behavior, with Space Data System Services (SDSS) used as an example

Each <u>mission</u> mode may cause multiple <u>vehicle</u> modes to occur or be blocked. Each <u>vehicle</u> mode may in turn cause multiple <u>subsystem</u> states to occur or be blocked. Similarly, each <u>subsystem</u> state may cause multiple <u>function</u> states to occur or be blocked. Activities at each level are linked to activities at other levels through the creation of commands, controls, and events which are detected by other entities at the same or other levels. These detections act as inputs to the detecting entity, causing it to act if necessary according to the rules governing that entity's behavior. The resulting sets of lower level configurations may be different for each higher level mode or state.

Mission Modes

Modes describe the control of the interactions of entities at the highest level of a mission, such as the space vehicle with other facilities or platforms. The mission entities are the major stand-alone elements or systems involved in a mission, and are under the operational control of a mission control entity. The behavior of the mission controller (MSN_CTRL) entity is described in [RW793] in a mission mode model. The key is that the mission controller (MSN_CTRL) is a processing entity which

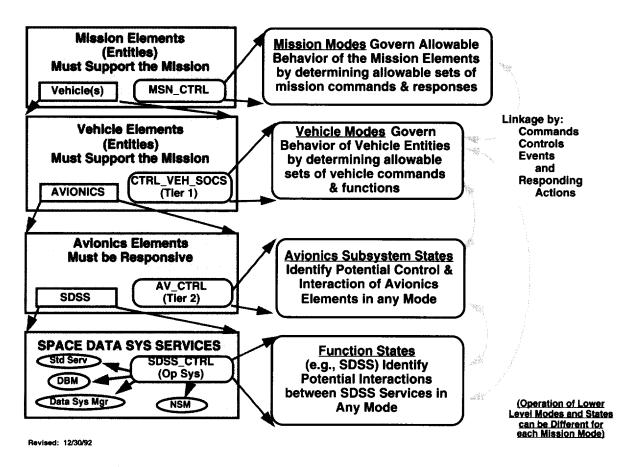


Figure 1. Four types of modes and states developed for the computer model.

governs the interactions of its "sibling" mission level entities. This controller determines what sets of mission commands and responses are allowed under what conditions, and at what times or in what sequences. Thus, the mission modes define the sets of allowable mission element behavior which the MSN_CTRL can effect. Each mode encompasses the set of commands, controls, events, conditions, and procedures needed to safely operate the mission in a stable manner.

Vehicle Modes

Vehicle modes describe the control of the major vehicle entities in support of the current mission mode. The vehicle entities are the major subsystems, such as the power, propulsion, fuels, and oxidizer, and avionics subsystems such as Guidance, Navigation and Control (GNC) and Communications and Tracking (C&T), etc., which constitute a spacecraft. Each of these major subsystems must be under the operational control of some control entity as defined in the SGOAA Space Operations Control Subsystem (SOCS). In the SSF program, CTRL_VEH_-SOCS is performed by the Integrated Station Executive.

The command and control software and the embedded avionics hardware associated with each vehicle subsystem can be partitioned into modes and states by a plane through the subsystem corresponding to the partitioning between subsystems command and control, and avionics elements. Thus, for each subsystem, the mode commands result in the vehicle subsystems achieving the mode associated with the command. Ten separate generic space vehicle modes were identified during this study and are described in [RW793]. For each mode, there are associated state controls issued to the avionics hardware. The state controls result in the avionics elements achieving the state associated with the commanded mode.

Subsystem States

Avionics subsystem states are the behaviors internal to a vehicle which identify the potential response configurations a subsystem may adopt or make in changing between modes. In this study we addressed only the avionics entities, i.e., the hardware, software, and processing procedures contained in the avionics subsystem states. The analysis methodology is extendable to major vehicle entities other than the avionics. The avionics subsystem states as defined in [RW793] describe the control of the major avionics entities in support of the mission and vehicle modes. Each of the major avionics subsystems must be under the control of some control entity such as GNC_CTRL, C&T_CTRL, SOCS_CTRL, and SDSS_CTRL. Since this analysis was intended to be implementation independent, an AV_CTRL entity was defined to be the sum of these separate _CTRL entities.

The key is that the avionics controller (AV_CTRL) is a processing entity which governs the interactions of its "sibling" avionics level entities. This controller determines what sets of mission, vehicle, and avionics commands and other inputs meet the predefined criteria for acceptance by the avionics, under what conditions these inputs are acceptable, the allowable (predefined) responses to these inputs, and at what times or in what sequences inputs will be accepted and responses initiated. This behavioral control is based on rules and procedures established by humans, and implemented by the avionics subsystems. These are states rather than modes because they are intervening steps the avionics establish in carrying out human commands. For each mode change, there may be several state transitions until the final mode is achieved.

Function States

Function states are the lowest level states shown in figure 1 and describe the control of the major functional entities within an avionics subsystem. In this study we focused on the SDSS Subsystem functional entities as defined in [WRA93]. These services are controlled by an operating system service and are the input/output data services, data base management, network services, and data system manager. The operating system is a component of the AV CTRL entity at the tier 2 level. The operating system is also defined to be the SDSS_CTRL entity or function. It controls its sibling SDSS functions. The analysis could be similarly performed for the functions in other avionics subsystems such as GNC or C&T. The function states as defined in [RW793] describe the control of the functional entities in the SDSS. Regardless of the mission mode, vehicle mode, or avionics state, any interaction within the system in other than OFF modes or states will require some support from SDSS service functions. For each avionics state change there may be several operating system and data system service calls until the final avionics state change is achieved.

Conclusions and Recommendations

The Mission and Vehicle Modes chosen by crew or ground control, and the Avionics Subsystem States subsequently selected, have no apparent effect on the definition of process states and their transition structure, as shown at the Function State transition level. What is affected is the capability of these functional processes to operate, which depends on what conditions and controls are true/false (not their transition structure). Mode changes can cause a switch from one state model to another, or from one set of allowable behaviors in a model to another set of allowable behaviors. Since it is the avionics functional processes and their state transitions which are actually implemented in hardware and software, this means their design is relatively insensitive to changes in desired use of modes and avionics subsystem states, which can thus be definitized later without drastic cost impact (as long as their scope is consistent).

Mode commands cause different sets of lower-level commands, controls, events, and conditions to govern when activities take place, but this is a <u>use</u> of the state transition diagrams, not impacting the structure of the diagrams. Thus, for example, the same services offered by SDSS are available for any subsystem or function to call upon regardless of the modes of the system. At higher levels of states and modes, the effects of crew or ground control desires become more pronounced. Specific crew or ground control desired actions can be broken into their component parts using this model of system behavior in order to determine if the system will respond in the way the developers intended.

This study identified the boundary conditions applicable to a simulation of the SDSS function state. Development of such a simulation is now under way to define the behavioral responses of the SDSS to possible activities generated in the other modes and states of an advanced generic avionics system.

It is recommended that simulations be developed for the complete behavioral model defined during this study. A mission mode simulation would enable the crew to investigate mission behaviors in a documented manner that could be captured by developers. A vehicle mode simulation would enable the potential interactions of the crew and subsystems to be investigated in a rigorous manner. An avionics subsystem state simulation would investigate the behavior of the system in responding to changes in vehicle modes. A function state simulation for each of the avionics functions could establish the boundaries of acceptable behavior, and identify unacceptable system/ subsystem responses. Defining such behavioral patterns

before designing future systems will reduce the costs of redesign or rebuilding systems or subsystems to meet unexpected and unacceptable behaviors discovered in development or flight testing.

References

- [PRU93] Pruett, D., "Avionics Reference Model," Research and Development Annual Report, NASA Technical Memorandum 104777, August 1993.
- [RW793] "An Analysis of the Modes and States for Generic Avionics," Job Order 60-911 for the JSC, LESC-30749, NASA CR-188253, July 1993.
- [SUL92]Sullivan, B. (Team Chairman), "Integrated Avionics Software Description PSAR Review Copy," IBM, 6 November 1992.
- [WRA93] Wray, R.B. and Stovall, J.R., "Space Generic Open Avionics Architecture (SGOAA) Reference Model Technical Guide," Job Order 60-911 for JSC, LESC-30347-A, NASA CR-188246, December 1992.

Acknowledgments

This document has been produced by Messrs. John R. Stovall and Richard B. Wray of LESC, codevelopers of the SGOAA and of the Modes and States Avionics Architecture Model presented in this paper. Special acknowledgment is also given to Mr. Dave Pruett of JSC for supporting this study, providing constructive criticism and for assisting in development of the SGOAA and performance of the Advanced Architecture study of Modes and States for Generic Avionics.

Arc-Jet Testing of Damaged RCC-3 Repaired Using Preceramic Polymers

Stuart T. Schwab,* Renee C. Graef,* Yi-Min Pan,*
Donald M. Curry, Vuong T. Pham, James D. Milhoan, and
Donald J. Tillson
Johnson Space Center/ES
*Southwest Research Institute

Abstract

Current techniques for repairing damage to coated carbon-carbon composites are costly and time consuming, largely because the part cannot be repaired in the field. The availability of repair techniques that could be applied in the field or on the shop floor could dramatically reduce the mission turnaround time required for systems containing critical carbon-carbon components, such as the Space Shuttle Orbiter vehicle. One approach to the development of field-applied repair techniques is based on the utilization of preceramic polymers, which are organometallic polymers that convert to ceramic at temperatures well below those required by current repair techniques. The Southwest Research Institute has developed a number of polymeric precursors to silicon nitride that have been shown to be effective in restoring useful lifetimes under static test conditions to coated ACC-4 and RCC-3 substrates that had suffered impact and other types of damage. This study presents the results of simulated reentry tests conducted on damaged RCC-3 that had been repaired using preceramic polymers. These results suggest that polymer-derived ceramic repairs can effectively protect carbon-carbon substrates from oxidation during reentry.

Introduction

Superior high-temperature mechanical properties and strength-to-weight ratio provide carbon-carbon composites with distinct advantages over other materials that are being considered for application in hypersonic vehicles.¹ Unfortunately, because carbon materials oxidize readily at temperatures above approximately 660°F (350°C), they must be coated if the structures composed of them are to have useful lifetimes. At present, ceramic coatings composed primarily of silicon carbon (SiC) or silicon nitride (Si,N_i) are used to protect carbon-carbon composites from oxidation. These coatings are applied using pack cementation, chemical vapor deposition, or a combination of these techniques.² Although these methods produce coatings which impart useful lifetimes to carbon structures, they require extreme conditions and specialized equipment. Structures with damage to the oxidation protection coating that results in exposure of the carbon-carbon substrate must be removed from the vehicle and shipped off site for repair. The availability of techniques which

can apply coatings in the field or on the shop floor could drastically reduce the time and costs associated with the manufacture and maintenance of carbon-carbon structures.

The field of polymeric precursors to ceramics has been reviewed.³ Preceramic polymers are composed of a chain or a backbone of main group inorganic elements with organic appendages. When heated to sufficient temperatures under the proper conditions, these organic appendages are shed through a process generally referred to as a pyrolysis, which yields an amorphous, covalent ceramic.⁴ Subsequent heat treatment transforms this amorphous material into a crystalline ceramic. Polymeric precursors to Si₃N₄ and SiC have been reviewed.⁵ Because the thermal expansion behavior of Si₃N₄ matches that of carbon-carbon more closely than does silicon carbide, ² it was felt that Si₃N₄ coatings might have the potential for superior performance as coating materials on carbon-carbon.

Approach

A particularly useful family of polymeric precursors to Si₂N₂ has been developed at the Southwest Research Institute (SwRI). These polymers, which are known as perhydro-polysilazanes, contain only the elements silicon, nitrogen, and hydrogen, and therefore convert to carbonfree ceramics when fired. These polymers are isolated as waxes or low-viscosity, thermosetting liquids that exhibit ceramic yields of 80% by weight or greater. Although originally developed as a binder for Si₃N₄ powder processing,6 these polysilazanes have been shown to be effective matrix precursors for the infiltration/pyrolysis processing of fiber-reinforced Si₂N₄ composites.⁷ We have also explored their utility in the repair of damaged oxidation protection coatings on carbon-carbon composites.8 We report here the performance of polymer-derived repairs made to RCC-3 when tested under simulated reentry conditions.

Experimental Results

Damage and Repair

Four coated RCC-3 specimens (specimen numbers 20, 22, 24, and 25, each 2.78 in. diameter) were received from JSC. The circular pattern shown in Figure 1 was

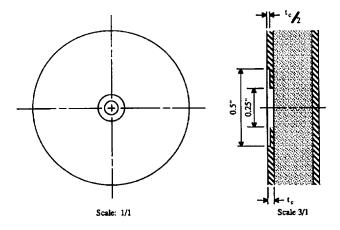


Figure 1. Damage pattern for RCC-3 specimens.

machined into the center of each disk. The machined specimens were subsequently dried at 175°F (80°C) under vacuum and were then transferred to a glove box. Before coating repair was initiated, the machined surfaces were roughened with sandpaper to promote mechanical adhesion between the coating and the substrate. A thin layer of pure polymer was applied with a small paint brush to the roughened surface, followed by polymer-loaded (70% by weight) material with submicron a-Si₃N₄, which was applied with a small spatula. The repaired specimens were cured in a vacuum bag under ambient applied pressure at 355°F (180°C) for 6 hours. After curing was complete, the specimens were removed from the vacuum bag and fired to 2550°F (1400°C) under flowing nitrogen. A second coating of powder-loaded polymer was applied, followed by three coatings of pure polymer (no powder loading), using the curing and firing procedure described above for each, for a total of five coating cycles. After the fifth coating cycle, the specimens were fired to 3090°F (1700°C) under nitrogen.

During optical examination of the repair sites following the 3090°F (1700°C) firing, two of the four specimens

(numbers 20 and 22) were found to have minor flaws (small pits) in the repair surface. The flaw sites were filled with powder-loaded polymer, and the specimens were cured and fired as before. The damage site received an additional overcoat of pure preceramic polymer (cured and fired as before) for a total of two additional coating cycles. These two specimens were subjected to an additional 3090°F (1700°C) heat treatment prior to delivery to JSC for testing. The rear faces of each specimen had some discoloration where the alumina specimen holder had contacted the sample during the final 2550°F (1400°C) firing. The pure preceramic had a tendency to spread over the surface of the entire specimen during cure. On firing, polymer-derived ceramic was deposited over the surface of each specimen, giving the specimens a somewhat mottled appearance.

Testing

Samples were tested at JSC in the 10MW Atmospheric Reentry Materials Structures Facility (ARMSEF).9 Specimen surface temperatures were determined using a 0.865µ pyrometer. The experimental matrix is summarized in Table 1—note that the two specimens which had undergone only five coating cycles (numbers 24 and 25) were subjected to two test cycles. The CAMA6G test procedure is designed to simulate a mission abort scenario and is described elsewhere. 9.10 The highest temperature reached during a typical CAMA6G cycle is approximately 3350°F (1843°C).

Specimen 20, which had a total of seven coating cycles, is shown prior to test in Figure 2 and after test in Figure 3. The specimen fell just short of the target temperature of 2900°F (1593°C), and it reached a steady state of approximately 2890°F (1588°C). Although some minor discoloration is evident, the repair area appears to have sustained little, if any, degradation. Microstructural analysis revealed no evidence of fiber or matrix oxidation.

Table 1. Summary of test conditions for RCC-3 specimens

Specimen	Coating Cycles	Test Cycles	Temperature (°F/°C)	Pressure (psf)	Cycle Duration	Accumulated Cycle Time (sec)
SwRI 24/604	7	1	2900/1593	100	900	900
SwRI 25/607	5	1	3000/1649	100	450	450
SwRI 25/607		2	3000/1649	100	450	900
SwRI 25/606	5	1	3100/1704	100	450	450
SwRI 24/606		2	3100/1704	100	450	900
SwRI 22/605	7	1	CAMA6G	CAMA6G	118	118

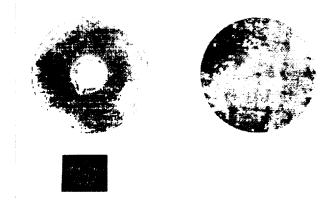


Figure 2. Repaired SwRI Specimen 20 prior to test.



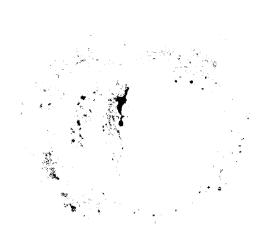
U-005 SWRI 20/604 POSTTEST 2900 °F FRONT

Figure 3. Test face of SwRI Specimen 20 after exposure to 2890°F (1588°C) at 100 psf for 15 minutes.

Specimen 24, which had a total of five coating cycles, is shown following the second test cycle in figure 4. Although discoloration and some surface roughness is evident in the repair region following the first test cycle, the polymer-derived ceramic materials appear intact. After the second test cycle (Figure 4), a small pit was observed near the center of the repair. However, microstructural analysis revealed no degradation to the RCC-3 substrate.



Figure 4. Test face of SwRI Specimen 24 after second 3100°F (1704°C) exposure.



SWRI 22 POSTTEST VIEW
CAMA-6G ENVIRONMENT
CONTROLLED SURFACE TEMPERATURE
TOTAL EXPOSURE: 1 CYCLE FOR 118 SEC.

Figure 5. Repaired SwRI Specimen 22 after exposure to the CAMA6G environment.

Specimen 22 is shown after exposure to the CAMA6G environment in Figure 5. Although it is clear that a substantial portion of the factory coating and the repair material did not survive the CAMA6G exposure, part of the central portion of the repair material appears to be present. Examination of the surface at higher magnification confirms total loss of the factory coating in the

blackened regions of the specimen and reveals the presence of what appears to be remnants of the polymer-derived ceramic in the repair area. The bubbled surface morphology of the repair region suggests substantial volatile formation. The conditions of the CAMA6G test are believed to be well beyond the transition from passive to active oxidation for both SiC and Si3N₄ materials, ¹¹ and it appears likely that the bubbles were produced by escaping SiO.

Conclusions

Despite its simplicity, the preceramic polymer repair technique provided excellent protection to the RCC-3 substrate at temperatures as high as 3100°F (1700°C) under simulated reentry conditions for short periods. The polymer-derived Si3N₄ may undergo the transition from passive to active oxidation at temperatures lower than those found for Si₃N₄ processed through other techniques; however, improved processing to yield stoichimetric and crystalline Si₃N₄ has the potential to raise substantially the active oxidation threshold. Further refinement of the preceramic polymer-based repair technique has the potential to yield a simple, but effective method of repairing damaged coatings on carbon-carbon composites—a technique that may shorten the time and expense required to refurbish the Space Shuttle Orbiter between missions.

Acknowledgment

This effort was funded by JSC through grant T-2940S. The authors acknowledge with gratitude the technical contributions of Ms. S. Salazar, Mr. R. J. Railsback, Mr. A. E. Nicholls, Mr. D. N. Weed, and Ms. L. L. Ramon. More details of this study can be found in NASA CP 3235, 17th Conference on Metal Matrix, Carbon and Ceramic Matrix Composites, 1993.

References

¹Buckley, J. D., *Cer.Bull*, 67, 1988. pp. 364-368.

²(a) Strife, J. R., and Sheehan, J. E., Cer. Bull., 67, 1988, pp. 369-374; (b) Sheehan, J. E., "Ceramic Coatings for Carbon Materials," in *Proceedings of the 4th Annual Conference on Materials Technology: Recent Research into Carbon-Carbon Technology*, M. Genisio, ed., Materials Technology Center, Southern Illinois Univ. at Carbondale, 1987, pp 56-98.

- ³(a) Wynee, K. J., "Ceramics via Polymer Pyrolysis," in Transformation of Organometallics into Common and Exotic Materials" Design and Activation, pp. 89-96; (b) Wynne, K. J., and Rice, R. W., Ann. Rev. Mat. Sc., 14, 1984, pp. 297-334; (c) Rice, R. W., A. Ceram. Soc. Bull., 62, 1983, pp. 889-892; (d) Peuckert, M., Vaahs, T., and Bruck, M., Adv. Mater., 2, 1990, pp. 398-411; (e) Toreki, W., Polymer News, 16, 1991, pp. 6-14; (f) Pouskouleli, G. Ceramics International, 15, 1989, pp. 213-119; (g) Mutsuddy, B. C., Ceramics International, 13, 1987, pp. 41-53.
- ⁴Soraru, G. D., Babonneau, F., and MacKenzie, J. D., *J. Mater. Sci.*, 25, 1990, pp. 3886-3893.
- ⁵Ziegler, J. M., and Fearon, F. W. G., (eds.), *Silicon Based Polymer Science*, Advances in Chemistry Series #224 (American Chemical Society, Washington, D.C., 1990).
- 6(a) Schwab, S. T., Graef, R. C., Davison, D. L., and Pan, Y.-M., Polymer Preprints, 32, August 1991, pp. 556-558; (b) Schwab, S. T., and Blanchard-Ardid, C. R., "The Use of Organometallic Precursors to Silicon Nitride as Binders," Mat.Res.Soc.Symp.Proc., 121, 1988, pp. 581-587; (c) Schwab, S. T., Blanchard, C. R., Graef, R. C., "The Influence of Preceramic Binders on the Microstructural Development of Pressureless Sintered Silicon Nitride" (submitted to J. Mater.Sci.).
- ⁷Schwab, S. T., Graef, R. C., Pan, Y. -M., and Davidson, D. L., "Infiltration/Pyrolysis Processing of SiC Fiber-reinforced Si₃N₄ Composites," NASA-CP 3175 (1992), Part 2, pp. 721-738.
- 8(a) Schwab, S. T., and Graef, R. C., "Repair of Oxidation Protection Coatings on Carbon-Carbon Using Preceramic Polymers," NASA-CP 3133 (1991), Part 2, pp. 781-798; (b) Schwab, S. T., Graef, R. C., and Lutfi, D. E., "Repair of Oxidation Protection Coatings on RCC-3 Using Preceramic Polymers," NASA-CP 3175 (1992), Part 2, pp. 599-622.
- Curry, D. M., Yuen, E. H., Chao, D. C., and Webster, C. N., "Space Shuttle Orbiter Carbon-Carbon Oxidation Performance," in *Damage and Oxidation Protection in High Temperature Composites*, ASME Publication AD-Vol. 25-1, 1991, pg. 47-64.
- ¹⁰Rochelle, W. C., Battley, H. H., Grimaud, J. E., Tillian, D. J., Murray, L. P., Lueke, W. J., and Heaton, T. M., "Orbiter TPS Development and Certification Testing at the NASA/JSC 10MW Atmospheric Reentry Materials and Structures Evaluation Facility," AIAA-83-0147.
- ¹¹Vaughan, W. L., and Maahs, H. G., *J. Am. Cer. Soc.*, 73, 1990, pp. 1540-1543.

3-10

EMU Electronic Cuff Checklist Development

Jose A. Marmolejo Johnson Space Center/EC

Abstract

An electronic version of the paper checklist currently used by crew members performing an extravehicular activity (EVA) from the Space Shuttle Orbiter is being developed at JSC. This electronic checklist is expected to improve EVA productivity by providing the astronauts with a portable, on-orbit programmable, self-contained information display system that will allow them to have access to a much larger database than is currently provided by the space suit paper checklist. In this paper, we describe the electronic cuff checklist design, its current development status, and a planned on-orbit evaluation of the unit in FY94.

Introduction/Background

Because EVA missions are more numerous and complex, the amount of information required by EVA astronauts has grown. Presently, astronauts who perform EVAs rely on a paper, cuff-mounted checklist. This checklist is limited to 25 3.5-in. by 4.5-in. sheets (50 pages including front and back). Its pages contain text and simple graphics that will aid the astronauts in performing a particular EVA mission. Although this cuff checklist is cumbersome to use, time-consuming to assemble, and difficult to maintain proper configuration management control on, it continues to be used in the Shuttle inventory on every EVA mission.

Problem Statement

For the last several years, engineers and human factors scientists at JSC have been exploring alternative methods to provide EVA astronauts with a more efficient information medium. Because of the high costs associated with redesigning the Shuttle extravehicular mobility unit (EMU) and the need to maintain current astronaut training regimens, these alternatives have been limited to portable, self-contained information display systems. Our final approach must not sacrifice any of the benefits of the current paper checklist. We must also take advantage of today's advances in displays, data access, electronics, and memory devices to improve EVA productivity by allowing crew members to have access to a much larger database that provides the added feature of data contents being modified on orbit.

Approach/Method

The electronic checklist we are developing consists of an off-the-shelf liquid crystal display, a touch screen (for screen selection), driver electronics (including microcontroller, memory, and serial data programming port), and a battery pack enclosed in an aluminum frame that is thermally protected by softgoods. Memory contents are accessed via the touch screen through a unique sextant screen protocol. The electronic cuff checklist, like the current paper cuff checklist, is worn over the space suit arm assembly. It thus provides easy access to text and graphics databases of greater than 500 pages. This database, which is both reprogrammable and expandable via a serial data port, accommodates the data requirements of various Shuttle EVA mission tasks. Software training tools have been developed to allow the efficient creation of pages and to load the checklist database. The additional benefit of better configuration management control can be achieved by using an access-controllable electronic database.

Results

FY93 activities include the development and crew test of a functional prototype. The functional prototype (Figure 1) was tested in a manned, vacuum environment in December 1993. Software training tools were devel-

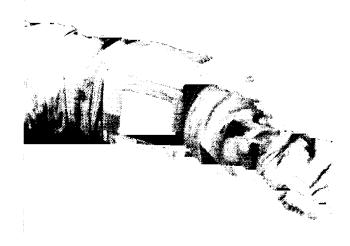


Figure 1. Functional prototype of electronic cuff checklist.

oped to allow the efficient creation of pages and to load the checklist database. Flight units, which are currently under construction, are to be tested both during an intravehicular flight experiment and during an actual EVA activity in FY94 (currently planned for STS-64, September 1994, DTO 672). The flight experiment, which is being sought, will assess key design and performance requirements prior to the development of future units (i.e., volumetric, weight/mass, accessibility to information, viewability, suit attachment, and operational concerns).

Our accomplishments to date include breadboard/ prototype models and various engineering design trades with valuable inputs provided from Crew, Flight Crew Support Division, Mission Operations (Flight Data File and EVA Crew Systems), and Crew and Thermal Systems Division (EVA Equipment Branch) personnel.

Conclusions

Since the electronic cuff checklist that is currently under development has been designed for a minumum of

25 Shuttle flights, it can be reused on future EVA missions. It is likely, however, that further improvements to the electronic cuff checklist will be made before this item becomes fully operational. These improvements will probably be only in the form of repackaging (e.g., lower profile package, reduced length dimension, rechargeable battery pack, etc.). Any improvements will be made in FY95 and beyond with proper support from the Crew Office, Engineering, and the EVA Project Office.

Acknowledgments

The following personnel have been involved in the development of the EMU electronic cuff checklist: Mark Lee and Pierre Thout, Astronaut Office; Daryl Schuck, Rockwell; Richard Bullock, Steve Poulos, Jr., and James McBarron II, Crew and Thermal Division; and Barbara Woolford, Flight Crew Support Division.

Development of Digital Technology for a Reprogrammable Receiver

Tim Early, Mark Chavez, *Brent Hill, and **Dave Sanderlin Johnson Space Center/EE *Lockheed Engineering & Science Company **Shason Microwave

Introduction

The objectives of this project are to develop the digital technology and its implementation into a "smart" transceiver for two-way communications between low-Earth-orbit (LEO) spacecrafts and ground stations using either NASA or commercial geosynchronous satellites. Specific objectives include:

- The transceiver shall remove the dynamic Doppler effects unique to LEO spacecraft and shall accomplish signal acquisition and lock-up in the presence of modulation.
- Digital techniques shall be used in the RF receiver to allow variable data rates and modulation formats.
- Low cost, reliability, and ease of operation are emphasized in the design and construction.
- After development of a prototype transceiver, transfer this technology to the private sector via a Space Act Agreement for low-cost commercialization.

Approach

These transceiver capabilities can be obtained by digital, rather than conventional analog, implementation of a transceiver. The Tracking and Communications Division at JSC has several programs under way which address these technical issues. Specifically, a space-qualified, 1.023 MHz telemetry subcarrier demodulator with 1, 2, 4, 8, 16, and 32 Kbps data rate capabilities in both NRZ and bi-phase modulation formats was developed for the S-Band Extended Range Payload Communications Link for communicating with detached payloads.

This digital demodulator was an in-house JSC project designed, tested, and space-certified.

In addition, Phase II of a Small Business Innovative Research project was recently initiated with Shason Microwave to develop a compact RF transceiver/modem. This prototype hardware integrates state-of-the-art digital signal processing and microwave integrated circuit technologies into a system which provides the flexibility to support various applications through modularity and reconfigurability. It is hoped that such a "building block" approach can significantly reduce the non-recurrent engineering which inevitably accompanies new spacecraft development programs.

As a target application for this project, an advanced space flight tracking and data network-compatible transponder was selected for development. This transponder will include improved acquisition features that will simplify spacecraft operations. The transponder will be compatible with the orbiter payload interrogator and spacecraft tracking and data network/deep space network (STDN/DSN) ground stations. Furthermore, the transponder will include features that will accommodate a return link through the Advanced Communication Technology Satellite (ACTS) satellite. The project will provide a test bed for insertion of emerging technologies, and will maximize knowledge transfer to NASA engineers in the area of digital transceiver design. Many possibilities for commercial applications exist, including very small aperture terminals, direct broadcast satellite systems, and terrestrial microwave systems.

One feature not incorporated into this design was Doppler compensation hardware and software. Doppler circuitry will be developed later in the in-house JSC program.

Application of Dexterous Space Robotics Technology to Myoelectric Prostheses

Clifford Hess, Larry C. H. Li, Kristin A. Farry,* and Ian D. Walker*
Johnson Space Center/ER
*Rice University

Abstract

Future space missions will require robots that are equipped with highly dexterous robotic hands to perform a variety of tasks. A major technical challenge in making this possible is an improvement in the way these dexterous robotic hands are remotely controlled or teleoperated. JSC is currently investigating the feasibility of using myoelectric signals to teleoperate a dexterous robotic hand. In theory, myoelectric control of robotic hands will require little or no mechanical parts and will greatly reduce the bulk and weight that are usually found in dexterous robotic hand control devices. An improvement in myoelectric control of multifinger hands will also benefit prosthetics users. Therefore, as an effort to transfer dexterous space robotics technology to prosthetics applications and to benefit from existing myoelectric technology, NASA is collaborating with the Limbs of Love Foundation, The Institute for Rehabilitation and Research, and Rice University to develop improved myoelectric control of multifinger hands and prostheses. In this paper, we will address the objectives and approaches of this collaborative effort and will discuss the technical issues associated with myoelectric control of multifinger hands. We will also report our current progress and discuss plans for future work.

Introduction

Robotics is one of the critical technologies necessary for future space explorations. Future space robots will require highly dexterous robotic hands to perform a variety of tasks. A major technical challenge in making this possible is an improvement in the way these dexterous robotic hands are remotely controlled or teleoperated. The required robotic hand teleoperation interface must be intuitive (requiring less operator training) and nonfatiguing (enabling longer shifts). A current method of teleoperation uses an exoskeleton glove controller to detect finger motions. These glove controllers are worn by an operator to control robotic hands located at a remote site. Glove controllers are usually bulky and heavy, and they sometimes interfere with hand movements. Consequently, JSC is investigating the feasibility of using myoelectric signals to control dexterous robotic hands.

While NASA is advancing dexterous robotic hand technology, the Limbs of Love Foundation, a foundation which is dedicated to providing prostheses to handicapped children, is actively searching for ways to improve the state of the art in prostheses. In an effort to transfer

advanced space technology to practical ground-based applications, NASA has teamed up with Limbs of Love and with a group of medical and prosthetics specialists, prosthetics users, insurance industry representatives, and university researchers to identify research objectives in prosthetic hands. ³² As part of this effort, the Automation and Robotics Division (A&RD) at JSC has been actively working with Rice University to improve dexterous hand design and to develop a method for myoelectric control of multifinger hands.

In this paper, we will describe the collaborative research between JSC and Rice University to develop improved prostheses. First, we will review previous work in dexterous robotic hands, prosthetics, and myoelectric controls, then we will outline the goals and objectives as well as the approaches we are taking in this joint effort. Second, we will report progress made in the areas of dexterous robotic hand development and myoelectric control. Our efforts in these areas have forced us to consider several difficult design issues which will be discussed. And third, we will conclude the paper by stating what our future work and expected accomplishments will be.

Previous Work

Over the past 3 decades, the myoelectric prostheses community reached a rough consensus that there are five types of grasp important in a person's daily activities: (1) the three-jaw chuck or pincher grasp used to hold small objects; (2) the lateral grasp, which is most often called a key grasp because it is used to hold a key while unlocking a door; (3) the hook grasp, which is used to carry items such as books or a briefcase; (4) the spherical grasp, where the thumb and fingers are wrapped around a spherical object; and (5) the cylindrical grasp, where the thumb and fingers are wrapped around a cylindrical object. 28,40,41 Some consider the flattened hand (with thumb rotated completely out of opposition of the fingers) a sixth grasp because it is essential in supporting flat objects such as trays.

Current commercial prostheses have a two-jaw pincher arrangement of fingers and thumb which gives some chuck and cylindrical grasping capability. More advanced prostheses—such as those described in references, 12, 13, 27, and 34—have incorporated chuck and key grasps with spherical and cylindrical grasp options being provided by passive finger compliance. Weight, size, cost, and reliability of these advanced prostheses have been major reasons why they never became commercial products; however, recent advances in

miniaturizing hardware and lowering power consumption and costs suggest that these problems may now be secondary to the control/user interface problem. In fact, the longest (over 15 years) multifunction prosthetic hand project, the Swedish hand, ended with this conclusion.²

In parallel with the prosthetics research effort, the robotics community has been developing the theory of grasping and manipulation by multifingered hands over the past decades. (See, for example, the books by Mason and Salisbury³⁶ and by Cutkosky.⁶ Some multifingered robotic hands have been constructed. Hess and Li¹⁶ provided an overview of several existing dexterous robotic hands for space applications, with the most dexterous of them being the Utah/MIT dexterous hand (UMDH)²³ and the Stanford/Jet Propulsion Laboratory (JPL) hand.³⁶ Based on their evaluations, Hess and Li have concluded that a 6-degree-of-freedom (DOF) robotic hand has sufficient articulation for grasping various shapes and providing some manipulation capability. Unfortunately, these early hands are too bulky and heavy to be feasible as a prosthetic device.

Although these complex robotic hands may not be feasible for prosthetics applications, they do serve as valuable tools to evaluate various grasping and manipulation strategies. These strategies usually involve complex algorithms and require sophisticated sensors that are now unavailable. One promising approach has been suggested by Speeter. To He uses a small set of basic grasping primitives, each of which is simple to program. This approach seems well-suited for application to teleoperation using probably a small set of myoelectric signals. Since each myoelectric input signal requires amplification, filtering, and processing, fewer inputs mean a less complex and less expensive user interface.

Research Objectives

Our review of previous work in dexterous robotic hand and myoelectric control has shown that, to develop an improved prosthetic hand, progress must be made in (1) increasing the articulation of prostheses beyond just a single DOF, and (2) improving the myoelectric sensing capability to recognize different muscle patterns and map them into various grasp primitives. To achieve progress in these two areas, we must accomplish the following set of objectives:

- Design a robotic hand with human compatible functions, weight, and size
- Develop electronics and algorithms for primitivebased hand control
- Develop a myoelectric pattern recognition technique for multifinger hand control

The first objective will make a dexterous robotic hand feasible for limb-deficient persons. This may mean increasing the number of active fingers and reducing weight and power consumption. The second objective is aimed at providing some local automation so that the user can interface with the hand using primitive-level commands (such as chuck grasp, key grasp, etc.). To differentiate one primitive command from another, we must be able to recognize the signature, or myoelectric pattern, associated with that particular primitive. Previous attempts to develop more capable myoelectric prosthetic hands have fallen victim to an inadequate myoelectric user interface. This is why the third objective is so essential.

By achieving these three objectives, both NASA and the prosthetics community will benefit from the results of this effort. In space, electrical power is a precious commodity and weight is a major concern. By making the robotic hands more compact and energy efficient, we are also making them more suitable for space applications. The electronics and algorithms for primitive-based control will fit in well with a layered architecture that also supports artificial intelligence technologies. If the third objective is also achieved, it will represent a breakthrough in teleoperation technology since cumbersome exoskeleton devices will not be required to operate dexterous robotic hands.

Approaches

To achieve the three objectives, we are pursuing two parallel paths: JSC is focusing on developing advanced dexterous robotic hands, and Rice University is concentrating on developing improved myoelectric signal processing technology. In addition, we are also soliciting feedback from robotic hand experts, prosthetics users, and specialists to continually improve our design. These two technology development paths will eventually merge in a test-bed environment where we can perform integrated evaluation of new prosthetics mechanisms and control.

Dexterous Robotic Hands

We began our dexterous robotic hand development by procuring and evaluating commercially available, state-of-the-art dexterous robotic hands while developing in-house expertise. By understanding the features of existing hands, we would not have to reinvent the technologies already developed by others. The results of our evaluation helped us to understand the trade-off between function (dexterity, sensing) and form (size, weight).

To establish a reference point for our performance evaluation, we first examined conventional parallel jaw grippers. Conventional parallel grippers are typically designed to execute a pinch grip. This type of grip depends heavily on contact friction rather than contact geometry for stability. Most grippers today have only a single DOF; therefore, they cannot perform manipulation or securely grasp objects of various shapes. Prosthetic hands today function essentially like parallel jaw grippers, except that prosthetic hands generally have a more human-like external appearance.

CTSD | Hand

For robotic applications, we took a minimalist approach in designing new hands. Instead of designing a highly complex robotic hand right away, we increased the complexity slowly, thus hoping to achieve the desired functions at a minimal cost. Our first attempt at robotic hand design resulted in the construction of the CTSD I hand. (CTSD is the acronym for Crew and Thermal Systems Division, the JSC organization responsible for developing the hand.)

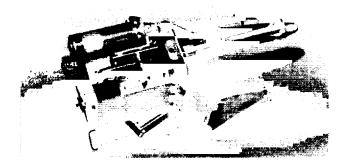


Figure 1. CTSD I hand.

The CTSD I hand (Figure 1) has three fingers driven by a single direct current (dc) motor. The three fingers are spaced 120 deg apart, and they open and close simultaneously. Each finger contains three sections connected by joints. The sections are coupled by direct linkages; therefore, the push-pull motion created by the rod inside the proximal finger section will cause the other sections to move also. As the fingers begin to close, the distal finger section will bend around the object and trap the object within the grip of the hand for a secure grasp. The motions of the three fingers are also coupled by a cable-pulley system, so when any one finger is forced to stop, the other two will continue to close until all three fingers have stopped. Although this hand is a step beyond the simple parallel jaw gripper, it still has some drawbacks. The hand does not have enough independently controlled, articulated joints to allow alternate grasp arrangements, and it lacks the human look that is highly desired in a prosthetic hand.

CTSD II Hand

To improve the dexterity of the CTSD I hand, we redesigned the fingers so they are modularized, which means each is capable of moving independently from the other fingers. The redesigned hand, named the CTSD II hand, also has three fingers. However, there are several important differences. The fingers of the CTSD II hand (Figure 2) are arranged in a two-opposing-one configuration to provide parallel grasping surfaces. This finger configuration is able to adapt to different shapes of objects better than the CTSD I hand configuration. The modular



Figure 2. CTSD II hand.

finger design also allows additional fingers to be added if necessary. Each finger is driven by a single dc motor contained within the finger module. We also introduced tactile sensors and strain gauges on each finger to provide sensory feedback. Silicon pads cover the tactile sensors to provide protection and to provide a compliant, friction surface for a more secure grasp. The maximum amount of force each finger can exert is controlled by current-limiting circuitry in the control electronics. The CTSD II hand contains many functional improvements over the CTSD II hand. For prosthetics applications, however, the CTSD II hand lacks adequate dexterity and a pleasing appearance.

Utah/MIT Dexterous Hand

Our search for a robotic hand with human-like dexterity and appearance led us to evaluate the UMDH.²⁴ The UMDH (Figure 3) is the most dexterous hand in the spectrum of hands available for our evaluation. It has 16 DOF arranged in an anthropomorphic configuration of three fingers and a thumb. The fingers and the thumb each have 4 DOF. Thirty-two pneumatic actuators operating at pressures up to 80 psi provide power to the hand. Tendons are used to transmit power from these pneumatic actuators to the joints through a system of pulleys and linkages called a remotizer. Each joint is controlled by a pair of antagonistic tendons. A linear Hall Effect sensor, which is located inside each joint, measures the joint angles. Hall Effect sensors are also located in the wrist to monitor the



Figure 3. Utah/MIT dexterous I hand.

tendon tensions. A control box containing analog feed-back control circuitry provides manual control of each joint with an interface for computer control that can be used in lieu of manual control. ¹⁶

It is obvious that the UMDH is not suitable for space robotics or for prosthetics applications. The pneumatic power system requires an air compressor that is too large to be portable, and the overall dimension of the hand system is too large to be mounted on a robot or a human user. However, the UMDH is a valuable test-bed facility for us to evaluate and develop various control algorithms and grasp strategies for space and prosthetics applications. Later in this paper, we will describe how the UMDH test-bed is being used for prostheses development.

Stanford/JPL Hand

We also evaluated the Stanford/JPL hand designed by Dr. J. Kenneth Salisbury of Massachusetts Institute of Technology (MIT). The hand has 9 DOF in a nonanthropomorphic finger arrangement and a large envelope of excursion. The hand has three fingers, each with three joints. The joints are driven by a set of steel cables that transmit mechanical power from 12 remotely located dc motors equipped with position encoders. Located behind the proximal joint of each finger are four strain gauges that measure the cable tensions. The tension signals may be translated into joint torque signals which are used in servo control. The fingertips are made of a highly compliant elastomer that provides the friction contact necessary for a secure grasp. Figure 4 shows the Stanford/JPL hand and its remote motor package.

Compared to the UMDH, the Stanford/JPL hand is more compact, and its electrical power system is more compatible with space and prosthetics applications. Although the size and weight of the Stanford/JPL hand are acceptable for space robots, they are not acceptable for a prosthetic hand. Also, the Stanford/JPL hand is not as anthropomorphic and visually pleasing as the UMDH.

Direct Link Prehensor

Our initial evaluation of the UMDH and the Stanford/ JPL hand showed us that a highly complex robotic hand will most likely require a large actuator package. This is



Figure 4. Stanford/JPL hand.

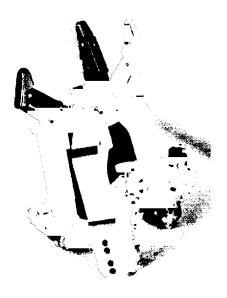


Figure 5. Direct link prehensor.

unacceptable for both space and prosthetics applications; however, a smaller actuator package usually means less dexterity. Therefore, a compromise must be achieved between dexterity and packaging. Our search for an optimal solution that takes both packaging and dexterity into account brought us to the direct link prehensor design.

The direct link prehensor (Figure 5) was originally developed by Ames Research Center and Stanford University to function as a space suit end effector that fits over the hand like a glove. The prehensor has a total of 6 DOF in an anthropomorphic configuration. It has two fingers and a thumb, with the thumb opposing the two fingers at a fixed angle to provide grasping capability as well as some manipulation capability. The mechanical fingers are directly coupled to their human counterparts through a mechanical linkage system.

The prehensor has been flown on the NASA KC-135 aircraft to evaluate grasping in a weightless environment using a mechanical hand.25 This evaluation showed the prehensor finger arrangement to be a good compromise between packaging and dexterity. A robotic implementation of the prehensor would require only six motors, which is substantially less than the UMDH and Stanford/ JPL hand. Even with only 6 DOFs, the prehensor is capable of grasping objects of various sizes and shapes. It is capable of chuck grasps, pinch grasps, power grasps, hook grasps, and key grasps. Although the thumb does not have abduction/adduction movement, it is mounted at a 45-deg angle to provide a motion with a horizontal component. Despite lacking some important movements, we were able to twist open a bottle cap, manipulate small flat plates, grasp balls and cylinders, and pick up luggage with the prehensor.

JH-3 Hand

After a fairly comprehensive evaluation of existing dexterous robotic hands, we selected the direct link prehensor design as the baseline for an in-house developed robotic hand. After several design iterations (JH-I through JH-2), we arrived at the JH-3 Hand. (JH stands for Jameson hand, named after the designer Dr. John Jameson.) As shown in Figure 6, the JH-3 hand has an integrated hand-wrist-forearm package that approximates the combined size of a human hand, wrist, and forearm. Seven dc motors are packaged in the forearm: one motor for each DOF and one that controls the tendon tension. The wrist on the JH-3 hand comes from a Remotec RM-10A robotic arm. Power is transmitted from the motors through a tendon-pulley system to each joint, much as the remotizer in the UMDH. This tendon-pulley system allows the hand to move freely with the wrist. The encoders on each motor and the strain gauges in the hand provide position and force feedback. Infrared proximity sensors were installed on the JH-3 hand to provide autonomous adaptive grasping capability. The entire hand package contains current drivers for the motors as well as signal amplifiers for the sensors. Although the overall weight and package are still not quite acceptable (15 lb), the JH-3 hand does contain major improvements in packaging and

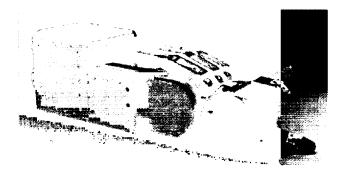


Figure 6. JH-3 hand.

sensing as compared to the UMDH and Stanford/JPL hand.

To evaluate the JH-3 hand, we mounted the hand on the extravehicular activity (EVA) retriever, which is an in-house developed, highly autonomous, free-flying robot that operated on an air-bearing floor at JSC. From our evaluation, we arrived at two key conclusions related to prosthetics development. First, the mechanism for remotizing the actuators tends to add weight, bulk, and complexity to the overall system. Instead, local actuation requiring a minimum number of power transmission components is desired. There is a design trade-off between remote actuation and local actuation. Remote actuation adds to the overall weight of the system, but allows a more desirable mass distribution for moment reduction. On the other hand, local actuation tends to concentrate mass near the hand and amplifies moments

about the elbow and shoulder. Second, the integrated hand-wrist-forearm design does not permit a simple integration of the JH-3 hand with commercial robotic arms. Because most commercial robotic arms already come with a forearm fully integrated, installing a JH-3 hand on these robotic arms requires redesign.

JH-4 Hand

Incorporating the lessons learned from the JH-3 hand evaluation, we developed the most recent hand design: the JH-4 hand. This hand (Figure 7) contains two fingers and a thumb, each driven by two motors located behind the proximal joint. Instead of remotizing the motors and transferring mechanical power through tendons and pulleys like the JH-3 hand, motors in the JH-4 hand drive the finger joints directly with a minimum number of gears. In

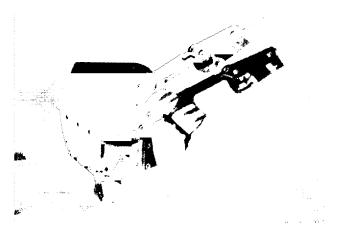


Figure 7. JH-4 hand.

making the fingers truly modular, we also packaged the drive electronics (e.g., current amplifiers, motion controllers) into each finger. An 80C196 microcontroller provides each finger with some local intelligence and serves as a high-level command interface.

The JH-4 hand represents our latest effort to develop a modular dexterous robotic hand that satisfies the stated objectives. The hand is near human-equivalent in terms of weight and size, and it provides a reasonable degree of dexterity with its two fingers and a thumb. The microcontroller embedded in each finger provides a high-level command interface for primitive-based hand control.

Rice Prosthetic Hand Prototypes

In parallel with these JSC dexterous robotic hand developments and with technical consultation from NASA A&RD experts, Rice University engineers have begun developing prototype anthropomorphic prosthetic hands. Two hands and one wrist unit have been built. Each hand has a thumb and four fingers with independent thumb and finger motion. One hand has a single-axis thumb which allows the thumb to swing through a full

range of opposition to the finger tips and independent finger control on the index, middle, and ring fingers; the little finger is coupled to the ring finger. The other hand has a two-axis thumb which can abduct, oppose, and flex at its base; an independent index finger; and the remaining fingers coupled to complete grasps. Both hands can perform key, chuck, cylindrical, spherical, and hook grasps and can also be completely flattened. The wrist unit is capable of flexing and roll. We are now beginning our second design iteration to simplify and strengthen the mechanisms to make them more reliable and easier to manufacture.

Myoelectric Control

To achieve our third objective, we are investigating the feasibility of using myoelectric signals to control the robotic hands. Our first efforts are exploring the remote control or teleoperation scenario. Myoelectric teleoperation of dexterous robotic hands will require no mechanical parts, and may greatly reduce the bulk and weight now found in dexterous robotic hand control devices. However, this teleoperation scenario requires advances in the state of myoelectric control art. Improvement in myoelectric teleoperation of multifingered hands will also benefit the prosthetics users. For example, the level of myoelectric control of a dexterous hand that is achieved by an intact teleoperator will establish an upper performance bound for the amputee. Furthermore, some of the myoelectric signal processing techniques developed for teleoperation will transfer into prosthesis control.

Research in using myoelectric signals (also called electromyographic or EMG signals) to control prostheses dates from the late 1940s.³⁵ By the early 1970s, researchers were treating the myoelectric signals as an amplitude-modulated signal whose amplitude was roughly proportional to the force developed in the muscle generating the myoelectric signal. The consensus was that most of the information in a myoelectric signal was in the amplitude.¹⁸ By the late 1970s, the model had matured to treating the myoelectric signal as amplitude-modulated Gaussian noise whose variance was proportional to the force developed by the muscle.^{31,37}

Today's commercial myoprocessors used in prosthesis control are based on only one dimension of the myoelectric signal, the force level, and, in a few cases, on its rate of change. Researchers have successfully refined force estimation from the myoelectric signal. 3.5.19.24,30,31,37. Parker's work forms the basis of control multiple functions using different force levels on a signal channel 37. Hogan's work was particularly significant in eliminating low-frequency noise from the force estimates due to the spatio-temporal sampling artifact inevitable with skin surface electrodes. 18.19 Jacobsen 24 refined use of the rate of change of force in elbow control of the UMDH. A version of the Swedish hand used rate of change of force to switch control functions. 13 Rice University researchers have investigated these force estimation results in

operating a proportionally controlled grasp force with a three-fingered robotic hand.

These force-estimation techniques require a separable muscle contraction for each function commanded, thus making simultaneous control of two or more joints very difficult. A number of researchers, beginning with Wirta and Taylor. 42 examined linear combinations of myoelectric force estimates from multiple channels to select different functions. The Swedish hand developers applied these methods to selecting wrist and grasp. 1.2.15 The Japanese research team applied the technique to wrist control in the Waseda Hand 3.27 Jacobsen22 and Jerard26 formalized the mathematics for this approach and applied it to upper limb above-elbow prostheses. These force-estimating approaches require at least one electrode pair and signal-processing channel for each muscle used—up to a dozen in some above-elbow experiments. Furthermore, force-estimating myoprocessors can be used only on superficial muscles, 19 while most motions involve both superficial and deep muscles. In fact, any deep muscle activity reaching a force-estimating myoprocessor is mistakenly interpreted as superficial muscle activity. Therefore, it appears to us that to obtain multifunction sensitivity that is intuitively easy to use, all information in the myoelectric signal must be exploited, rather than just the force estimate. In addition to using superficial muscles (to which force-estimation techniques are limited), the deep muscles must also be used in myoelectric control

Some researchers have considered shape and spectral characteristics of the myoelectric signal in addition to force estimation. Recent findings suggest that there is considerable information in the myoelectric spectra, if we can understand its coding. Examples include:

- Small muscles generally have fewer fibers per single motor unit (SMU) and, therefore, have power spectra containing more high-frequency activity than larger muscles with larger SMUs.³³
- Tissue (including other muscles) between the active muscle and the measuring electrode acts as a low pass filter to myoelectric signals; thus, excessive low-frequency power densities may indicate cross talk from adjacent muscles.³³
- Action potential conduction velocity decreases with fatigue, causing gradual shifts in power from higher to lower frequencies during sustained forceful contractions,³³
- SMU recruitment order is stable for a given task.⁷
 Short-time spectra of myoelectric signals associated with a given rapid movement does not vary as much as previously thought.¹⁴

The full spectrum of the myoelectric signal has been examined using techniques involving statistical pattern and spectral analyses.^{8,9,10,11,29,38} Evidence of movements having distinct spectral signatures has been reported by Lindstrom and Magnusson,³³ DeLuca,⁷ and by Hannaford

and Lehman. ¹⁴ The spectral signature of the initial muscular recruiting phase of arm motions to select up to six functions of an upper limb prosthesis from a single myoelectric signal has also been exploited recently by Hudgins. ²⁰

Hudgins' use of spectra-related parameters, such as zero-crossing and slope changes, and the use of short time Fourier transforms by Hannaford led us to focus on the time-varying spectrum of the myoelectric signal in our research. We have been studying the correlation between the myoelectric spectrum in the initial recruiting phase of a motion with the type of motion. We are following the lead of Saridis, 38 Doerschuk, 8 Kelley, 29 and Hudgins 20 in using the traditional single-muscle signals. Our work differs from previous work of other researchers, however, in that we are using the actual frequency spectrum to discriminate different grasping motions. Also, previous work has focused on arm, not hand, motions and on parameters derived from the spectrum rather than the actual spectrum.

Myoelectric Experimental Setup

To evaluate various myoelectric control techniques, we developed a unique myoelectric data collection system which enables us to capture up to eight myoelectric data streams while simultaneously recording the motion of the subject's hand. Previous myoelectric researchers have had only limited, if any, capability to measure motion while measuring myoelectric signals.

Figure 8 is a block diagram of the data capture system. We use the dexterous hand master (DHM), an exoskeleton glove manufactured by EXOS, Inc., of Cambridge, Massachusetts, to measure the subject's joint angles. The DHM glove, which is also used by JSC as a master to teleoperate dexterous robotic hands, measures parameters related to joint angles for four joints on the thumb and each of three fingers (index, middle, and ring).⁴³

We use the Grass Instruments (Quincy, Massachusetts) Model 12 amplifier to measure myoelectric signals. It consists of a differential amplifier, a high-pass filter (with roll-off frequency adjustable from 0.01 to 300 Hz) to block dc and motion artifact, a low-pass filter (adjustable from 30 to 20,000 Hz) to limit aliasing, an adjustable gain amplifier stage, and an isolation to protect the subject from the electric shock hazards of power supply and computer equipment. This sequence amplifies the differential myoelectric signal from skin-surface electrodes (around 1 millivolt in amplitude) to several volts. Differential input reduces the 60 Hz interference (typically much larger than the myoelectric signal) from lights and equipment.

Both DHM and myoelectric amplifiers are connected through Burr-Brown MPV950S analog-to-digital converter (ADC) boards to 68020-based Ironics IV3204 and IV3201 microcomputers. These capture up to 32 channels of data at 1000 samples per second per channel. An 80386 Radix personal computer (PC) transfers data to MATLAB format disk files. The ADC and Ironics and Radix computers are on a VME bus, and they do double duty as the control computer for the UMDH, with which we plan to demonstrate myoelectric teleoperation. We used the Math Work (Natick, Massachusetts) MATLAB software, Version 4.1, for off-line data analysis and plotting.

Based on our early findings in the myoelectric spectra, Rice University also developed a real-time myoelectric control implementation test-bed consisting of miniaturized myoelectric amplifiers with fixed 20 to 500 Hz bandwidth and a PC incorporating an Elf-31TM board and signal processing development software by Atlanta Signal Processors. The Elf-31 includes high-speed analog-to-digital conversion and digital signal processor (TMS320C31). With this system, we can capture multiple myoelectric signals, compute their spectra on the Elf-31, and process the spectra into a grasp selection using the PC—all in real time. If the user chooses a neural network approach, NWorksTM software by Neural Ware, Inc.

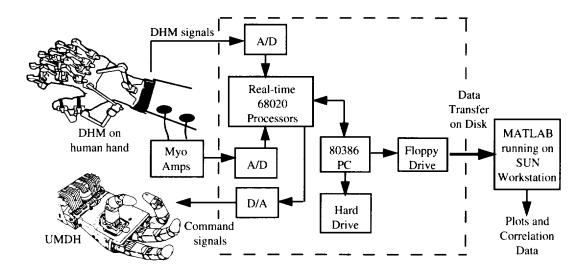


Figure 8. Myoelectric data capture system.

(Pittsburgh, Pennsylvania) facilitates development of neural networks for the classification of the spectra.

Preliminary Myoelectric Results

Our first use of these systems investigated direct use of the myoelectric spectrum to differentiate the key and the chuck grasps. The key and the chuck grasps differ in thumb position relative to the fingers. The thumb opposes the side of the index finger in the key grasp, while it opposes the tips of the index and ring fingers in the chuck grasp. Anatomy suggests that differentiating between these grasps requires measuring intrinsic thumb muscle activity in the hand and extrinsic finger and thumb activity in the forearm. We restricted measurements to the forearm, however, to keep the teleoperator's hand free of movement-encumbering hardware and to increase the applicability of our work to the prosthetics community.

We used the JSC data collection system (mentioned earlier) to capture myoelectric data during these two grasps. The human subject did a series of key and chuck grasps with the lateral side of the forearm resting on a horizontal surface or hanging vertically. We made no attempt to control the starting position (a relaxed posture) or to grasp precisely. The subject was the judge of consistency in these positions. We later used DHM finger trajectory data to check for consistency and correctness of the grasp and to locate the initiation phase of the corresponding myoelectric signals.

We are now testing various myoelectric signal processing schemes on these data streams. One was an adaptation of the approach by Hudgins et al.,²⁰ at the University of New Brunswick, where they computed mean absolute value, mean absolute value slope, zero crossings, and waveform length on biceps and triceps in 40 ms windows in the first 240 ms of arm motions, such as elbow flexing and humeral rotation. A multilayer Perceptron neural network used these features to classify the arm motions with 70% to 98% accuracy, depending on the human subject. Our initial implementation of this scheme yielded a maximum of 80% correct accuracy for our grasping test set. We believe that the decreased accuracy may be due to (1) increased difficulties in detecting the grasp start (since the myoelectric signal amplitude is smaller) and (2) differences in the way muscles used in fine motion control (such as grasping) and coarse motion (such as arm motion) are recruited. Inaccuracies due to the latter may be reduced by reoptimizing window size and characteristics. More algorithm experimentation and trials on more human subjects are needed to confirm this, however.

We have also tested several schemes which use the myoelectric signal magnitude spectra directly. The most successful of these have used the upper portion of the myoelectric spectrum, the 75 to 250 Hz range. Muscle fiber length, diameter, and action potential conduction velocity as well as distance to the electrode dominate this portion of the myoelectric spectrum. A multilayer

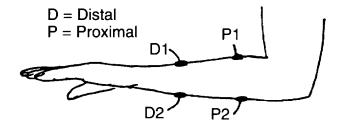


Figure 9. Dual channel electrode configuration.

Perceptron that was receiving inputs of the 75 to 250 Hz spectrum in six 40 ms windows (as in the UNB scheme) from the distal channel in figure 9 classified the test set signatures 93% correctly.

We have also experimented with multiple channel configurations. Figure 9 shows our dual-channel electrode configuration; the distal electrode pair (D1 and D2) measures extrinsic thumb muscle activity while the proximal pair (P1 and P2) measures finger flexion and extension activity. Computing 6 values of the 75 to 250 Hz spectrum in larger (240 ms) windows on both channels during the motion initiation phase yields a set of 12 features that a multilayer Perceptron can classify 86% to 91% correctly, depending on the human subject. We implemented this approach in real time on our real-time myoelectric control implementation test-bed and used it to teleoperate the Rice-developed prosthetic hands described previously.

Although still below our grasp discrimination goal of 100%, these early results refute the long-held assumption that myoelectric signals from the forearm are inadequate for differentiating thumb motions.

We have begun experimenting with the 3 to 75 Hz portion of the myoelectric spectrum, which is dominated by muscle recruitment dynamics. Theoretically, task-specific SMU recruitment should show up in this portion of the spectrum, and this may be the key to increasing grasp selection accuracy above 93%. To date, we have not been successful with direct use of the magnitude spectrum in this region, despite the implied usefulness in references 7,14, and 20 and the results of the adaptation of the UNB scheme, which implicitly used the entire spectrum. The UNB scheme has phase information embedded, however. Because we expect the recruitment portion of the spectrum to be much more time varying, it will be especially sensitive to window characteristics. We are continuing experiments with varying window size, overlap, and type.

Conclusions and Future Work

This ongoing joint research effort between JSC and Rice University is entering its third year. In the past 2 years, we have made significant progress in accomplishing the three stated objectives. We have evaluated several commercially available dexterous hand designs and have gone through several iterations of our own in-house designs. We made progress in reducing weight and

packaging of dexterous robotic hands while maintaining an acceptable level of dexterity, and we realized the current design in the JH-4 hand. We have begun development of prosthetic hands that incorporate lessons learned from robotic hand design and control.

Meanwhile, we also made significant progress in our understanding of myoelectric control theory. We have developed a unique myoelectric data collection system featuring recording of joint motion, and we have developed a test-bed for evaluating various signal processing techniques. Initial results of over 90% correct grasp discrimination suggest that myoelectric commanding of grasp primitives is feasible. Eventually, we plan to evaluate the feasibility of myoelectrically controlling individual fingertips to augment grasp primitives.

If myoelectric control of dexterous robotic hands can be made both intuitive to operate and repeatable, a myriad of opportunities in both space robotics and prostheses development will open up.

References

- ¹Almstrom, C., "Myoelectric Control of Multifunctional Hand Prostheses - Contributions to the Pattern Recognition Approach, to Signal Acquisition, and to Clinical Evaluation," Technical Report No. 79, School of Electrical Eng., Chalmers University of Technology, Goteborg, Sweden, 1977.
- ²Almstrom, C., et al., "Experience with Swedish Multifunctional Prosthetic Hands Controlled by Pattern Recognition of Multiple Myoelectric Signals," *Int. Orthopaedics*, Springer-Verlag, Vol. 5, pp. 15-21.
- ³Bottomley, A., "Progress with the British Myoelectric Hand," Proc. of the Int. Sym. on External Control of Human Extremities, Dubrovnik, Yugoslavia.
- ⁴Brand, P., *Clinical Mechanics of the Hand*, The C. V. Mosby Co., St. Louis, 1985, pp. 194-195.
- ⁵Childress, D., "An Approach to Powered Grasp," Proc. of the 4th Int. Sym. on External Control of Human Extremities, Dubrovnik, Yugoslavia, August 28 September 2, 1972.
- ⁶Cutkosky, M., *Robotic Grasping and Fine Manipulation*, Boston, Kluwer, 1985.
- ⁷DeLuca, C., "Physiology and Mathematics of Myoelectric Signals," *IEEE Trans. on Biomedical Eng.*, BME-26, No. 6, June 1979, pp. 313-325.
- ⁸Doerschuk, P., et al., "Upper Extremity Limb Function Discrimination Using EMG Signal Analysis," *IEEE Trans. on Biomedical Engineering*, BME-30, No. 1, January 1983, pp. 18-29.
- Graupe, D., "Multifunctional Prosthesis and Orthosis Control via Microcomputer Identification of Temporal Pattern Differences in Signal Site Myoelectric Signals," *Journal of Biomedical Eng.*, Vol. 4, 1982, pp. 17-22.
- ¹⁰Graupe, D., et al., "A Microprocessor System for Multifunctional Control of Upper-Limb Prostheses via Myoelectric Signal Identification," *IEEE Trans. on Auto. Control*, AC-23, No. 4, August 1978, pp. 538-544.

- ¹¹Graupe, D., and Cline, W., "Functional Separation of EMG Signals via ARMA Identification Methods for Prosthesis Control Purposes," *IEEE Trans. on Systems,* Man, and Cybernetics, SMC-5, No. 2, March 1975, pp. 252-259.
- ¹²Hagg, G., and Spets, K., "SVEN Project I Electrically Controlled Hand Prosthesis - Final Report," Res. Inst. of the Swedish National Defence, Dept 2, S-104 50 Stockholm 80 FOA 2 report A 2575-H5.
- ¹³Hagg, G., and Oberg, K., Adaptive EMG-Controlled Hand Prosthesis for Wrist Disarticulated Patients, Ean-Holmgren Orthopaedic Co., Bergsbrunnagatan 1, S-753 23 Uppsala, Sweden, pp. 441-449.
- ¹⁴Hannaford, B., and Lehman, S., "Short-Time Fourier Analysis of the Electromyogram: Fast Movements and Constant Contraction," IEEE Trans. on Biomedical Eng., BME-33, No. 12, December 1986, pp. 1173-1181
- ¹⁵Herberts, H., et al., "Hand Prosthesis Control Via Myoelectric Patterns," *Acta Orthopaedia Scandinavia*, Vol. 44, 1973, pp. 389-409.
- ¹⁶Hess, C., and Li, L. C., "Smart Hands for the EVA Retriever," Proceedings of Third Annual Workshop on Space Operations Automation and Robotics (SOAR '89), pp. 441-446, 1989.
- ¹⁷Hlawatsch, F., and Boudreaux-Bartels, G., "Linear and Quadratic Time-Frequency Signal Representations," *IEEE Signal Proc. Mag.*, Vol. 9, No. 4, pp. 21-67, 1992.
- ¹⁸Hogan, N., "A Review of the Methods of Processing EMG for Use as a Proportional Control Signal," *Biomedical Engineering*, March 1976, pp. 81-86.
- ¹⁹Hogan, N., and Mann, R., "Myoelectric Signal Processing: Optimal Estimation Applied to Electromyography," IEEE Trans. on Biomedical Eng., BME-27, No. 7, July 1980, pp. 382-410.
- ²⁰Hudgins B., et al., "A New Strategy for Multifunction Myoelectric Control," IEEE Trans. on Biomedical Engineering, No. 40, pp. 82-94, 1993.
- ²¹Ichie, M., et al. "EMG Analysis of the Thumb and Its Application to FNS," IEEE 8th Annual Conf. of the Eng. in *Med. & Biol. Soc.*, Fort Worth, TX, November 7-10, 1986, pp 60-64.
- ²²Jacobsen, S., "Control Systems for Artificial Arms," Ph.D. Dissertation, Dept. of Mechanical Eng., Massachusetts Institute of Technology, January 1973.
- ²³Jacobsen, S., et al., "Design of the Utah/MIT Dexterous Hand," IEEE International Conference on Robotics and Automation, San Francisco, CA, April 1986.
- ²⁴Jacobsen, S., et al., "Development of the Utah Artificial Arm," *IEEE Trans. on Biomedical Eng.*, BME-29, No. 4, April 1982, pp. 249-269.
- ²⁵Jameson, J., Report on the Zero-G Grasp Experiment with the Direct Link Prehensor, NASA/JSC, March 15, 1988.
- ²⁶Jerard, R., "Application of a Unified Theory for Simultaneous Multiple Axis Artificial Arm Control,"
 Ph.D. Dissertation, Dept. of Mechanical and Industrial Eng., University of Utah, December 1976.

- ²⁷Kato, I., and Okazaki, K., "Electro-Pneumatically Controlled Artificial Hand," *Bulletin of Science and Engineering Research Laboratory*, Waseda University, No. 44, 1969, pp. 25-34.
- ²⁸Kay, H. and Rakic, M., "Specifications for Electromechanical Hands," Proc. of the 4th Int. Sym. on External Control of Human Extremities, Dubrovnik, Yugoslavia, August 2 to September 2, 1972.
- ²⁹Kelly, M., et al., "The Application of Neural Networks to Myoelectric Signal Analysis: A Preliminary Study," *IEEE Trans. on Biomedical Engineering*, BME-37, No. 3, March 1990, pp. 221-230.
- ³⁰Kreifeldt, J., "Signal Versus Noise Characteristics of Filtered EMG Used as a Control Source," *IEEE Trans.* on Biomedical Eng., BME-18, No. 1, January 1971, pp. 16-22.
- ³¹Kreifeldt, J., and Yao, S., "A Signal-to-Noise Investigation of Non-Linear Electromyographic Processors," *IEEE Trans. on Biomedical Engineering*, BME-21, No. 4, July 1974, pp. 298-308.
- ³²Limbs of Love, "An American Initiative: The Next Generation of Myoelectric Prostheses," Workshop Report, NASA/JSC, Research Triangle Institute, 1991.
- ³³Lindstrom, L., and Magnusson, R., "Interpretation of Myoelectric Power Spectra: A Model and Its Applications," *Proceedings of the IEEE*, Vol. 65, No. 5, May 1977, pp. 653-662.
- ³⁴Lozach, Y., et al., "On The Evaluation of a Multifunctional Prosthesis," Proc. of the 7th World Congress of the Int. Soc. of Prosthetics and Orthotics, Chicago, IL, June 28 - July 3, 1992, p. 185.
- ³⁵Mann, R., "Cybernetic Limb Prosthesis: The ALZA Distinguished Lecture," *Annuals of Biomedical Engineering*, Vol. 9, 1981, pp. 1-43.

- ³⁶Mason, M., and Salisbury, J., Robot Hands and the Mechanics of Manipulation, Cambridge, MA, MIT Press, 1985.
- ³⁷Parker, P., et al., "Signal Processing for the Multistate Myoelectric Channel," *Proceedings of the IEEE*, Vol. 65, No. 5, May 1977, pp. 662-647.
- ³⁸Saridis, G., and Gootee, T., "EMG Pattern Analysis and Classification for a Prosthetic Arm," *IEEE Trans. on Biomedical Engineering*, BME-29, No. 6, June 1982, pp. 403-412.
- ³⁹Speeter, T., "Control of the Utah/MIT Hand: Hardware and Software Hierarchy," *Journal of Robotic Systems*, Vol. 7, No. 5, May 1990, pp. 759-790.
- ⁴⁰Spinner, M., Kaplan's Functional and Surgical Anatomy of the Hand, Philadelphia, PA, JBLippincott Co., 3rd Ed., pp. 9-10.
- ⁴⁾Todd, R., and Nightingale, J., "Adaptive Prehension Control for a Prosthetic Hand," Proceedings of the 3rd Int. Symposium on External Control of Human Extremities, Dubrovnik, Yugoslavia, August 25-30, 1969, pp. 171-183.
- ⁴²Wirta, R., and Taylor, D., "Development of a Multiple-Axis Myoelectrically Controlled Prosthetic Arm," Proc. of the 3rd Int. Sym. on External Control of Human Extremities, Dubrovnik, Yugoslavia, August 25-30, 1969.
- ⁴³Wright, A., and Stanisic, M., "Kinematic Mapping Between the EXOS Handmaster Exoskeleton and the Utah/MIT Dexterous Hand," IEEE International Conference on Systems Engineering, Pittsburgh, PA, August 9-11, 1990, pp. 101-104.

Electromagnetic Probe Technique for Fluid Flow Measurements

G. D. Arndt, Thanh Nguyen, and J.R. Carl*
Johnson Space Center/EE
*LESC

Abstract

The probes described in this paper, in various configurations, permit measurement of the volume fraction of two or more fluids flowing through a pipe. Each probe measures the instantaneous relative dielectric constant of the fluid that is in immediate proximity. As long as separation of the relative dielectric constants of each fluid is possible, several or even many fluids can be measured in the same flow stream. By using multiple probes, the velocity of each fluid can generally be determined as well as the distribution of each constituent in the pipe. The values are determined by statistical computation. There are many potential applications for probes of this type in industry and Government. Possible NASA applications include measurements of helium/hydrazine flow during rocket tests at White Sands, liquid/gas flow in hydrogen or oxygen lines in Orbiter engines, and liquid/gaseous Freon flow in zero-g tests with the KC-135 aircraft at JSC. Much interest has been shown in the probes recently by the oil industry. In the oil industry, a good method is needed to measure the fractions of oil, water, and natural gas flowing in a pipeline and the velocity of each. This particular problem involves an extension of what has been developed to date. Our plans to solve this problem are discussed.

Introduction

During tests of a reaction control system (RCS) thruster jet at the White Sands Facility, we needed a way to monitor the flow of monomethyl hydrazine and helium through an inlet pipe. To achieve this, we developed a microwave technique for measuring two-phase flow. The relative amounts of helium and hydrazine flowing into the thruster jet could not be measured instantaneously. It was realized that, since the dielectric constants of helium (approximately 1) and hydrazine (19.2) are sufficiently different, the load impedance seen by a microwave capacitance probe should also be sufficiently different to be easily separable.

The microwave technique described in this paper measures the phase angle of the reflection factor, S11, associated with reflected energy from a flush-mounted probe. The system is being modified to include multiple probes within the pipe. This system has another potential space application for measuring the flow of liquid and gaseous oxygen or hydrogen under zero-g conditions within the Space Station. The technique also has a ground-based application for measuring gas-water-oil

flow from undersea oil wells—as well as other possible uses in measuring volume fractions and the velocity of multiple liquids that have different dielectric constants.

Description of Applications

Single Nonintrusive Probe

There are many potential applications for a single, nonintrusive probe. For example, a single probe mounted

- At the top of a pipe can perform well as a bubble detector or void detector.
- At the bottom of a pipe could be used to continuously monitor the purity of fluid.
- At an appropriate position on a mixing tank could monitor a change from fluid A to fluid B as a function of time.
- Strategically could be used to identify laminar or turbulent flow.

A single probe may be all that is needed to monitor some point of interest in a pipeline. Combined with apriori information, flow regimes may be indentifiable using a single probe. Of course, a single probe could be used to identify a full or an empty tank, or an intermediate threshold level.

Multiple Nonintrusive Probes

Multiple nonintrusive probes could do any of the things mentioned previously. Identifying flow regimes and calculating volume fractions could probably be accomplished better with multiple probes located at different positions on the pipe and performing additional processing. Velocity computations would require at least two probes at a known downstream spacing.

Multiple Intrusive Probes

To monitor directly what is happening in the interior of a pipe or reservoir, intrusive probes must be used (if using the type probe discussed in this paper). If multiple interior locations are to be monitored, multiple probes are required. An example of this type of requirement comes from the oil industry. They have a need to measure the volume fraction of oil, water and natural gas flowing through a pipe and the velocity of each. In this case, it may be necessary to gather data at the interior of the pipe.

If probes are internal, they must be made as minimally intrusive as possible. Also, they must be rigid enough to withstand flow and tough enough to withstand corrosion and abrasion for long periods of time.

System Description

The major components of a single probe system are shown in figure 1. This system has been built and used in a test program that will be described later.

Method of Operation

The small capacitance of the probe is used as the sensor. This capacitance is a function of the relative dielectric constant of the medium into which the probe is terminated. The short probe "sees" fluid that is no more than a short distance away. If it must see further into the medium, it would be necessary to increase the length of the probe to increase the volume around the center conductor that forms the probe capacitance.

The phase, or change of phase, associated with the reflected signal at the probe is the quantity measured. The complex S parameter associated with reflected energy S11 is given by:

$$S_{II} = \left(\frac{Z_O - Z_L}{Z_O + Z_L}\right) \tag{1}$$

where: Z_0 is the characteristic impedance of the transmission line from phase detector to probe.

$$Z_i$$
 is the probe input impedance = $R + X$

Typically, Z_0 is equal to 50 ohms. If negligible energy is coupled to the media, the probe resistance is very small. The input impedance is essentially a capacitive reactance in which case equation (1) can be written:

$$S_{11} = \left(\frac{50 - jX}{50 + jX}\right)$$
where:
$$X = \frac{-1}{2\pi FC\epsilon_r}$$

C = probe capacitance ε_r = relative dielectric constant F = frequency of operation

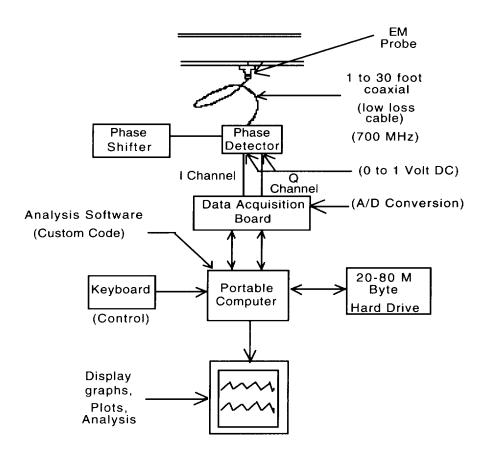


Figure 1. Electromagnetic (EM) probe system block diagram.

The phase Φ on S_{11} , from equation (2), can be extracted as:

$$\Phi = \tan^{-1} \left(\frac{100 \,\mathrm{X}}{2500 - \mathrm{X}^2} \right) \tag{3}$$

For certain cases of interest, where X is large with respect to $Z_{_{0}}$ and where Φ is small, equation (3) reduces approximately to:

$$\Phi \approx -100/X \text{ rad}$$

$$\Phi \approx -5730/X \text{ deg} \tag{4}$$

For a certain 1 mm probe, probe capacitance has been measured to be approximately 0.04 pf. Using this value and using a frequency of 700MHz, equation (4) reduces to the convenient form:

$$\Delta \Phi \approx \Delta \varepsilon_{\star}$$
 (5)

For this model of the probe—i.e., a capacitive reactance termination for the transmission line—predictions can be made for probe capacitance given frequency, probe length, and effective relative dielectric constant of the media. Also, the sensitivity of the probe can be readily formulated.

Test Results

The results shown in Figure 2 were extracted from the test results of a flapper valve experiment performed at JSC in November 1992. The flush probe was mounted at the top of a 1.5-in. pipe, and the flow of distilled water and dry nitrogen passing at various specific rates through the pipe was monitored. The volume fraction of water and nitrogen were varied. The top graph (Figure 2) shows that the probe works well as a bubble detector in this configuration. The lower two graphs show two different conditions of slug flow. The precise volume fractions and flow rates are not immediately evident from these graphs, but by processing the data, introducing apriori knowledge, and influencing the calculation with calibration data, perhaps reasonably accurate volume fractions and flow rates could be determined using only a single probe.

Conclusions

Certain potential applications of the ac fluid flow probe require the use of multiple probes placed in a flow stream. For example, we might consider the problem of measuring the volume fraction of oil, water, natural gas, and oil/water emulsions (flowing in a pipe line). Various flow regimes which may influence the choice of probe

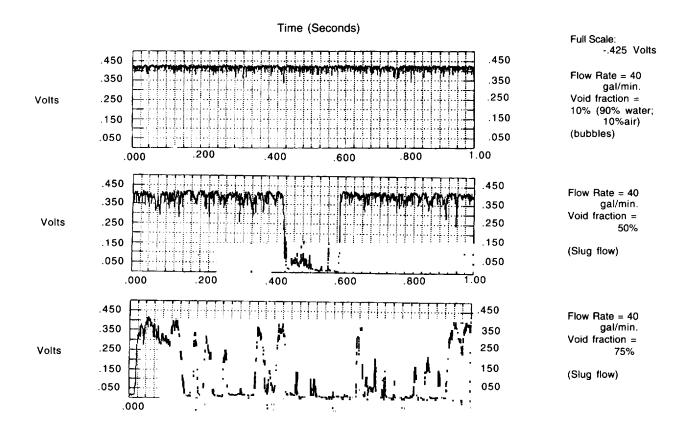


Figure 2. Flapper valve experiment using distilled water and nitrogen.

locations in the flow stream are possible. By placing probes at various strategic locations within a cross-section of pipe, the volume fractions of each constituent can be calculated statistically by the technique described in this paper. Also, by using an identical probe configuration downstream from the first probe, the velocity of each constituent can be measured in most cases.

Multiple in-flow probes can be used to measure many parameters, such as

- volume fractions of each constituent
- · velocity of each constituent
- blob statistics
- flow regimes
- flow profiles

Hybrid Regenerative Water Recovery System

Charles E. Verostko, Marybeth A. Edeen, and Nigel J.C. Packham, Ph.D.*

Johnson Space Center/EC

*LESC

Abstract

Long-duration manned space missions will require integrated biological and physical/chemical processes to recover resources from wastes. In this report, we will discuss a hybrid regenerative biological and physical/chemical water recovery system that was designed and built in the Crew and Thermal Systems Division. The system is sized for a four-person crew and consists of a two-stage, aerobic, trickling filter bioreactor; a reverse osmosis system; and a photocatalytic oxidation system. The system was designed to accommodate high organic and inorganic loadings and a low hydraulic loading. The bioreactor was designed to oxidize organics to CO, and H,O; the reverse osmosis system reduces inorganic content to potable quality; and the photocatalytic oxidation unit reduces residual organic content (parts per million range) to potable quality and provides in situ disinfection.

Introduction

For long-duration exploratory space missions, the reclamation of water for potable and hygiene uses from waste water is of vital importance. Approximately 230 kg of waste water are generated by a four-person crew during the course of normal daily activities. Efforts to recover this water have focused primarily on physical/chemical methods such as phase change and/or membrane processes. It is likely, however, that because of the additional waste components generated in a lunar/Mars habitat, some biological method may have sufficient advantages (low temperature, low pressure operation, etc.) over physical/chemical methods. The decision was therefore made to investigate a hybrid biological and physical/chemical system for water reclamation.

The hybrid regenerative water recovery system (HRWRS) is housed in the building 241 facility at JSC. It has been funded primarily from Center Directorate Discretionary funds since start-up in December 1991.

Problem Statement

The objectives of the HRWRS are to investigate the efficiency of a hybrid system to reclaim potable water from waste waters; to determine the chemical characteristics of individual sources of waste water; to assess the water usage amounts using current Space Station Freedom water allotments; and to determine the feasibility of a hybrid system for water recovery for long-duration missions (longer than 1 year).

Approach/Method

The system is comprised of two major components; the waste water collection and transport system (WWCTS) and the three treatment processes (a two-stage aerobic trickling filter bioreactor, a reverse osmosis (R.O.) unit, and a photocatalytic oxidation system). A schematic of the system is shown in Figure 1. The components of the system are described in detail below.

Waste Water Collection and Transport System

The WWCTS is comprised of the five production sources (shower, hand wash, urinal, laundry, and dishwasher), the facility use control system, the waste water production measurement system, and the transport system. Although each component of the waste water production source was a commercially available item, every effort was made to modify the components for limited water usage. Operation of the HRWRS is under complete computer control. Volunteers provide waste water from shower, hand wash, and urinal sources and also provide clothes for laundry. Dish wash waste water is provided every other day using dinnerware from the JSC cafeteria. The volumes and the frequency of collection of waste water from each production source are shown in Table 1.

Bioreactor

Bioreactor design goals were to (1) replace pretreatment chemicals required for urine and waste water stabilization; (2) stabilize volatiles, such as ammonia, to prevent carryover to the R.O. system; and, (3) accomplish organic removal down to 50 mg/l or less. The reactor was sized for a four-person crew.

Bioreactor Design

A fixed-film, aerobic reactor was chosen. The design of the bioreactor was based on the mass flow rate of water in the system, the expected organic carbon loading of the system, and the municipal design criteria. The mass flow rate of water in the system was based on Space Station water requirements for urine flush, shower, hand wash, and laundry water. A two-stage reactor was designed in which most of the organic carbon would be removed in the first stage and the remainder would be removed in the second stage, with the second reactor also accomplishing the nitrification of ammonia.

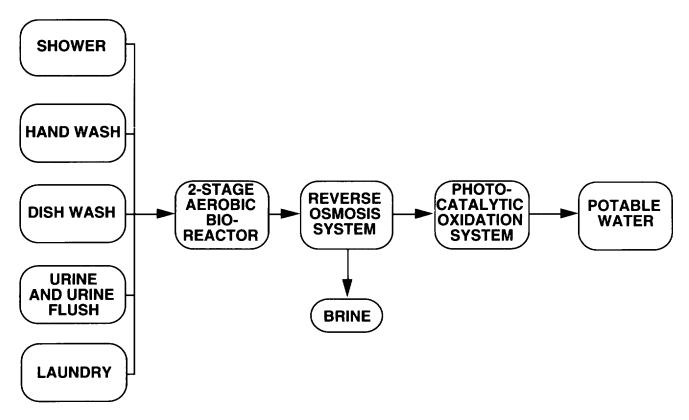


Figure 1. Hybrid regenerative water recovery system schematic.

Table 1. Production sources use mass and frequency

Production Source	Mass Per Use (kg)	Uses Per Day
Shower	5.44	4
Urinal*	0.50	16
Hand Wash	1.02	16
Laundry	49.90	1
Dishwasher	45.72	0.5
Total Mass	118.84	-
Per Day (kg)		

^{*} Includes 0.125 kg/use flush water

Reactor Fabrication

Reactors were fabricated from high-strength plastic. The first stage is acrylic and has a cross-sectional area of 335 cm.² The second stage is a standard polyethylene tube with a cross-sectional area of 190 cm.² Both reactors were fitted with sample ports and thermocouples at the inlet and the outlet and at depths of 0.30, 0.91, and 1.52 m into the bed. Flow distribution plates were designed to ensure distribution of the flow over the entire cross-sectional area of the reactor. Underdrains collected effluent water and directed it to small settling tanks at the bottom of the reactors. Feed for the downstream processes and for recycle

around the reactors is drawn from the middle of these settling tanks. Air is forced through the reactors from the bottom to the top with a blower.

Reactor Inoculation and Acclimation

Bioreactors were inoculated with effluent water from the Vince Bayou Waste Water Treatment Plant in Pasadena, Texas, on December 12, 1991. This plant was chosen because it uses a rock-trickling filter as one of the initial treatment steps for the waste material so the residual microflora should have been well adapted to fixed-film growth. Also, it is a municipal system with some industry effluent feeding into it, which means the microflora were expected to be very diverse. After inoculation, the waste concentration was slowly increased to full strength.

Two cartridge filters (35 and 8 μ , respectively) were placed in the line between the effluent from bioreactor two and the R.O. system to remove large particulates and biomass from the water stream. An additional 5- μ filter was included on the R.O. system itself.

Reverse Osmosis System

A commercial R.O. system was procured from Applied Membranes (San Marcos, California). This system uses two Filmtec seawater-type membranes (spiral

wound) that are 11.4 cm in diameter, are 101.6 cm in length, and are run in series. Unlike most applications for R.O., a requirement of 85% recovery of water from the bioreactor was imposed. Additionally, the water quality requirement for the permeate was less than 100 mg/l total dissolved solids (TDS). At flow rates of 0.76 l/m (concentrate), 22.71 l/m (recirculate), and 6.06 l/m (permeate), and with the above requirements met, the result is a concentrate of approximately 10,000 to 12,000 mg/l TDS. Typical operating pressures are 2070 to 2760 kPa. No chemical additives were injected into the system to avoid biofouling and/or chemical deposition (as in normal operations). Instead, a daily 5-minute flush of the system with deionized water was performed. Plans to recover the 15% water lost as concentrate by using a wick evaporation technique are now being developed.

Photocatalytic Oxidation System

The principle of photocatalysis of residual organic material is well known. The catalyst material is TiO_2 . Interaction between ultraviolet light (254 nm wavelength), oxygen, water, and the organic material to be oxidized produces a hydroxyl radical—a species with a very high affinity for organic material. The resulting oxidation of organics produces CO_2 and $\mathrm{H}_2\mathrm{O}$.

Results (FY93)

Bioreactor

For approximately 21 months, since inoculation in December 1991, the bioreactor has been in continuous operation.² The performance of the bioreactor in terms of total organic carbon (TOC) removal efficiency has been outstanding (Figure 2). For 81% of the time (when using the water allotments shown in table 1), the performance criterion of 50 mg/l TOC (parts per million) in the effluent from the second stage bioreactor was met. After several periods of upset conditions, the bioreactor returned to nominal performance in a short period of time (hours to days). Nitrification of the waste water was also observed.

Reverse Osmosis System

Analysis of R.O. performance is based on two factors: percent recovery and percent rejection. In terms of percent recovery, during long-term testing, the system continually operated at between 85 to 87% recovery and at a permeate quality below 75 mg/l TDS.

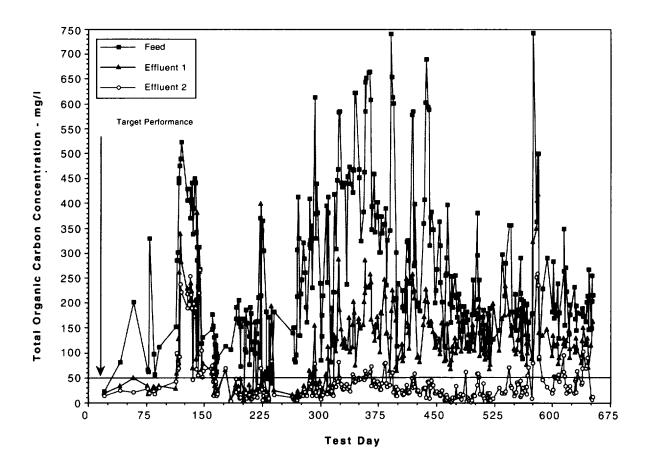


Figure 2. Performance of the bioreactors in terms of TOC removal efficiency during 21 months of testing.

Photocatalytic Oxidation System

Several approaches using photocatalytic oxidation were investigated. The original subsystem we tested, which was developed by Photocatalytics Incorporated (Phase II SBIR),³ proved to have insufficient rates of oxidation. An alternate, flow-through subsystem (Matrix Incorporated) that was based on the same principle also exhibited kinetics unsuitable for long-term, continuous operation. An evaluation of alternate post-treatment methods is in work.

Conclusions

It has been demonstrated that a hybrid biological and physical/chemical system is capable of treating waste water from shower, urinal, hand wash, laundry, and dishwasher sources and can produce potable water from such waste water.

A facility now exists which is automated to collect and process waste water. The system has flexibility for testing and evaluating biological and physical/chemical water recovery system processes.

The bioreactor has operated for 21 months without interruption and has demonstrated high performance in removing organic impurities from waste water. The R.O. system continues to demonstrate the ability to remove dissolved solids.

The major difficulties encountered during this period of investigation have been mechanical in nature. Specifically, mechanical difficulties are associated with pump design for low flow rates with high suspended solids levels.

The post-treatment subsystems tested to date have proven to be unsuitable for system integration. An alternate method of post-treatment is currently under evaluation

System closure will be maximized by (1) the recovery of the 15% brine from the R.O. system, (2) the closure of the gas loop from the bioreactor effluent, and (3) the

development of a methodology for the treatment of bioreactor solids.

No expendable materials have been used in the HRWRS except for infrequent changeout of cartridge filters between the bioreactors and the R.O. system. This represents a substantial advantage over past and present water recovery systems.

Acknowledgments

We would like to acknowledge the following individuals at the Crew Thermal Systems Divsion, JSC: A. F. Behrend, Manager, Advanced Programs; H. E. Winkler, Chief, Life Support Systems Branch; C. D. Thompson, Deputy Chief, Life Support Systems Branch; Dr. C. H. Lin, Chief, Systems Engineering Analysis Branch; C. E. Verostko, Aerospace Technologist, Life Support Systems Branch; M. A. Edeen, Systems Analysis Engineer, Systems Engineering Analysis Branch; and Dr. D. L. Henninger, Chief Scientist for Regenerative Life Support Systems, Life Support Systems Branch. We would also like to acknowledge the following individuals in the Crew Systems Department at Lockheed Engineering and Sciences Company: R. J. Gillen, Manager, Crew Systems Department; N. J. C. Packham, Senior Scientist; and M. S. Johnson, Engineering Assistant

References

"Environmental Control and Life Support System (ECLSS)," Revision D, NASA, Space Station Program, Architectural Control Document SSP-30262, 1991.

²Verostko, C. E., Edeen, M. A., and Packham, N. J. C., 22nd International Conference on Environmental Systems, Seattle, WA, July 1992.

³Cooper, G., and Ratcliff, M. A., Photocatalytics, Inc., Boulder, CO., Final Report NASA Contract NAS 9-17987, June 1990.

Hybrid Vision Eye Tracking

Richard D. Juday Johnson Space Center/EE

Abstract

The JSC Hybrid Vision program is developing hardware for a medical purpose. Hybrid Vision is a highspeed image processing device, an optical joint Fourier transform correlator, that JSC has patented for use in retinal laser treatment. During 1993, laboratory results showed that the patented method has the necessary speed, and the patent was licensed to Pinnacle Imaging.

Introduction

The Hybrid Vision program at JSC combines optical and digital image processing for various purposes. Among the optical processing elements under development are optical correlators, spatial light modulators, and optimal filter theory. Among the digital processing elements are digital stereo, video rate geometric image warping, and space variant image sensing. One method we recently patented¹⁻⁴ is a method of rapidly tracking the apparent motion of the detailed image structure of a surface. The effect as seen from the sensor is that the surface is stabilized. Its potential space applications include navigation for autonomous planetary landing, detection of previously unmodeled landing hazards, and autonomous rendezvous and capture.

We are also pursuing Earth-bound applications for our techniques, significantly in human vision. Two such applications are most significant. The first is prosthetic image warping for field defect problems such as maculopathy and retinitis pigmentosa, currently under study at NASA, the University of Houston, and the University of Pennsylvania. The second, the focus of this article, is surface tracking by means of the optical joint Fourier transform, described above, for tracking the motion of surface features. We have patented its application to track the motion of the retina for use in laser photocoagulation of diseased retinal structures. In this application, we have allied ourselves formally with the Army Missile Command (MICOM) and with Pinnacle Imaging. The military interest in the Hybrid Vision program is as a very fast aid to the passive identification of friend or foe, which might be able to reduce fratricide in battlefield situations. MICOM is contributing practical experience in correlator technology.^{5,6} Pinnacle has licensed the technology from NASA and is developing a test-bed for the concept described in the next section. Figure 1 is reproduced from the patent.

Problem Statement/Description

The need for the image stabilization method arose from the need to land an autonomous vehicle on a planetary surface in the presence of unknown obstructions. JSC proposed image stabilization based on the optical joint Fourier transform, and it led a proposal including

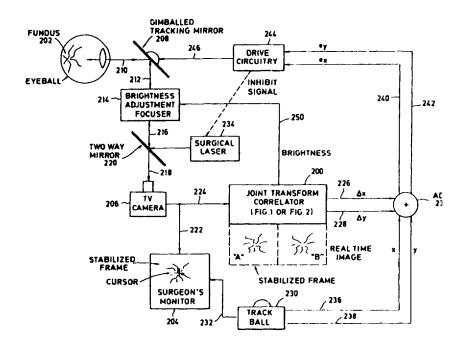


Figure 1. Optical joint correlator for real-time image tracking and retinal surgery.

Ames Research Center (ARC) and the Jet Propulsion Laboratory (JPL) to develop a highly sophisticated vision system. This system would fully model the visible obstructions based on optic flow, which is the differing motions of elements in the field of view as the viewpoint is translated. The joint transform correlator (JTC) would provide the gross tracking, and the digital image processing modules developed by ARC and verified by JPL would analyze the second-order image motion for the underlying three-dimensional basis. Although the fully competent vision system was not funded, the various pieces continue in separate development, including the joint transform correlation stabilization. The technology developed for planetary landing was transferred into the medical arena as a result of professional networking. Juday described the image analysis method to H. John Caulfield of the University of Alabama, who knew of a medical practitioner who had need of the technique. In retinal laser treatment there is a need for "landing" the laser onto only the desired portions of the retina. Caulfield put Juday in touch with Steve Charles of Pinnacle Imaging, and the project is now under way.

Approach/Method

The method of the optical joint Fourier transform¹⁻⁶ offers a fast, reliable, and inexpensive method to correlate images with reference images. In the medical field, the laser eye surgeon needs rapid registration of retinal images to facilitate hitting exactly the spot on the retina that the surgeon wishes to photocoagulate. Pinnacle Imaging has shown the medical practicality of a digital method for rapid registration; however, the digital method is too expensive for commercialization. The optical image processing method using the JTC promises to be sufficiently inexpensive to be commercially attractive. The digital method was technically confounded by torsion of the eye—a problem JSC is attempting to solve by digital processing of the reference image.⁷

JSC developed the JTC method of image stabilization for automated planetary applications, notably the extraction of shape-from-motion owing to translation of the sensing platform with respect to a three-dimensional structure. The JTC method can remove the image motion that originates in camera position jitter, rather than in differing perspective points on the object, and is thus regarded as noise to the process. The method has been substantiated in laboratory measurements.²⁻⁶

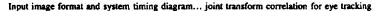
Results

Significant results have occurred since the previous report to this forum. First, Rocketdyne⁸ showed in the laboratory that, using present-day spatial light modulators, the method has the necessary speed. Second, the patent was licensed to Pinnacle Imaging, Inc. Third, Pinnacle has become formally allied with OCA Applied Optics to

design the overall optical system for ophthalmic procedures. (The JTC, which measures the apparent retinal position, is just one optical device. The system also comprises high speed and high image quality cameras, laser diodes of several wavelengths for various treatments, illumination sources, intraocular lens aberration correction, and other elements.) In addition to the necessary technical partners, we have organized funding for the Government's part of the project. In-house and under grant to the University of Missouri/Kansas City (UMKC), we are developing techniques to extend the range of eyeball torsion over which the correlation holds up. Additionally at UMKC, we are developing fast adaptive methods of correcting for initially unknown aberrations arising in the intraocular lens. We are applying the theory and laboratory practice that we have developed for Fourier optics pattern recognition using commercially available liquid crystal television projection systems. Funding for Government activities comes from three sources: the NASA Technology Utilization Office, discretionary funds from the JSC Tracking and Communications Division, and a widow's mite from the JSC Legal Office that had accumulated from previous licensing fees. Our preliminary request for information brought in a set of responses that were incorporated into a request for proposal (RFP) we intended to issue. A substantial number of organizations (approximately 50) expressed a desire to receive the RFP, but we were unable to issue it because our military partner, MICOM, had a shortfall in funding. Figure 2 outlines how we expect to convert laboratory work into actual timing of a production model JTC. At 400 Hz, an image is received, its position is measured with respect to a previously grabbed frame, and that position is reported to the mirror that nulls the apparent position to accomplish the tracking. Rocketdyne, which is actively interested in the project despite our inability to fund their work, demonstrated that the joint transform method would function in two important respects: first, that retinal imagery has sufficient detail to correlate on; and second, that the current state of the art in spatial light modulators will support the necessary speed.

Conclusions

The basic technique is proven. We have worked around a severe funding shortfall. Work is proceeding on several aspects of the problem.



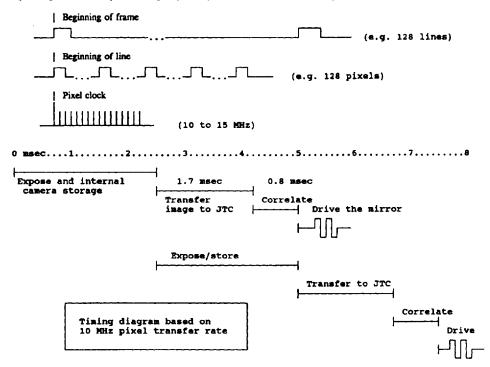


Figure 2. Example timing diagram as necessary for retinal tracking for photocoagulation.

References

- ¹Optical joint correlator for real-time image tracking and retinal surgery, U. S. Patent 5,029,220, July 1991.
- ²Knopp, Jerome, and Juday, Richard D., "Optical joint transformation correlation on the DMD," Proc. SPIE 1053, 208-215 (1989).
- ³Knopp, Jerome, "Spatial weighting of synthetic reference objects for joint correlation by random pixel mixing," Proc. SPIE 1295 (1990).
- ⁴Tam, Eddy C., Yu., Francis T. S., Gregory, Don A., and Juday, Richard D., "Autonomous real-time objects tracking with an adaptive joint transform correlator," *Optical Engineering*, April 1990, 314-320.

- ⁵Gregory, Don A., Loudin, Jeffrey A., and Yu, F. T. S., "Illumination dependence of the Joint Transform Correlation," *Appl. Opt.* Vol. 28, No. 15, 1989, 3288.
- ⁶Yu, F. T. S., Jutamulia, Suganda, and Gregory, Don A., "Adaptive real-time pattern recognition using a liquid crystal TV based joint transform correlator," *Appl. Opt.* Vol. 26, No. 8, 1987, 1370.
- ⁷Juday, Richard D., and Bourgeois, Brian, "Convolution-controlled rotation and scale invariance in optical correlation," Proc. SPIE 938, 1988, 198-205.
- 8Schehrer, K. L., Roe, M. G., and Dobson, R. A., "Rapid tracking of a human retina using nonlinear joint transform correlator," Proc. SPIE 1959, 1993.

The Materials Chemistry of Atomic Oxygen: Low Earth Orbit (LEO) and the Laboratory

Steve L. Koontz, Lubert J. Leger, James T. Visentine, Mike Richardson,* Jon B. Cross,** and Don Hunton†

Johnson Space Center/ES5, *Johnson Space Center/IA

**Los Alamos National Laboratory

†USAF Phillips Laboratory

Abstract

Neutral atomic oxygen is the most abundant component of the ionospheric plasma in the low Earth orbit (LEO) environment (200 to 700 kilometers altitude). In this report, we will summarize JSC investigations of atomic oxygen effects on spacecraft materials which culminated with the Evaluation of Oxygen Interactions With Materials-III (EOIM-III) flight experiment conducted during STS-46. To produce a more complete understanding of the materials chemistry of atomic oxygen, the chemistry and physics of O-atom interactions with materials were determined in three radically different environments: (1) the Space Shuttle cargo bay in LEO (EOIM-III), (2) a high-velocity neutral atom beam system at Los Alamos National Laboratory (LANL), and (3) a microwave-plasma flowing-discharge system at JSC. The Space Shuttle and the high-velocity atom beam systems produce atom-surface collision energies ranging from 0.1 to 7 eV (hyperthermal atoms) under high-vacuum conditions, while the flowing discharge system produces a 0.065 eV surface collision energy at a total pressure of 2 Torr. The EOIM-III flight experiment contained a mass spectrometer and O-atom dosimeters which were calibrated for O-atom flux and fluence measurements both before and after flight in the LANL atom beam system. Excellent agreement was obtained between EOIM-III instrument measurements and predictions of the O-atom fluence made with the MSIS-86 model of the thermosphere. Data obtained in the three different O-atom environments referred to above show that the rate of O-atom reaction with polymeric materials is strongly dependent on atom kinetic energy, which obeys a reactive scattering law that suggests that atom kinetic energy is directly available for overcoming activation barriers in the reaction. General relationships between polymer reactivity with O-atoms and polymer composition and molecular structure have been demonstrated. In addition, vacuum ultraviolet photochemical effects have been shown to dominate the reaction of O atoms with fluorocarbon polymers. Finally, studies of the materials chemistry of O atoms have produced results which may be of interest to technologists outside the aerospace industry. Atomic oxygen spin-off technologies in the areas of microelectronic materials and device processing, porous solids chemistry are described.

Introduction

Oxygen atoms are the most abundant neutral constituents of the Earth ionosphere at altitudes ranging from 200 to 700 km1-3 (low Earth orbit or LEO) and have been shown to be one of the more important environmental factors involved in the degradation of several important classes of spacecraft materials.^{4,5} The primary objective of the Evaluation of Oxygen Interactions With Materials-III (EOIM-III) flight experiment, in combination with supporting laboratory measurements, was to produce benchmark atomic oxygen reactivity data for a wide range of materials.6 Reactivity data are needed to support materials selection for long-lived LEO spacecraft and to validate the various approaches to ground-based atomic oxygen testing. Secondary objectives included: (1) mass spectrometric characterization of the gaseous reaction and scattering products formed when the ambient atmosphere in LEO interacts with various materials, (2) characterization of the induced environment produced by interaction of the ambient atmosphere in LEO with the EOIM-III experiment and the Space Shuttle cargo bay, and (3) characterization of the chemical reaction dynamics of the O-atom interactions with polymeric materials. In this report, we present an overview of the JSC component of EOIM-III. EOIM-III was a team effort with coinvestigators from all major NASA field centers, the United States Air Force, the European, Japanese, and Canadian space agencies, and the Ballistic Missile Defense Office.

Our approach to achieving our atomic oxygen materials chemistry objectives was based on measurements of sample properties before and after exposure to known O-atom fluences in three well-characterized environments: (1) the LEO environment during the EOIM-III flight experiment, ^{7,8} (2) the high-velocity neutral-atom beam (HVAB) system at the Los Alamos National Laboratory (LANL), ^{9,10} and (3) a flowing discharge or downstream plasma system at JSC. ^{11,12} Detailed characterization of the exposure environments was accomplished by determining such factors as O-atom flux and fluence as well as the O-atom kinetic energy distribution function on collision with the sample surface, sample temperature, ultraviolet/vacuum ultraviolet (UV/VUV) radiation dose, and surface contamination.

Materials and Methods

The materials chemistry of atomic oxygen was determined in three different experimental systems: (1) the EOIM-III atomic-oxygen materials-chemistry experiment, 7.8 (2) a high-velocity O-atom nozzle beam system, 9,10 and (3) a flowing plasma discharge (remote plasma) apparatus.^{11,12} The extent of O-atom reaction with the polymer film or sheet specimens was determined by mass loss measurements and/or surface recession measured by profilometry. O-atom reactivity measurements made by weight loss and profilometry were compared, wherever possible, to check on the accuracy of the two measurement methods. In most cases, the polymer film or sheet samples were used, as received, from various commercial suppliers (table 1). Prior to atomic oxygen exposures, polymer film and sheet samples were subjected to 48 hours of vacuum baking, at the maximum temperature expected during the exposure, to remove absorbed water and other volatile substances before preexposure weighing. After weighing, the polymer samples were cleaned by brief rinsing with Q Clean™ Solvent, (Thermo Analytical Inc., Monrovia, California) to remove surface contaminants, such as silicones, which could interfere with O-atom reactions. Polymers were tested for compatibility with the cleaning solvent before use. Polymer surfaces were analyzed before and after exposure by

X-ray photoelectron spectroscopy (XPS) both to evaluate the extent of surface oxidation and to verify surface cleanliness.

The HVAB at LANL has been described. 9.10 Briefly, a laser-sustained gaseous discharge (50% O₂/Ar or O₂/Ne at pressures on the order of 2000 Torr) undergoes supersonic nozzle expansion to form a seeded beam of oxygen atoms (O³P electronic ground state) and inert gas atoms. Adjusting the location of the gaseous discharge relative to the expansion nozzle permits control of the kinetic energy distribution function in the final beam so that the average kinetic energy can be varied between 0.4 and 3 eV. Beam velocity distribution functions were determined directly using well-known velocity selector—time of flight (TOF)—methods 9.10 with mass spectrometric detection of atomic and molecular species. A schematic diagram of the HVAB system is shown in Figure 1.

The O-atom flux in the beam was determined using both relative abundance from the TOF data and from the pressure rise in an accommodation chamber as was previously reported. Accommodation chamber pressure was measured using both a spinning rotor gauge (total pressure) and a residual gas analyzer (partial pressures at steady state) that were calibrated (for stable gas species such as Ar, Ne, O₂) using the same spinning rotor gauge. The pressure rise in an accommodation chamber was measured with the high-velocity atom beam entering the

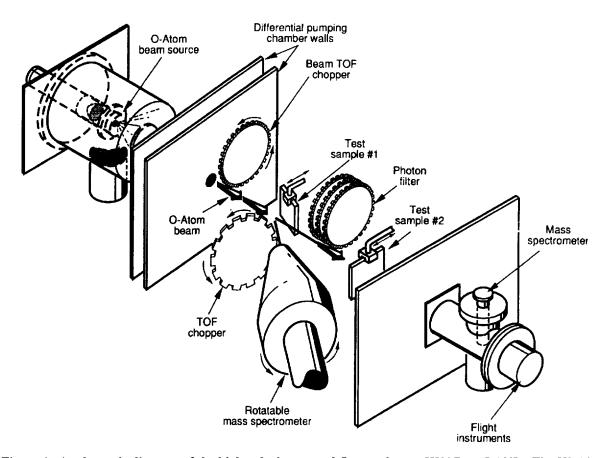


Figure 1. A schematic diagram of the high-velocity neutral O-atom beam (HVAB) at LANL. The HVAB was developed and operated under contract to JSC.

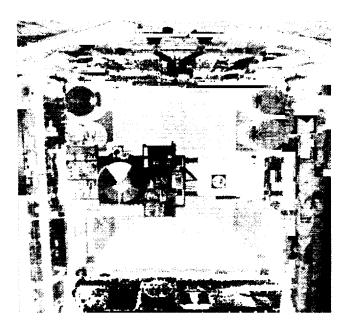
chamber and the chamber turbo pump gated off. Under these conditions, the inert-gas effusive flux out of the chamber equals the inert gas beam flux into the chamber so that the inert gas flux in the high-velocity atom beam can be immediately calculated. Given the inert gas flux in the beam and the relative abundances from phase-sensitive mass spectrometry, the fluxes of all other beam species, including atomic oxygen, were calculated using known values of electron impact cross sections and the mass spectrometric transmission function.

For O-atom reactivity studies, polymer film specimens were mounted on a heat sink to control heating by thermal radiation from the HVAB source. The typical Kapton film temperature during O-atom bombardment was 45°C, and the samples could be heated to determine Arrhenius activation energies. Gaseous reaction products were detected using modulated beam techniques with phase-sensitive mass spectrometric detection to reject vacuum system background. 9.10

The atomic oxygen materials chemistry experiment (EOIM-III) was conducted during STS-46 at an altitude of 223 km. ^{7,8} The total O-atom fluence was 2.3 ± 0.3 x 10²⁰ atoms/cm² as determined by calculation using a wellestablished mathematical model of the thermosphere and by direct measurement using a mass spectrometer, which was calibrated for O-atom measurements before and after flight in the HVAB referred to above, as well as Kapton film dosimeters also calibrated for O-atom fluence measurements in the HVAB. The materials samples and related instruments were oriented so that the angle between the surface plane and the incident atom flux was 90 degree (normal incidence). In addition to the passive sample carriers, three sample trays were thermostated at 60°C, 120°C, and 200°C to permit determination of

Arrhenius activation energy parameters of the atomic oxygen reaction with various materials. The average temperature of the passive sample carriers during the EOIM-III O-atom exposure period was 19°C. A schematic diagram of the EOIM-III payload is shown in Figure 2. A key component of the EOIM-III flight experiment pack-age was the mass spectrometer shown in the payload schematic. The mass spectrometer was calibrated for high-velocity O-atom flux measurements both before and after STS-46 in the HVAB at LANL. 7,8,10 The MSIS-86 model of the thermosphere3 was used to calculate O-atom fluence for the EOIM-III exposure using as-flown orbit data for STS-46 and daily average values of the solar geomagnetic parameters. Daily average values were used instead of monthly averages because significant magnetic substorm activity was observed during the STS-46 mission.7,8

The methods and apparatus used to determine the O-atom reactivities of polymers in the flowing discharge (remote plasma) apparatus have been described. 11-13 Briefly, a working gas (10% O₂/Ar or 10% N₂O/Ar), at total pressures on the order of 2 Torr, was passed through a 2.45 GHz Evenson discharge cell and flowed downstream of the discharge before coming into contact with the polymer samples, which meant that the gas had cooled to room temperature but still contained O-atoms in the O³P electronic ground state. The O-atom concentration was determined by chemiluminescent titration using NO₃, ^{14,15} and the atom flux on sample surfaces was determined using well-known methods for modeling flowing reaction-diffusion systems.¹³ The flowing discharge approach was selected because a substantial database on the gas phase chemical kinetics of atomic oxygen has been produced in flowing discharge-type



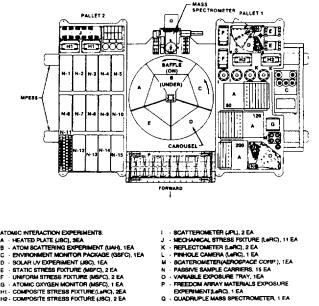


Figure 2. The EOIM-III flight experiment: (a) a photograph of the payload in the Space Shuttle cargo bay prior to launch, and (b) a schematic diagram of the payload components.

Table 1. Polymer Reaction Efficiencies

POLYMER	Re (EOIM-III) x 10 ²⁴	Re (STS-8) x 10 ²⁴	Re (STS-41) x 10 ²⁴	Re LDEF x 10 ²⁴
KAPTON (LeRC R.R.)	3.1	3.0	3.3	3.0
EYMYD-F (ETHYL CORP.)	2.7			
CR-39 POLYCARB.	6.1	6.0		
PEEK (ICI)	3.4		4.3	
XYDAR (AMOCO)	2.9			
LCP-4100 (DuPONT)	3.2			
MYLAR A (DuPONT)	3.8	3.9		
PE, (LeRC R.R.)	4.4	3.7		
HDPE (PHILLIPS, EMH6606)	3.7	3.7	3.5	
POLYMETHYLPENTENE (MITSUI)	5.3			
POLYPROPYLENE	5.5		4.4	
TEDLAR (DuPONT)	3.5	3.2		
TEFZEL (CLEAR, DuPONT)	0.9		0.2	
TEFZEL (BLUE, RAYCHEM)	1.1			
TEFZEL (WHITE, RAYCHEM)	0.9			
KYNAR (PENWALT)	1.2			
KEL-F (PCTFE)	0.9			
HALAR (ALLIED)	1.9			
ACLAR 33C ALLIED)	1.0			
FEP TEFLON (LeRC R.R.)	0.05	< 0.03	< 0.03	0.3
TFE TEFLON	0.06	< 0.03		0.5
EYPEL-F, (ETHYL CORP.)				
POLY(BISTRIFLUOROPR				
O-PYLPHOSPHAZENE)	<0.03			

equipment in the past 30 years^{14,15} so that the O-atom environment is well characterized. Both samples and reactive gas could be heated to determine Arrhenius activation energies. In addition, VUV discharge lamps could be installed to provide known doses of VUV radiation simultaneously with O-atom exposure. A schematic diagram of the flowing discharge apparatus is shown in Figure 3. The flowing discharge environment differs from both the HVAB and on-orbit environments in three important respects: (1) O atoms arrive at the polymer sample surface by diffusion from an isotropic gas, not as a well-defined directed flux or beam; (2) the pressure is on

the order of 2 Torr, not 10⁻⁵ Torr, so that gaseous reactive intermediates can return to react with the polymer surface; and (3) the flux of molecular oxygen is much higher in the flowing discharge than in the LEO or HVAB environments described above, although large variations in O₂ partial pressure have revealed no effects on the reactivity of Kapton polyimide in this system.¹² The dominant process is still O-atom reaction with the polymer surface so that, with some caveats, the flowing discharge system can still provide useful measurements of the reactivity of low kinetic energy (0.065 eV) O atoms.

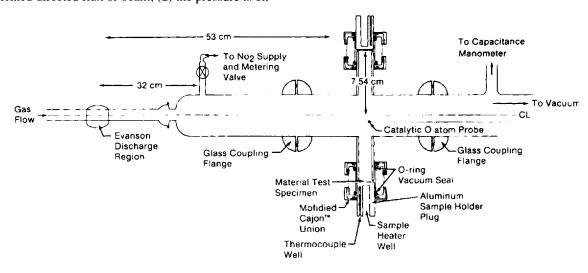


Figure 3. The JSC flowing discharge apparatus.

Results and Discussion: Polymer Reactivity

Polymer reactivity with O atoms is reported as the reaction efficiency, Re, which is easily calculated by dividing the surface recession in centimeters by the total O-atom fluence in atoms/cm². Re has units of cm³/atom. Re allows a meaningful comparison of the O-atom reactivity of polymers independent of variations in atom dose or polymer composition and density as long as the polymer is in the form of a full-density solid. Polymer Re values (cm³ of material removed per incident O atom), which were determined following exposure on orbit in the EOIM-III passive trays, are shown in Table 1 where EOIM-III measurements are also compared with those made following previous flight experiments. The reaction efficiencies reported in Table 1 were determined by weight loss only. The repeatability of the measurement is indi-cated as the difference between the largest and smallest measurement, if more than one sample was exposed on orbit. Comparison of the EOIM-III reaction efficiency data in table 1 with those of previous missions demon-strates that the polymer reaction efficiency database has been both enlarged and verified.

The reliability of the weight loss measurements was checked by direct comparison with profilometry measurements. The results of replicate measurements of the reaction Re of Kapton polyimide demonstrate excellent agreement between the profilometry and weight loss measurements. Weight loss on four Kapton samples produced a reaction efficiency of $3.05\pm0.1 \times 10^{-24} \text{ cm}^3/\text{atom}$ while profilometry produced a reaction efficiency of $3.16\pm0.1 \times 10^{-24} \text{ cm}^3/\text{atom}$, using $2.3 \times 10^{20} \text{ atoms/cm}^2$ as the fluence estimate. Both numbers are in excellent agreement with the Kapton reaction efficiencies produced by other onorbit materials experiments such as STS-8¹⁶ (3 x 10⁻²⁴), the Long-Duration Exposure Facility¹⁷ (LDEF) (3.0 x 10^{-24}), and the Intelsat Solar Array Coupon (ISAC) experiment flown on STS-41¹⁸ (3.1 x 10^{-24}). However, the

STS-8, ISAC, and LDEF reaction efficiency measurements were all dependent on the MSIS-86 model of the thermosphere for O-atom fluence. An independent measure of Kapton reaction efficiency was made in the LANL HVAB as part of the kinetic energy dependence study reported below, and it was found to be 3.3 x 10⁻²⁴cm³/atom—within 10% of the value based on the spaceflight exposures.

Several general trends in the relationship between O-atom reactivity and molecular structure are visible in Table 2. For example, polyethylene, Tedlar, Tefzel, Kynar, and Tefton are all linear carbon chain polymers with increasing fluorine content and decreasing hydrogen content as we move along the series from polyethylene, (CH₂-CH₂)n, or polypropylene, to Teflon, (CF₂-CF₂), or FEP Teflon. As can be seen in Table 2, increasing fluorine content results in decreasing O-atom reaction efficiency, which is as we would expect if hydrogen atom abstraction is a rate-limiting process and fluorine atom abstraction occurs to a very limited extent, if at all. The EOIM-III reaction efficiency for Teflon is between that reported from STS-8¹⁶ and LDEF.¹⁹ We attribute the observed range of reaction efficiency values to different net doses of solar UV/VUV radiation in the different mission environments. Laboratory studies in the JSC flowing discharge system have shown that vacuum UV photo-chemistry is the controlling factor in the O-atom chemis-try of Teflon and Kel-F.²⁰ The EOIM-III payload received a larger VUV radiation dose than did STS-8 as a result of the solar inertial hold period following deployment of the European Retrievable Carrier satellite during an earlier portion of the STS-46 mission.

In contrast, incorporating two CF₃ groups into a polyimide structure results in little or no change in reaction efficiency, as can be seen by comparing the reaction efficiencies of Kapton polyimide and Eymyd-F. In general, the aromatic polymers displayed significantly lower reaction efficiencies than did the linear straight-chain

Table 2. The effects of atom-surface collision energy on the reaction efficiency, Re, and the parameters of the empirical Arrhenius equation, Re = A x EXP(-Ea/kTs), where Ts is polymer surface temperature and Ea is the activation energy in eV. Re is in cm³/atom.

POLYMER	Re, LEO	Ea, LEO	Re,HVAB	Ea,HVAB	Re, FDS	Ea, FDS
KAPTON	3.1E-24	0.02 eV	3.3E-24	0.01 eV	2 E-28	0.3 eV
MYLAR	3.8E-24	0.05 eV			3 E-28	0.4 eV
D4PE	3.8E-24	0.0 eV			2 E-27	0.2 eV
PE	3.7E-24	0.0 eV			4 E-27	0.2 eV
KYNAR	1.2E-24	0.0 eV			3 E-29	0.4 eV
TEFZEL	0.9E-24	0.04 eV			3 E-29	0.5 eV
LCP-4100	3.2E-24	0.04 eV				
XYDAR	2.9E-24	0.05 eV				
CR-39	6.1E-24	0.04 eV				
EYMYD-F	2.7E-24	0.03 eV				
PEEK	3.4E-24	0.03 eV				

hydrocarbons, with the notable exception of the polycarbonate. The very low reaction efficiency of the poly (bistrifluoropropylphosphazene)-based polymers X-221, X-222, and Eypel-F all showed little or no evidence of reaction, confirming earlier work in ground-based test facilities.²¹ Eypel-F is a durable, high-temperature elastomer which should find application in spacecraft atomic oxygen environments.

Table 2 shows the temperature dependence of the polymer reaction efficiencies determined following exposure to a known O-atom fluence on the EOIM-III heated trays, in the flowing discharge apparatus, and in the HVAB. The temperature dependence of the O-atom reaction efficiency is shown as an empirical Arrhenius activation energy-i.e., the natural logarithm of the reaction efficiency is plotted against the reciprocal of the polymer sample temperature in degrees Kelvin—and the activation energy is determined from the slope. For all of the cases examined to date, straight-line Arrhenius plots have been obtained with correlation coefficients between 0.95 and 0.99. Inspection of Table 2 shows that a large decrease in the Arrhenius activation energy is obtained when moving from the flowing discharge to the HVAB or orbital environments. The large decrease in activation energy is accompanied by a large increase in polymer reaction efficiency.

O-atom kinetic energy does not appear in the Arrhenius equation. As a result, the activation energy calculated by this method can vary with O-atom kinetic energy, if atom kinetic energy is available to overcome energetic barriers to reaction as has been previously proposed.11,22 Alternately, the mechanism of reaction could change as atom-kinetic energy approaches a threshold value. Simple, empirical power laws or exponential functions have been shown to produce reasonable agreement with the limited data available at that time in the 0.065 to 5.0 eV kinetic energy range, which suggests that a single reaction mechanism as well as a single energetic barrier to reaction may determine the reaction efficiency in the Oatom kinetic energy domain of interest. The question cannot be resolved without reaction efficiency data taken at several kinetic energies between 0.1 and 1.0 eV.

The LANL HVAB was used to obtain reaction efficiency data on Kapton polyimide at average atom kinetic energies (first moments of the kinetic energy distribution function) of 0.44, 0.72, 0.79, and 2.1 eV. Velocity distribution functions and HVAB compositions measured were determined as described in the apparatus and methods section above. A typical HVAB O-atom kinetic energy distribution function (average kinetic energy = 0.79 eV) is shown in Figure 4. For comparison purposes, the kinetic energy distribution functions for ram-incident O atoms in LEO (average kinetic energy = 5.6 eV) and for O atoms striking a surface immersed in flowing discharge gas (average kinetic energy = 0.065 eV) are shown in figure 5. The flowing-discharge kinetic-energy distribution function is calculated for an effusion beam, not for the normal component of the collision energy.

The normal component is probably not appropriate in this case because the polymer surfaces are not highly oriented or highly crystalline.

The measured reaction efficiency of Kapton polyimide is plotted against the first moment (average value) of the kinetic distributions described in the previous paragraph (Figure 6). A rapid increase in reaction efficiency is seen between 0.065 and 1.0 eV followed by relatively little change between 1.0 and 5.6 eV. The data shown in Figure 6 suggest that a simple line-of-centers or Beckerle reactive collision model can be used to describe the data. Such models have proven highly successful in describing the kinetic energy dependence of a number of gas phase reactive scattering processes.²³⁻²⁶ An empirical inverse exponential model used to describe the collisioninduced chemisorption of methane on nickel²⁷ should also provide a useful description of the kinetic energy dependence of O-atom reactions with polymers. Given the width of the kinetic energy distribution functions, a simple direct fit of the data plotted in Figure 6 to such models is a gross oversimplification. A more accurate test of the kinetic energy dependence hypothesis is needed.

To test the hypothesis that the simple line-of-centers and Beckerle collision models provide a reasonably accurate description of the reaction dynamics of O atoms with

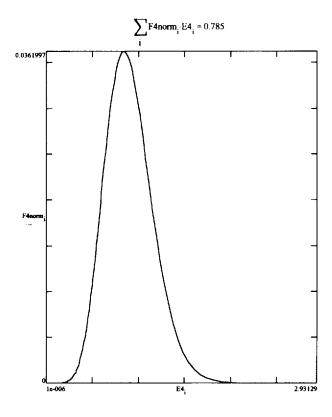


Figure 4. The kinetic energy distribution function of HVAB O atoms in the lab frame. HVAB operating parameters were set to produce an average kinetic energy of 0.79 eV.

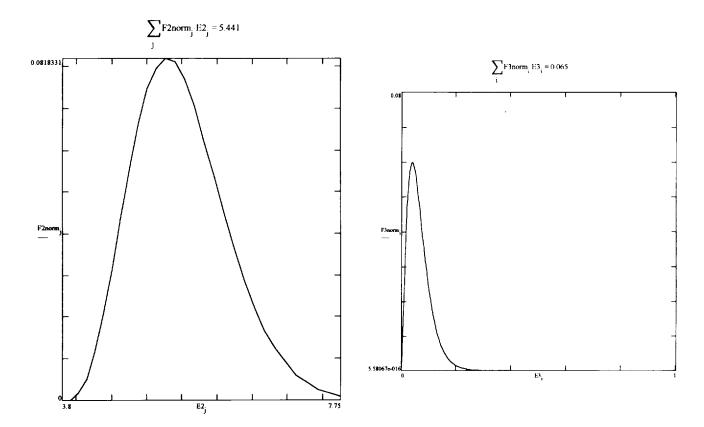


Figure 5. The kinetic energy distribution functions for: (a) O atoms striking a ram-oriented surface in LEO, and (b) O atoms striking a surface in the flowing discharge apparatus.

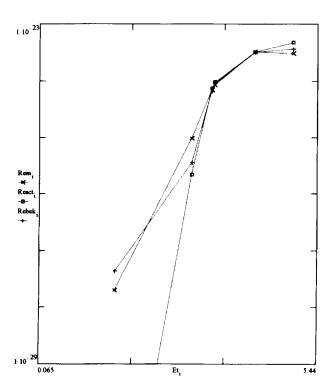


Figure 6. Measured values of Re of Kapton polyimide and Re values calculated with the Beckerle and line-of-centers models which are both plotted against the first moment (average value) of the corresponding O-atom kinetic energy distribution functions.

polymers, we form the convolution integrals of the models with the normalized kinetic energy distribution function, f(Et), as shown in the equations below and then determine if the Re vs. Et data can be fit to the resulting functions. Finally, we ask if the Re equations, with parameters determined by least squares curve fitting to the HVAB data, can predict values of Re for the flowing discharge and on-orbit environments.

Line-of-Centers Model

Re =
$$\int_{0}^{\infty} A \left(1 - \frac{Ea}{Et}\right) f(Et) d(Et)$$
, ...
$$A = 5.3 \times 10^{-24} cm^{3} / atom$$

$$Ea = 0.64 eV \qquad \Delta = 0.016$$
 (1)

Beckerle Model

Re =
$$\int_{0}^{\infty} \frac{A}{1 + \exp(-n(Et - Ea))} \times f(Et) d(Et)$$

 $A = 3.7 \times 10^{-24} \qquad n = 10$
 $Ea = 0.98 \qquad \Delta = 0.008$ (2)

Re, as defined by the Re equation above, is the average of a large number of reaction efficiencies, one for

each kinetic energy interval in the kinetic energy distribution function of interest. The Re equation allows us to calculate the reaction efficiency given the normalized kinetic energy distribution function, f(Et), and values for the parameters Ea, the magnitude of the energetic barrier to reaction, and A, the limiting reaction efficiency at large kinetic energies. The term is the residual sum of squares error at the conclusion of the curve-fitting process.

We test the hypotheses represented by the Re equations as follows. First, because a priori values for A and Ea are not available, a gaussian least squares curve-fitting process is used with A and Ea as adjustable parameters. A and Ea are adjusted so that the Re equation gives the best fit (minimum sum of squares error between measured and calculated Re) to the Re data produced by exposing Kapton samples in the four different atom beam kinetic energy distribution functions produced by the HVAB. The success of the curve-fitting operation, both in terms of the reasonableness of the A and Ea values obtained and the magnitude of the sum of squares error at the end of the curve-fitting process, is one test of the validity of the model. A second test involves asking how accurately the Re equations, with A and Ea values determined as described above, can predict Re values for kinetic energy distributions well outside the range of values used in the least squares process. Specifically, can the Re equations, with A and Ea determined with HVAB data, predict Re values obtained from the flowing discharge and EOIM-III experiments?

The predictions of the Re equations are plotted with the measured Re values in Figure 6. Clearly, the Beckerle equation provides a reasonably accurate description of the kinetic energy dependence of the Kapton Re over a 4-order-of-magnitude range in reaction efficiency and a 2-order-of-magnitude range in atom kinetic energy. The agreement between theory and experiment is excellent, given that the EOIM-III and flowing discharge Re values were not included in the original data-fitting process and in light of the significant differences between the three O-atom environments. In contrast, the line-of-centers model provides a good fit to the HVAB data and a reasonably accurate prediction of the on-orbit reaction efficiency, but it underestimates the thermal atom reaction efficiency by 6 orders of magnitude. The line-of-centers model assumes a collision diameter and potential energy surface for the reactive event, which is independent of the collision kinetic energy. Further work in this area will focus on developing improved line-of-centers models, which account for changes in the shape of the potential energy surface of the reaction with changing O-atom kinetic energy.

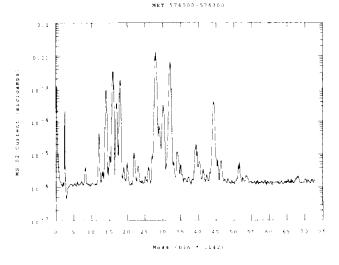
Results and Discussion: O-Atom Fluence Measurements

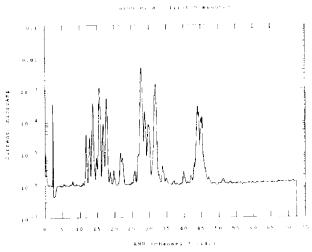
The sensitivity of the EOIM-III mass spectrometer decreased significantly with increasing O-atom fluence during calibrations in the LANL HVAB as well as on

orbit during STS-46. The effect was reversible, although several days were required for recovery of full sensitivity. Different relationships between mass spectrometric sensitivity and O-atom fluence were obtained on orbit and at LANL so that the ground-based calibration function could not be applied directly to on-orbit measurements. As a result, the following procedure was used to calculate the EOIM-III mass spectrometric fluence from mass spectrometer data. The calibration factor relating the mass 16 peak area, which is corrected for contributions from fragmentation of molecular oxygen and water ions, to O-atom flux at low O-atom fluence proved highly repeatable during ground-based calibrations both before and after flight. That factor was multiplied by an empirical sensitivity decay function that was obtained by fitting the corrected mass 16 peak area to an exponential decay curve; i.e., by assuming the average O-atom flux was constant except for diurnal variations. Average O-atom fluxes were then calculated for contiguous 5-minute intervals (whenever the mass spectrometer was on and in O-atom flux measurement mode) and were summed to obtain a fluence estimate for that time period. Compari-son with MSIS-86 calculations during the same time periods shows that mass spectrometer fluences and MSIS-86 fluences were in good agreement. The mass spectro-meter fluence value for the entire mission is 2.3±0.7 x 10²⁰ atoms/cm² compared to an MSIS-86 value of $2.3 + 0.3 \times 10^{20}$ atoms/ cm² and a Kapton dosimeter value of $2.3 \pm 0.07 \times 10^{20}$ atoms/cm².

During EOIM-III, the mass spectrometer produced nearly 46,000 useful spectra—only about half of which were directly related to O-atom fluence measurements. Mass spectra of the induced gaseous environment, which were formed when the ambient atmosphere interacted with the sectors of a sample materials carousel, 7.8 show the gaseous reaction and scattering products. Mass spectra of the incident thermospheric species, the induced environment in a carousel sector coated with C13 Kapton polyimide, and the same carousel sector with a movable cover which blocks direct ram ambient are shown in Figures 7a-c. The mass spectra are displayed on a logarithmic signal intensity scale so that an ion-signal-current dynamic range of about 6 orders of magnitude is shown on each plot. Mass peaks corresponding to isotopes labeled CO and CO, are clearly visible in the carousel spectra. The reaction product spectrum is reduced, but not eliminated, when the cover is moved into position because ambient ram species as well as ambient species, which have thermalized and reacted in the cargo bay environment, can still reach the carousel sector by scattering.

In addition, the mass spectrometer could operate in a mode (ion mode) designed to produce spectra of naturally occurring ionospheric ions. Figures 8a-c show the ambient ionospheric ram flux and the natural induced ionic environment in the C¹³ Kapton carousel sector both within and without the carousel sector cover in place. The ion mode mass spectra in the carousel sector show isotopes labeled CO and CO₂, which are most likely formed by





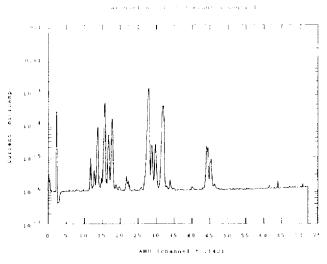


Figure 7. Mass spectra produced by the EOIM-III mass spectrometer at an altitude of 223 km: (a) typical O-atom flux measurement spectrum with the mass spectrometer sampling aperture directed along the velocity vector (ram), (b) mass spectrum with the mass spectrometer sampling aperture directed at the carousel sector lined with C¹³ Kapton with the sector cover off, and (c) same as (b) with the sector cover on.

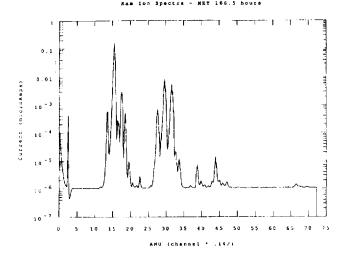
charge exchange between incoming ambient ram ions and gaseous products produced by reaction of the much more abundant neutral O atoms with the carousel sector surfaces. The sector cover was more effective in eliminating ram ambient species from the carousel sector compartment in this case because ions are efficiently neutralized on collision with surfaces.

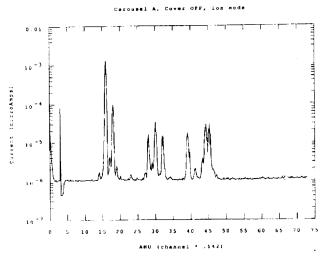
The EOIM-III mass spectrometric database constitutes a rich resource for characterization of the Space Shuttle cargo bay environment. The effects of jet firings, water dumps, venting, outgassing, and rarefied gas dynamics of ambient atmosphere interaction with the cargo bay can all be profitably investigated using the EOIM-III mass spectra database. Verification of contamination and induced environment models using the EOIM-III data is an especially important area for further work.

Results and Discussion: Dual-use Technology

Investigating the materials chemistry of atomic oxygen in the LEO environment has led directly to two new technologies with commercial potential. The first is the anisotropic etching of photoresists or other microelectronic materials using high-velocity O-atom beams that result directly from the strong dependence of reactivity on the kinetic energy of the atomic projectile coupled with very efficient momentum accommodation in nonreactive collisions. (Scattered atoms are much less reactive than primary projectiles.) The second is the reaction-diffusion kinetics of low-velocity (thermal) atomic oxygen in porous solids that can be exploited to engineer a new class of porous solid materials with different pore surface chemistries in different parts of the solid. Application areas for the resulting distributed pore chemistry (DPC) solids include supports for cell and tissue culture in the biotechnology industry, membranes for separation and catalysis, chromatographic separation media, and supported reagents for organic synthesis.

Anisotropic etching of polymer films by high-velocity neutral O atoms was first suggested by electron photomicrographs of polymer films exposed to ram O-atom flux in LEO. 16-18 Small inert particles on the polymer film surface have clearly acted as adventitious etch masks, thus protecting the underlying polymer from attack and resulting in the formation of the tall tower-like features visible in Figure 9. Trilayer-photoresist anisotropic-etching targets were obtained from AT&T Bell Laboratories and were subjected to O-atom beam etching in the HVAB at LANL, and the results of this are shown in Figure 10. Anisotropic etching with high-velocity O-atom beams is capable of submicron resolution. Because the plasma processes that produce device damage are not available in the HVAB, submicron device structures may be fabricated without plasma-induced device damage. Additional work is in progress at LANL, which is funded by the Department of Energy (DOE), work that explores other uses of high-velocity O-atom beams in the fabrication of





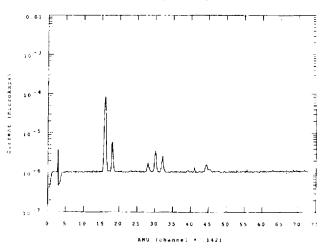


Figure 8. Mass spectra produced by the EOIM-III mass spectrometer at an altitude of 223 km: (a) typical ambient ion flux measurement spectrum with the mass spectrometer sampling aperture directed along the velocity vector (ram), (b) ion mass spectrum with the mass spectrometer sampling aperture directed at the carousel sector lined with C¹³ Kapton with the sector cover off, and (c) same as (b) with the sector cover on.

micorelectronic materials. Low-temperature formation of pure gallium arsenate films on gallium arsenide and the annealing of oxide type high-temperature superconducting thin films²⁸ is the principal objective of the DOE work. Both DOE and JSC atomic oxygen experts serve on the SEMATECH neutral beam working group. SEMATECH is a Government-industry consortium that is chartered to maintain American supremacy in semiconductor fabrication technology.

The application of thermal-energy O atoms to surface chemistry engineering of porous solids was suggested by the peculiar patterns in the loss of waterproofing from porous silica tiles used in the Space Shuttle thermal protection system which could not be explained by reentry heating.²⁹ Waterproofing consists of blocking the hydrophilic silanol (Si-OH) groups on all pore surfaces throughout the tile with hydrophobic trimethyl silyl groups (Si-O-Si(CH₂)₂). Atomic oxygen removes waterproofing by oxidizing the methyl groups to carbon oxides and water, leaving a new layer of Si-OH lining the pores. When a fully waterproofed porous solid is placed in the oxygen plasma asher or flowing discharge environment, oxidation of methyl groups proceeds as a sharply defined reaction-diffusion front that moves into the porous solid from the exterior surfaces.30 As a result, a well-defined boundary exists between the hydrophilic and hydrophobic regions in the porous solid. The observation that thermal O atoms change the surface chemistry of porous solids from the outside in, thus creating well-defined regions with different surface chemistry rather than a uniform alteration of the whole porous solid, is the basis of DPC solids technology.

By controlling total pressure, O-atom concentration, and exposure time, we have produced DPC solids from trimethyl silylated 80/100 mesh size Porasil C as well as



Figure 9. Scanning electron photomicrograph of Kapton polyimide polymer film samples: (a) exposed to ram atomic oxygen during EOIM-III, and (b) control. Anisotropic etching around unreactive film inclusions is visible as tower-like structures.

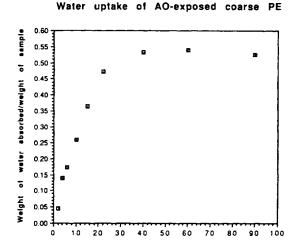


Figure 10. Results of anisotropic etching of a trilayer photoresist etching target provided by AT&T Bell Labs. The HVAB at LANL was the high kinetic energy O-atom source in this case.

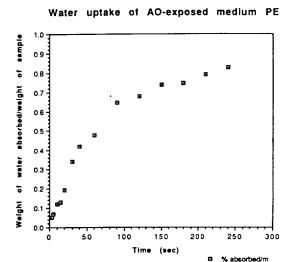
from 10-micron-diameter porous silica beads used in the chromatographic separation of peptides and proteins (300 Angstrom nominal pore size, C₈- or C₁₈-bonded stationary phase). In addition, porous membranes made of a variety of polymeric materials have been prepared with opposing hydrophilic and hydrophobic surfaces. The hydrophilic surfaces produced by O-atom attack on polymers contain functional groups which can be used to covalently attach a wide range of molecules to fine-tune surface properties for specific applications. In addition, Porex porous polyethylene materials have been rendered hydrophilic to controlled depths³⁰ (Figures 11 and 12). In contrast with surface modification, which proceeds rapidly inward from the exposed surface, net mass loss and pore enlargement were observed to occur uniformly throughout the Porex sheets that were up to 3 mm thick.³⁰ The application of DPC materials to biotechnology problems is the subject of continuing work in this area.

Summary and Conclusions

Characterization of the materials chemistry of atomic oxygen in the LEO environment has provided valuable data for the NASA Space Station Program, the Ballistic Missile Defense Program, and other programs using the



(sec)



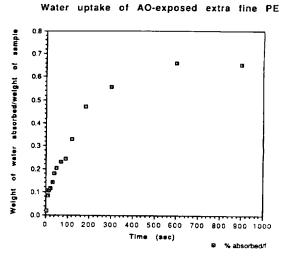


Figure 11. The development of hydrophilic properties in Porex polyethylene following exposure to thermal energy O atoms in the JSC flowing discharge. The weight of water taken up by the treated Porex is plotted against exposure time for: (a) coarse, (b) medium, and (c) fine porosity Porex.

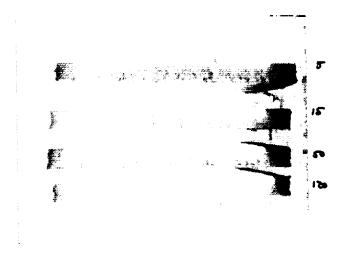


Figure 12. The movement of the hydrophilic region into fine-porosity Porex as a function of time. The hydrophilic region, marked by blue dye, moves from the surface exposed to the O atom that contains gas into the interior of the solid as a function of time. Top to bottom: (a) 5 seconds, (b) 15 seconds, (c) 50 seconds, and (d) 120 seconds.

LEO environment. The role of O-atom kinetic energy on collision with the reacting surface has been demonstrated unequivocally, as has the role of VUV radiation in the reactivity of some materials. An extensive database of polymer reaction efficiency data has been produced and verified and is available to the technical community. Improved understanding of the mechanism and dynamics of O-atom reactions leads directly to more reliable ground-based materials testing protocols and, ultimately, to more reliable spacecraft. Investigating the dynamics and mechanisms of O-atom reactions has also resulted in some significant contributions to the applied chemical and materials sciences as well as several promising spin-off or dual-use technologies in the areas of micorelectronic circuit fabrication technology and materials for applied chemistry and biotechnology.

References

- ¹Jursa, A. S., ed., *Handbook of Geophysics and the Space Environment*, Air Force Geophysics Laboratory, United States Air Force, 1985 (National Technical Information Service).
- ²Hedin, A. E., "A Revised Thermospheric Model Based on Mass Spectrometer and Incoherent Scatter Data: MSIS-83," *J. Geophys. Res.*, Vol. 88, No. 10, pp. 170-188, 1983.
- ³Chamberline, J. W., *Theory of Planetary Atmospheres*, Academic Press, New York, 1978, p. 305.
- ⁴Leger, L. J., Visentine, J. T., and Santos-Mason, B.; "Selected Materials Issues Associated with Space Station Freedom," *SAMPE Quarterly*, Vol. 18, No. 2, pp. 48-54, January 1987.

- ⁵Visentine, J. T., comp., NASA Technical Memorandum 100459, "Atomic Oxygen Effects Measurements for Shuttle Missions STS-8 and STS-41G: Vol. I-III," September 1988.
- 6Visentine, J. T., and Leger, L. J., "Materials Interactions with the Low-Earth Orbit Environment: Accurate Reaction Rate Measurements," AIAA paper AIAA 85-7019, AIAA Shuttle Environments and Operations II Conference, November 1985, p. 168.
- ⁷Koontz, S. L., Leger, L. J., Visentine, J. T., Hunton, D. E., Cross, J. B., and Hakes, C. L., "An Overview of the Oxygen Interactions with Materials III Experiment: Space Shuttle Mission 46; July-August 1992," in Proceedings of the Third LDEF Post-Retrieval Symposium, A. Levine, ed., November 8-12, 1993, Williamsburg VA, a NASA Conference Publication.
- ⁸Koontz, S. L., Rickman, S. L., Leger, L. J., Cross, J. B., Hakes, C. L., and Bui, D. T., "EOIM-III Mission and Induced Environments," in Proceedings of the Third LDEF Post-Retrieval Symposium, A. Levine, ed., November 8-12, 1993, Williamsburg VA, a NASA Conference Publication.
- ⁹Cross, J. B., and Blais, N. C.; "High Energy/Intensity CW Atomic Oxygen Beam Source," *Progress in Aeronautics and Astronautics*, Vol. 116, pp. 143-155, American Institute of Aeronautics and Astronautics, Washington, D.C., 1989.
- ¹⁰Koontz, S. L., Cross, J. B., and Lan, E., "Characterization and Calibration of the EOIM-III Flight Mass Spectrometer in a High Velocity Atom Beam," in *Materials_Degradation in Low-Earth Orbit (LEO)*, Srinivasan, V., Banks, B. A., eds., The Materials, Metals and Minerals Society, 1990.
- ¹¹Koontz, S. L., Albyn, K., and Leger, L. J., "Atomic Oxygen Testing with Thermal Atom Systems: A Critical Evaluation," *J. Spacecraft*, Vol. 28, No. 3, pp. 315-323, May-June 1991.
- ¹²Koontz, S. L., Albyn, K., and Leger, L., "Materials Selection for Long Life in Low Earth Orbit," *Journal of the IES*, March/April 1990, pp. 50-59.
- ¹³Koontz, S. L., and Nordine, P., "The Reaction Efficiency of Thermal Energy Oxygen Atoms with Polymeric Materials," in *Materials Degradation in Low Earth Orbit (LEO)*, Banks, B. A., Srinivasan, V., eds., The Minerals, Metals and Materials Society, Warrendale, PA, 1990, pp. 189-205.
- Huie, R. E., and Herron, J. T., "Reactions of Atomic Oxygen (O³P) with Organic Compounds," *Progress in Reaction Kinetics*, Vol. 8, No. 1, pp. 1-80, 1975.
- ¹⁵Fergeson, E. E., Feshenfeld, F. C., and Schmeltenkoph, A. L., "Flowing Afterglow Measurements," in *Advances in Atomic and Molecular Physics*, Vol. 5, pp. 12-13, Academic Press, New York, 1969.
- ¹⁶Visentine, J. T., Leger, L. J., Kuminecz, J. F., and Spiker, I. K., "STS-8 Atomic Oxygen Effects Experiment," AIAA paper AIAA-85-0415, 23rd Aerospace Sciences Meeting, January 14-17, 1985, Reno, NV.

- ¹⁷Personal communication, Professor John Gregory, Chemistry Department, University of Alabama, Huntsville, Alabama.
- ¹⁸Koontz, S., King, G., Dunnet, A., Kirkendahl, T., Linton, R., and Vaughn, J., "The ISAC Atomic Oxygen Flight Experiment," *J. Spacecraft.*, in press, 1994.
- ¹⁹Steigman, A. E., Brinza, D. E., Anderson, M. S., Minton, T. K., Laue, E. G., and Liang, R. H., "An Investigation of the Degradation of Fluorinated Ethylene Propylene (FEP) Copolymer Thermal Blanketing Materials Aboard LDEF and in the Laboratory," JPL publication 91-10, May 15, 1991, Jet Propulsion Laboratory, Pasadena, CA.
- ²⁰Koontz, S. L., Leger, L. J., Albyn, K. A., and Cross, J., "Ultraviolet Radiation/Atomic Oxygen Synergism in Materials Reactivity," *J. Spacecraft*, Vol. 27, No. 5, pp. 346-348, May-June 1990.
- ²¹Fewell, L., and Fenney, L., *Polymer Comm.*, Vol. 32, No. 13, pp. 393-396, 1991.
- ²²Arnold, G. S., Peplinski, D. R., and Cascarano, F. M., "Translational Energy Dependence of the Reaction of Atomic Oxygen wtih Polyimide Films," *J. Spacecraft*, 24(5), pp. 454-458, 1987.
- ²³Gonzalez Urena, A., "Influence of Translational Energy upon Reactive Scattering Cross Section: Neutral-Neutral Collisions," in Advances in Chemical Physics, Prigogine, I and Rice S. A., eds., Vol. LXVI, John Wiley and Sons, New York, 1987, pp. 231-335.
- ²⁴Stienfeld, J. I., Francisco, J. S., and Hase, W. L., Chemical Kinetics and Dynamics, Chapter 8,

- "Dynamics of Bimolecular Collisions," Prentice Hall, NJ, 1989.
- ²⁵Zeiri, Y., and Lucchese, R. R., "Collision of hyperthermal atoms with an absorbate covered solid surface II: Collision induced desorption," *Surface Science*, 264, pp. 197–206, 1992.
- ²⁶Levine, R. D., and Bernstein, R. B., "Post Threshold Energy Dependence of the Cross Section for Endoegric Processes: Vibrational Excitation and Reactive Scattering," *J. Chem. Phys.*, 56(5), March 1, 1972.
- ²⁷Berkerle, J. D., Johnson, A. D., Yang, Q. Y., and Ceyer, S. T., "Collision Induced Dissociative Chemisorption of CH₄ on Ni: The Mechanism for Chemistry With a Hammer," *J. Chem. Phys.*, 91(9), pp 5756-5777, 1989.
- ²⁸Cross, J. B., Hoffbauer, M. A., and Bermudez, B. M.; "Growth of Oxide Layers on Gallium Arsenide with a High Kinetic Energy Atomic Oxygen Beam," *Appl. Phys Letters*, 57 (21), pp. 2193-2195, November 1990.
- ²⁹Stevens, E. G., "Shuttle Thermal Protection System Atomic Oxygen Exposure Study," Laboratory Test Report 4081-4546, Rockwell International, Space Transportation System Division, February 1985.
- ³⁰Koontz, S. L., and Wu, C., "Surface Chemistry Engineering of Porous Solids," in Proceedings of the Dual-Use Space Technology Transfer Conference, Lyndon B. Johnson Space Center, Houston, TX, February 1-3, 1994.

A Mobile Communications Space Link Between the Space Shuttle Orbiter and the Advanced Communications Tracking Satellite

P. Fink, G. D. Arndt, M. Chavez, R. Robinson, P. Bondyopadhyay, S. Kim, and R. Shaw*
Johnson Space Center/EE
*Shason Microwave Corp.

Abstract

In this paper, a communications link between the Space Shuttle Orbiter and the advanced communications technology satellite is described. The prime objectives are to demonstrate a Ka-band low Earth orbit to geostationary orbit link as well as to provide a test bed for a high definition television video compressor. Both 20 GHz and 30 GHz hardware for the experiment have been breadboarded, including a 144-element, circularly polarized phased array antenna and a 1 W hybrid power amplifier, both at 29.5 GHz.

Introduction

A Ka-band, mobile communications link between the Space Shuttle Orbiter and the advanced communications technology satellite (ACTS) has been proposed as a joint effort of JSC, the Jet Propulsion Laboratory, and Honeywell, Inc. The Orbiter will communicate with JSC by low bit-rate, convolutional encoded data. A compressed, high definition television (HDTV) signal constitutes the source.

The objective for the Orbiter/ACTS flight experiment (OAFE) is several-fold. First, the experiment will demonstrate the utility of ACTS technology in future commer-

cial low Earth orbit to geostationary orbit satellite relays. Second, the experiment will serve as a test bed for an HDTV compression algorithm developed by Honeywell, Inc. Also, monolithic microwave integrated circuit (MMIC) and Ka-band hybrid solid-state technologies used in the transmitter will further advance the application of these technologies in a space environment. Future satellite systems expanding on ACTS technology would benefit greatly by extended use of MMICs, which are often regarded as unproven in a space environment. Other objectives of the experiment are to evaluate a moderate gain antenna using computer steering in the dynamic environment of a maneuvering Orbiter and to evaluate multibeam communication links for direct distribution of experiment data for manned space applications.

The OAFE definition has been modified several times as a result of budgetary constraints. In this paper, we will address the hardware as it was originally conceived and developed for the experiment: as a return link transmitting from the Orbiter to JSC via the ACTS.

OAFE: Return Link

This version of the OAFE was conceived as a return link from the Orbiter to JSC via the ACTS. Low bit-rate

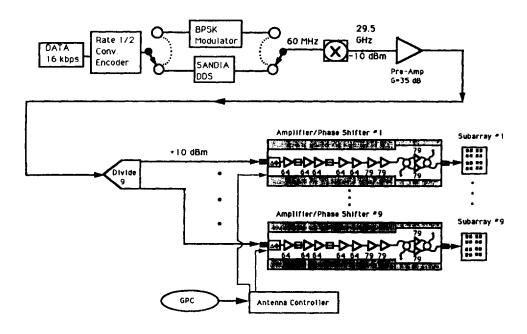


Figure 1. Ka-Band phased array transmitter.

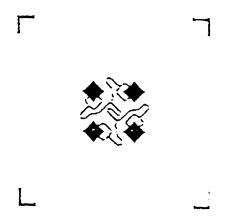


Figure 2. A 4-element cluster.

data are radiated through a phased array antenna to the ACTS 1-m steerable antenna. The ACTS, which is configured in the microwave switch matrix mode, relays the signal to JSC, where the signal is received by a 1.2-m dish antenna.

Link Performance. A 4.32-dB link margin exists for the return link experiment. The phased array consists of nine subarrays, each driven by a 1-W amplifier, to provide a transmit power of approximately 9 dBW. With an array antenna gain of 25 dBi and circuit losses totaling 2 dB, the effective isotropic radiated power is 32 dBWi.

The received signal is demodulated by a long phase-locked loop with 2.5-dB implementation/demodulation loss. A 5.0-dB coding gain is necessary to close the loop with a 4.3-dB margin for a bit rate of 16 kbps. The link margin is determined primarily by the uplink (Orbiter to ACTS) since the gain of the ACTS 1-m antenna is considerably less than that of the isolated spot beams.

Antenna and Doppler Considerations. The ACTS 1-m steerable antenna will have an instantaneous maximum angular rate of 0.20 mrad/s when tracking the Orbiter. The Doppler shift and Doppler rates reach maxima of ± 750 kHz and ± 1 kHz/s, respectively. Because the Doppler profile is well known, the shift is readily precompensated.

The onboard phased array receives pointing data from the Orbiter guidance, navigation, and control to determine the phase shifter bits. The Orbiter payload bay is pointed to the ACTS within 10° , and the array points, open-loop, to $\pm 8^{\circ}$ in steps of 1.3° (element spacing = 0.7.

Flight Hardware

A block diagram of the transmitter for the OAFE Return Link is shown in Figure 1. Audio data at 16 kbps are rate 1/2 convolutionally encoded. The signal is biphase shift keying (BPSK) modulated and upconverted to 29.5 GHz. A more recent design allows for Doppler precompensation by replacing the BPSK modulator with a direct digital synthesizer. Although the receiver is capa-

ble of tracking through the ± 750 kHz of Doppler shift, precompensation will allow for a faster implementation.

The 29.5 GHz signal is preamplified before a 9-way power divider routes the signal to nine subarrays. Each subarray is preceded by a 1 W phase shift/amplifier module. The phase shifter is a 4-bit MMIC developed by Honeywell. Input power to each module is +12 dBm. A 10-dB insertion loss associated with the phase shifter and 30 dB of amplifier gain result in 1 W being delivered to each subarray.

Ka-Band Antenna Array. The transmitting antenna at 29.5 GHz consists of a 144-element circularly polarized microstrip phased array arranged as a 3x3 array of 16-element subarrays. Each subarray consists of a 2x2 array of a 4-element cluster designed as a single-feed, circularly polarized microstrip compound radiating element. One version of the 4-element cluster is shown in Figure 2. A 4-bit phase shifter in each of the nine subarrays will provide electronic scanning in a conical space of approximately 10°.

This design of the compound radiating element employs dual-feed, square microstrip patch elements in conjunction with sequential feeding and rotation technique to enhance the axial ratio bandwidth. Impedance and axial ratio bandwidths of over 1 GHz at the center frequency of 29.5 GHz are very easily achieved. The typical radiation pattern of the 16-element subarray (Figure 3a), which consists of a 2x2 array of the 4-element cluster, is shown in Figure 3b.

The wide bandwidth for this version comes at the expense of a small loss in the subarray gain. For this particular experiment, the bandwidth required is less than 200 MHz. This will permit the use of a more efficient version where single-feed, structurally perturbed square microstrips are used to design the 4-element cluster.

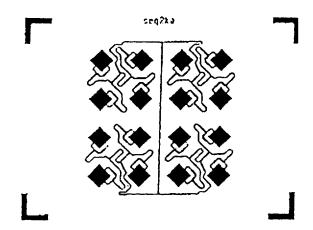


Figure 3a. The 16-element subarray.

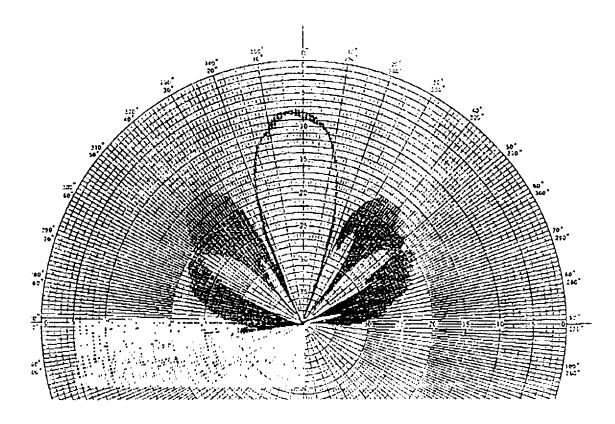


Figure 3b. Radiation pattern of the 16-element subarray.

Phase Shift/Power Amplifier Module (PSPA)

Electrical. A prototype GaAs FET hybrid power amplifier was developed for the experiment. Characteristics of the amplifier are as follows:

Gain	30dB
Bandwidth	760 MHz
1 dB compression	25.5 dBm
Saturated Power	28.5 dBm
Efficiency	4%

Small signal and 1.5-dB compression plots of gain are shown in Figure 4. The prototype uses seven series transistor stages and one balanced output stage. In addition, one stage at the input is designated for a 4-bit MMIC phase shifter. A newer revision, which is currently being developed, uses three stages of MMIC amplifiers to achieve a goal of 30 dBm from 29.5 GHz to 38 GHz.

Mechanical. The final revision of the PSPA module is shown in Figure 5. The amplifier unit has dimensions of 7.0 in. x 1.1 in. x 1.1 in. (not including the heat sink). For ground use, flanges on both the input and output sides provide a convenient method of locking the module in the heat sink. The input flange would be absent on the flight unit to allow for a front-loading array structure.

Both ends of the module have a K-connector interface that accepts either a two-hole flange SMA female or flush mount female-female interconnect. The SMA female connector is used on the output for lab testing, while in operation a 1.1 in. x 1.1 in. x 0.25 in. antenna

carrier plate mounts flush onto the PSPA flange. In addition to the K-connector interface, a miniature D-connector resides on the input side. The D-connector accepts regulated power at +12V and -5V as well as four transistor-transistor logic (TTL) phase shift bits.

Voltage regulation for the PSPA resides in a recess in the heat sink. The heat sink also mounts a 1.2-W miniature fan over the output side of the PSPA. The fan draws 5.30 ft³ of air per minute along the sides of the PSPA module and through holes between the bottom heat sink fins. An additional air channel runs aft to the regulator compartment.

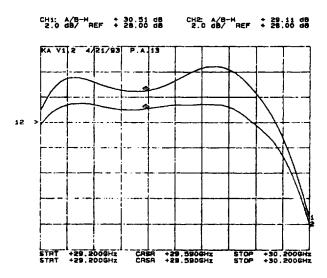


Figure 4. Small signal and 1.5-dB compression gain.

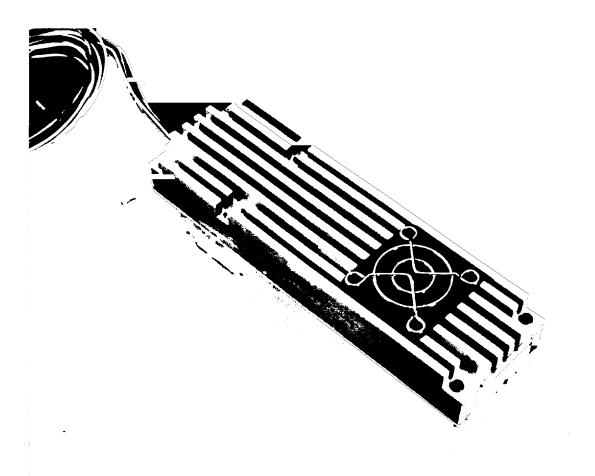


Figure 5. Final revision of PSPA module.

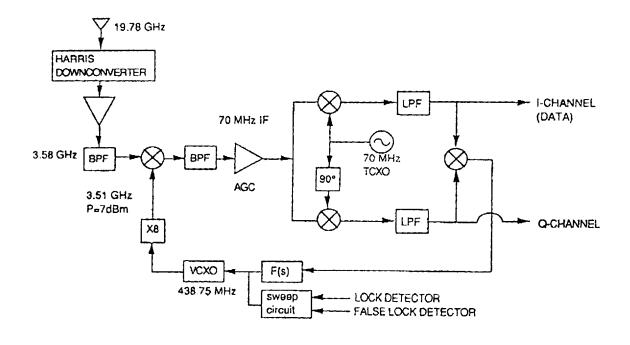


Figure 6. The 19.78-GHz superheterodyne receiver.

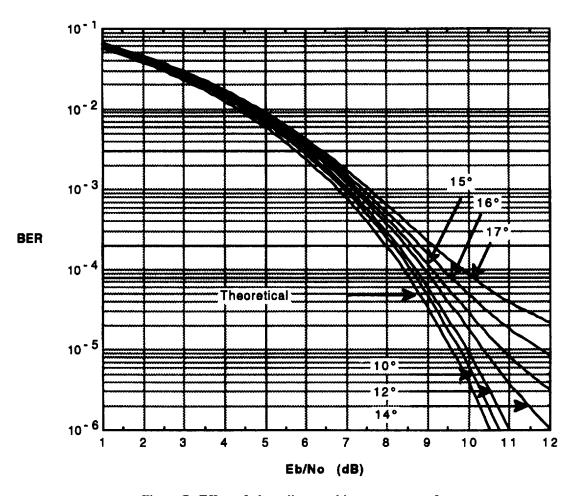


Figure 7. Effect of phase jitter on bit error rate performance.

Ground Station

A 19.78 GHz superheterodyne receiver (Figure 6) is being developed for the JSC ground station. An existing MMIC 20 GHz receiver developed by Harris Corporation will be used to downconvert the signal to 3.58 GHz. A long phase-locked loop will track the Doppler shift to maintain a constant interface of 70 MHz. The quadrature phase detector then demodulates and produces the voltage controlled crystal oscillator (VCXO) control voltage. The demodulated data are then input into an application specific integrated circuit (ASIC) bit synchronizer to establish a clock and recover the data. Finally, the data are decoded. To improve acquisition time, the VCXO is swept when the loop is not phase-locked. The acquisition time, without Doppler compensation, is approximately 3.5 sec.

With the current BPSK system, performance is degraded by the phase jitter produced by the phase noise of the ACTS local oscillators. Figure 7 shows the effect of phase jitter on bit error rate performance. The minimum calculated root mean square phase jitter for the experiment is 11.4°, which results in a degradation of 3 dB. A study is currently being performed to determine if differential phase shift keying (DPSK) will improve system performance. DPSK has a greater immunity to phase jitter, but it is not as efficient as BPSK.²

References

¹Holmes, J. K., <u>Coherent Spread Spectrum Systems</u>, Krieger Publishing Co., 1990.

²Spilker, J. J., <u>Digital Communications by Satellite</u>, Prentice-Hall, 1977.

Orbital Debris Radar Design Study

Brian Bourgeois Senior Resident Associate of the National Research Council Johnson Space Center/EE

Abstract

Accumulation of space debris in low Earth orbit is an ever-increasing threat to the Space Station. An effective system must be developed to provide adequate protection to the Space Station, while avoiding unnecessary interruptions to Station operations. The purpose of this study is to define an on-orbit radar system capable of detecting small (1-10 cm) particles traveling through an electronic fence in front of and behind the Station.

Introduction

Current orbital debris tracking methods, based on ground tracking provided by United States Space Command, are limited to debris particles greater than 10 cm in diameter and may not provide sufficient accuracies to prevent unnecessary Station maneuvers (false alarms). Shielding methods will protect for small particles (less than 1 cm). No method currently exists for dealing with debris between 1 and 10 cm in diameter. Shielding is not practical for these debris particles, leaving tracking and avoidance as the only viable option.

Problem Statement

The purpose of this study is to define an on-orbit radar system which will provide timely updates to the state vector of potentially hazardous debris as determined by ground radar. The debris warning system envisioned here is illustrated in Figure 1, with the ground radar stations tracking and cataloging all debris particles greater than 1 cm in diameter. The Space Station radar system must be capable of detecting small (1-10 cm) particles traveling through an electronic fence in front of and behind the Station, as shown in Figure 2. The updates provided by the system are necessary in order to keep the annual maneuver rate below 10 so as not to interrupt microgravity experiments onboard the Station.

An initial study of radar system requirements and design parameters has been completed. The radar must be able to detect particles as small as 1 cm out to a distance of 300 km moving at high relative velocities (up to 14 km/sec) with high Doppler and Doppler rates of change. The radar system will have reconfigurable features such as antenna size, transmitter power level, pulse length, and pulse repetition frequency so as to optimize performance according to a priori information from the ground. The system will require significant signal processing on the ground to determine time of plane-crossing, elevation, range, and possibly Doppler.

Approach

The main focus in this initial study into an onboard radar system is a tradeoff of antenna size and transmitter

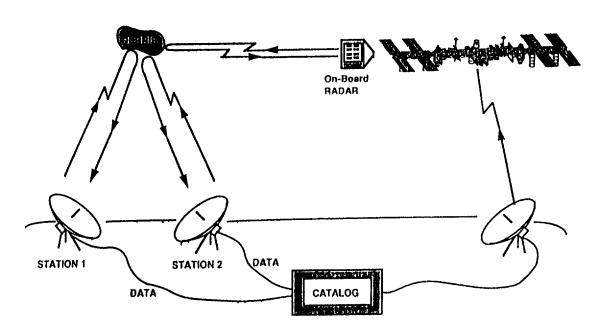


Figure 1. Ground/space radar detection system for orbital debris.

C-3.

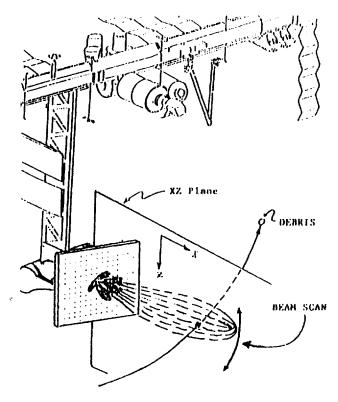


Figure 2. Radar beam scan for debris defection.

power versus signal enhancement from ground processing. For the antenna system to be compatible with expected size and prime power constraints, ground processing of the return signals digitally sampled at the output of the radar receiver must provide improvements on the order of 30 dB. Conventional analog processing of the radar data will not be able to meet the expected requirements and constraints.

In support of the radar design study, implementation of a Monte Carlo computer simulation is under way to determine accuracy requirements of the radar.² Since the Space Station requires a minimum advance notice of one to two revolutions (1.5 to 3 hours) prior to predicted conjunction in order to execute a maneuver, it is crucial to be able to predict debris trajectories for that period of time. Accuracy of trajectory prediction is directly related to maneuver rate and acceptable risk of collision. This is a difficult problem primarily due to the effect of atmospheric drag on the small particles.

The simulation employs high-fidelity gravity and atmospheric density models to propagate trajectories of particles of random size, shape, composition, and tumbling rate in an environment of random atmospheric density fluctuations, assuming an ideal position and velocity sensor. The result of the simulation is a statistical analysis of position difference between two types of debris geometries. The first is that of an aluminum sphere of fixed size in an atmosphere whose density is determined using forecast geomagnetic and solar radiation indices. This object represents a best estimate of orbit propagation. The second type of debris geometry is a tumbling flat

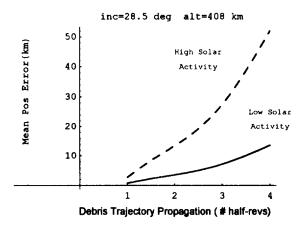


Figure 3. Mean position error of tumbling flat plate vs. aluminum sphere.

plate with random diameter and density, propagating through an atmosphere whose density is calculated using random deviations in the forecast geomagnetic and solar radiation indices (figure 3). This object represents actual orbit propagation.

Results

Initial calculations indicate "ballpark" parameters for an onboard system could include an antenna size of 16 m², RF losses of 5 dB, a SNR of 13 dB, a noise figure of 2 dB, and a transmitter power of 20 to 200 kW, depending upon the amount of ground signal processing enhancement that can be achieved.

In addition, tradeoff studies into possible operating frequency ranges to enhance detection capabilities indicate Ku-band may be a good choice. A sample curve showing maximum radar operating range (under a specific set of groundrules) as a function of frequency is shown in figure 4. The curve in the region of interest of 300 km or less will vary slightly depending on the assumed groundrules.

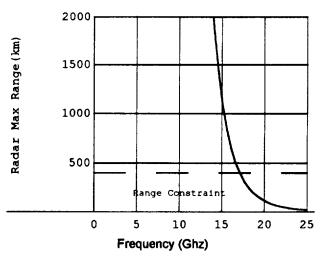


Figure 4. Carrier frequency vs. maximum range.

References

- ¹J. R. Carl, G.D. Arndt, B. Bourgeois, I. Paz, "Spaceborne radar detection of orbital debris," *Proceedings of IEEE Globe Comm 1993*, Houston, TX, December, 1993.
- ²B. Bourgeois and K. Dekome, "Orbital debris trajectory modeling," *Space Instrumentation and Dual-Use Technologies*, SPIE Proc. Vol 2214, April, 1994.

Rendezvous and Prox Ops Program New Capability Development

Scott Tamblyn
Johnson Space Center/EG

Abstract

Rendezvous and Prox Ops Program (RPOP) software underwent its first full year of development and flight certification in 1993. This work is being done by the Guidance and Prox Ops Section of the Engineering Directorate Navigation, Control and Aeronautics Division. The evolving development of RPOP is based on existing, certified software capabilities. The primary purpose of RPOP is to provide the necessary information to Shuttle pilots to assist them in meeting the operational flight constraints during approach to and departure from the Space Station. RPOP is a laptop-computer piloting aid which processes sensor measurements from various sensors and Orbiter general purpose computer data to compute and display guidance and navigation information to the pilot. RPOP is designed to fly on the Orbiters payload and general support computer.

Introduction

The purpose of this paper to present an overview of the RPOP project for FY93. In this paper we present the motivation behind the RPOP project as well as the approach taken to accomplish the project objectives. In describing the work plan, the major aspects of the development of RPOP are detailed with respect to their related milestones. The achievements of the RPOP project during FY93 will be summarized and the paper will conclude with a discussion of the next step in the project evolution plan.

Problem Description

During standard rendezvous and proximity operations, Shuttle pilots control the vehicle based on out-thewindow viewing through the crewman optical alignment sight, reading digital data displays in the cabin (range, range rate, etc.), and pilot training, where they learn and practice strict operational procedures. The only trajectory information they have is inferred through manual interpretation of visual and digital data. These piloting procedures are quite adequate for retrieving satellites and other payload bay-sized vehicles. Rendezvous with a significantly large space structure such as Space Station, however, will require a higher degree of piloting performance during final approach. The design of Space Station is such that operational constraints must be imposed on the Orbiter trajectory to satisfy structural loading constraints. These trajectory constraints include a conic flight corridor as well as restrictions on range rate and jet firing frequencies. The increase in operational flight constraints

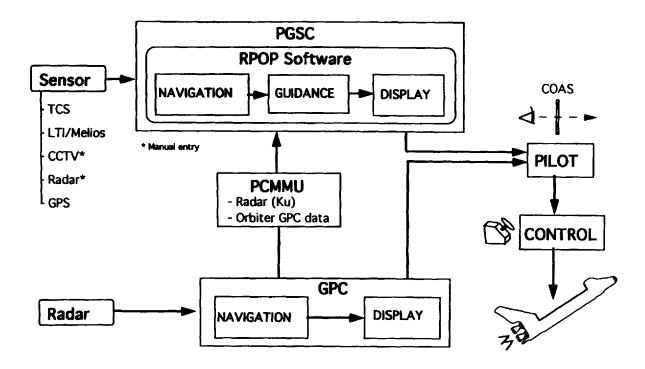


Figure 1. RPOP concept.

required for Space Station approach has resulted in the need to provide the Shuttle pilot with more trajectory information than is currently present in the Shuttle systems.

The Rendezvous and Prox Ops Program (RPOP) is a low-cost, efficient software solution for providing a pilot with the trajectory information needed to assist in meeting operational flight constraints. The concept behind RPOP is to run navigation, guidance, and display software on the Orbiter payload and general support computer (PGSC) to process raw sensor data into meaningful, current information. The PGSC is a laptop DOS-based personal computer (PC). Sensors may be connected to the PGSC via the computer serial ports. It is the use of the PGSC, rather than of the Orbiter general purpose computers (GPCs), which makes this software solution inexpensive and expeditious. Figure 1 shows a diagram of the RPOP concept.

Approach

The approach to implementing the RPOP concept was to begin with existing PGSC software and to develop from there based on an evolutionary work plan. At the time, the existing, certified prox ops software was a program called Payload Bay (PLBAY), which had been developed within the Astronaut Office. The RPOP evolutionary plan was formulated based on functional software requirements gathered and documented at the end of 1992.

The evolution of PLBAY into RPOP encompassed two major milestones during FY93. The first milestone was the initial modification of PLBAY to support development test objectives (DTOs) 700-5 and 700-7 on STS-51. This effort culminated with RPOP version 1.2A. The second milestone consisted of a series of significant upgrades to further support DTOs 700-5 and 700-7 on STS-60 as well as to certify RPOP for operational use as a situational awareness tool. This effort culminated with RPOP version 2.0, which will become operational beginning with STS-60.

RPOP Version 1.2A

The development of RPOP version 1.2A began with the PLBAY program. PLBAY is a real-time prox ops program which receives raw data inputs and computes and displays the in-plane motion of the Orbiter as it relates to the local vertical local horizontal (LVLH) reference frame—a target-centered frame. The display shows the Orbiter trajectory history as well as the current position that was propagated from the last data input. The LVLH pitch attitude of the Orbiter is also graphically represented. Additionally, the Orbiter predicted coasting trajectory is continuously displayed in the form of nine predictor bugs at 1-minute intervals. Another significant feature of PLBAY is the user's ability to enter fictitious translational hand controller (THC) inputs into the

program to see how the predicted coasting trajectory would be affected. This capability, which is dubbed the "what if" capability, allows the user to get a feel for how certain THC inputs would affect the Orbiter motion if the inputs were actually made. There are many other features of the program, but these are too numerous to discuss in the scope of this paper. This description does serve as a basic overview, however.

Sources of raw data inputs into PLBAY may be either manual or automatic. Manually entered data may include Ku-band radar measurements and closed-circuit television (CCTV) camera angles. This information is available digitally on various displays in the Orbiter cockpit. Handheld laser (HL) data, which consist of range and range rate, may be automatically received by PLBAY via serial port connections of the HL sensor to the PGSC. The HL of Laser Technologies Incorporated (LTI) is an existing, operationally certified tool.

The objective of the first RPOP milestone was to modify PLBAY to support two new sources of automatic data input. The two new technologies, which flew on STS-51 as DTOs, were the trajectory control sensor (TCS), DTO 700-5, and the PCDecom/Pulse Code Master Memory Unit (PCMMU) capability, DTO 700-7. The TCS is a payload bay-mounted laser sensor which measures range, range rate, azimuth, elevation, angle rates, and relative attitude. PCDecom is commercial off-the-shelf software that can extract specified parameters of interest from the Orbiter PCMMU, which contains the entire downlist of the GPC data. PCDecom must run on its own, dedicated PGSC—provided that computer has an expansion chassis.

The RPOP team modified PLBAY to accept and incorporate both TCS and PCMMU data, thereby making the prox ops tool "hands off." The presence of TCS and PCMMU data at a high frequency eliminates the previous need for the crew member to manually enter data from the rendezvous radar while increasing the accuracy of the trajectory information. TCS data are received via a serial port connection between the sensor and the PGSC. PCMMU data are accessed via an intermediate, serially connected PGSC which is running PCDecom. The PCMMU data that RPOP receives contain GPC-filtered Orbiter and target inertial state vectors, Orbiter inertial attitude, and raw radar data. RPOP uses the radar data to compute the relative state and uses both the Orbiter inertial state vector and the attitude data to compute LVLH pitch attitude. This modified version of PLBAY became the first version of RPOP (version 1.2A) and flew for the first time on STS-51.

RPOP Version 2.0

The development of RPOP version 2.0 began with RPOP version 1.2A. The objective of this second RPOP milestone was to continue the evolution of RPOP by using the TCS and PCMMU data sources and to certify

RPOP for operational use beginning with STS-60. For STS-60, the rendezvous with the Wake Shield Facility (WSF), both TCS and PCDecom/PCMMU were slated to fly once again as DTOs (DTOs 700-5 and 700-7, respectively). However, TCS was demanifested just as the development of RPOP version 2.0 was nearing completion. The RPOP team modified RPOP version 1.2A to include the following new capabilities:

- Introduction of two new user modes to enhance accuracy and display of relative states and Orbiter attitude
- Ability to use GPC navigation states (via PCMMU) to compute and plot relative motion
- Ability to time-synchronize PCMMU state vectors with the quaternion to eliminate time biases
- Addition of a Kalman filter for TCS laser measurements for relative state updates (removed after demanifestation of TCS from STS-60)
- Ability to compute and display (graphically and digitally) the target vehicle LVLH attitude using TCS and PCMMU data
- Improvement of user interface (function key design and layout)
- Addition of out-of-plane propagation for digital display
- Ability to use HL data in combination with PCMMU data for relative state updates
- Ability to manually scale trajectory display (tick marks added to LVLH axes)

In addition to these primary upgrades, a variety of peripheral upgrades were made, including enhancements to the digital data displays, online help, user friendliness, program robustness, and data reasonableness checking. Figure 2 contains a picture of the trajectory display for RPOP version 2.0.

Results

Major milestones in the RPOP evolutionary work plan were achieved in FY93 in support of STS-51, the rendezvous with the Space Pallet Satellite (SPAS), and STS-60, the rendezvous with WSF.

STS-51

RPOP version 1.2A was successfully developed (from PLBAY), tested, and validated for use as a DTO on STS-51. The validation report for RPOP version 1.2A (Refs. 1 and 2), which details all the modifications and upgrades to PLBAY as well as the functional, integration, and regression tests performed, was delivered to the Mission Operations Directorate (MOD) for approval of the software. RPOP version 1.2A was successfully tested in the flight-like, integrated environment of the Shuttle mission simulator and was used extensively during rendezvous crew training. The software was loaded onto the flight PGSC and short-duration tests were performed. RPOP version 1.2A successfully flew on STS-51 during SPAS deploy and rendezvous using the PCMMU data. RPOP was evaluated as a situational awareness aid by the crew during rendezvous and proximity operations and met with favorable review. Postflight data analyses showed that RPOP performed nominally; RPOP results agreed well with the actual flight profile data.

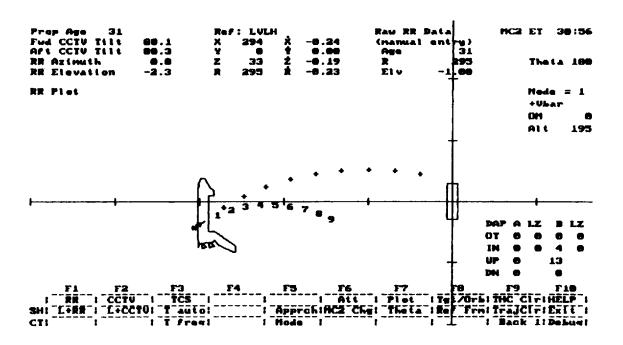


Figure 2. RPOP trajectory display.

STS-60

RPOP version 2.0 was successfully developed (from RPOP version 1.2A), tested, and validated for use as a certified operational PGSC software, beginning with STS-60. The validation report for RPOP version 2.0 (Refs. 3 and 4), which details all of the modifications and upgrades to RPOP version 1.2A as well as the validation tests performed, was delivered to the MOD for approval of the software. RPOP version 2.0 was tested and validated to meet the Level II validation criteria for certified PGSC software. RPOP has been certified for operational use as a situational awareness tool and will replace PLBAY on the PGSC. Additionally, RPOP was tested in the flight-like, integrated environment of the SMS and was used extensively during rendezvous crew training. The software was loaded onto the flight PGSCs, and short-duration tests were performed. By the close of 1993, RPOP version 2.0 was flight ready and awaiting launch in early 1994.

Conclusions

The RPOP project has had a productive year of design, development, testing, and validation, including its maiden flight. The RPOP team will continue sustained engineering of RPOP as operational PGSC software. In addition, the RPOP team is continuing development of RPOP according to the evolutionary work plan, which is laid out through the launch of Space Station. Currently, tasks include the development of a Windows version of RPOP, the development of a Kalman filter for relative attitude, and the integration and evaluation of approach

guidance algorithms. RPOP will continue to evolve toward its overall objective of aiding Space Station approach as it continues to support upcoming rendezvous flights.

Acknowledgments

The RPOP team is an in-house effort consisting of civil servants and a variety of support contractors, including Lockheed Engineering and Sciences Company (LESC), McDonnell Douglas Aerospace (MDA), and Charles Stark Draper Labs (CSDL). The following individuals comprise the RPOP team and have been elemental to the success of the project. They are, in alphabetical order: Jack Brazzel, MDA; Fred Clark, LESC; Heather Hinkel, JSC/EG42; Tom Manning, MDA; Scott Merkle, JSC/EG43; Leroy McHenry, CSDL; and Pete Spehar, LESC.

References

- ¹Tamblyn, W. S., and Brazzel, J. P., "Rendezvous and Prox Ops Program Version 1.0 (including Version 1.1 Update) Validation Report," May 1993.
- ²Tamblyn, W. S., and Brazzel, J. P., "Rendezvous and Prox Ops Program Version 1.2A Update to RPOP v1.0 Validation Report," August 1993.
- ³Tamblyn, W. S., and Brazzel, J. P., "Rendezvous and Prox Ops Program Version 2.0 Validation Report," December 1993.
- ⁴Tamblyn, W. S., and Brazzel, J. P., "Supplement to Rendezvous and Prox Ops Program Version 2.0 Validation Report," December 1993.

Standards-Based Autocode Generation for Flight Computers

Robert L. Shuler, Jr. Johnson Space Center/EK

Abstract

In this paper, we describe one in a series of investigations undertaken to identify and resolve issues in using standards-based flight system components and development tools in an integrated fashion to produce new spaceflight avionics systems extremely rapidly and at low cost but that are of comparable reliability to previous systems. By building on prior work integrating a commercial autocode generator into real-time ground systems, but using a Shuttle-derived digital autopilot application, the generated code is integrated into a functional equivalent flight target computer.

Issues are identified in interfacing to the customized Ada run-time system handling the peer-to-peer voting scheme of the redundant set, as well as by automatically identifying and accessing the inputs, outputs, and internal state variables of the autocoded software. Each case of departure from the use of standard interfaces, and each incompleteness in the automatically translated code specification, is shown to reduce productivity and reliability benefits disproportionately. Future work to define an application programming interface for redundancy management is suggested, along with continued refinement of data management interfaces.

Introduction

Historically, manned spacecraft computing systems have been characterized by a high degree of redundancy both in the implemented hardware and software as well as in the process of design and test. Often highly custom systems have been developed, and even the tools for programming those systems have been custom developed. Although hardware performance requirements have been modest, programming systems have needed to be more nearly state of the art. For a more detailed summary and index into the literature see Reference 1.

Although there is no contemplation of near-term changes to the core flight control system of the U.S. Shuttle Orbiter, the need to deploy similarly reliable systems arises from three areas: (1) experiments which possibly incorporate hazardous functions and their associated control systems; (2) ancillary vehicles such as the assured crew return vehicle, which although possibly based on the spacecraft of other countries will require avionics upgrades to provide control in new mission envelopes; and (3) unmanned spacecraft, which by virtue of the lack of possibility of intervention or operation in critical maneuvering envelopes, derive reliability requirements similar to manned spacecraft.

Problem Description

We perceive the relative need for high reliability and sophisticated software engineering with modest performance to remain true for the systems of interest described above. In the future, emphasis will be on deploying systems more rapidly at lower cost and continuing to meet the reliability objective.

Work on Space Station has already shown that custom software engineering systems can no longer keep pace with the mature, mass-market-driven systems provided by industry,² and that highly customized versions of commercial products offer little cost or schedule benefit over customized versions of military products, which are the more usual source of spacecraft computers. One continuing obstacle to the rapid development of Space Station was the lack of sufficiently equivalent target computer hardware and software platforms for early prototyping, development, and integration, as well as the cost of providing these items to the many participants.

Ground simulation and control systems are using much more sophisticated programming systems than the procedure-oriented languages (POLs) such as Ada and C. Economies as great as five times in both cost and schedule of deploying production systems have been reported by both Honeywell and McDonnell Douglas. This is consistent with JSC experience. Unique issues arise in applying this technology to flight systems with their associated redundancy management and specialized space-qualified computers.

Although several different advanced programming systems are available, the type investigated here and the basis of the above observations is an autocode generator. This allows a system to be described and simulated in block diagram form roughly at a level corresponding to detailed requirements. Real-time code is then generated in C or Ada after correct function is verified in the analytical or simulation mode. This approach contrasts with Shuttle-era technology of redevelopment of flight code based on the requirements specifications and consequent low-level retesting. Thus, our approach presents a significant opportunity for schedule and cost compression. Some issues exist with the performance of this class of tools. Often, for their generality they depend on scheduling and determinacy of data exchange techniques which result in undesirable data latency.3 This has usually been avoided in highly custom hand-coded flight software, but this also results in much analysis and testing and in some brittleness (a tendency to break when changed).

Another approach for the class of Earth-to-orbit or return-from-orbit vehicles is reuse of the Shuttle software

or algorithms. The existing software is coded in Houston Aerospace Language, which, though notable as a pioneering effort in software engineering, makes for current difficulty in reclaiming the software for another target due to the problems associated with custom software development environments cited above. Recoding the software from requirements is possible, but any such recoding would not take advantage of the advanced programming technology available to unify the analytical and production software steps just described.

Approach

The observations on Space Station work above lead to consideration of commercial software tools and to the use of commercial standards, whether formally or de facto standardized, for the data system platform. Actual use of commercial products is usually not feasible for radiation and other environmental or reliability reasons, but the use of the standards which these products employ makes possible the use of the commercial products that are sufficiently equivalent to flight hardware to be useful immediately and at low cost for early prototyping, development, and integration.

Often, test and development equipment compatible with such standards already exist within subcontractor labs and can be reused from other projects rather than provided anew. Use of such standards, especially the requirement that they be in prior widespread use when practical, narrows and eliminates system engineering choices early in a program so as to speed agreement on interfaces and to eliminate competition to supply custom or proprietary interfaces.

Hardware Components

A key to the success of a standards-based strategy is the availability of sufficient performance margin to eliminate the actual need for highly tailored systems. The emerging availability of 32-bit space-capable processors with performance of several million instructions per second (mips) or higher at modest power consumption has, in the opinion of many avionics suppliers, met this precondition. Although some 16-bit processors were marginally fast enough, their addressing limitations required custom tailoring of software. The processor selected for this investigation was the MIPS R3000, for which chip-sets exist with good radiation properties, and which is comparable to space processors being developed by two major suppliers.

Partly based on its almost universal usage and familiarity, and partly on the availability of reusable space-qualified components from JSC projects, the Versa-Module Eurocard (VME) backplane standard was selected for both electrical and form-factor specifications. VME is proven in space, worked well on this project from the standpoint of readily available components, and meets any foreseeable spaceflight performance requirements.

Because JSC prefers box-level redundancy, the backplane is not usually a factor in redundancy management; however, techniques and often products exist for almost any conceivable configurability or performance requirement, including live-insertion and power management.⁴ The availability of space-qualified components for any non-vendor-specific backplane is an issue needing attention.

The 1553B was selected as a commonly available avionics bus. We recognize that this is an old standard, but it is suitable for small- to medium-sized applications, and will need to be revisited for large applications. For example, Shuttle uses a precursor version of the 1553 and is burdened with an excessively complex bus structure due to performance limitations.

Software Components

Ultimately, POSIX is the selection of choice for the run-time layer. Its real-time capabilities were not standardized at the beginning of this investigation, and good real-time POSIX operating systems were too expensive for our budget and required too much memory for lowend applications. This led to the selection of the partially compliant Wind River VxWorks product, which is a de facto standard within the industry.

Although we actually acquired a dual-string configuration using this software, only an initial single-string hosting and an evaluation of the application have been conducted on it so far. We were able to acquire the use of a 4-string Boeing Integrated Fault Tolerant Avionics System (IFTAS) from a related project which conformed to our requirements in every way except that a somewhat customized bare-Ada run-time was used instead of VxWorks or VADSworks. We decided to conduct our investigation on this system before implementing any redundancy mechanism on our somewhat limited 2-string system. For a general description of the operation of such systems, including Byzantine resilience, and of the Draper Fault-Tolerant Parallel Processor, which we also intend to evaluate, see Reference 5.

Although Ada was selected for this project, the question of Ada or C remains open, with Ada likely to continue for projects requiring more sophistication and C for non-software-critical projects with a low budget. Although we consider Ada far superior, the tools are more expensive and are often not available for a desired target platform. As noted above, custom tool development not supported by the marketplace is no longer considered feasible. When using a POL as a platform or host layer for higher level tools, it is also a consideration that higher level tools are not always available for Ada or are available only in more restricted forms.

Prior work⁶ had investigated conversion of Shuttle software to another POL via hand-coding techniques relative to recoding the software using high-level specification tools as described above. The Shuttle software is interesting not only for its reuse potential, but also as a well-understood performance benchmark thought to cover

the performance and reliability requirements that any of the avionics systems under consideration would face. At first we were planning to use a recoded C or Ada version for benchmark purposes, but we found that the autocoded digital autopilot (DAP) application was available which held out the promise of reuse and of evaluating more closely the performance of these new techniques; therefore, we selected this version. This autocoded version used the same MATRIXx family of tools provided by Integrated Systems, Inc., (ISI) that was the subject of an earlier investigation in which some of us participated. This effort had integrated the tool with a ground simulation system oriented around Ada and with various data management and scheduling techniques of interest.7 In particular, elegant resolutions of problems that were identified in the effort to merge two systems which expected to independently control rate-monotonic scheduling of tasks had been incorporated into this tool by the vendor. This was accomplished by relying on standard Ada tasking rather than on custom scheduling.

The application, which represents about 40% of the ascent processing load of the Shuttle, was the DAP already mentioned. The AP101B computers on the Shuttle deliver about 1.2 mips. The DAP is designed as a multirate set of tasks, with the highest rate being 25 Hz (40 ms cycle time). There is a latency requirement from data input at the flight computer to command output of 18 ms. This constraint must be met by the scheduler in addition to the overall rate. The DAP takes inputs from other software or from the crew which represent desired attitudes and headings, and outputs commands to the three main and the two booster engine gimbals. Availability in block-diagram/autocode form made it easy to also pro-

duce a single-rate version, which was one technique of dealing with the latency issue.

Lab Configuration

For our purpose, a simulation run was made in which the inputs to the DAP were recorded. These were prestored to drive the DAP in our target environment in an open-loop mode. The nature of how the DAP is thus separated from the rest of the flight software is explained further in Figure 1. Initially these data were prestored in excess memory in the flight target, along with output data for comparison. Later, the inputs and outputs were provided over 1553 buses to and from an assortment of other computers in which they were simply stored as before, so the simulation remained open loop. As of this writing only 3 of the external 1553 interfaces have been made to function, which is no problem to the Boeing IFTAS as it begins by failing out the bad channel and running in the 3-string mode.

The addition of a development system, which doubled as a somewhat inadequate real-time display, completes the description of the lab components depicted in Figure 2. VI Corp.'s DVdraw was used for the real-time display because it was available and easy to use. Future plans include a real-time link to Silicon Graphics machines for improved display. Either of these qualifies as a standard display mechanism, one being more sophisticated than the other. By contrast, ISI-supplied display capability does not qualify as a standard because it is not usable with anything other than their target AC100, which in turn has little relevance as a functional equivalent of a flight target processor.

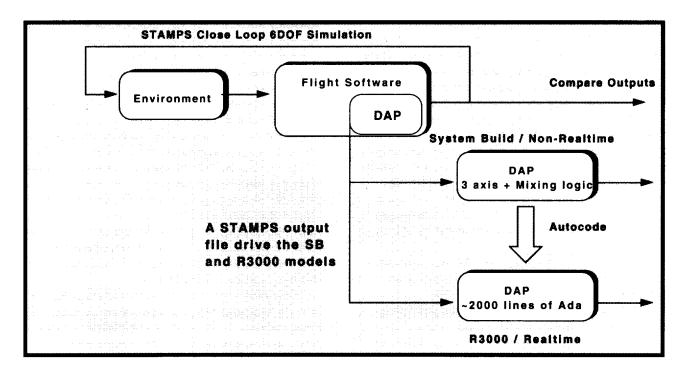


Figure 1. Case implementation of the Shuttle ascent flight software

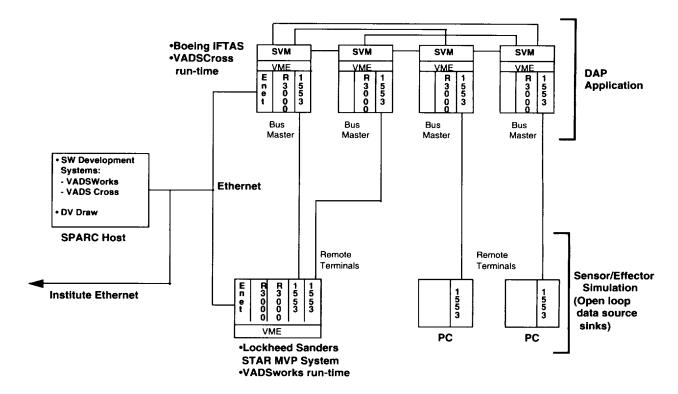


Figure 2. Lab configuration.

Redundancy Management

The architecture of the Boeing IFTAS may for our purposes be considered as four commercial off-the-shelf R3000/VME processors with intelligent communication channels which handle the interprocessor voting (using Boeing proprietary technology). The application interface to this function is by designated memory locations for voted data, initialization and frame synchronization interrupts, and auxiliary tables which define to the voting system the memory locations, frame rates, and 1553 input/ output (I/O) requirements for various mission modes. More elaborate voting, such as mid-value select, is the responsibility of the application as well as the deterministic operation within each minor frame to meet the tabledefined voting times. Ada tasking had been removed from the run-time in favor of a custom scheduler driven by the frame synchronization interrupt.

Hosting the DAP

ISI provides three means to control the generated code: a set of utility libraries which provides initialization and I/O may be modified or replaced; a template provides some control over autocoded package structure and scheduling; finally, user code blocks (UCBs) may be included by reference in the block diagram specification (BDS). Notice that neither the first two means nor any auxiliary tables required by the IFTAS are linked to the BDS.

Hosting the DAP was taken in four steps. First, code generated using the standard templet was run on the R3000 target using VADSworks, and numerical and timing performance were verified. Running the code required modification of the ISI templet to allow start times other than zero, and verification required modification of the utilities to eliminate unnecessary and confusing output. The utilities were also modified to provide near-real-time reduced-rate output to the DVdraw display by showing graphs of key parameters and graphic representations of engine gimbal positions (the integrated display capability ISI provides works only with the ISI AC100). Timing was verified at this step only to the extent necessary to rule out the need for the multirate DAP.

Second, the rehosted code was run in a single-string nonvoting mode on the Boeing IFTAS. This required a rebuild of the run-time to restore the Ada tasking, because no one was sure just how to use the custom scheduler. Once this was done the DAP ran immediately, due to the use of standard Ada and due to compatibility between VADSworks and VADScross on file system features used to load the test data.

Third, the DAP was adapted to voting, but it was run in a single computer only with a special voting test cable. Unfortunately, the synchronization interrupt had been removed because it was inextricably linked to the custom scheduler. After some investigation it was determined that the expertise was not available to install a new interrupt handler in a timely manner, and a crude polling system was adopted which took advantage of the posting of

initialization and frame synchronization to a memory location. Test data buffers in the ISI utilities were removed and replaced by references to voting locations. Test data were then provided and accumulated by the IFTAS in a special test mode. There is no validation of data into or out of the autocode except for number of parameters. All parameters are floating point. We investigated and determined that it would be easy to vote state data, because the ISI template makes data available contiguously in a floating-point array. Future releases of ISI tools will use a variety of data types and will complicate this import/export situation in ways we are not yet able to assess.

Since the autocode does not output data until the beginning of the next frame, the standard output feature would not meet the DAP's 18-ms output latency requirement. Two methods were evaluated for meeting this requirement. One was the use of a UCB to do the output, which would be executed in-line as part of the current frame computation. The other was to modify the template to extract the output data from internal locations and move the data to the output voting locations. Neither method was actually implemented due to resource diversion into getting the DAP to run in voting mode. High-resolution timing facilities that were available as part of the IFTAS test gear were used to verify performance.

Fourth, the DAP was run redundantly, with data supplied and captured via the 1553 rather than the internal test buffers. Our approach was changed at this step. Because our experience in step 3 indicated our approach would evolve, and because we intended to use the DAP to evaluate other redundant systems, peculiarities pertaining to the Boeing IFTAS were removed from all parts of the DAP at this time and were placed in a voting package. A few key features of this package are illustrated below:

```
with SA_TYPES; use SA_TYPES;
                                       - ISI type definitions
package VOTE is
      type Vote_ID_Type is private;
                                       - voting group "handle"
      procedure Establish_Vote_ID ( id : out vote_id_type;
                                       index : in integer; — IFTAS table index
                                       bufsize: in integer; - amount of data);
       procedure Get_Voted_Input
                                                 id: in vote_id_type;
                                      (
                                       values: out real_array); - ISI type defn.
      procedure Vote_Outputs
                                      ( id : in vote_id_type;
                                       values : in real_array );
      procedure Initial_Voter_Sync;
      procedure Wait_For_Next_Frame;
end VOTE;
```

Results

Wherever standard interfaces were used, such as Ada or VME, the commercial products and custom modules plugged together and operated correctly within hours or days. This included establishment of the Ethernet development connection, which hosts the DAP on VADSworks on the R3000, and the use of UNIX standard I/O pipes to get data into the DVdraw display. Getting

the 1553 to work took a maximum of 2 weeks. The VME and C interfaces were aptly demonstrated by a related project using the same lab equipment, which moved a custom analog board and its associated C software from a 68040 system to the R3000 within days.

The lack of a standard Ada scheduler on the Boeing IFTAS cost over a month because it required time to analyze options, to rebuild the kernel, and to develop workarounds for lack of synchronization interrupts. It was known a priori that no standards existed for interfacing to the data portions of either the autocode or the IFTAS. Despite excellent efforts and provisions from both vendors, and despite advance availability of documentation, each side of this interface took well over a month.

Worst-case performance of the single-rate DAP was 1 ms. This indicates an excellent margin in meeting the 18-ms requirement. It also indicates usage of only about 60% more resources than the hand-tailored flight code. We estimate about half of this is due to autocode, and half is due to going to the single-rate rather than multirate DAP. Numerical accuracy was well within tolerance, although neither the autocoded computation sequence nor the floating-point representation of the R3000 could have been identical to the reference flight code.

The DAP BDS corresponded closely to the Shuttle Flight Software System Requirements (FSSR), and the providing organization was satisfied that their productivity goals had been met. FSSR-level specifications not found in the BDS include the timing requirement and the state data voting requirement. FSSR-level specifications not fully autocoded include the above plus the I/O requirements. An annotation capability within BDS was used to provide documentation and additional specification, but there was no flowdown from the annotation into the autocode.

Conclusions

We were able to verify productivity and reliability goals both from the use of standard interfaces and from autocoding. The benefits come only for those parts of the system using the advantageous techniques. As tools and techniques are developed to improve various parts of an avionics system design, use of standard interfaces between the parts will become relatively more important in realizing a gain in the overall system development process that is commensurate with the gain in the parts. Both official and de facto standards are useful, with degree of vendor support for the standard a critical factor.

Relating to the completeness of the BDS, a means needs to be provided not only to fully annotate the BDS but to flow information into the BDS from higher level engineering tools, and to flow information from the BDS to the UCBs, the template, and the utilities so that requirements that are not processed by the autocoder—perhaps that are even unique to a particular project—can be automatically processed and validated as part of the code

build process. Manual intervention into an automated code production process was judged qualitatively by our team to be actually more hazardous than a traditional manual process. Further work to define the BDS to user code interface could result in the vendor community incorporating these features as they have in the past, in which case standards among them can then be discussed.

Relating to functional partitioning in the redundancy management (RM) system, provision needs to be made to flow application domain specifications from and to the application, ultimately the BDS. This includes the data to be voted, moding and timing requirements, and fault notification. For example, the BDS needs to know if the system operation has changed from fully operational to fail safe so that the appropriate mission mode can be selected. Certain information about the configuration of the RM system can optionally be kept separate. For example, the control part of an application does not need to know whether it is running single or multiple string, or repeatedly for error checking within a single string. Mapping to the hardware configuration could be externally supplied. Because RM is a relatively more mature discipline than is autocoding, and because capabilities of competing systems are very similar, this area is likely to benefit from an immediate effort to standardize on an application programming interface (API).

APIs have already been developed for real-time data management, such as the Space Station run-time object database. The complexity of this API and the lack of a viable way to get an implementation independent of other parts of Space Station avionics suggest some refinement is in order to make it a true standard. In this case, it would have been used to communicate the voted data from and to the autocode. In an anticipated future case where several different programming tools are mixed in an avionics system, such as a control law autocoder and a spacecraft command language, standardization of this data management interface will be critical.

Lastly, interfaces to diagnostic and display tools deserve mention. ISI tools were not used because their interface to the autocode depended on other company products. Instead a tool was used which has a standard

UNIX interface. Tools which interface generally with the other existing or proposed interfaces and components described in this paper, such as the data management interface above, would be more advantageous.

Acknowledgments

Our thanks to Gene McSwain and John Craft of the Navigation Control and Aeronautics Division for providing the DAP application used in this investigation. Ron Wood and other personnel with McDonnell Douglas provided ideas about how to put together a demo display rapidly, and Rich Ellenberger of Flight Data Systems assisted with our initial efforts to get autocoded software running on our target platform. We appreciate the loan of Lore Rice's time to provide the simulated 1553 inputs, and the hard work of task personnel from Boeing and Lockheed—especially Beth Holley, who provided numerous suggestions and comments on this paper.

References

- ¹Tomayko, James E., NASA's Manned Spacecraft Computers, *Annals of the History of Computing*, vol. 7, no. 1, January 1985.
- ²Bell, Janet, Software Support Environment Lessons Learned, JSC Doc. no. TBD, December 1993.
- ³Lockhart, Steve, The Effect of Cyclic Versus Rate Monotonic Scheduling on Math Model Performance in Real-Time Simulation, Intermetrics white paper provided to JSC, December 1989.
- ⁴Tesmer, Steven, VMEbus History and Fundamentals, Seminar at Real Time Computer Show, 1993.
- ⁵Harper, Richard E., and Lala, J. H., Fault-Tolerant Parallel Processor, *AIAA Journal of Guidance & Control*, vol. 14, no. 3., May-June 1991.
- ⁶Hodges, Deidra R., HAL/S-to-Ada Code Translation, Report to JSC under a contract with Martin Marietta, Undated.
- ⁷Ellenberger, Ling, Buscher, Uhde-Lacovara, and Shuler, Robert, *Simulation*, vol. 61, no. 5, November 1993.

REPORT DOCUMENTATION PAGE

Form Approved OMB No. 0704-0188

Public reporting burden for this collection of information is estimated to average 1 hour per response, including the time for reviewing instructions, searching existing data sources, gathering and maintaining the data needed, and completing and reviewing the collection of Information. Send comments regarding this burden estimate or any other aspect of this collection of information, including suggestions for reducing this burden, to Washington Headquarters Services, Directorate for information Operations and Reports, 1215 Jefferson Davis Highway, Suite 1204, Arlington, VA 22202-4302, and to the Office of Management and Budget, Paperwork Reduction Project (0704-0188), Washington, D. 20503.

Sui	te 1204, Allington, VA 22202-4302, and to the C				
1.	AGENCY USE ONLY (Leave Blank)	2. REPORT DATE	3. REPORT TYPE AND DATES COVERED		
		Aug/94	NASA Technical Memorandum		
4.	TITLE AND SUBTITLE The JSC Research and Developm	ent Annual Report 1993		5. FUNDING NUMBERS	
6.	AUTHOR(S)				
7.	Lyndon B. Johnson Space Center Houston, Texas 77058			8. PERFORMING ORGANIZATION REPORT NUMBERS S-757	
9.	National Aeronautics and Space A Washington, DC 20546-0001			10. SPONSORING/MONITORING AGENCY REPORT NUMBER TM-104787	
11	. SUPPLEMENTARY NOTES				
	Unclassified/unlimited Available from the NASA Center 800 Elkridge Landing Road Linthicum Heights, MD 21090-29 (301) 621-0390 ABSTRACT (Maximum 200 words)	for AeroSpace Information	ect Category: 99	12b. DISTRIBUTION CODE	
13	. ADSTRACT (Maximum 200 Words)				

Issued as a companion to Johnson Space Center's Research and Technology Annual Report, which reports JSC accomplishments under NASA Research and Technology Operating Plan (RTOP) funding, this report describes 47 additional projects that are funded through sources other than the RTOP. Emerging technologies in four major disciplines are summarized: space systems technology, medical and life sciences, mission operations, and computer systems. Although these projects focus on support of human spacecraft design, development, and safety, most have wide civil and commercial applications in areas such as advanced materials, superconductors, advanced semiconductors, digital imaging, high density data storage, high performance computers, optoelectronics, artificial intelligence, robotics and automation, sensors, biotechnology, medical devices and diagnosis, and human factors engineering.

14. SUBJECT TERMS	15. NUMBER OF PAGES 216		
Research Projects, Research and Technology Experiments	16. PRICE CODE		
17. SECURITY CLASSIFICATION OF REPORT	18. SECURITY CLASSIFICATION OF THIS PAGE	19. SECURITY CLASSIFICATION OF ABSTRACT	20. LIMITATION OF ABSTRACT
Unclassified	Unclassified	Unclassified	Unlimited

NSN 7540-01-280-5500

